TECHNISCHE UNIVERSITÄT MÜNCHEN

Physik-Department
Lehrstuhl für Funktionelle Materialien

Near-surface composition of pressure sensitive adhesive films and its impact on adhesion

Alexander Diethert

Vollständiger Abdruck der von der Fakultät für Physik der Technischen Universität München zur Erlangung des akademischen Grades eines

Doktors der Naturwissenschaften (Dr. rer. nat.)

genehmigten Dissertation.

Vorsitzender: Univ.-Prof. Dr. Martin Zacharias
Prüfer der Dissertation:
1. Univ.-Prof. Dr. Peter Müller-Buschbaum
2. Univ.-Prof. Dr. Thorsten Hugel

Die Dissertation wurde am 29.06.2011 bei der Technischen Universität München eingereicht und durch die Fakultät für Physik am 15.07.2011 angenommen.

Abstract

Acrylic pressure sensitive adhesive (PSA) films comprising either two or three different components were prepared on solid support. A structural characterization of the near-surface region was performed. X-ray reflectivity revealed information about the composition profile perpendicular to the film surface. In all investigated samples, the near-surface composition deviated from the bulk. Different sample preparation protocols were applied in order to elucidate the possibilities of a deliberate tailoring of the near-surface composition profiles. Furthermore, the obtained results were related to the mechanical behavior of the PSA films as monitored with probe tack tests or contact angle measurements to determine the surface tension. The mechanical properties as well as the morphology changed significantly when the film thicknesses were reduced to a sub-micrometer scale.

Acrylatbasierte drucksensitive Haftklebstofffilme (PSA Filme), bestehend aus entweder zwei oder drei verschiedenen Komponenten, wurden auf harten Substratmaterialien hergestellt und ihre oberflächennahen Bereiche wurden strukturell charakterisiert. Mithilfe von Röntgenreflektion wurden die Zusammensetzungsprofile senkrecht zur Filmoberfläche bestimmt. Die oberflächennahe Zusammensetzung wich in allen untersuchten Proben von der Volumenzusammensetzung ab. Es wurden verschiedene Probenherstellungsprotokolle angewendet, um die Möglichkeiten einer bewussten Steuerung der oberflächennahen Zusammensetzungsprofile zu untersuchen. Desweiteren wurden die erhaltenen Ergebnisse mit dem mechanischen Verhalten in Tack-Experimenten und Kontaktwinkelmessungen zur Bestimmung der Oberflächenspannung korreliert. Sowohl die mechanischen Eigenschaften als auch die Morphologie änderten sich signifikant sobald Filmdicken im Sub-Mikrometerbereich gewählt wurden.

Contents

Chapter 1

Introduction

Different classes of materials, such as paper, glasses, metals, ceramics and polymers can be efficiently connected by the use of adhesives [1]. This versatility of utilizing adhesive bondings is only one of the reasons why meanwhile adhesives can be found in a large variety of products. Conventional techniques like riveting, welding or the use of bolted connections are more and more replaced by employing adhesive joints. Prominent examples can be found in the construction sector or in the aeroplane and car industry.

Depending on the respective application, not always a maximization of the strength of the adhesive bonding is aspired. Most of such applications making use of moderate adhesion can be found in every day life as packaging material, self-adhesive tapes or stick-on notes. These products require a releasable connection between two materials. The necessary property of the involved adhesive to allow for a releasable bonding is provided by the so-called class of **pressure sensitive adhesives** (PSAs).

PSA films stick to adherents upon applying a slight contact pressure [2]. The resulting bonding forces are typically of van der Waals type. Neither chemical reactions nor any evaporation of solvent are involved in the bonding process. Once the bond is formed, it can sustain a certain level of stress until debonding occurs [2]. The debonding is a very complex process which includes the deformation and mechanical failure of the adhesive. As a consequence, the performance of a PSA does not only originate from a good stickiness but also the mechanical properties of the adhesive contribute substantially [3].

The physical processes, which are present during the debonding, are still not well understood. One reason is that the mechanical deformation of the viscoelastic adhesive is in a highly non-linear regime. Another reason is that, in most cases, the PSA materials are not homogeneous and comprise numerous ingredients. In commercially available PSAs, many different components are involved to optimize the complex and often conflicting interplay between sticky PSA surfaces and internal mechanical stiffness, i. e. cohesion. The exact influence of each of the components is mostly unknown. Furthermore, it is conceivable

that compositional fluctuations can occur close to the interfaces. Up to now, there are no works directly quantifying the impact of such an inhomogeneous spatial distribution of the ingredients.

In general, different types of PSAs are available. In this work, so-called acrylic PSAs are selected. They typically consist of statistical copolymers comprising the different monomeric components which are necessary for the desired performance [2]. The components are acrylates such as ethylhexylacrylate being soft and sticky and methylmethacrylate as a hard and stiff material. Optimized PSAs contain many different components, maybe even different statistical copolymers. The exact formulations of commercially available PSAs are in most cases not accessible. In industry, the mechanical optimization of these products is performed empirically and a deeper understanding of the influence of the involved materials is still missing.

For a basic structural and mechanical investigation it is, however, not advisable to start with such multi-component PSA systems. It is necessary to study model systems with a reduced number of components so that the individual contributions to the observed effects remain distinguishable. At the same time, the basic architecture of the PSA must be preserved. Thus, in this work most of the studied acrylic PSA model systems consist of two components, one of which is tacky and the other one is glassy.

In literature, there are already works addressing the adhesive performance of films of such model systems [4, 5]. The new aspect, which is added by the presented thesis, is the investigation of the distribution of the involved components near the interface and the resulting impact on the adhesion. Thereby, the focus is on the interface between the PSA film and the surrounding air because this region represents the area which is contacted by possible adherents. A suitable method for such structural characterization is x-ray reflectivity, with which the near-surface composition is monitored as a function of distance from the sample surface.

In this work, the film preparation is mostly based on solution casting. For this purpose, the statistical copolymer based PSAs are dissolved in an organic solvent, the solution is spread on a solid support and a dry film is obtained after the solvent has evaporated [6]. The selected film thickness of solution cast films is 50 μm and it is kept constant throughout this work. The solvent evaporation kinetics during drying is crucial for the resulting near-surface composition. Therefore, after considering the theoretical aspects related to the presented work (chapter 2) and describing the different characterization techniques (chapter 3), the first issue, which is investigated, is the spatial distribution of the solvent as a function of time during the solution casting (chapter 4).

For the produced PSA films, it is distinguished whether the films are prepared under ambient conditions or under certain types of atmospheres. The case of ambient conditions

is probably the most relevant scenario for standard applications. To understand the observed near-surface compositions for the case of ambient conditions, different influencing factors are investigated in chapter 5: the type of copolymerized material, the molecular weight and the sample age. Furthermore, the near-surface composition of solution cast PSA films is compared to films processed via the almost solvent-free doctor-blading technique.

Chapter 6 provides a discussion of if an additional fine tuning of the near-surface composition by performing the film preparation under a controlled atmosphere is achievable. In this context, different relative humidities and solvent vapor atmospheres are applied. Also the additional influence of the choice different solvents for the solution casting is elaborated. Most important for applications is the question: Do such controlled environments alter the mechanical performance of the PSAs?

Once a certain state of the near-surface composition is generated, it is interesting to examine the stability of the molecular arrangement. Or in other words, is there a rearrangement of the involved components? And if so, does it depend on the initial near-surface composition profile and is there an influence of the storage conditions? Besides a discussion of this so-called aging process, chapter 7 reveals whether there are also structures parallel to the film surface.

Finally, the preparation method is changed to spin-coating in order to process films with thicknesses down to the sub-micrometer regime (chapter 8). The resulting film morphologies are compared to those obtained for thick, solution cast films. Furthermore, for the first time the macroscopic tackiness of such ultra-thin PSA films is successfully studied. The influence of the contact force of an adherent as well as the influence of the film thickness within the ultra-thin regime are investigated.

Chapter 2

Theoretical aspects

In this work, the impact of interfacial phenomena on the mechanical properties of solution cast pressure sensitive adhesive (PSA) films consisting of statistical copolymers is addressed. It is therefore important to understand possible driving forces that influence the obtained morphologies and the resulting tackinesses. For the morphologies, solubility effects which are responsible for selective transport during the solution casting process and surface tensions of the involved components are crucial. In close connection to these aspects, also the interaction of the sample surface with adherents as well as the mechanical properties of the adhesive itself play a key role for the resulting adhesive performance. However, it will be shown that due to, for example, non-equilibrium conditions and material failure, still, a theoretical description of the physical processes in a so-called probe tack test remains difficult.

It is important to note that the morphologies do not only depend on external driving forces. In a theoretical work, Flory and Huggins quantified parameters which are helpful in the description and prediction of phase separation phenomena. This theory is introduced for the example of binary polymer blends. Despite the significantly higher complexity of the case of statistical copolymers, predictions concerning nano-phase separation for this type of polymer are possible.

The resulting spatial distribution of the individual components in the adhesive is monitored with reciprocal scattering techniques. X-ray reflectivity being highly sensitive to the electron density is capable of probing the composition profiles perpendicular to the sample surface. Structures that are arranged parallel to the film-air interface can be monitored with grazing incidence small angle x-ray scattering. Both techniques have a similar theoretical background which will be presented at the end of this chapter.

2.1 Solution cast pressure sensitive adhesive films

In order to be able to explain many of the observed near-surface morphologies, it is necessary to recall some practical aspects concerning the solubility of a polymer in a solvent. The resulting near-surface chemical composition after solution casting is essential for the interaction characteristics (see section 2.1.2) with potential adherents. One important aspect, that is addressed next, is the wetting behavior which is driven by the surface tensions of the involved materials. But for a good adhesive bonding, also the mechanical strength of the PSA is decisive. These are often monitored with rheological measurements (section 2.1.5). Finally, theoretical approaches towards the description of probe tack tests are discussed.

2.1.1 Miscibility of solvents and polymers

Due to the enormous prevalence of solution based coating techniques of polymeric products, there are many different approaches how to quantify the respective solubilities. Among these are the Kaouri-Butanol number, the solubility grade, the aromatic character, the analine cloud point, the wax and the heptane number as well as the Hildebrand solubility parameter [7]. The latter and even more complex derivations like the Hildebrand number, the hydrogen bonding value, the Hansen parameter or the fractional parameter are widely used. For this study, in which the polarities of the involved components are relatively low, especially the Hildebrand parameter turned out to be a powerful tool for the understanding of the obtained composition profiles.

In general, a polymer will dissolve in a solvent when the dissolution leads to a decrease in the Gibbs free energy G of the system. We focus on the Gibbs free energy change upon mixing

$$\Delta G_m = \Delta H_m - T\Delta S_m, \tag{2.1}$$

where T is the temperature, ΔH_m the corresponding change in enthalpy and ΔS_m the change in entropy [8]. It is obvious that the latter is always positive in dissolution processes. Therefore, the sign and magnitude of the enthalpy term is decisive for the miscibility.

The polymer and solvent molecules, that are used in this work, are mainly held together by van der Waals forces. To create a solution, it is therefore necessary that the solvent molecules are positioned between and around the solute molecules. As a consequence, it is advantageous when the molecular attraction forces of the polymer chains are similar to those of the solvent. This is quantified by Hildebrand [9] and Scatchard [10] in the

equation

$$\Delta H_m = V_m \left(\left(\frac{\Delta E_1^v}{V_1} \right)^{1/2} - \left(\frac{\Delta E_2^v}{V_2} \right)^{1/2} \right)^2 \Phi_1 \Phi_2, \tag{2.2}$$

in which V_m is the volume of the mixture, ΔE_j^v is the energy change upon isothermal vaporization at infinite volume, V_j the molar volume and Φ_j the volume fraction of the polymer ($j = 1$) and the solvent ($j = 2$), respectively. The **Hildebrand solubility parameters** of the polymer ($\mathfrak{D}_1$) and the solvent ($\mathfrak{D}_2$) are defined as the square roots of the respective cohesive energy densities [8].

$$\mathfrak{D}_j = \left(\frac{\Delta E_j^v}{V_j} \right)^{1/2} \qquad (j = 1, 2) \tag{2.3}$$

They are a suitable measure for the adhesive strength between the molecules of the material. With these parameters, equation (2.2) simplifies to

$$\Delta H_m = (\mathfrak{D}_1 - \mathfrak{D}_2)^2 V_m \Phi_1 \Phi_2 \geq 0. \tag{2.4}$$

In order to minimize ΔH_m and, thus ΔG_m, the solubility parameters of the solvent and the solute must therefore have a similar value. Or, in other words, this is the case when the attraction forces between the molecules of each of the two materials are similar. More details can be found in references [7] and [8].

2.1.2 Van der Waals forces

Now we leave the preparation step and assume a solvent free PSA film. In contrast to many other classes of adhesives, the bonding of a PSA to an adherent takes place in the solid state. The interface forces which are present in a PSA film are almost exclusively van der Waals forces [2].

Van der Waals forces are non-covalent, electromagnetic forces between typically uncharged atoms or molecules which are based on electric dipole interactions [11]. In this work we focus on the case of (polymer) molecules. The origin of the van der Waals forces is the electric **polarizability** which means that molecules may have an inhomogeneous charge distribution. The latter can be described by the so-called **dipole moment**

$$\vec{\mu} = \int \varrho_e(\vec{r}) \vec{r} \, \mathrm{d}V, \tag{2.5}$$

which is calculated as the integral over the charge densities $\varrho_e(\vec{r})$ at all positions $\vec{r}$ in the molecule. The polarizability α is defined as $\mu = \alpha E_{el}$ for a given electric field $\vec{E}_{el}$. The resulting van der Waals forces basically consist of three contributions which are detailed in the following.

The directions of the dipole moments $\vec{\mu_1}$ and $\vec{\mu_2}$ of two molecules, which can freely rotate, will change when the distance d between the molecules is sufficiently small. Opposite charges tend to face each other and equal charges will increase their distance from each other. The consequence is an attractive force between these molecules. The energy which corresponds to the force between randomly oriented dipoles is referred to as **Keesom energy**

$$W_{orient} = -\frac{C_{orient}}{d^6} = -\frac{\mu_1^2 \mu_2^2}{3(4\pi\epsilon_0)^2 k_B T d^6}, \tag{2.6}$$

where k_B is the Boltzmann constant and ϵ_0 the dielectric permittivity in vacuum [11].
A similar case is the so-called **Debye interaction**, where a static dipole interacts with a non-polar molecule of polarizability α [11]. Under the assumption of a freely rotating dipole, the corresponding Helmholtz free energy is

$$W_{ind} = -\frac{C_{ind}}{d^6} = -\frac{\mu^2 \alpha}{(4\pi\epsilon_0)^2 d^6}. \tag{2.7}$$

Finally, there is a third attractive force which acts between two non-polar molecules with polarizabilities α_1 and α_2. It is called the **London** or **dispersion force** [11]. Its origin are temporary dipoles due to quantum mechanical fluctuations of the electron cloud. When two such oscillators approach and influence each other, attractive configurations have a higher probability than repulsive ones. The corresponding Helmholtz free energy between two molecules with ionization energies $h\nu_1$ and $h\nu_2$ is

$$W_{disp} = -\frac{C_{disp}}{d^6} = -\frac{3\alpha_1 \alpha_2 h \nu_1 \nu_2}{2(4\pi\epsilon_0)^2 (\nu_1 + \nu_2) d^6}. \tag{2.8}$$

In reality, the Keesom, Debye and London interactions are present at the same time. Their individual contributions sum up to the total van der Waals force. Because all three corresponding energies are proportional to d^{-6}, the corresponding prefactors can simply be added and the final potential energy of the interaction between two molecules A and B can be written as

$$W_{AB} = -\frac{C_{AB}}{d^6} = -\frac{C_{orient} + C_{ind} + C_{disp}}{d^6}. \tag{2.9}$$

In order to derive the potential energy per surface area w between two objects with plane and parallel surfaces at a certain distance d, the van der Waals energy between a homogeneous solid of type A and a single molecule of type B has to be calculated first. For this purpose, the contributions of all molecules in the solid have to be summed up. This is done by an integration of the molecular density ϱ_A over the volume of the solid.

$$W_{molecule/solid} = -C_{AB} \iiint \frac{\varrho_A}{\tilde{d}^6} \, \mathrm{d}V = -\frac{\pi \varrho_A C_{AB}}{6 d^3} \tag{2.10}$$

w is calculated via a similar integration, where all the contributions of the molecules of type B are summed up. As a result,

$$w = -\frac{A_H}{12\pi d^2} \tag{2.11}$$

is obtained, where the so-called **Hamaker constant** $A_H = \pi^2 C_{AB} \varrho_A \varrho_B$ is used [11]. The force per unit area f, which is the negative derivative of w, follows as

$$f = -\frac{A_H}{6\pi d^3}. \tag{2.12}$$

As an example, the Hamaker constant of a polystyrene film on a SiO_2 substrate [12] is $2.2 \cdot 10^{-20}$ J. The resulting van der Waals forces at a distance of 100 nm are calculated to be 1.2 N/m^2, which shows that these forces are, compared to a molecular scale, of long ranged nature. Further aspects of van der Waals forces are elaborated in [11].
It is important to note that the equations for the van der Waals forces do not hold for arbitrary distances d. At very short distances, the electron orbitals of the molecules overlap and the interaction becomes repulsive [13]. Whereas the attractive intermolecular van der Waals forces show a proportionality to d^{-6}, the repulsive forces have the opposite sign and are assumed to be proportional to $d^{-n_{rep}}$, where n_{rep} is usually chosen between 9 and 16 [14]. As a consequence, the repulsive forces outweigh the attractive ones for sufficiently small d. For $n_{rep} = 12$, the total potential is called **Lennard-Jones potential** and, by introducing a weighting factor of the repulsive forces C_{AB}^{rep}, it can be written as

$$W_{AB} = \frac{C_{AB}^{rep}}{d^{12}} - \frac{C_{AB}}{d^6}. \tag{2.13}$$

2.1.3 Adhesion, cohesion and surface tension

Based on the knowledge about the contributions to van der Waals forces, we define the work of adhesion and cohesion from a thermodynamical point of view [14]. Although these quantities represent a very important aspect of the (de-)bonding mechanisms of a PSA, they are not sufficient for a full description. The reason is that, among other phenomena, the deformation of the adhesive is not taken into account. Therefore, the work of adhesion is not to be mixed up with the tack energy obtained in a probe tack test.
The reversible work, or in other words the free energy change, that is necessary to separate unit areas of two materials A and B from contact to infinite distance (see figure 2.1), is called **work of adhesion** W_{AB} [14]. For the materials used in this work, it fully originates from the van der Waals forces attracting the two materials which have to be overcome. The two materials do not necessarily have to be solids. For the case of a liquid in contact with a solid, the work of adhesion is often denoted as W_{SL}.

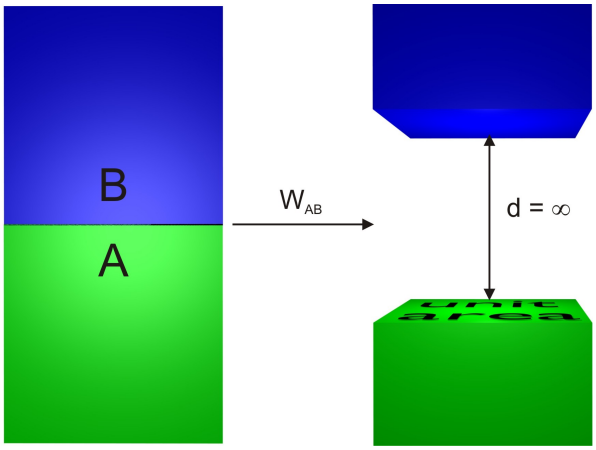

Figure 2.1: *Illustration of the work of adhesion. Two materials A and B are separated to infinite distance.*

In contrast to adhesion, the cohesion describes the physical interaction forces between the same type of molecules [15]. They are for example responsible for the structural integrity of a polymer film. The definition of the corresponding **work of cohesion** is equal to that of the work of adhesion, except that the two materials are the same ($A = B$) [14]. The work of cohesion is denoted as W_{AA}.

The **surface energy** or the **surface tension** γ_A is a material property which is closely related to the work of cohesion. Strictly speaking, the term surface energy is a property of solids, whereas the surface tension is related to liquids. The reason for the terminology is the different measurement techniques. But in many cases, and also in this work, these terms are not distinguished.

The surface energy is defined as the free energy change when the surface area of a material is increased by unit area. As illustrated in figure 2.1, when an object with a cross section of unit area is split into two parts, then a surface of two unit areas is created. As a consequence, in terms of the work of cohesion [14]

$$\gamma_A = \frac{1}{2} W_{AA} \tag{2.14}$$

is obtained. It is common to write γ_S when the material is a solid, and γ_L for liquids, respectively.

The concept of surface tension can be extended towards the case of adhesion. When two immiscible materials A and B get in contact, their interfacial area will change in order to minimize the free energy. The so-called **interfacial energy** or **interfacial tension** is the resulting free energy change per unit area. It can be calculated via

$$\gamma_{AB} = \frac{1}{2} W_{AA} + \frac{1}{2} W_{BB} - W_{AB} = \gamma_A + \gamma_B - W_{AB}, \tag{2.15}$$

which is also called **Dupré equation** [14]. It can be understood by splitting the process into two steps. Before the contact is closed, in a first step, the surface areas of the

two materials have to be changed. This means, that there is work of cohesion for both materials. In a second step, the materials with the altered interfacial area are brought in contact and the energy, which corresponds to the work of adhesion, is released. The Dupré equation is often used for the description of solid-liquid interfaces and thus, can often be found in the form

$$\gamma_{SL} = \gamma_S + \gamma_L - W_{SL}. \tag{2.16}$$

Finally, we increase the complexity by one more step. In reality, the separation of two materials, as illustrated in figure 2.1, is not performed in vacuum (although for many cases this is a good approximation) but in a certain medium C, which can be for example a gas or a liquid. In analogy to the above derivation [14], the corresponding energy change is given by

$$W_{ACB} = W_{AB} + W_{CC} - W_{AC} + W_{BC} = \gamma_{AC} + \gamma_{BC} - \gamma_{AB}. \tag{2.17}$$

2.1.4 Contact angles

The surface and interfacial tensions, which were introduced in the previous section, determine the deformation of liquid droplets on a solid support [14]. The contact angle Θ between the initially spherical droplet (material B) and the solid support (material A), as it is illustrated in figure 2.2, is an important parameter. Assuming that the droplet and the solid support, on which it is placed, are embedded in a medium C, the total surface energy of the system is

$$W_{tot} = \gamma_{BC}(A_c + A_f) - W_{ACB}A_f, \tag{2.18}$$

where A_c is the curved and A_f the flat area of the droplet [14]. The equation can be understood by imagining again a two-step process in which first, the in medium C isolated droplet is deformed from the spherical to its final shape on the solid support and, second, the deformed droplet is placed on material A.

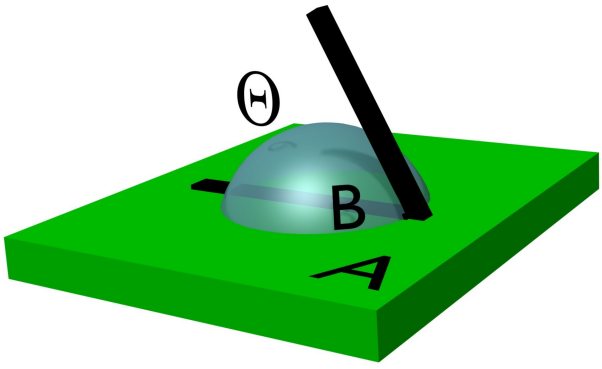

Figure 2.2: *Contact angle of a liquid droplet (material B) on solid support (material A).*

At equilibrium, the total derivative of W_{tot} is zero and thus

$$\gamma_{BC}(\mathrm{d}A_c + \mathrm{d}A_f) - W_{ACB} \cdot \mathrm{d}A_f = 0. \tag{2.19}$$

Using additionally the geometric identity $\mathrm{d}A_c/\mathrm{d}A_f = \cos(\Theta)$ leads to

$$\gamma_{BC}(1 + \cos(\Theta)) = W_{ACB} \overset{2.17}{=} \gamma_{AC} + \gamma_{BC} - \gamma_{AB} \quad \text{and} \tag{2.20}$$

$$\gamma_{AB} + \gamma_{BC}\cos(\Theta) = \gamma_{AC}. \tag{2.21}$$

If medium C is replaced by an inert atmosphere, these expressions simplify and the famous equations of Young and Dupré follow [14].

$$\gamma_B(1 + \cos(\Theta)) = W_{AB} \qquad \textbf{(Young-Dupré equation)} \tag{2.22}$$

$$\gamma_{AB} + \gamma_B\cos(\Theta) = \gamma_A \qquad \textbf{(Young equation)} \tag{2.23}$$

The Young-Dupré equation relates the work of adhesion between a liquid droplet and a solid to the corresponding contact angle and the surface tension of the liquid. In contrast to that, the Young equation does not directly use the work of adhesion. It tells how to calculate the interfacial tension between a liquid and a solid, when the surface tensions of the materials are known and the contact angle is measured.

Based on the Young equation, Owens and Wendt [16] developed a method with which the surface tension of a solid (in our case a polymer film) can be determined. For this purpose, the contact angles of droplets of different test liquids with respect to the solid support under investigation are measured. The method requires the knowledge of the surface tensions of the involved liquids.

This so-called **Owens-Wendt method** uses theoretical considerations which were published by Fowkes [17]. He postulated that the surface tensions of both, the solid and the liquid can be written as a sum of contributions which are referred to as **dispersive** and **polar part** (superscripts d and p, respectively) of the surface tension. The dispersive contribution fully originates from the London forces, whereas the polar part encompasses the Keesom and Debye interactions (see section 2.1.2). Using again S and L for solid and liquid (instead of A and B), Fowkes' ansatz can be written as

$$\gamma_L = \gamma_L^d + \gamma_L^p \quad \text{and} \quad \gamma_S = \gamma_S^d + \gamma_S^p. \tag{2.24}$$

In addition to that, he related these components to the solid-liquid interfacial tension via

$$\gamma_{SL} = \gamma_S + \gamma_L - 2\sqrt{\gamma_S^d\gamma_L^d} - 2\sqrt{\gamma_S^p\gamma_L^p}. \tag{2.25}$$

In combination with the Young equation, Owens and Wendt derived in a straightforward calculation [16]

$$1 + \cos(\Theta) = 2\sqrt{\gamma_S^d}\frac{\sqrt{\gamma_L^d}}{\gamma_L} + 2\sqrt{\gamma_S^p}\frac{\sqrt{\gamma_L^p}}{\gamma_L}. \tag{2.26}$$

For the sake of convenience, in this work we leave out the subscripts for the liquids, which have all known surface tensions and write $\gamma = \gamma_d + \gamma_p$. For the polymers under investigation we write $\gamma(\text{polymer}) = \gamma_d(\text{polymer}) + \gamma_p(\text{polymer})$, accordingly. With this simplified denotation, a rearrangement of equation 2.26 leads to

$$\frac{(1+\cos(\Theta))\,\gamma}{2\sqrt{\gamma_d}} = \sqrt{\gamma_d(\text{polymer})} + \sqrt{\gamma_p(\text{polymer})}\sqrt{\frac{\gamma}{\gamma_d} - 1}. \tag{2.27}$$

This is a linear equation with $\sqrt{\gamma_d(\text{polymer})}$ as the y-axis intercept and $\sqrt{\gamma_p(\text{polymer})}$ as the slope. All other terms are known except for the contact angle Θ, which is measured. Because this equation holds for any liquid, the measurement of Θ of two different test liquids would in principle be sufficient do determine $\sqrt{\gamma_d(\text{polymer})}$ and $\sqrt{\gamma_p(\text{polymer})}$. In reality, however, experimental errors have to be taken into account and the resulting values would not be satisfactorily accurate. That is why in this work six test liquids with a broad range of polarities are chosen. A linear fit to the data then reveals reliable values for the components of the surface tensions.
The latter is probably the biggest advantage of the method of Owens and Wendt [16]: not only the surface tension of a polymer film is determined in a non-destructive way, but also information about the type of van der Waals interaction in the near-surface region of the polymer under investigation is obtained.

2.1.5 Rheology

The surface tension of a PSA film is crucial for the wetting behavior on a potential adherent. The same holds for the viscosity which is also an important issue when the surfaces, that get in contact for the adhesion, are not perfectly plane and defects have to be compensated. During debonding, the performance of a PSA is also determined by the ability to sustain a certain level of stress [18]. As most polymers, PSA films exhibit viscoelastic behavior, which means that they combine viscous and elastic properties. All these aspects can be nicely quantified by so-called rheological measurements. In the following, a brief introduction in rheology will be given and some features which are characteristic for PSAs will be presented.
Assuming that the applied forces are sufficiently small, the corresponding deformation of a polymeric sample can be described by linear equations [19]. This regime is called linear viscoelastic range. The simplest case is the so-called **creep experiment**, in which a constant force acts instantaneously perpendicular to the sample surface (z-direction) and the elongation in z-direction ΔL_z is recorded as a function of time t. It is common to normalize the elongation with respect to the initial sample thickness L_z so that the so-called time-dependent longitudinal **strain** $e_{zz}(t) = \Delta L_z(t)/L_z$ is monitored. Furthermore,

the force is normalized to the area to which it is applied, so that a constant tensile **stress** σ^0_{zz} is obtained. We use the standard convention that the first z in the index points in the direction of the normal vector of the surface upon which the force acts and the second z indicates the direction of the stress component [19]. The tensile **creep compliance** is finally defined as $\tilde{D}(t) = e_{zz}(t)/\sigma^0_{zz}$.

In contrast to the creep experiment, one can also instantaneously impose a constant tensile strain e^0_{zz}, and measure the stress σ_{zz} as a function of time. The result of such a so-called **stress relaxation experiment** [19] is the **tensile modulus** $\tilde{E}(t) = \sigma_{zz}(t)/e^0_{zz}$.

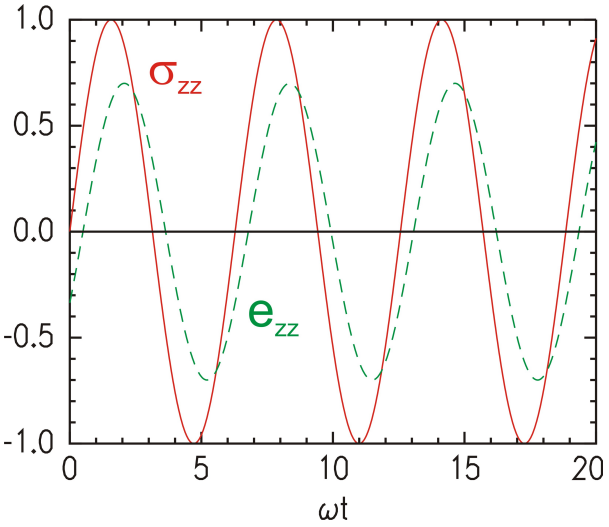

Figure 2.3: *Periodically varying stress field in a dynamic-mechanical measurement (solid line). The dashed line represents a typical resulting strain, which exhibits a different amplitude and a phase lag.*

In practice, most information can be gathered with dynamic-mechanical experiments [19], where for example a periodically varying stress field with amplitude σ^0_{zz} and frequency ω is applied: $\sigma_{zz}(t) = \sigma^0_{zz} \exp[-i\omega t]$. The resulting time-dependent strain also varies periodically. The amplitude e^0_{zz} of the periodicity of the strain is a function of ω and exhibits an ω-dependent phase lag $\tilde{\Phi}$ (see figure 2.3) so that the strain obeys the equation

$$e_{zz}(t) = e^0_{zz} \exp[i\tilde{\Phi}] \exp[-i\omega t]. \tag{2.28}$$

Due to the complex arguments of the exponential functions, the corresponding **dynamic tensile compliance** can be written as

$$\tilde{D}(\omega) = \frac{e_{zz}(t)}{\sigma_{zz}(t)} = \tilde{D}' + i\tilde{D}'', \tag{2.29}$$

with real numbers $\tilde{D}'$ and $\tilde{D}''$.

In analogy to the stress relaxation experiment, one can also impose a periodically varying strain, and monitor the resulting stress [19]. The result is the **dynamic tensile modulus** $\tilde{E}(\omega) = (\tilde{D}(\omega))^{-1} = \tilde{E}' + i\tilde{E}''$.

Due to practical reasons, for PSA films mostly dynamic shear experiments are performed, in which the applied force is perpendicular (for example x-direction) to the surface normal. As a result, the **dynamic shear modulus**

$$G(\omega) = \frac{\sigma_{zx}(t)}{e_{zx}(t)} = \frac{\sigma^0_{zx} \exp[-i\omega t]}{e^0_{zx} \exp[i\tilde{\Phi}] \exp[-i\omega t]} = \frac{\sigma^0_{zx}}{e^0_{zx}} \exp[-i\tilde{\Phi}] = G'(\omega) + iG''(\omega) \tag{2.30}$$

is obtained [19]. In order to gain as much information as possible, the dynamic-mechanical experiments are carried out over a broad frequency interval. In this context, the variation of the temperature is an established tool to extend the accessible frequency range. Parts of the curves of G' and G'', that are measured at different temperatures, are merged to a master curve by applying a shift factor a_T to the ω-values [19].

G' is a measure for the energy exchange in a dynamic-mechanical experiment, whereas G'' represents the dissipated power. That is why G' and G'' are referred to as **storage** and **loss modulus**, respectively [19].

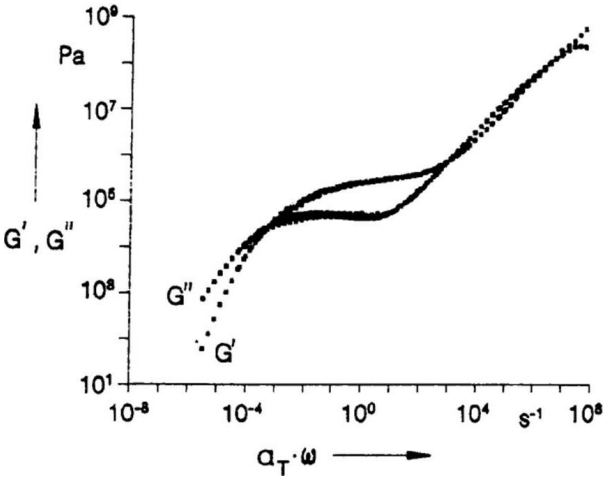

Figure 2.4: *Storage and loss modulus of polyisobutylene obtained from a dynamic-mechanical shear experiment. The image is taken from reference [20].*

Figure 2.4 shows typical ω-dependencies of G' and G'' of an uncrosslinked adhesive, which is polyisobutylene in this case [20]. The data show two points of intersection at approximately 10^{-3} s^{-1} and 10^3 s^{-1} which gives rise to identify basically three prominent regions. The first one is the so-called flow regime for small frequencies, in which the loss modulus dominates ($G' < G''$). Furthermore, the proportionalities $G' \propto \omega^2$ and $G'' \propto \omega$ are obtained. The intermediate region between the intersections is called rubbery regime. It is characterized by a constant storage modulus, that is significantly higher than the loss modulus. In the final (dynamically clamped) glass transition zone at high frequencies, the values of G' and G'' are very similar and exhibit power law behavior [20].

2.1.6 Probe tack test

The previous sections have shown that possible experiments to probe the mechanical properties of PSA films are on the one hand rheological measurements which focus on the bulk properties and, on the other hand, contact angle measurements characterizing the interfacial interactions. Although those parameters are important for adhesive applications, the most important property of a PSA, the tackiness, is not directly examined. In order to do so, different techniques have been established. Among these are the Johnson-Kendall-Roberts method [21], the finger [22], shear adhesion [23], rolling ball [24, 25], rolling cylinder [26], loop tack [27] or the peel test [28]. When ultra-thin adhesive layers are concerned, also atomic force microscopy is a meaningful tool [29, 30].

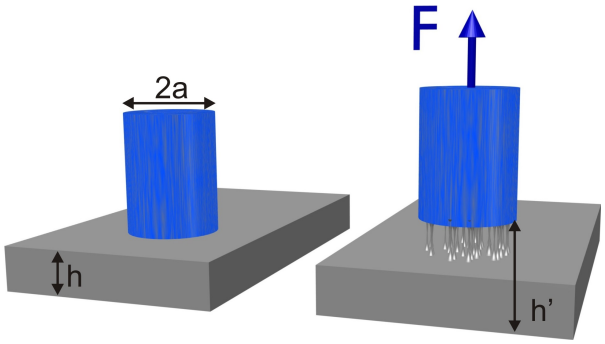

Figure 2.5: *Principle of a probe tack test. Step 1 (left): cylindrical punch is pressed onto the adhesive film. Step 2 (right): retraction process and formation of fibrils.*

Most useful, however, is the so-called probe tack test [31, 32, 33]. Its main advantage is the possibility to monitor the debonding process in detail. The principle of operation is that a cylindrical punch with radius a applies a nominal stress σ_N to the adhesive film of thickness h for a well-defined time interval (see figure 2.5, left). After this, the punch is retracted at constant speed (figure 2.5, right) and the force F corresponding to the nominal stress σ_{zz} is measured as a function of distance $d = h' - h$. The **confinement** in the system is defined as a/h [34].

For the sample systems in this work, it is important to note that the connection between the PSA film and the substrate is assumed to be perfect. This means that the punch can not simply lift off the complete film. For debonding, either the punch surface has to be separated from the PSA surface (adhesive failure) or the PSA itself has to be torn apart (cohesive failure).

The pressure distribution under the cylindrical probe is inhomogeneous [35]. For large values of a/h, edge effects are negligible and a parabolic pressure distribution

$$p(r) = -\sigma_{zz}(r) = p_0 - 2L\sigma_N \left(1 - \frac{r^2}{a^2}\right) \tag{2.31}$$

is obtained, where r is the radial distance from the cylinder's center of symmetry, p_0 is the atmospheric pressure and $L = h'/h$ the extension ratio. It is important to note that this

equation only holds for homogeneous and full contact between probe and adhesive. The presence of fibrils, which are the result of elongated voids or cavities, makes the situation more complex.

Following Shull and Creton [36], the average strain underneath the punch is given by $e = (h' - h)/h$ and, under the assumption of an incompressible elastic solid with shear modulus G, the nominal stress is

$$\sigma_N = \frac{8G(h' - h)}{\pi a}. \tag{2.32}$$

The performance of a PSA depends very much on the fibrillation process. The underlying mechanism is the expansion of so-called cavities, which are small defects or voids inside the PSA or at the PSA-punch interface. The fibrils are then the remaining material between the elongated voids. The origin of the cavities is, however, not fully clarified. One proposed explanation is that the PSA and the punch surface have roughnesses (for definition, see equation 2.79) on different length scales giving rise to interfacial defects [37]. But besides the roughness, also the polymer chain length determines the size and number of cavities. Furthermore, the cavities appear at different stages of the debonding process and exhibit age-dependent growth rates [38].

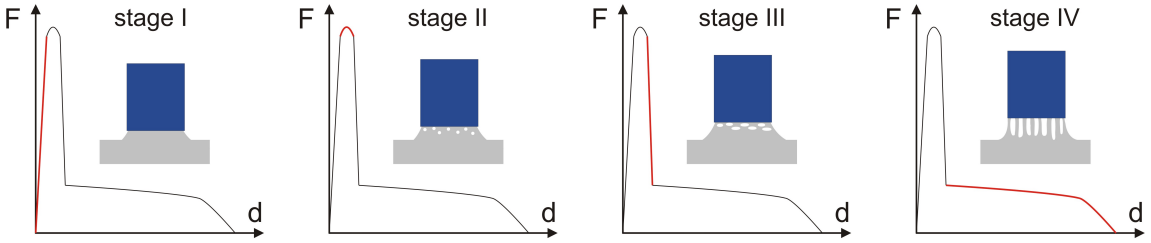

Figure 2.6: *Four-stage model of cavitation in a probe tack test introduced by Creton [39]. The graphs show the typical shape of the obtained force-distance curves. The insets schematically illustrate the stage of the cavitation process. The respective stages coincide with the time interval at which the highlighted (red color) parts of the force-distance curves are measured.*

Creton introduced a four-stage model of debonding (see figure 2.6). In detail, he divided typical force-distance curves in four parts to each of which he attributed a specific phase of cavity growth [39]. In the beginning of the debonding process (stage I), the PSA material expands homogeneously and no cavities are present. At the same time, a strong linear increase of the force is obtained. In the region around the force maximum, first defects or voids appear in the elongated material (stage II). For thick acrylate based PSA films, which are used in this work, the locus of the defects is expected to be in a region close to the punch [40]. In stage III, these voids then expand mostly laterally which causes a drop in the measured force. By further increasing d (stage IV), the cavities finally grow

vertically. Although the exact shape of the force-distance curves within stage IV depends on the chosen material and the experimental parameters, the respective slope is mostly smaller than in stage I. In this work, strictly negative slopes are obtained in stage IV. In any case, due to adhesive or cohesive failure the force drops to zero at the end of stage IV.

To approach the problem of cavity growth theoretically [36], we assume one spherical void (see stage II of figure 2.6) of initial radius R_c^0 that is filled with an ideal gas. The void (or bubble) is embedded in an inelastic, infinite and incompressible material of surface tension γ. The pressure difference between inside and outside the bubble is the so-called Laplace-pressure which is $-2\gamma/R$ for spherical objects of radius R [36]. Outside the bubble, the pressure is the applied pressure p, whereas inside the void, the deviation from the initial pressure p_0 can be calculated via the ideal gas equation. Consequently, under the additional assumption that the spherical shape is preserved (which is not completely in accordance with Creton's four-stage model), the extension ratio L_R of the bubble radius fulfills the equation [36]

$$p = \frac{p_0}{L_R^3} - \frac{2\gamma}{L_R R_c^0}. \tag{2.33}$$

In the more, but still not sufficiently, realistic case of an elastic medium, in which the bubble is embedded, this description is oversimplified. Correction terms have to be added to account for the additional elastic inflation pressure which is necessary to maintain the elastic deformation of the material. For this purpose, a model has to be assumed to describe the strain energy density of the deformed material. The so-called neo-Hookean material is the simplest model describing the elasticity of rubber at finite strains. Applying this model leads to

$$p = \frac{p_0}{L_R^3} - \frac{2\gamma}{L_R R_c^0} - \frac{1}{6}\left(5 - \frac{4}{L_R} - \frac{1}{L_R^4}\right) E_Y, \tag{2.34}$$

where E_Y is the Young's modulus [36].

The model as it is presented so far, is a promising ansatz for a theoretical description of probe tack tests. However, it does not describe the pronounced vertical growth of the cavities, it assumes complete reversibility of the processes, i. e. no plastic deformation or flow, it does not account for coalescence of voids and it does not consider failure mechanisms at large strains. Although further analysis [36] and different approaches [41, 42] provide additional insights, a full understanding of all the processes has not been achieved yet.

Finally, it has to be emphasized that also the confinement plays an important role for the resulting deformation phenomena [43]. Besides the already described cavitation process, which predominantly takes place in the experiments presented this work, also external

and and internal cracks can occur [44]. These cracks are interfacial failures originating from the PSA-punch contact area. For the external crack, the defects are located at the edge of the punch. In contrast to that, there is no contact between the internal cracks and the punch boundary. The internal cracks are surrounded by PSA material and can be treated as initially debonded areas.
Creton and coworkers developed a so-called deformation map, which in principle allows for a prediction of the deformation behavior of a given PSA [44]. The resulting landscape encompasses the three described phenomena bulk cavitation, internal crack and external crack (see figure 2.7). Which of those three types dominates the behavior of the PSA under investigation depends on the confinement (x-axis) and the value of $\mathcal{G}_0/Ea$ (y-axis). Whereas the elastic modulus E is a bulk parameter, the interfacial parameter $\mathcal{G}_0$ is a critical energy release rate which characterizes the adhesion between the punch and the PSA. In reality, however, predictions are difficult because in most cases $\mathcal{G}_0$ is not known [44].

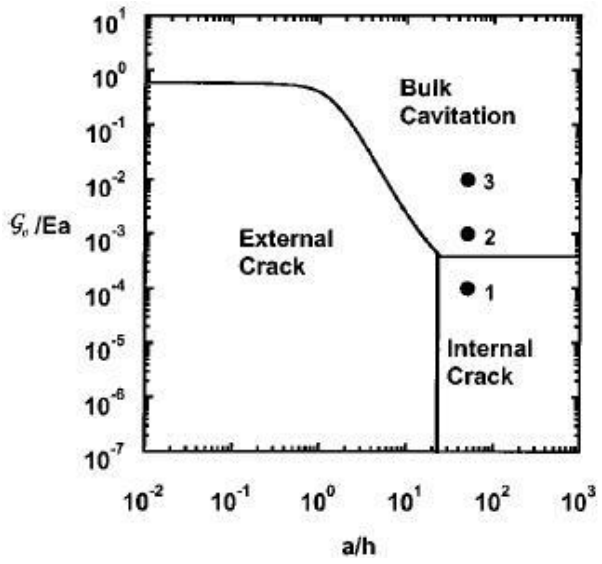

Figure 2.7: *Deformation map by Creton and coworkers. The points which are labeled with the numbers* 1, 2 *and* 3 *indicate corresponding measurements which were performed by the authors. The image is taken from reference [44].*

2.2 Phase separation phenomena

Up to this point, it was sufficient to assume homogeneous materials in order to understand the described phenomena. But most investigated samples in this work consist of at least two components which are combined in a so-called statistical copolymer. This adds additional complexity due to phase separation effects. Therefore, a brief introduction into the categorization of copolymers is given, before the theoretical foundations of phase separation of different types of polymer systems are presented.

2.2.1 Categorization of polymers

A polymer is a macromolecule comprising a large number of molecular units, the **monomers**, which are connected by covalent bonds. In this work, the architecture of all investigated polymers is linear which means that the spatial arrangement of the monomers is chain-like. If there is only one monomer of type A, then the polymer is referred to as **homopolymer** PA or P(A). If the polymer molecule consists of more than one type of monomer, then it is called **copolymer** [19].
Different types of copolymers can be obtained depending on the type of sequence of the monomeric units [45]. For example, a copolymer consisting of two blocks, which both contain only one type of monomer (A or B), is called a diblock copolymer P(A-b-B). Depending on the number of blocks it can also be a triblock or multiblock copolymer. For an unspecified number of blocks the general term is **block copolymer**. If a monomer of type A is followed by a monomer of type B and also the other way around, an **alternating copolymer** P(A-alt-B) is present [19].

Figure 2.8: *Schematic view of different types of (co-)polymers: a) homopolymer, b) diblock, c) alternating and d) statistical copolymer*

The most important type of copolymer in this work is the **statistical copolymer** P(A-stat-B) (or P(A-stat-B-stat-C) for three components) in which the sequence of the monomers is statistical. The exact definition of a statistical copolymer is provided by the International Union of Pure and Applied Chemistry (IUPAC): it is "a copolymer consisting of macromolecules in which the sequential distribution of the monomeric units obeys known statistical laws" [46]. The introduced types of (co-)polymers are illustrated in figure 2.8.
Besides the type of monomer sequence, a very important parameter for a polymer molecule is the number of monomers N which is also called **degree of polymerization** [19]. As for any molecule, the molecular weight M is also an important parameter. In polymeric materials, however, the chain lengths of the corresponding molecules do not have a constant value, or in other words, the individual molecular weights follow a certain distribution function $p(M)$. This distribution function must be normalized [19]:

$$\int_0^\infty p(M)\,\mathrm{d}M = 1. \tag{2.35}$$

The **number average** molar mass is then defined as

$$M_n = \int_0^\infty p(M) M \, \mathrm{d}M, \tag{2.36}$$

and the **weight average** is

$$M_w = \frac{\int_0^\infty p(M) M^2 \, \mathrm{d}M}{\int_0^\infty p(M) M \, \mathrm{d}M}. \tag{2.37}$$

With these measures, the **polydispersity** is introduced as [19]

$$P = \frac{M_w}{M_n} \geq 1. \tag{2.38}$$

It has to be noted that in reality, polymeric materials are never monodisperse ($\Leftrightarrow P \neq 1$), but always exhibit a certain polydispersity ($P > 1$).
Finally, we quantify the size of a single polymer chain. For this purpose, a polymer with N monomers is assumed. Each monomer has the mass m_j and it can be localized by its position vector $\vec{r}_j$ ($1 \geq j \geq N$). The simplest measure for the chain extension is the so-called **end-to-end distance** R_e [19]. It is calculated via $R_e = |\vec{r}_N - \vec{r}_1|$.
The disadvantage of R_e is that it solely accounts for the positions of the chain ends. Thus, without having additional knowledge, an estimation of the volume occupied by the polymer is impossible. An improved measure, which involves the spatial distribution of all monomers of one molecule, is the **radius of gyration**

$$R_g = \sqrt{\frac{\sum_{j=1}^N m_j \left|\vec{r}_j - \vec{r}_c\right|^2}{\sum_{j=1}^N m_j}}, \tag{2.39}$$

where $\vec{r}_c$ denotes the center of gravity [19].

2.2.2 Homopolymer mixtures

To understand phase separation phenomena, we first start with the simplest case of two monodisperse homopolymers PA and PB. The theory is based on the work of Flory and Huggins [47, 48] and is a mean field description. This means, that each polymer chain is treated independently and it interacts with an average field that is generated by all the other polymer chains in the system [19].
We assume to have $\tilde{n}_A$ moles of PA occupying a volume V_A and, correspondingly, $\tilde{n}_B$ moles of PB in a volume V_B. By removing the boundary between the two phases, the polymers have the possibility to intermix. Possible volume changes are neglected so that

the total volume is $V = V_A + V_B$. Whether mixing occurs depends on the Gibbs free energies of the components (G_A and G_B) and of the mixed state (G_{AB}). The Gibbs free energy of mixing can be written as [19]

$$\Delta G_{mix} = G_{AB} - (G_A + G_B) = \Delta G_{loc} - T\Delta S_t. \tag{2.40}$$

A necessary condition for mixing is $\Delta G_{mix} < 0$. In equation 2.40, ΔG_{loc} accounts for the changes of the local interactions and motions of the monomers. It is usually positive and, thus, opposes mixing because attractive forces between equal monomers are most often stronger than such between different ones. The translational entropy ΔS_t is related to the centers of mass of the molecules. Upon mixing ΔS_t is strictly positive. The corresponding values can be calculated via

$$\Delta S_t = -\tilde{R}\left(\tilde{n}_A \ln \Phi_A + \tilde{n}_B \ln \Phi_B\right), \tag{2.41}$$

with the ideal gas constant $\tilde{R}$ and the volume fractions $\Phi_K = V_K/V$ ($K \in \{A, B\}$), and

$$\Delta G_{loc} = \tilde{R}T\frac{V}{\tilde{v}_c}\chi\Phi_A\Phi_B, \tag{2.42}$$

respectively [19]. In the latter equation $\tilde{v}_c$ is the molar volume of a reference unit common to both polymers, for example the volume which is occupied by one monomer. The most important value in equation 2.42 is the so-called **Flory-Huggins parameter** χ, which is the local free energy change per reference unit [19]. It has to be noted that ΔG_{loc} is not purely enthalpic because locally, the number of possibilities how the polymer chains can orient themselves is altered. This gives rise to an entropic term [19]:

$$\Delta G_{loc} = \Delta H_{mix} - T\Delta S_{loc}. \tag{2.43}$$

Bringing all equations together and introducing the molar volumes $\tilde{v}_K$ that fulfill the equations $\tilde{n}_K\tilde{v}_K = V\Phi_K$ ($K \in \{A, B\}$), the Gibbs free energy change upon mixing is

$$\Delta G_{mix} = \tilde{R}TV\left(\frac{\Phi_A}{\tilde{v}_A}\ln\Phi_A + \frac{\Phi_B}{\tilde{v}_B}\ln\Phi_B + \frac{\chi}{\tilde{v}_c}\Phi_A\Phi_B\right). \tag{2.44}$$

With the molar number of reference units $\tilde{n}_c = V/\tilde{v}_c$ and the degrees of polymerization relative to the number of structure units $N_K = \tilde{v}_K/\tilde{v}_c$ ($K \in \{A, B\}$), this so-called **Flory-Huggins equation** [19] can be rearranged to

$$\Delta G_{mix} = \tilde{R}T\tilde{n}_c\left(\frac{\Phi_A}{N_A}\ln\Phi_A + \frac{\Phi_B}{N_B}\ln\Phi_B + \chi\Phi_A\Phi_B\right). \tag{2.45}$$

For polymers with very large degrees of polymerization, the first two addends of equation 2.45 are very small so that the sign of χ determines the sign of ΔG_{mix}. As a consequence, there is mixing of PA and PB for $\chi < 0$, and they are immiscible for $\chi > 0$.

The decomposition of ΔG_{mix} in an entropic and an enthalpic part is obtained as follows [19]:

$$\Delta S_{mix} = \frac{\partial \Delta G_{mix}}{\partial T} = \tilde{R}V \left(\frac{\Phi_A}{\tilde{v}_A} \ln \Phi_A + \frac{\Phi_B}{\tilde{v}_B} \ln \Phi_B + \frac{\Phi_A \Phi_B}{\tilde{v}_c} \frac{\partial(\chi T)}{\partial T} \right), \text{ and} \tag{2.46}$$

$$\Delta H_{mix} = \Delta G_{mix} + T\Delta S_{mix} = \tilde{R}T \frac{V}{\tilde{v}_c} \Phi_A \Phi_B \left(\chi - \frac{\partial(\chi T)}{\partial T} \right). \tag{2.47}$$

These equations imply that the Flory-Huggins parameter χ is the sum of an enthalpic (χ_H) and an entropic (χ_S) contribution. To be purely enthalpic, $\partial(\chi T)/\partial T$ has to vanish which is equivalent to $\chi \propto T^{-1}$. That is the reason for the widely used notation [19]

$$\chi = \chi_S + \frac{\chi_H}{T}. \tag{2.48}$$

The next step is to examine the conditions which enable mixing without going to the limit of very long chains. We start with a simplified system, in which both polymers have the same degree of polymerization ($N = N_A = N_B$). Using $\Phi_B = 1 - \Phi_A$, the Gibbs free energy has the form

$$\Delta G_{mix} = \frac{\tilde{R}T\tilde{n}_c}{N} \left(\Phi_A \ln \Phi_A + (1 - \Phi_A) \ln(1 - \Phi_A) + \chi N \Phi_A (1 - \Phi_A) \right). \tag{2.49}$$

The value of χN is decisive for the overall shape of the function ΔG_{mix}. The left panel of figure 2.9 exemplarily shows plots of ΔG_{mix} as a function of Φ_A for different values of χN. The shape of the curves changes upon crossing the critical value of $(\chi N)_c = 2$. For $\chi N < 2$ the curves are strictly negative and convex having a global minimum at $\Phi_A = 0.5$. In this region, the polymers are perfectly miscible. For $\chi N > 2$, however, a local maximum at $\Phi_A = 0.5$ appears. In addition to that, there are two minima at positions Φ'_A and Φ''_A, with $\Phi'_A < \Phi''_A$ equidistant to 0.5.

Whether mixing occurs depends on the combination of the values χN and Φ_A. From a two-dimensional plot, the so-called **phase diagram**, regions of either one or two phases can be identified. The boundary between the one-phase and the two-phase region is called **binodal** [19]. At this boundary $\Delta G_{mix}(\Phi_A)$ is minimal. Therefore, the corresponding first derivative has to vanish which is equal to

$$0 \stackrel{!}{=} \frac{N}{\tilde{R}T\tilde{n}_c} \frac{\partial \Delta G_{mix}}{\partial \Phi_A} = \ln(\Phi_A) - \ln(1 - \Phi_A) + \chi N(1 - 2\Phi_A). \tag{2.50}$$

The trajectory of the minima and, thus, the binodal directly follows as

$$\chi N = \frac{1}{1 - 2\Phi_A} \ln \frac{1 - \Phi_A}{\Phi_A}. \tag{2.51}$$

For the case of $\chi N > 2$ with a maximum of ΔG_{mix} at $\Phi_A = 0.5$, there are two possibilities for the behavior of the system. When Φ_A is close to 0.5, the free energy can be further reduced by phase separation in two phases with volume ratios Φ'_A and Φ''_A, respectively (see curve for $\chi N = 2.4$ in the left panel of figure 2.9).
Close to Φ'_A and Φ''_A, there is an energy barrier for the polymers to phase separate resulting in meta-stable homogeneous system. According to the "Gibbs criterion of stability", the system is in the meta-stable situation as long as $\Delta G_{mix}(\Phi_A)$ is convex which is fulfilled in two intervals around Φ'_A and Φ''_A, respectively [19]. The region around $\Phi_A = 0.5$ is concave.
The boundary between the metastable one-phase and the two-phase region is called **spinodal** [19]. According to the above explanation, it coincides with the trajectory of the inflection points of $\Delta G_{mix}(\Phi_A)$. This trajectory is determined via the roots of the second derivative, which is

$$0 \stackrel{!}{=} \frac{N}{\tilde{R}T\tilde{n}_c}\frac{\partial^2 \Delta G_{mix}}{\partial \Phi_A^2} = \frac{1}{\Phi_A} + \frac{1}{1-\Phi_A} - 2\chi N. \tag{2.52}$$

As a consequence, the spinodal is characterized by

$$\chi N = \frac{1}{2}\left(\frac{1}{\Phi_A} + \frac{1}{1-\Phi_A}\right). \tag{2.53}$$

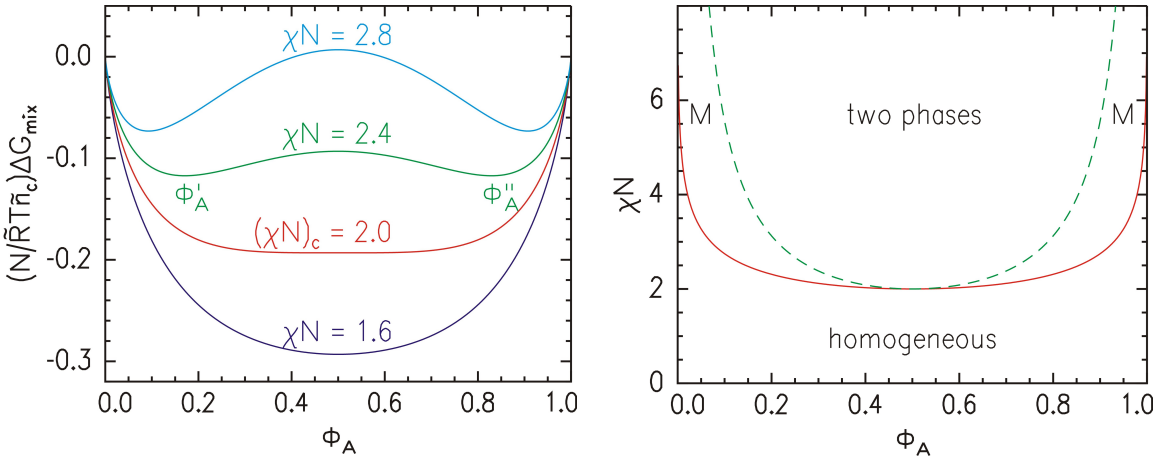

Figure 2.9: *Left: Normalized Gibbs free energy of mixing of a blend of two polymers with equal degrees of polymerization. The dependence of the curve on the variable χN is exemplarily illustrated for $\chi N = 1.6$, 2.0, 2.4 and 2.8 as indicated by the labels. Right: Corresponding phase diagram. The binodal (solid line) separates the homogeneous regime. The spinodal (dashed line) is the boundary between a two-phase and a metastable one-phase (M) regime.*

The positions of the phase boundaries are summarized in the right panel of figure 2.9

showing the phase diagram of a binary polymer mixture with equal degrees of polymerization.
For different degrees of polymerization ($N_A \neq N_B$), the phase diagram is no longer symmetric. For this case [19], the critical value of the Flory-Huggins parameter is

$$\chi_c = \frac{1}{2}\left(\frac{1}{\sqrt{N_A}} + \frac{1}{\sqrt{N_B}}\right)^2, \tag{2.54}$$

and the minimum of the spinodal is located at $\Phi_A = \sqrt{N_B}/(\sqrt{N_A} + \sqrt{N_B})$.

2.2.3 Block copolymers

Similar to polymer blends, which were described in the latter section, also block copolymers can phase separate [19]. Due to the covalent bonds between the different monomer species, the length scale of the obtained structures is significantly smaller than in polymer blends giving rise to the term **micro-phase separation**. However, the tendency to remain in a homogeneous phase is higher. This is indicated by the critical value $(\chi N)_c = 10.495$ of a symmetric diblock copolymer [49].
In addition to that, depending on the volume ratios of the involved blocks (Φ_A+Φ_B=1), there are different geometric arrangements of the separated phases among which are spheres, cylinders, gyroids or lamellae. In this section, we focus on the lamellae, which are also referred to as layered structure, occurring in diblock copolymers. N_K ($K \in \{A, B\}$) denotes the number of monomers in the individual blocks and $N_{AB} = N_A + N_B$ is the degree of polymerization.
The change in the Gibbs free energy per molecule upon the transition from the homogeneous towards the layered phase can be written as [19]

$$\Delta g_p = \Delta h_p - T\Delta s_{p,if} - T\Delta s_{p,conf}. \tag{2.55}$$

The three contributions follow from a change in enthalpy Δh_p and in entropy, whereas the latter splits up in two contributions. The first one is due to the alignment of the junction points along the interfaces ($\Delta s_{p,if}$) and the second one results from the altered chain conformations ($\Delta s_{p,conf}$). Under the assumption of perfect segregation,

$$\Delta h_p = -k_B T \chi N_{AB} \Phi_A (1 - \Phi_A) + \Delta h_{p,if} \tag{2.56}$$

is calculated [19]. The additional term $\Delta h_{p,if}$ arises from the fact that within a certain interfacial area of thickness d_t, the different species remain mixed. This leads to an increase in enthalpy which is proportional to χ. As a result,

$$\Delta h_{p,if} \approx k_B T \chi \frac{o_p d_t}{\tilde{v}_c} \tag{2.57}$$

is obtained, where o_p is the interfacial area per polymer [19]. For the calculation of $\Delta s_{p,if}$, the thicknesses of the A and B lamellae are denoted with d_A and d_B, respectively, leading to a periodicity of $d_{AB} = d_A + d_B$. From statistical thermodynamics it is known that [19]

$$\Delta s_{p,if} \approx k_B \ln \frac{d_t}{d_{AB}}. \tag{2.58}$$

The sign of the second entropic contribution $\Delta s_{p,conf}$ is negative because the layer formation causes a stretching of the polymer chains. The end-to-end distance of the homogeneous phase R_e^h expands to a higher value R_e^l in the layered phase. The resulting conformational contribution to the entropy is [19]

$$\Delta s_{p,conf} \approx -k_B \left(\frac{R_e^l}{R_e^h} \right)^2. \tag{2.59}$$

The assumption of a linear relation between d_{AB} and R_e^l in addition to the usage of the obvious relation $o_p d_{AB} = N_{AB} \tilde{v}_c$ implies that o_p is the only independent variable in the expression for Δg_p. Therefore, $\mathrm{d}\Delta g_p / \mathrm{d}o_p = 0$ is a necessary condition for o_p to minimize the Gibbs free energy and, thus, for equilibrium. A straightforward calculation leads to the result [19]

$$d_{AB}^3 = \frac{N_{AB}^3 \tilde{v}_c^3}{o_p^3} \propto \chi d_t \tilde{v}_c^{2/3} N_{AB}^2, \tag{2.60}$$

which relates the periodicity of the layered structure to the degree of polymerization and the Flory-Huggins parameter. For further reading about block copolymers and polymer blends, please refer to reference [19].

2.2.4 Statistical Copolymers

Compared to polymer blends or diblock copolymers, the theoretical description of phase separation phenomena in statistical copolymers is much more sophisticated. Further complexity is added by the fact that due to the chemical processing methods there is no perfect randomness of a certain monomer species at a certain position within a polymer chain. In this section, the ansatz of the theoretical analysis of phase separation of a two-component, monodisperse statistical copolymer [50] as well as some results from simulation studies are presented.

When a polymer chain is synthesized, the monomers subsequently link together. This process is also called polymerization. The probabilities of the corresponding bimolecular reactions depend on the individual species A and B. For example, the reaction rate between two A monomers might be different from an A-B reaction. For the finally polymerized

material, this is strongly correlated with the conditional probability p_{KL} $(K, L \in \{A, B\})$ of a monomer of type K being followed by a monomer of type L [50].

As a consequence, a full description of the A-B sequences in the statistical copolymer is provided by the mole fraction f of monomer A in addition to a (2×2) matrix P having the entries p_{KL}. The latter fulfill the obvious conditions $p_{AA} + p_{BA} = 1$, $p_{AB} + p_{BB} = 1$ and $f = fp_{AA} + (1 - f)p_{AB}$. Therefore, the matrix has only one degree of freedom which is chosen to be the respective eigenvalue $\lambda^* = p_{AA} + p_{BB} - 1$. The eigenvalue is in the range $\lambda^* \in [-1; 1]$ and it is a measure for the type of sequence which is obtained during polymerization [50]. In the extreme case $\lambda^* = -1$, the copolymer type is alternating whereas $\lambda^* = 1$ means that a mixture of homopolymers PA and PB has been processed. An ideal copolymerization with no correlations between the chemical identities of two successive monomers is present for $\lambda^* = 0$.

To set up a microscopic model, i. e. a Hamiltonian, incompressibility of the copolymer melt and a degree of polymerization N are assumed. In the following, $k_B T$ and the total monomer density are both unity. For the parametrization of the Hamiltonian, $\left\{\vec{R}_j(s) \mid j \in \{1, 2, \ldots, n_p\},\ s \in \{1, 2, \ldots, N\}\right\}$ is the set of monomer coordinates in which j indexes the polymer chains (the system comprises n_p polymer molecules) and s indexes the monomer position on a chain. In analogy to the coordinates, $\{\Theta_j^*(s)\}$ is the set which attributes the respective species to each monomer. Monomers of type A are represented by the value 1 and B monomers by -1. With the microscopic density of type-K monomers ϱ_K and the monomer segment length b^*, the Hamiltonian is [50]

$$\begin{aligned}\mathcal{H}\left(\{\vec{R}\}, \{\Theta\}\right) = \frac{3}{2(b^*)^2} \sum_{j=1}^{n_p} \sum_{s=1}^{N-1} \left|\vec{R}_j(s) - \vec{R}_j(s+1)\right|^2 + \\ + \int \mathrm{d}\vec{r} \int \mathrm{d}\vec{r'} \varrho_A\left(\vec{r}\right) \varrho_B\left(\vec{r'}\right) \chi^*\left(\left|\vec{r} - \vec{r'}\right|\right).\end{aligned} \tag{2.61}$$

The interaction term describes the difference between the interactions of dissimilar monomers (u_{AB}) and such of equal monomers (u_{AA} and u_{BB}):

$$\chi^*\left(\vec{r}\right) = u_{AB}\left(\vec{r}\right) - \frac{1}{2}\left[u_{AA}\left(\vec{r}\right) + u_{BB}\left(\vec{r}\right)\right]. \tag{2.62}$$

From this model, Fredrickson and Milner [50] derived the existence of three different phases for the case of $|\lambda^*|^N \ll 1$. A perfectly mixed state and a stable two-phase region are predicted. In addition to that, there is an inhomogeneous mesophase for which λ^* is the decisive parameter whether the structures possess long-range order. The model even allows for an exact determination of the phase boundaries (see figure 2.10). The solid line between the one phase and the two phase region fulfills the condition

$$4f(1-f)\chi^* = \frac{2N(1-\lambda^*)^2}{N(1-\lambda^*)^2 + 2\lambda^*\left(N(1-\lambda^*) + \lambda^{*N} - 1\right)}. \tag{2.63}$$

With the introduction of two additional dimensionless parameters κ_2 and κ_4, which are both associated with the interaction range, the dotted line follows the equation

$$4f(1-f)\chi^* = \frac{2(1-\lambda^*)}{1+\lambda^*} + \frac{2\left(\lambda^* + 6\kappa_2(1+\lambda^*)^2\right)^2}{\lambda^*(1-\lambda^*)(1+\lambda^*) + 72\kappa_4(1+\lambda^*)^4}, \text{ and} \tag{2.64}$$

$$4f(1-f)\chi^* = \frac{2(1-\lambda^*)}{1+\lambda^*} + \frac{12}{N}\left(\frac{\lambda^*}{(1+\lambda^*)^2} + 6\kappa_2\right) \tag{2.65}$$

parametrizes the dashed curve. The point denoted with "Lif" is called isotropic Lifshitz multicritical point [50]. A different study [51] confirmed that, for $\lambda^* = 0$ and large N, within the mesophase layered structures are possible. The latter are obtained experimentally for the first time in this work and described in later chapters.

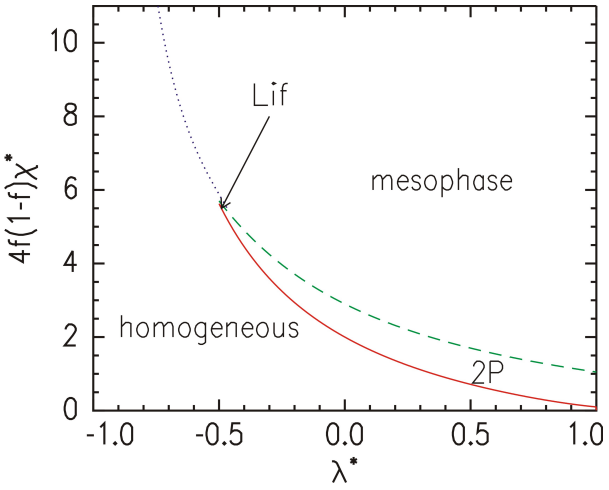

Figure 2.10: *Phase diagram of a two-component statistical copolymer derived by Fredrickson and Milner [50]. Three different regions are predicted: a homogeneous phase, a mesophase and a two-phase region (2P). For the calculation $\kappa_2 = 0.25$, $\kappa_4 = 0.025$ and $N = 20$ are assumed.*

The improved availability of computational power in the last decade enabled large scale Monte Carlo simulations of statistical copolymer melts. Based on the model, which is described above, Houdayer and Müller carried out simulations for rather blocky copolymers [52]. In detail, the authors assumed copolymers that are comprised of 5 blocks of 4 monomers ($\Rightarrow N = 20$) all of which are either type A or B. The sequence of the the blocks is random. As can be seen from figure 2.11, the cluster size of either pure A or pure B material increases with increasing incompatibility χ^*. From left to right the corresponding interaction parameters are $\chi^* = 0.267$, 0.475, and 0.806.

Under the additional assumption of an interface towards a surrounding medium, also the interactions with that medium have to be taken into account. These interactions may favor one of the two components and, thus, lead to an enhanced adsorption of the corresponding monomer species at the interface. This case is very close to the sample

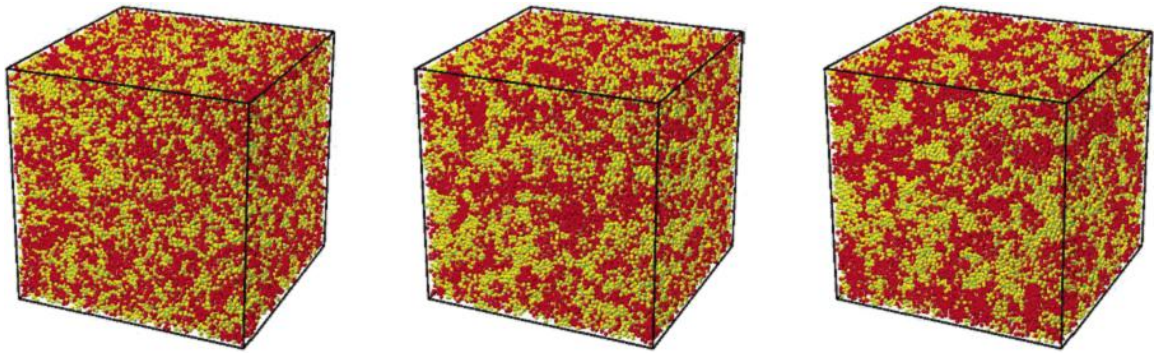

Figure 2.11: *Snapshots of copolymer melts as described in the main text. The two different components are represented by either red or yellow color. The side length of the cubic simulation volume corresponds to nine times the end-to-end distance of the copolymers. The incompability of the components increases from left to right. The image is taken from reference [52].*

systems which are investigated in this work. From an experimental point of view, the selectivity with respect to one of the components of the statistical copolymer can for example be tailored via the relative humidity of the surrounding air, or in other words, with the polarity of the interfacial interactions.

And indeed, in a computational study, Klos et al. [53] found that for a two-component statistical copolymer P(A-stat-B) the type A monomer density at the surface increases with the surface selectivity with respect to the type A monomers (see figure 2.12, top). They simulated the monomer distribution in a box with hard walls. The box is divided into 256 slabs, which are enumerated from $z = 1$ (sample surface) to $z = 256$. The lateral dimension consists of 128×128 lattice points. In total, 2048 chains, each comprising 128 monomers, are introduced into the system. The chains are assumed to be ideally copolymerized ($\lambda^* = 0$). The overall ratio of type A monomers is set to $p_A = p = 0.2$, and the ratio of type B monomers is $p_B = 1 - p = 0.8$, correspondingly. The interface selectivity χ is defined via the energy decrease ΔE_{ad} of a type A monomer which adsorbs at the surface [53].

$$\chi = \frac{\Delta E_{ad}}{k_B T} \tag{2.66}$$

With increasing χ there is not only an increase in density of type A monomers ρ_A at the surface, but also a depletion zone with decreasing ρ_A follows underneath. For higher z, the density profile converges monotonically to an equilibrium value. In addition to that, the panel at the bottom of figure 2.12 shows that the type B monomers behave accordingly: whereas the respective density ρ_B at the surface decreases with increasing χ, the concentration of type B monomers underneath increases. Similar to the type A

monomers, ρ_B is constant for sufficiently large z values [53]. It has to be noted that these findings by Klos et al. are in good agreement with the experimental results obtained in this work.

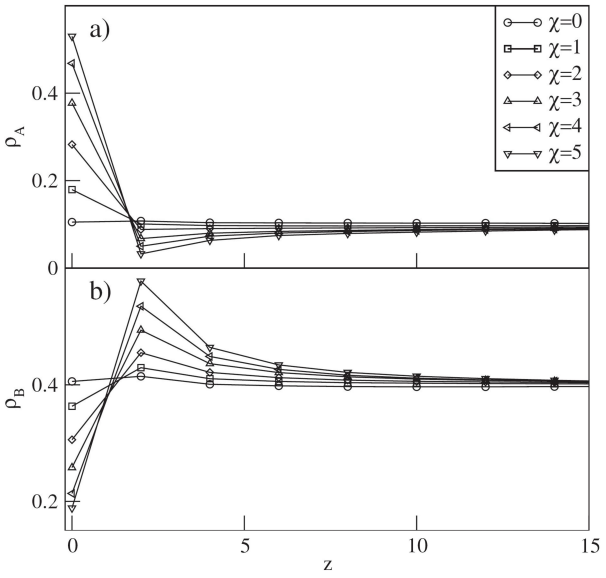

Figure 2.12: *Densities of type A (top) and type B (bottom) monomers as a function of distance from the surface z for different interface selectivities χ. The image is adapted from reference [53].*

2.3 Scattering methods

A powerful tool to provide experimental evidence for the phase separation structures, which are described in the latter section, is x-ray or neutron scattering. This section is dedicated to the theoretical background of x-ray and neutron reflectivity (XRR and NR) as well as grazing incidence small angle x-ray scattering (GISAXS) which are the most important methods within this work. With XRR and NR, composition profiles perpendicular to the sample surface are monitored, whereas GISAXS is capable of detecting lateral structures, too. All of these methods deal with elastic scattering, i. e. the energy of the beam and, thus, the wavelength before and after the scattering event is conserved.

2.3.1 Basic principles

The propagation of an electromagnetic plane wave through a medium with a position dependent refractive index $n(\vec{r})$ can be described by the corresponding electric field vector

$$\vec{E}(\vec{r}) = \vec{E}_0 \exp[i\vec{k}_i\vec{r}]. \tag{2.67}$$

$\vec{E}_0$ encompasses the amplitude and the polarization, $k = \left|\vec{k}_i\right| = 2\pi/\lambda$ is the modulus of the wavevector and λ the wavelength. The electric field fulfills the **Helmholtz equation**

$$\Delta\vec{E}(\vec{r}) + k^2 n^2(\vec{r})\vec{E}(\vec{r}) = 0. \tag{2.68}$$

The refractive index for x-rays can be written as $n(\vec{r}) = 1 - \delta(\vec{r}) + i\beta(\vec{r})$. This complex notation accounts for the dispersion (real part) and the absorption (imaginary part) of the x-rays [54]. For polymers, these two contributions are calculated as the sum over all atoms composing one monomer [55]:

$$\delta(\vec{r}) = \frac{\lambda^2}{2\pi} r_e \varrho(\vec{r}) \frac{\sum_j \left(f_j^0(\lambda) + f_j'(\lambda)\right)}{\sum_j M_j} \quad \text{and} \tag{2.69}$$

$$\beta(\vec{r}) = \frac{\lambda^2}{2\pi} r_e \varrho(\vec{r}) \frac{\sum_j f_j''(\lambda)}{\sum_j M_j}, \tag{2.70}$$

where r_e is the classical electron radius, $\varrho(\vec{r})$ is the macroscopic polymer mass density and the M_j are the atomic weights. f_j' and f_j'' are the real and the imaginary part of the correction terms to the atomic form factor which is the Fourier transform of the electron cloud [56]. For the geometries in this study, which all use small incident angles, f_j^0 can be well approximated by the number of electrons in the respective atom.

For x-rays, the real parts of the refractive indices of the investigated materials are smaller than one as a result of $\delta \approx 10^{-6}$. Consequently, the media are optically thinner than vacuum or air. Therefore, under the assumption of zero absorption, when an x-ray beam impinges onto a surface under a certain incident angle, total external reflection occurs as long as the angle is smaller than the **critical angle** of the material.

It has to be noted that for visible light ($n > 1$), this is not the case which is one of the reasons for the choice of x-rays in the presented experiments instead of visible light. The critical angle can be approximated by $\alpha_c \approx \sqrt{2\delta}$. All angles in this work are measured with respect to the interface and not with respect to the surface normal. A schematic view of the reflection geometry, in which the exit angle of the reflected beam α_f is equal to the incident angle α_i, is given in figure 2.13. The reflected beam for this geometry is also referred to as **specularly reflected** beam.

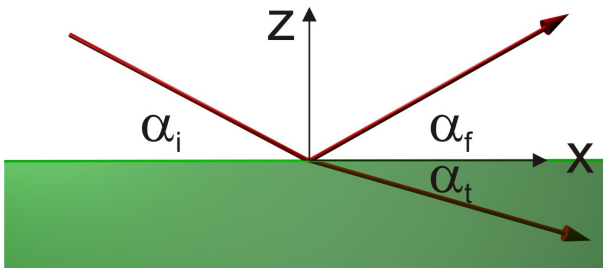

Figure 2.13: *Reflection of x-rays at an interface. A part of the intensity is transmitted under an angle α_t. The point of origin coincides with the point of reflection.*

Assuming a beam impinging under an incident angle α_i, we focus on the intensities of the reflected and transmitted beam. The angle between the interface and the transmitted wave vector is denoted with α_t and can be calculated via Snell's law of refraction. Both

intensities are directly proportional to the squares of the amplitude ratios with respect to the incoming beam. These amplitude ratios are also referred to as **Fresnel reflection coefficient** r^F and **Fresnel transmission coefficient** t^F, respectively [54]. For the case of x-rays, the impact of the polarity of the incident wave is only minor and the coefficients are [54]

$$r^F = \frac{\sin(\alpha_i) - \sqrt{n^2 - \cos^2(\alpha_i)}}{\sin(\alpha_i) + \sqrt{n^2 - \cos^2(\alpha_i)}} \qquad \text{and} \qquad t^F = \frac{2\sin(\alpha_i)}{\sin(\alpha_i) + \sqrt{n^2 - \cos^2(\alpha_i)}}. \tag{2.71}$$

The **reflectivity** is defined as $R^F = \left|r^F\right|^2$. It can be explicitly calculated via [54]

$$R^F = \frac{(\alpha_i - p_+)^2 + p_-^2}{(\alpha_i + p_+)^2 + p_-^2}, \text{ with} \tag{2.72}$$

$$p_\pm^2 = \frac{1}{2}\left(\sqrt{\left(\alpha_i^2 - \alpha_c^2\right)^2 + 4\beta^2} \pm \left(\alpha_i^2 - \alpha_c^2\right)\right). \tag{2.73}$$

A Taylor expansion of $R^F(\alpha_i)$ leads to the conclusion, that for $\alpha_i > 3\alpha_c$ the reflectivity at a perfectly plane interface to an infinitely thick sample can be estimated as [54]

$$R^F \approx \left(\frac{\alpha_c}{2\alpha_i}\right)^4. \tag{2.74}$$

Furthermore, a straightforward calculation shows that the intensity of the transmitted beam is directly proportional to $\exp[-k\,|z|\,p_-]$, where $|z|$ is the distance from the sample surface. This means that the corresponding amplitude of the electric field decays exponentially. The **penetration depth** Λ is defined as that $|z|$, at which the amplitude of the electric field is $1/e$ of its value at the interface. As a consequence, Λ can be written as [54]

$$\Lambda = \frac{1}{kp_-} = \frac{\lambda}{\sqrt{2}\pi}\left(\sqrt{\left(\alpha_i^2 - \alpha_c^2\right)^2 + 4\beta^2} - \left(\alpha_i^2 - \alpha_c^2\right)\right)^{-1/2}. \tag{2.75}$$

For scattering experiments, however, it is more common to make use of the so-called **scattering** or **information depth**. This measure also takes the absorption of the already scattered beam, which exits the medium, into account. It is therefore approximated as half of the penetration depth [57].

As an example, the penetration depth of x-rays with a wavelength of 0.154 nm which impinge under an angle of 0.5° onto polymethylmethacrylate (PMMA) ($\alpha_c = 0.163°$) is approximately 25 μm. The respective scattering depth is therefore only 12.5 μm. Consequently, for most samples which are investigated in this work having thicknesses in the range of 50 μm, the x-ray beam does not penetrate the complete sample volume for low incident angles.

2.3.2 X-ray reflectivity (XRR)

A sketch of the basic setup of XRR has already been shown in figure 2.13. The reflected intensity is recorded as a function of the incident angle α_i. For data presentation it is, however, common to plot the z component of the **scattering vector**, whose x and y components are zero,

$$q_z = (\vec{k}_f - \vec{k}_i)_z = \frac{4\pi}{\lambda}\sin(\alpha_i) \tag{2.76}$$

instead of α_i. q_z is proportional to the momentum change of the photons upon scattering. For the calculation and simulation of reflectivity curves, the simple assumption of the latter section of only one interface is in most cases not sufficient. This is not only because most polymer films are supported by a substrate but also a certain layering inside the sample has to be taken into account. In addition to the absorption, the x-rays can be reflected or refracted at any interface in the system [54].

Using the coordinate system of figure 2.13, the interfaces are assumed to be at positions z_j ($j \in \{1, 2, \ldots, N\}$), where $z_1 = 0$ is the coordinate of the sample surface. Note that for all $j > 1$ the z_j are negative. Layer 1 represents the vacuum and layer $N + 1$ is the substrate. The thickness of each layer is $d_j = z_{j-1} - z_j$ and its refractive index is $n_j = 1 - \delta_j + i\beta_j$ ($2 \leq j \leq N$). In addition to that, the substrate has a refractive index of $n_{N+1} = 1 - \delta_{N+1} + i\beta_{N+1}$ but its thickness is assumed to be infinite so that $z_{N+1} = -\infty$ [54].

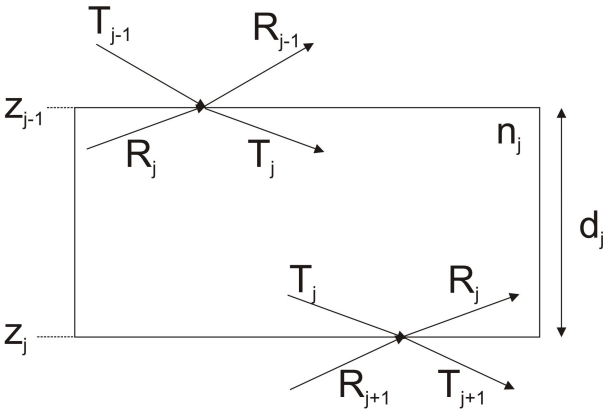

Figure 2.14: *Illustration of the nomenclature used in the Parratt algorithm: transmitted and reflected waves at the interfaces at positions z_{j-1} and z_j, respectively.*

For the calculation, it is assumed that the wave has an initial amplitude of $T_1 = 1$. Inside each layer j, $\vec{k}_{i,j}$ is the wavevector and T_j the amplitude of the transmitted wave. $\vec{k}_{f,j}$ and R_j are the respective values of the wave after the reflection at the interface at position z_j. A schematic view of all involved waves in layer j is given in figure 2.14. With this denotation, $R_{N+1} = 0$ and the aim is the calculation of R_1. Using this model, R_1 was successfully calculated for the first time by Abelès using a matrix formalism [58].

Here, an equivalent but numerically more efficient recursive algorithm developed by Parratt is presented [59]: when the ratio $X_{j+1} = R_{j+1}/T_{j+1}$ is known for the layer $j+1$, it can be calculated for layer j via

$$X_j = \frac{R_j}{T_j} = \exp[-2ik_{z,j}z_j]\frac{r_{j,j+1} + X_{j+1}\exp[2ik_{z,j+1}z_j]}{1 + r_{j,j+1}X_{j+1}\exp[2ik_{z,j+1}z_j]}, \tag{2.77}$$

$$\text{where} \qquad r_{j,j+1} = \frac{k_{z,j} - k_{z,j+1}}{k_{z,j} + k_{z,j+1}} \tag{2.78}$$

is the Fresnel reflection coefficient of interface j and $k_{z,j} = k\left(n_j^2 - \cos^2(\alpha_i)\right)^{1/2}$ is the z-component of the wavevector in layer j. Starting from $X_{N+1} = R_{N+1} = 0$, all X_j can be calculated iteratively. The total reflected intensity is $Int = R^F = |X_1^2|^2 = |R_1^2|^2$.
Up to this point, the formalism assumes perfectly flat interfaces which is equal to a jump in the refractive index from one layer to the next. In reality, however, the interfaces are rough leading to a smooth transition of the refractive indices. To quantify the roughness of the j-th interface, the distances $\left|z_j^k - z_j\right|$ of the individual points on the wavy interface (here: N_{τ_j} sampling points) from the nominal interface level z_j are averaged. For example, the **average roughness** τ_j^a and the **root mean square roughness** τ_j^{RMS} of the j-th interface are defined as

$$\tau_j^a = \frac{1}{N_{\tau_j}}\sum_{k=1}^{N_{\tau_j}}\left|z_j^k - z_j\right| \quad \text{and} \quad \tau_j^{RMS} = \sqrt{\frac{1}{N_{\tau_j}}\sum_{k=1}^{N_{\tau_j}}\left(z_j^k - z_j\right)^2}, \tag{2.79}$$

respectively [60]. The interfacial roughness between the layers j and $j+1$ is schematically illustrated in figure 2.15. The sampling points are distributed along the wavy line which represents the rough interface. Using the coordinate system which is defined in figure 2.3.1, the point of origin for the roughness calculation is situated at (0, 0, z_j). It is important to note that, although the assumption of perfectly flat interfaces is dropped, the positions of the individual interfaces are still well-defined. Each z_j is assigned to that value to which the corresponding value of τ_j^{RMS} is minimal.

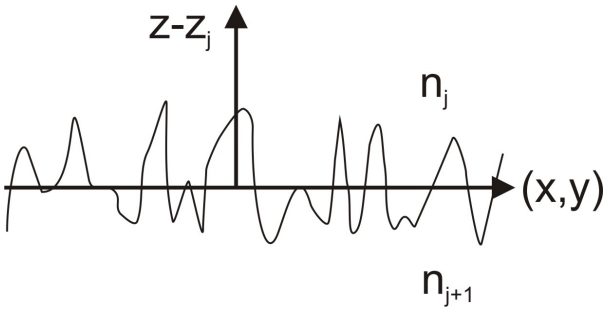

Figure 2.15: *Schematic view of the roughness of the interface between layer j and layer $j+1$.*

For XRR, only the change of the refractive index in z direction influences the data. That is why the interface structures are averaged over the (x, y)-plane and a one-dimensional refractive index profile

$$n_j(z) = \iint n_j(x, y, z)\,\mathrm{d}x\mathrm{d}y \tag{2.80}$$

is obtained [54]. In principle, also the shape of $n_j(z)$ plays a role for the calculation of the reflectivity curve. For most cases, a symmetric shape of $n_j(z)$ is assumed [61]. Névot and Croce, for example, modeled the transition from layer j to layer $j+1$ with an error function [62]

$$n_j(z) = \frac{n_j + n_{j+1}}{2} - \frac{n_j - n_{j+1}}{2}\mathrm{erf}\left(\frac{z - z_j}{\sqrt{2}\tau_j^{RMS}}\right), \tag{2.81}$$

where the error function is defined as $\mathrm{erf}(z) = \int_0^z \exp[-t^2]\,\mathrm{d}t$.
Névot and Croce showed that with this ansatz the roughness can be included in the described algorithm just by correcting the Fresnel reflection coefficients (see 2.78) by an additional factor. The corrected coefficients are

$$\tilde{r}_{j,j+1} = r_{j,j+1} \exp\left[-2k_{z,j}k_{z,j+1}\left(\tau_j^{RMS}\right)^2\right]. \tag{2.82}$$

The exponential function is called **Névot-Croce** factor. The limits of this correction are reached when the roughness is large compared to the layer thickness. However, this problem can be overcome by splitting the corresponding layer in sub-layers [63]. This procedure is also called **slicing**. Further details on theoretical aspects of XRR can be found in [54].
To summarize this section, some calculated XRR data for simple sample systems using the software *Parratt32* [64] are shown. In the left panel of figure 2.16, the reflectivity of a homogeneous, $d_2 = 20$ nm thick PMMA film which is supported by a SiO_2 substrate is shown for different interfacial roughness values τ_2^{RMS}. The surface roughness τ_1^{RMS} is zero for all three curves. The prominent equidistant intensity oscillations are called **Kiessig-fringes** [65]. The distance of two subsequent local maxima Δq_z and the film thickness are related via $d_2 \approx 2\pi/\Delta q_z$. The amplitude of the fringes decreases with increasing τ_2^{RMS}. In this work, it will be shown that in case of statistical copolymer based PSA films with very high interfacial roughnesses (except τ_1^{RMS}), these fringes vanish completely.
As it was shown in equation 2.75, also the penetration depth of the x-rays is limited. As a consequence, for such thick PSA films the influence of the substrate can be neglected. This is illustrated in the right panel of figure 2.16 where the XRR data of a 100 μm thick PMMA film are compared to such of an unsupported film of the same thickness. Due to the coincidence of the curves, the refractive index of the substrate, which is silicon or

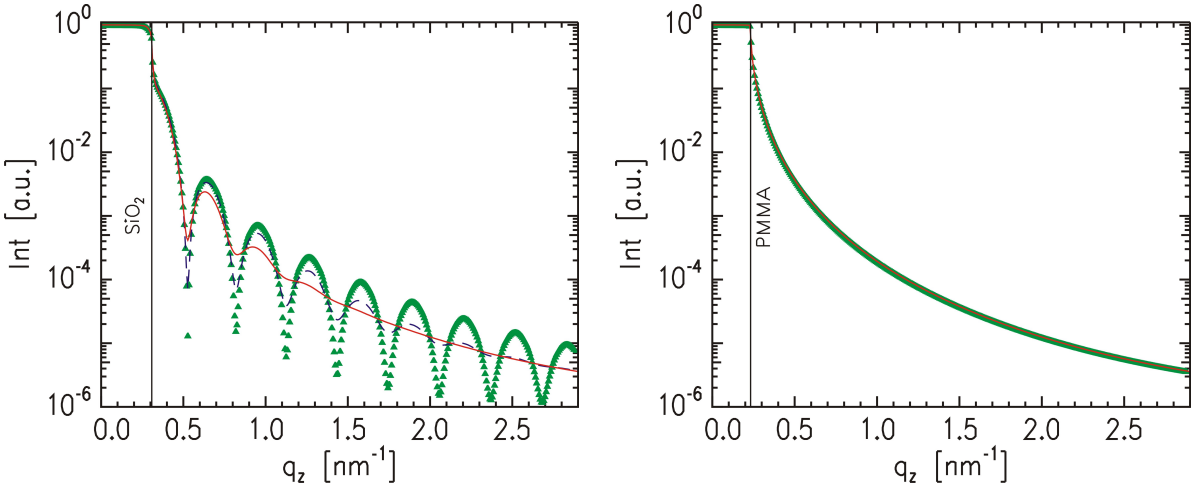

Figure 2.16: *Left: Comparison of XRR simulations of samples with different interfacial roughnesses. With decreasing amplitude of the Kiessig fringes, the corresponding values are* $\tau_2^{RMS} = 0$ *(symbols),* 1 *nm (dashed line) and* 2 *nm (solid line). Right: XRR data of a thick PMMA film supported by a substrate (symbols) and data of the same film without substrate (solid line). The vertical line in each panel is positioned at the* q_z *value corresponding to the critical angle of* SiO_2 *(left) and PMMA (right). For all curves, a constant background of* 10^{-6} *is assumed.*

glass, is replaced by the refractive index of the PSA in the simulations shown in later chapters.

Furthermore, the critical angle of reflection is positioned at the value of PMMA, whereas for thin films it is at the value corresponding to the substrate material (see left panel of figure 2.16). In other words, for such thick films the position of the so-called **critical edge** is only determined by the type of polymer.

2.3.3 Neutron reflectivity (NR)

The electromagnetic field of x-rays interacts with the electron cloud of the involved atoms. When neutrons are used instead of x-rays while leaving the geometry unchanged (see figure 2.13), the situation is different. The interaction of the uncharged neutrons is entirely with the atomic nuclei.

Anyhow, the theoretical description of both types of experiments remains very similar. The reason can be found in the Helmholtz equation 2.68 which is, as shown in the latter section, one-dimensional for the purposes of XRR. It is of the same type as the one-dimensional Schrödinger equation which determines the z-component of the wave function of the neutrons $\psi_N(z)$. The Schrödinger-equation can be written as

$$\left[-\frac{\hbar}{2m_N}\Delta + V(z)\right]\psi_N(z) = \mathcal{E}\psi_N(z), \tag{2.83}$$

where $\hbar$ is Planck's constant and m_N the rest mass of the neutron. The potential

$$V(z) = -\frac{\hbar k_N^2 n_N^2(z)}{2m_N} + \mathcal{E} \tag{2.84}$$

shows the analogy to the Helmholz equation [56], where k_N is the wave vector of the plane wave solution of the Schrödinger equation.
The only difference arises in the calculation of n_N, which is called **scattering length density** (SLD) for neutrons, and not refractive index. For materials which consist of one type of molecule, it is calculated via

$$n_N = \frac{\sum_k \mathcal{B}_k}{v_{mol}}, \tag{2.85}$$

where the $\mathcal{B}_k$ are the bound scattering lengths of the atoms in the molecule [66] and v_{mol} is the molecular volume. For polymers with degree of polymerization N, v_{mol} can be expressed as

$$v_{mol} = \frac{N\sum_j M_j}{\varrho}. \tag{2.86}$$

The sum is over all atoms (with atomic weight M_j) composing one monomer and ϱ is the polymer density. Furthermore, in equation 2.85 the sum over all atoms of the polymer can be simplified to N times the sum over all atoms (summation index j) of the underlying monomer. As a consequence, the SLD of a polymer can be written as

$$n_N = \varrho\frac{\sum_j \mathcal{B}_j}{\sum_j M_j}. \tag{2.87}$$

In order to account for the absorption of the neutrons, the $\mathcal{B}_j$ are chosen to be complex and are written as

$$\mathcal{B}_j = \mathcal{B}_j' + i\mathcal{B}_j''. \tag{2.88}$$

Under the assumption of coherent scattering (see reference [46]), the values of $\mathcal{B}_j'$ and $\mathcal{B}_j''$ are closely related to the total scattering cross section and the absorption cross section [67]. Nevertheless, it is common to adapt the the terminology of x-ray scattering experiments and express the SLD as

$$n_N = 1 - \delta_N + i\beta_N. \tag{2.89}$$

It has to be noted, however, that in literature the imaginary part β_N is often neglected [68] and the δ_N is referred to as scattering length density [69].
One of the strengths of NR is based on the fact that the $\mathcal{B}_j$ exclusively reflect properties of the respective atomic nuclei and, thus, depend on the isotope of the corresponding element. As a consequence, by choosing appropriate isotopes, the neutron contrast between different components of the sample can be manipulated without changing their chemical properties. Most common is the exchange of hydrogen with deuterium.

2.3.4 Grazing incidence small angle x-ray scattering (GISAXS)

In addition to specular reflection, the roughness, which was introduced in the last section, gives rise to diffuse scattering in y-direction. Such scattering is not monitored with XRR. Furthermore, in many polymer samples, and also in those which are examined in this study, there are regular, lateral structures as a product of phase separation which exceed simple interfacial roughness. The contribution of the size, shape and distance of such objects to the diffuse scattering is presented in this section. We restrict ourselves to the case of cylindrical objects which are distributed on a substrate [56]. This is to be understood as a basic model from which only slight variations are necessary to enable an analysis of realistic lateral structures in a PSA film.
GISAXS as investigation method is ideal to monitor the diffuse scattering [70, 71]. With a two-dimensional (2D) detector, one recorded image contains the complete diffuse scattering pattern. Due to the need of high intensity, such experiments are usually carried out at synchrotrons. The GISAXS geometry in combination with a sketch of the assumed sample is illustrated in figure 2.17.

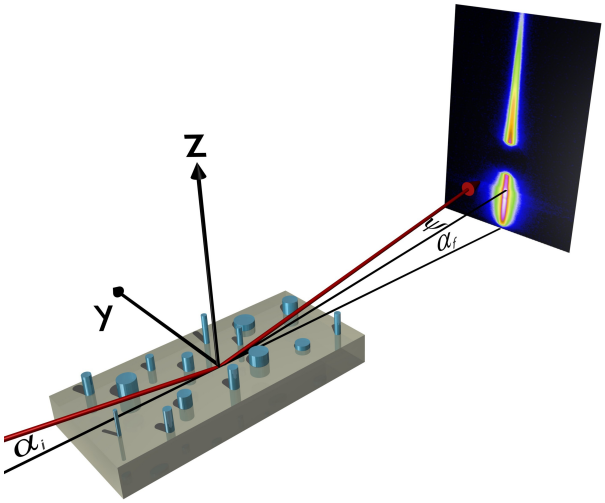

Figure 2.17: *Schematic illustration of the GISAXS geometry. The coordinate system is equal to that of XRR. The sample is a sketch of the assumptions described in the main text to calculate the diffusely scattered intensity. The corresponding color-code for the intensity distribution is typically on a logarithmic scale.*

In contrast to XRR, the incident angle is kept fixed at a value which is typically on the order of $\alpha \approx 0.4°$ for polymeric samples. Every spot on the detector can be located using

the exit angle α_f and the so-called out-of-plane angle ψ [72]. The corresponding scattering vector can be expressed by

$$\vec{q} = \frac{2\pi}{\lambda} \begin{pmatrix} \cos(\alpha_f)\cos(\psi) - \cos(\alpha_i) \\ \cos(\alpha_f)\sin(\psi) \\ \sin(\alpha_f) + \sin(\alpha_i) \end{pmatrix}. \tag{2.90}$$

The samples which are investigated in this work exhibit high interfacial roughnesses and refractive index fluctuations parallel to the sample surface. For the analysis and simulation of such data, the so-called **distorted-wave Born approximation** (DWBA) provides a suitable framework [73, 74]. It is a quantum-mechanical first-order perturbation theory which treats the scattering from a layered sample with flat interfaces as the unperturbed case. The interfacial roughnesses are included as the corresponding disturbance [75, 76]. The differential cross section in the DWBA is [77]

$$\frac{\mathrm{d}\sigma}{\mathrm{d}\Omega} = \frac{A_{ill}\pi^2}{\lambda^4} \left(1 - n^2\right)^2 \left|t_i^F\right|^2 \left|t_f^F\right|^2 P_{diff}(\vec{q}), \tag{2.91}$$

where A_{ill} is the illuminated sample area. t_i^F and t_f^F are the Fresnel transmission functions of the incident and the scattered beam (see equation 2.71). Their contribution to the diffuse scattering is maximized when either α_i (which is fixed) or α_f is equal to the critical angle of the material. The Fresnel transmission functions in equation 2.91 are therefore the reason for an enhanced diffuse scattering when the exit angle matches the critical angle of one of the involved materials. The corresponding intensity maximum is also referred to as **Yoneda peak** [78].
Anyhow, the transmission functions as well as the other prefactors only act as overall scaling factors [73]. As a consequence, GISAXS directly probes the diffuse scattering factor P_{diff} which is proportional to the scattered intensity.
In the following, the scattered intensity is calculated for the case of cylindrical objects on a substrate (see figure 2.17). The cylinders exhibit a certain size and distance distribution. The scattered intensity is the sum of a coherent (I_{coh}) and an incoherent scattering term which accounts for the fact that the size distribution of the objects is not monodisperse. For the coherent contribution, we assume N_{cyl} identical cylindrical objects. In this case I_{coh} can be expressed as [79]

$$I_{coh}(\vec{q}) \propto N_{cyl} S(\vec{q}) \left|F_{cyl}(\vec{q})\right|^2, \tag{2.92}$$

where $S(\vec{q})$ is the **interference function** and $F_{cyl}(\vec{q})$ the **form factor**, which equals the Fourier transform of the electron density distribution $\varrho_e(\vec{r})$ of the object:

$$F_{cyl}(\vec{q}) = \int_V \varrho_e(\vec{r}) \exp[-i\vec{q}\vec{r}]\, \mathrm{d}V. \tag{2.93}$$

For cylindrical objects with radius R and height H, the form factor follows as

$$F_{cyl}(\vec{q}, R, H) = 2\pi R \frac{\mathcal{J}_1(\sqrt{q_x^2 + q_y^2}R)}{\sqrt{q_x^2 + q_y^2}} \sin\left(\frac{1}{2}q_z H\right) \exp\left[\frac{1}{2}q_z H\right]. \tag{2.94}$$

Here, $\mathcal{J}_1$ is the first order Bessel function [80]. For the interference function, the objects in this work are assumed to be arranged in a **one-dimensional paracrystal** [81]. In other words, there is no constant nearest-neighbor distance, but the inter-particle distances D follow a Gaussian distribution with a central value D_c and a width ω_D:

$$p(D) = \frac{1}{\omega_D\sqrt{2\pi}} \exp\left[\frac{-(D - D_c)^2}{2\omega_D^2}\right]. \tag{2.95}$$

In this context, the term "one-dimensional" is not to be understood in a way that the cylinders are aligned along one line. It means that within the plane, in which the objects are situated, there is no preferential direction. On average, the environment around one cylinder is independent of the viewing direction. With $\Phi(q) = \exp[\pi q^2 \omega_D^2]$, Hosemann [81] derived the interference function

$$S(\vec{q}) = \frac{1 - \Phi^2(q)}{1 + \Phi^2(q) - 2\Phi(q)\cos(qD_c)}. \tag{2.96}$$

Up to this point, the objects are not distributed in size, i. e. only the coherent contribution is calculated. In order to account for the different object sizes, the so-called **local monodisperse approximation** [82] is employed. This is a common approximation for very broad structural size distributions and it assumes that the object size is monodisperse within an area corresponding to the coherence length of the x-ray beam [83]. Like this, coherently scattering domains corresponding to scattering intensities $N_{cyl}^j S^j(\vec{q}) \left|F_{cyl}^j(\vec{q})\right|^2$ are obtained and the total intensity is the sum over all domains

$$I(\vec{q}) \propto \sum_j N_{cyl}^j S^j(\vec{q}) \left|F_{cyl}^j(\vec{q})\right|^2. \tag{2.97}$$

For the simulation of the measured data, in this work two types of cylinders with radii R_1, R_2 and heights H_1, H_2 are modeled. The probability of a cylinder to be type 1 does not necessarily have to be 0.5, but can be treated as a free parameter. All structural lengths $\xi \in \{R_1, R_2, H_1, H_2, D\}$ follow distribution functions in analogy to equation 2.95.

So far, the theory only encompasses scattering events which is not sufficient for a successful data modeling. It is important to account for the reflections of the x-rays before and after the scattering event. This becomes possible by applying the DWBA. In this framework, three more scenarios (see figure 2.18) arise in addition to the single scattering event which is illustrated as the first scenario. Using the DWBA, they enter the calculation as three correction terms to the form factor presented in equation 2.94. Each term corresponds to

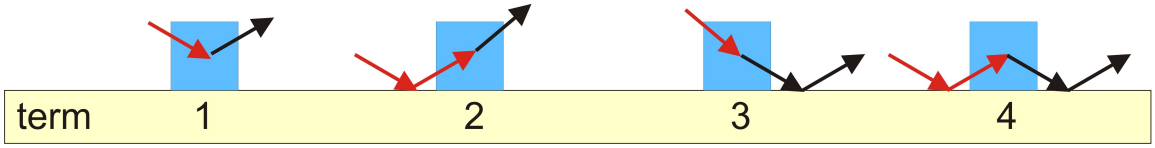

Figure 2.18: *Schematic view of the four scenarios which enter as four terms into the form factor within the distorted-wave Born approximation.*

one of the scenarios of figure 2.18 so that the corrected form factor [84] can be expressed as

$$\begin{aligned}\mathcal{F}_{cyl}(q_x, q_y, (\vec{k}_i)_z, (\vec{k}_f)_z) = F_{cyl}(q_x, q_y, (\vec{k}_f - \vec{k}_i)_z) + r^F(\alpha_i) F_{cyl}(q_x, q_y, (\vec{k}_f + \vec{k}_i)_z) + \\ + r^F(\alpha_f) F_{cyl}(q_x, q_y, (-\vec{k}_f - \vec{k}_i)_z) + \\ + r^F(\alpha_i) r^F(\alpha_f) F_{cyl}(q_x, q_y, (-\vec{k}_f + \vec{k}_i)_z).\end{aligned} \tag{2.98}$$

The Fresnel reflection coefficients correspond to the substrate material and are roughness corrected by the Névot-Croce factor which was presented in section 2.3.2.
For the GISAXS data analysis which is performed in this work, the objects are not assumed to be situated directly on the substrate but either on top of a supported polymer thin film or embedded in a polymer matrix [85, 86]. Both cases require slight corrections of 2.98. For more details, please refer to reference [56].

Chapter 3

Experiments

In this chapter, all experimental techniques and the corresponding routes towards data analysis are presented. Motivated by the possibility to tailor PSA morphologies by choosing the conditions for the sample preparation, different protocols are detailed at the end of this chapter. In the beginning, the polymers that are used in this study are listed.

3.1 Investigated polymers

All examined polymers were statistical copolymers synthesized by *BASF SE*. They consisted of two or three components, one of which was sticky and the other components were glassy. Two types of sticky monomers were used: ethylhexylacrylate (EHA) and n-butylacrylate (nBA). The non-tacky monomers were styrene (S), maleic acid anhydride (MAA), methylmethacrylate (MMA), methylacrylate (MA), hydroxyethylacrylate (HEA) and acrylic acid (AA).
Table 3.1 lists all homopolymers related to the investigated monomers. In addition to that, the corresponding mass density ϱ and the real part of the refractive index δ are given. In this study, δ is the most important parameter for the identification of the components in a phase separated statistical copolymer based PSA. It is calculated for a wavelength of $\lambda = 0.154$ nm, as it was provided by the x-ray reflectivity setup.
Comprising these monomers, different statistical copolymers were available (see table 3.2). In principle, they can be categorized in three different sample series: a comonomer series with EHA as the majority component and three different glassy copolymers; a molecular weight series of P(nBA-stat-MA); and a series of statistical copolymers which consisted of three different components. The molecular weights within the first and the third series were comparable. Furthermore, when for example the influence of the preparation conditions was investigated, the copolymer P(EHA-stat-20MMA) was chosen.
All statistical copolymers are listed in table 3.2 together with the respective composi-

polymer	$\boldsymbol{\varrho}$ $\left[\frac{\mathrm{g}}{\mathrm{cm}^3}\right]$	$\boldsymbol{\delta}$ $[\cdot 10^{-6}]$
PEHA	0.903	3.21
PS	1.05	3.62
PMAA	1.48	4.25
PMMA	1.17	4.06
PnBA	1.08	3.79
PMA	1.22	4.19
PHEA	1.31	4.50
PAA	1.09	3.70

Table 3.1: *List of homopolymers which are related to the components of the statistical copolymers used in this study together with the corresponding mass densities and x-ray refractive indices.*

tion ratios, molecular weights, polydispersities and calculated refractive indices δ. The calculation of δ of the statistical copolymers was performed by weighting the refractive indices of the homopolymers related to the corresponding component by their composition ratios. This is possible because of the direct proportionality of δ to the electron density (see equation 2.69). The nBA based copolymers additionally contained 0.3 % of a photoinitiator which was not used in this study. For the determination of δ for these polymers, an nBA content of 80 % was assumed, neglecting the contribution of the small amount of photoinitiator.

copolymer	**composition** [%]	$\boldsymbol{M_w}$ $\left[\frac{\mathrm{kg}}{\mathrm{mol}}\right]$	$\boldsymbol{\delta}$ $[\cdot 10^{-6}]$	$\boldsymbol{P}$
P(EHA-stat-S)	90 / 10	182	3.25	
P(EHA-stat-MAA)	90 / 10	187	3.31	
P(EHA-stat-MMA)	90 / 10	165	3.29	
P(EHA-stat-20MMA)	80 / 20	248	3.38	2.8
P(nBA-stat-MA)	79.7 / 20	54	3.87	3.9
P(nBA-stat-MA)	79.7 / 20	192	3.87	6.4
P(nBA-stat-MA)	79.7 / 20	600	3.87	13.6
P(nBA-stat-MA-stat-HEA)	79.7 / 15 / 5	193	3.89	6.7
P(nBA-stat-MA-stat-MMA)	79.7 / 10 / 10	195	3.86	7.0
P(nBA-stat-MA-stat-AA)	79.7 / 15 / 5	191	3.85	7.1

Table 3.2: *List of statistical copolymers used in this study together with the corresponding molecular weights, refractive indices and the available polydispersities.*

The EHA containing copolymers were synthesized via radical solution polymerization [87]

in a semi-batch procedure in iso-butanol at 100 °C with a peroxide starter. The PSAs which contain nBA were polymerized in methylethylketone or in n-butylacetate at 80 °C. As it is typical for industrial polymers, they showed broad molecular weight distributions. The available polydispersity values are listed in table 3.2.
In addition to the statistical copolymers which are listed above, probe tack measurements were performed with the homopolymer PEHA.

3.2 Characterization methods

Different methods were employed to investigate the PSA films. The morphology was monitored with the reciprocal space techniques x-ray reflectivity, which is the main investigation method in this work, in-situ neutron reflectivity and grazing incidence small angle x-ray scattering. The film thickness was determined using white light interferometry and gravimetry. The mechanical characterization is based on contact angle measurements and probe tack tests, for which the corresponding punch roughness was determined with atomic force microscopy. Finally, optical microscopy was used to monitor the material distribution on the substrate for the case of unstable films.

3.2.1 X-ray reflectivity (XRR)

The XRR (see section 2.3.2 for a theoretical description) experiments were carried out with a *Siemens D5000 Diffraktometer* under room temperature conditions. In order to keep the PSA surface untouched, the sample was fixed by a vacuum chuck. A 12 mm wide x-ray beam with a wavelength of 0.154 nm, which corresponds to the Cu-K_α line, was chosen for all measurements. The beam was collimated with a slit system in combination with a tantalum knife edge. The reflected beam was detected with a scintillation counter situated behind a graphite monochromator to filter the Cu-K_β line. To avoid detector saturation resulting from the high intensities for small incident angles and thus wrong counting rates, an absorber reducing the intensity by a factor of approximately 100 was used.
In order to account for a possibly slightly tilted PSA surface originating from dust particles underneath the glass substrate or a slight misalignment during the film preparation procedure, a so-called rocking scan was performed before each measurement. In more detail, the x-ray source was positioned at an angle of 0.2° and, on the opposite side, the detector at an angle of 0.4° with respect to a nominal zero angle. The sample was then moved between 0.15° and 0.25° with an angular resolution of 0.001°. Simultaneously, the detector recorded the resulting intensity as a function of the sample holder angle. The corresponding intensity distribution had the shape of a single peak. The position of this

peak was fitted assuming a Gaussian and the extracted value was subsequently set to 0.2° guaranteeing specular reflection geometry throughout the experiment.
In the following measurement, the position of the x-ray source was kept fixed, whereas the sample and the detector moved simultaneously by the angles α_i and $2\alpha_i$, respectively, and the intensity was recorded as a function of q_z. The reflectivity curves covered an angular range of $0 < \alpha_i < 3.5°$ with a maximum resolution of 0.005°. For the samples which do not exhibit small features in the XRR data for higher angles, the resolution was relaxed to 0.015° in order keep the exposure to x-rays as short as possible. Moreover, to account for the lower counting rates at higher incident angles, the angular range was divided into three overlapping intervals with adjusted measurement times which were merged according to the selected integration times.

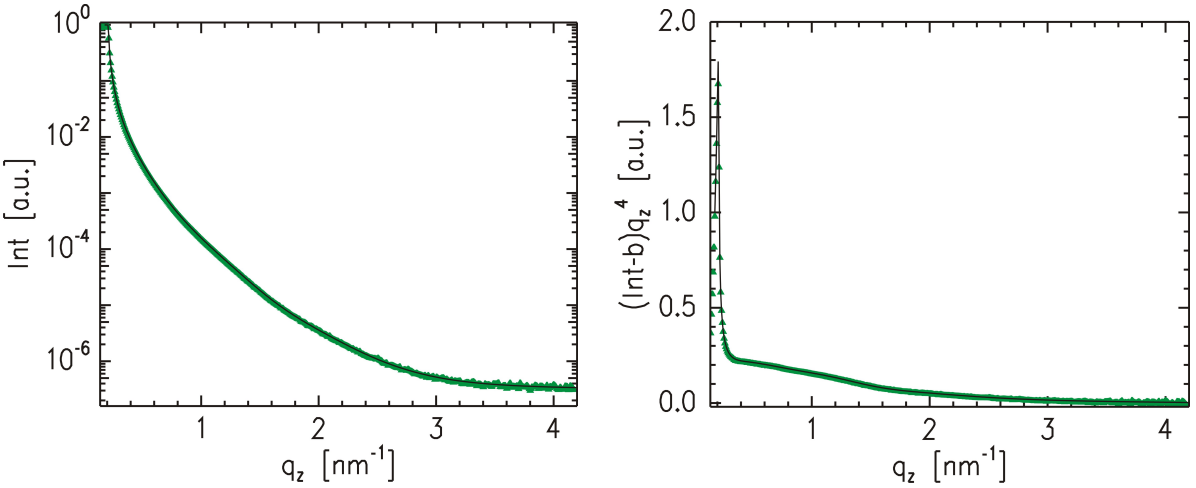

Figure 3.1: *Left: XRR data (symbols) and respective model fit (solid line) of a thick P(EHA-stat-20MMA) film which was solution cast under ambient conditions. Right: Corresponding Fresnel-normalized representation with background* $b = 3.3 \cdot 10^{-7}$.

For the thick PSA films investigated in this work, the weak features in the XRR data are most evident when the q_z-axis is linear and the intensity Int is replaced by $(Int - b)q_z^4$, where b is a constant background. This so-called **Fresnel-normalized** representation compensates the decay of the reflected intensity at a single interface (see equation 2.74) and all appearing features originate from fluctuations in the refractive index. The need for such an improved plotting is best visible when comparing the classic XRR data presentation as used in figure 2.16 with the Fresnel-normalized one.
This is demonstrated in figure 3.1 for a freshly prepared, 50 μm thick P(EHA-stat-20MMA) film, which was cast from a toluene based solution under ambient conditions (please refer to section 3.3.2 for further details). Whereas in the classical, single-logarithmic representation (left) the curve appears almost featureless, there are more pronounced

modulations in the range $0.3 < q_z < 3.4$ nm^{-1} for the Fresnel-normalized data (right). As a consequence, in this work the Fresnel-normalized representation is chosen for all XRR data of solution cast PSA films.

The data analysis was performed with the reflectivity simulation and analysis tool *Parrat32* [64]. With this software, the reflectivity of an assumed refractive index profile can be calculated via the layer based Parratt algorithm which was described in section 2.3.2. The calculated reflectivity of an initially assumed model is compared to the measured data, the assumed refractive index profile is then modified, and again, the reflectivity is calculated. Iteratively, a fit to the data is achieved and the correct refractive index profile is obtained.

Using the in section 2.3.2 introduced nomenclature, the layer model for this PSA film is shown in table 3.3. As explained, for the modeling of thick films the substrate is always replaced by the bulk material, which is homogeneous and its refractive index equals that of the underlying statistical copolymer (in this case: P(EHA-stat-20MMA)). Because the absorption coefficients of the individual components do not differ significantly and because within this range, there is no prominent influence of β on the calculated reflectivity, a constant absorption is assumed throughout all layers.

layer	$\boldsymbol{d}$ [nm]	$\boldsymbol{\delta}$ [$\cdot 10^{-6}$]	$\boldsymbol{\beta}$ [$\cdot 10^{-9}$]	$\boldsymbol{\tau^{RMS}}$ [nm]
1	–	0	0	0
2	1.09	3.44	5.72	0.42
3	2.28	3.95	5.72	0.30
4	3.91	3.39	5.72	1.14
5	0.94	3.27	5.72	1.11
6	3.60	3.31	5.72	7.01
7	∞	3.38	5.72	4.16

Table 3.3: *Layer model of a P(EHA-stat-20MMA) film which fits the measured XRR data shown in figure 3.1.*

Although different layers are entered into the software, the corresponding refractive index profile (see figure 3.2), which is the distance from the sample surface plotted over the refractive index δ, does not exhibit well-defined layering. Using the coordinate system of figure 2.13 this distance is, strictly speaking, $0 - z$, where z is negative. It is, however, common to denote the distance from the surface with z, where $z > 0$.

The reason for the smeared out profile in figure 3.2 can be found in the high interfacial roughness values, some of which even exceed the corresponding layer thickness (e. g. $\tau_6 > d_6$). As a consequence, the physical meaning of the d, δ and τ parameters is no

longer valid. These parameters are rather used to model the refractive index profiles. The deviation can for example be seen from the maximum values of δ: it is $\delta_3 = 3.95 \cdot 10^{-6}$ in the layer parameters, whereas it is only $3.91 \cdot 10^{-6}$ in the resulting refractive index profile. Nevertheless, within the scattering depth of the x-rays, the refractive index profile as it is shown in figure 3.2 provides the correct value of the refractive index at any distance z from the sample surface.

This is confirmed by slicing the profiles in 0.1 nm thin slabs until homogeneous bulk material is reached and, thereby, introducing several hundred layers. The refractive index of each slab is assigned according to the refractive index profile and due to the small thickness of 0.1 nm, the roughness of all slabs can be assumed to be zero. This new many-layer model now has the same refractive index profile compared to that described in table 3.3. The advantage is, however, that due to the missing roughness, the Parratt algorithm works reliably and calculates the reflectivity correctly. From the coincidence of the calculated XRR data from both layer models (which both fit the data) for all investigated samples, we conclude the justification of the refractive index profiles. Therefore, for the rest of this work the focus is on the profiles and the layer parameters are sacrificed.

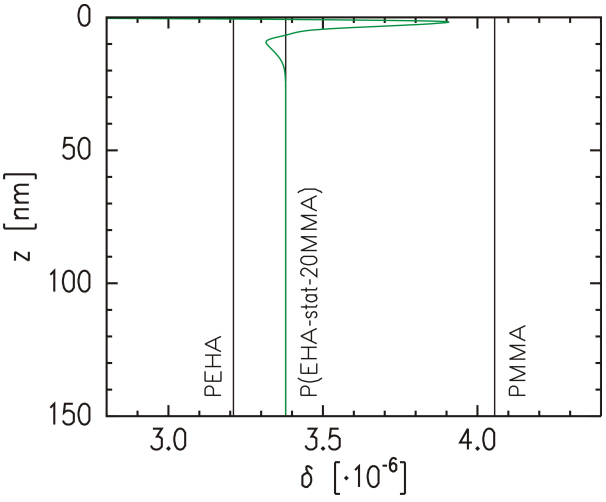

Figure 3.2: *Refractive index profile of a P(EHA-stat-20MMA) film freshly prepared under ambient conditions. The vertical lines mark the values of the refractive index of the statistical copolymer and the related two homopolymers as shown by the labels.*

The described procedure was performed by programming a *Microsoft Excel* based *Visual Basic* code (see appendix A.1) which reads in the refractive index profile of the initial model. Then, the program creates the new many-layer model in the correct syntax of *Parratt32*. With *Parratt32*, the corresponding XRR data are simulated and can easily be compared to the initial fit.

For copolymers which consist of two components, the refractive index profile $\delta(z)$ can be transferred into a composition profile. The reason is that, due to the proportionality of the refractive index to the electron density, the measured refractive index is a linear combination of the known refractive indices of the components (in this case δ(PEHA) and

δ(PMMA)). For example, in the presented sample the PMMA concentration (PMMA volume per unit sample volume) at a given depth z is calculated via

$$c_{\mathrm{PMMA}}(z) = \frac{\delta(z) - \delta(\mathrm{PEHA})}{\delta(\mathrm{PMMA}) - \delta(\mathrm{PEHA})}. \tag{3.1}$$

For a better illustration, it is often more convenient to show the composition in a grayscale coded way (see figure 3.3). In this visualization, PEHA is represented by white and PMMA by black color. Mixed compositions are illustrated by using the RGB code scheme and assigning the color $(255 \cdot c_{\mathrm{PMMA}}(z), 255 \cdot c_{\mathrm{PMMA}}(z), 255 \cdot c_{\mathrm{PMMA}}(z))$ to the corresponding line of the image. Also for this purpose, a *Visual Basic* program was written whose code code can be found in the appendix A.2.
As a result, a PMMA enriched zone is identified at the sample surface. This is followed by an enrichment of PEHA before the composition converges towards homogeneous bulk material.

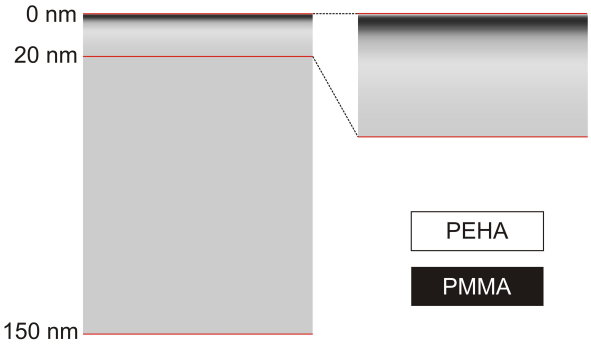

Figure 3.3: *Left: Direct conversion of the refractive index profile into a grayscale-coded composition profile. Right: Zoom into the upper 20 nm (top) and corresponding grayscale code (bottom).*

For all investigated samples, there are no prominent features in the composition profiles for $z > 20$ nm except the convergence to the bulk composition. That is why in this work, zoomed-in profiles of the region close to the surface ($0 < z < 20$ nm) are shown (see right panel of figure 3.3). This even allows for an enhanced pronunciation of the features close to the film surface.

3.2.2 In-situ neutron reflectivity (NR)

The most important sample preparation technique in this work is solution casting: the polymer is dissolved in a solvent, the solution is distributed on the desired substrate and a dried polymer film is obtained after the solvent has evaporated. The solvent distribution during drying under ambient conditions is monitored with in-situ NR. The experiments were performed at the *FIGARO* instrument of the *Institut Laue-Langevin* (ILL) in Grenoble (France).

The instrument uses the so-called time-of-flight (TOF) mode [88], where the q_z values are not changed classically by a variation of the incident angle. On the contrary, the incident angle is fixed and, instead, a polychromatic neutron beam is used. By registering the different wavelengths λ of the neutrons, different values of q_z are obtained (see equation 2.76).

The drying of the cast polymer solutions was followed in-situ with NR during 300 min with a time resolution of 30 s between successive measurements, so that in total 600 measurements were performed to record the drying. For these kinetic measurements, the nominal angle at which the neutrons impinged on the sample surface was $\alpha_i = 0.62°$. Immediately after each drying experiment, a full neutron reflectivity curve was recorded using the two different incident angles 0.62° and 3.82°. This final measurement is also referred to as static measurement. The corresponding integration time was set to 120 min, which was split up in 30 min for $\alpha_i = 0.62°$ and 90 min for $\alpha_i = 3.82°$, respectively. The two parts of the reflectivity curve composing the static NR data were merged according to the selected accumulation times.

Owing to the TOF mode, neutrons in a wavelength range between $\lambda = 0.2$ and 3 nm were collected simultaneously by registering their respective times of flight. As a consequence, no mechanical displacements of any part of the setup had to be done during the kinetic measurements. For all investigated samples, the resulting range of the scattering vector $0.045\ \text{nm}^{-1} < q_z < 1.2\ \text{nm}^{-1}$ was sufficiently broad to produce meaningful reflectivity curves. As a consequence, disturbing vibrations due to motor movements were avoided. In addition, the sample chamber was mounted on an anti-vibration table to decouple the system from mechanical noise from the experimental hall.

A further advantage of the TOF mode is that the whole q_z-range of the probed reflectivity curve is averaged over the same time interval. This is not possible for classical single-wavelength NR experiments because different incident angles have to be measured at different times. Especially for experiments with fast kinetics, this can lead to a misinterpretation of the experimental data. The necessary pulsing of the neutron beam was done by a four-disc system of choppers with two controlling and two inactive (dephased) choppers. The distance between the middle of the controlling choppers and the sample was 5331 mm.

The data were recorded with a *Bidim26* wire-grid detector, which was positioned at a distance of $d_{SD} = 3054$ mm from the sample and which had a pixel size of $d_{px} = 2.017$ mm in the vertical direction. A typical raw-data image, as it is obtained by the *Lamp* software during the kinetic measurement, is shown in figure 3.4. It depicts the pixel position of the reflected neutrons as a function of the wavelength measured in Angstroem. The number of detected neutrons per pixel is color-coded. The image was taken in the beginning of

the drying process of a solution cast P(nBA-stat-MA) film with $M_w = 54$ kg/mol.

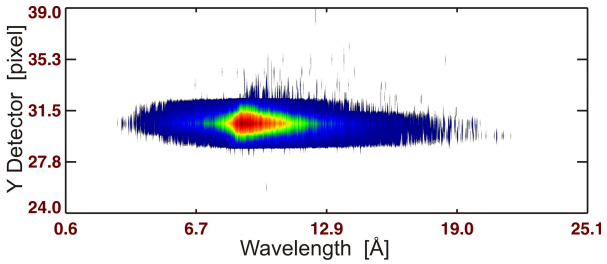

Figure 3.4: *Raw data as obtained from the Lamp software. For the intensity, a linear color code is used.*

The neutrons, which exactly impinge on pixel number 30, fulfill the specular condition with $\alpha_i = 0.62°$. Thus, the final reflectivity curve for $\alpha_i = 0.62°$ is equal to a horizontal cut in the raw data (see figure 3.4) along pixel 30. In order to improve statistics, however, the data were integrated over a small interval around the specular reflection. To additionally enhance the signal-to-noise ratio, several 30 s measurements were added, depending on the time-dependent overall reflected intensity and the solvent evaporation kinetics.

The reflected intensity strongly depends on the amount of deuterated material in the sample. In this case, the deuterated component was the evaporating solvent toluene. As a consequence, the registered number of neutrons per time t decreased in the course of the kinetic measurement. Furthermore, the solvent evaporation became slower towards the end of the experiment. Therefore, the number of 30 s measurements which were chosen to comprise one reflectivity curve increased with time.

The intensity evolution during the kinetic experiment is directly seen from figure 3.5. It is calculated out of all 600 measurements of the kinetic part of the experiment. For this purpose, each raw data image (as exemplarily shown in figure 3.4), was reduced to the intensity as a function of the pixel number. In more detail, for each pixel the intensities which are attributed to all the different wavelengths are summed up. Under the assumption of perfect alignment and no diffuse scattering, i. e. when all neutrons would be reflected to pixel 30, the corresponding function would be zero except for pixel 30. In this gedankenexperiment, the intensity at pixel 30 would be the integrated intensity of the complete reflectivity curve.

Each horizontal line in figure 3.5 represents one raw data image which was reduced as described above. The intensity is color-coded (see scale bar). In total, the image consists of 600 horizontal lines, each calculated out of one 30 s measurement. It can be seen that the reflected intensity was not centered around pixel 30 (dashed line) as it should have been the case for an incident angle of $\alpha_i = 0.62°$. The position of the reflection even changed as a function of time.

The reason can be found in a non-perfect sample alignment which was performed using the reflection of the neutron beam from the bare silicon substrate. Due to the high substrate

roughness, the available signal was very weak causing errors in the choice of the correct tilt of the substrate. Without touching or moving the substrate any further, the solution was dispersed on the substrate and the measurement was started.

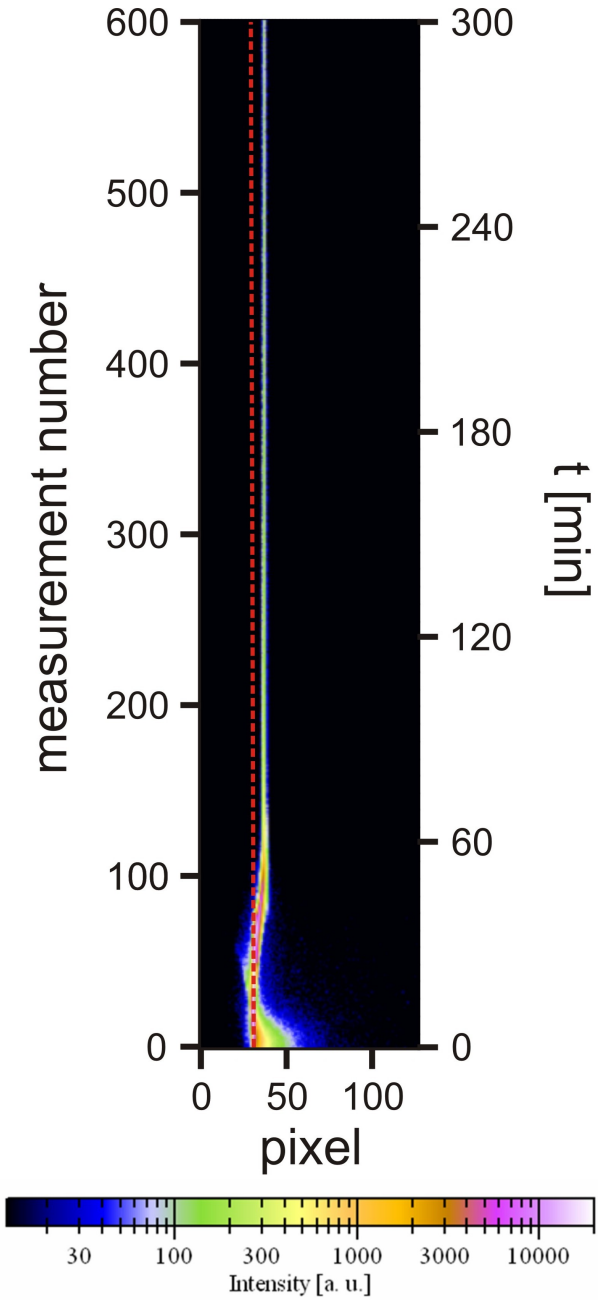

Figure 3.5: *Change of the position of the specular reflection during drying of a P(nBA-stat-MA) film with M_w = 54 kg/mol. One pixel in the image is the over all wavelengths integrated intensity of a single 30 s measurement (for a fixed pixel in the raw data). A horizontal line in the image represents the integrated information of a single 30 s measurement. From bottom to top, the measurement number increases (left axis) which is equal to an increase in time (right axis). The dashed line is positioned at pixel 30. The logarithmic intensity scale is shown at the bottom.*

For small times t, the still liquid film compensated the slight misalignment better than for large t due to the tendency of the surface to orient perpendicular to the gravity field. Therefore, in the beginning of the experiment more of the neutrons were reflected in the vicinity of pixel 30 and, thus, the incident angle was closer to 0.62° as compared to larger t. Due to the viscosity of the polymer, the angle of the drying sample surface deviated

more and more from the initially liquid surface. This implies that the real incident angle with respect to the misaligned sample changed as a function of time.
The reflectivity curves were extracted out of the raw data using the *Lamp* software. Because the instrument is dedicated to liquid surfaces which are always perpendicular to the gravity field and because the absolute angle of the impinging neutrons is always the same, the underlying algorithm assumes α_i to be exactly 0.62°. That is why for the sample systems used in this work, the calculated values of the scattering vector of all measurements had to be corrected depending on the deviation of the incident angle. The correct values of q_z can be calculated out of the uncorrected ones (q_z^u) by using the equation

$$q_z = q_z^u \cdot \frac{\sin(\alpha_i + \alpha_{off})}{\sin(\alpha_i)}. \tag{3.2}$$

α_{off} is the offset of the incident angle with respect to the nominal $\alpha_i = 0.62°$. Because both, the incident and also the exit angle exhibit this offset, it corresponds to half of the deviation of the specularly reflected beam from pixel 30. In order to determine α_{off}, the pixel p_{sp} around which the specularly reflected neutrons impinged had to be determined for all reflectivity curves.

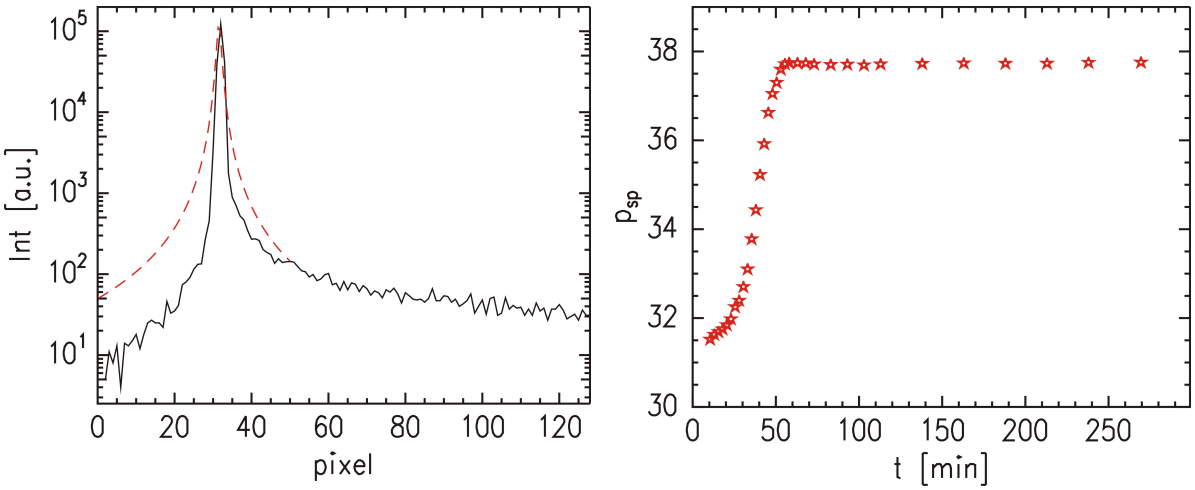

Figure 3.6: *Left: Horizontal cut (solid line) through the two-dimensional image depicted in figure 3.5. Fitting of a Gaussian (dashed line) to the observed peak leads to the value of p_{sp}. Right: Position of the specular reflection during drying of a solution cast P(nBA-stat-MA) film with $M_w = 54$ kg/mol as a function of time.*

For this purpose, horizontal cuts from the two-dimensional images corresponding to figure 3.5 were extracted. Several cuts were added depending on the number of raw data images which were combined in one reflectivity curve. The peak position originating from the

specular reflection was determined by fitting a Gaussian. The left panel of figure 3.6 shows the cut (solid line) which includes the raw data shown in figure 3.4. In this case, the fit (dashed line) leads to $p_{sp} = 31.5$. The change of p_{sp} as a function of time is depicted in the right panel of figure 3.6. Finally, for the correction of the reflectivity data with equation 3.2, geometrical considerations reveal that α_{off} can be calculated via

$$\alpha_{off} = \frac{1}{2}\left(\arctan\left[\frac{(p_{sp} - 30)d_{px} + d_{SD}\sin(\alpha_i)}{d_{SD}}\right] - \alpha_i\right). \tag{3.3}$$

3.2.3 Grazing incidence small angle x-ray scattering (GISAXS)

All GISAXS experiments (see section 2.3.4 for a theoretical description) were carried out at the beamline BW4 at HASYLAB (DESY, Hamburg, Germany) [89, 90]. A monochromatic x-ray beam with a size of 40 μm $\times$ 20 μm and a wavelength of $\lambda = 0.138$ nm impinged under an incident angle $\alpha_i = 0.36°$ on the sample surface. The incident angle was chosen to be well above the critical angles of the components of all investigated copolymers.
The diffusely scattered intensity was recorded by a two-dimensional (2D) *MarCCD* detector (2048 $\times$ 2048) pixels with a pixel size of 79 μm $\times$ 79 μm, which was positioned at a distance of 2003 mm measured from the probed spot of the sample. The detector was protected from the specularly reflected intensity by a point-like beamstop.
Two prominent line cuts, which are perpendicular to each other, are usually extracted. For both cuts, the intensity of five pixels was integrated in order to improve statistics. The first, vertical cut, which is referred to as **detector cut**, was taken along α_f and coincides with the symmetry axis at $\psi = 0$. The second, horizontal cut is called **out-of-plane cut** and is taken along ψ at that exit angle α_f which is equal to the critical angle of the material whose spatial distribution in the PSA is investigated. Due to the symmetry of the 2D GISAXS patterns, only one half of the out-of-plane cut was used. To recall the geometry, please refer to figure 2.17.
It is common to show the line cuts as a function of the corresponding component of the scattering vector $\vec{q}$ (see equation 2.90), which is q_z for the detector cut and q_y for the out-of-plane cut. The out-of-plane cut mostly contains information about lateral structures (parallel to the sample surface), whereas the detector cut is mostly determined by the structuring in z-direction [91].

3.2.4 White light interferometry (WLI)

Another optical investigation technique, which was employed in this work, is WLI. With this method, the thickness of supported polymer films can be determined over a wide thickness range [92]. In this work, WLI was used when the thickness of spin-coated (see

section 3.3.4) films exceeded the range in which a reliable determination with XRR is possible.
Similar to XRR, the reflectance of the film under investigation was measured. The incident beam, however, impinged on the sample under a constant angle of 90°. Instead of the incident angle, the wavelength of the light beam was varied, so that the reflectance was measured as a function of the wavelength of the incident beam. The data were analyzed using the software provided by the device manufacturer. The involved calculations are similar to those composing the Parratt algorithm (see section 2.3.2).
For the experiments, an *Filmmetrics Inc. F20 Thin-Film Measurement System* was mounted on top of a sample chamber (60 mm × 60 mm) equipped with a suitable hole to irradiate the sample. Like this, possible disturbances of the experiment originating from a slight wobbling of the interferometer were avoided. The spot size of the light beam could be varied between 0.5 and 10 mm and the maximal accessible wavelength range with the used setup was between 340 and 1100 nm.
To make WLI applicable, a strong reflection from the substrate is required. Therefore, the corresponding samples were prepared on silicon wafers and not on transparent glass slides.

3.2.5 Gravimetry

For the sample preparation, gravimetry was established as control experiment. In this work, it served for two purposes: first, to monitor in-situ the weight loss during solvent evaporation of solution cast films. Such experiments were performed in the context of the in-situ NR experiments which were introduced in section 3.2.2. The second field of application is either to cross-check the obtained film thickness or to measure the residual solvent content of films which were processed following solution casting based protocols that are presented in section 3.3.3.
The gravimetric measurements for a full monitoring of the drying procedure were carried out on a *Sartorius 1006* precision balance with an accuracy of 1 mg and with a chosen time resolution of 10 s. The balance was connected to a computer via an RS232 interface. The mass was registered as a function of time using a *TestPoint* program developed by Dr. V. Körstgens. For the evaporation experiments the balance was kept in a similar environment as compared to the in-situ NR experiments.
For the second type of experiments, a *Sartorius BP 210D* precision balance with an accuracy of 0.1 mg was used. In order to measure the average film thickness, it was necessary to determine the mass of the substrate m_S before the coating step. Under the assumption of a full coverage of the substrate and an ashlar-formed polymer film, the film thickness of the dried film was calculated via

$$h = \frac{m(\text{sample}) - m_S}{A_S \varrho(\text{polymer})}, \tag{3.4}$$

where m(sample) is the mass of the dried sample (including the substrate) and A_S the area of the substrate. The density of the copolymer ϱ(polymer) is calculated by weighting the densities of the individual components (see table 3.1) by their respective composition ratio.

3.2.6 Contact angle measurement

Two types of mechanical investigations were performed with the obtained PSA films. One of them was the determination of the surface tension via contact angle measurements. The underlying theoretical concept is elaborated in section 2.1.4.
The contact angle measurements were carried out on a *dataphysics Contact Angle System OCA* at a temperature of 20 °C which was kept constant by air-conditioning. A sessile droplet with a volume of 2 μL was dispensed by a computer controlled syringe and brought in contact with the surface of the adhesive film under investigation by a movable sample stage. Immediately after placing the droplet onto the sample, the stage was moved into the focus of a pre-aligned camera with high magnification and a movie of the droplet was recorded for around 70 s with a frame rate of 15 images per second.

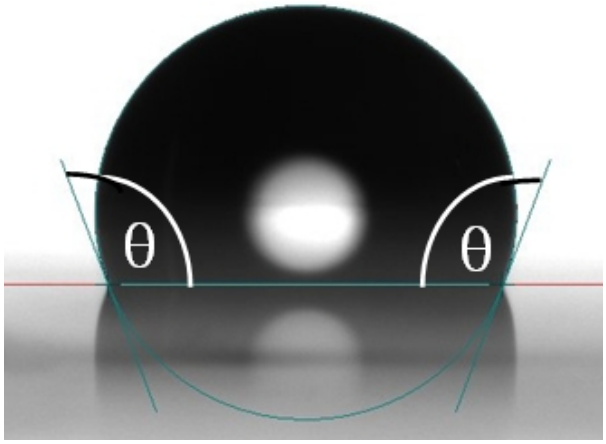

Figure 3.7: *Representative image of a movie monitoring the contact angle of a droplet on a PSA film. An elliptical contour was fitted to the droplet and the corresponding contact angle was calculated.*

The contact angle Θ of the droplet with respect to the sample was extracted with the *dataphysics SCA20* software from each image of the movie by fitting an ellipsoidal contour to the droplet shape (see figure 3.7). The software determines the left and the right contact angle independently from each other. In case they are not equal, the corresponding mean value is registered. In figure 3.7, both angles are equal to $\Theta = 110.7°$. The influence of gravity on the droplet shape can be neglected for such small volumes justifying the assumption of an ellipsoidal shape [93].

In this work, six different test liquids are used for the droplets. In table 3.4, they are listed together with their dispersive and polar contribution to the surface tension [94]. The terminology of equation 2.27 is used. From top to bottom the **polarity**, which is defined as the ratio between the polar component of the surface tension and the total surface tension, increases.

liquid	$\boldsymbol{\gamma_d}$ $\left[\frac{\mathrm{mN}}{\mathrm{m}}\right]$	$\boldsymbol{\gamma_p}$ $\left[\frac{\mathrm{mN}}{\mathrm{m}}\right]$	**polarity**
paraffin oil	29.5	0	0
diiodomethane	47.4	2.6	0.0549
ethylene glycol	29.0	19.0	0.655
formamide	23.5	33.4	1.42
glycerol	21.2	41.5	1.96
water	19.9	52.2	2.62

Table 3.4: *Dispersive and polar contribution to the surface tension of the test liquids which are used for the contact angle measurements in this study.*

As already mentioned, for the PSA films in this study Θ was determined as a function of time t. This was necessary because the liquid droplets on PSA surfaces did not equilibrate immediately. A monotonic decay of the contact angle with time, which slowed down and approached a limiting value, was observed for all test liquids. Due to the onset of evaporation [95, 96] and dissolution of the polymer it was not possible to measure until the equilibrium angle Θ_f was reached.
This observation had already been made by Kano and Akiyama who described the contact angle of organic solvents on a copolymer comprising PEHA and PAA as an exponential decay [97]. Lavi and Marmur introduced one additional parameter when modeling the spreading behavior of partially wetting liquids [98]. In this work, their function is translated to the problem of equilibrating contact angles, so that the measured data were fitted with

$$\Theta(t) = \Theta_f + (180^\circ - \Theta_f) \exp\left[-k_\Theta \left(t - t_0\right)^{m_\Theta}\right]. \tag{3.5}$$

The fitting function is defined for $t \geq t_0$. At $t = t_0$, the droplet gets in contact with the substrate. At this point the contact angle is $\Theta(t_0) = 180^\circ$. For large times t, $\Theta(t)$ converges to Θ_f being the equilibrium contact angle. Θ_f, k_Θ, m_Θ and t_0 are the fitted parameters, where k_Θ and m_Θ account for the interaction kinetics of the droplet with the adhesive. t_0 can be understood as an experimental parameter describing the time delay between the first contact of the droplet with the sample and the start of the measurement. The values of k_Θ and m_Θ are in the interval $(0, 1.5)$, and t_0 is on the order of seconds.

At least seven data sets $\Theta(t)$ were recorded for each sample to achieve sufficient statistical significance. The given values of Θ_f represent the statistical average and the errors are calculated as the corresponding standard deviation.

3.2.7 Probe tack test

The second technique applied for a mechanical characterization of the PSAs was the probe tack test, which was introduced in section 2.1.6. The experiments were performed under room temperature conditions. A custom-designed apparatus, which is depicted in figure 3.8, was used for all measurements.

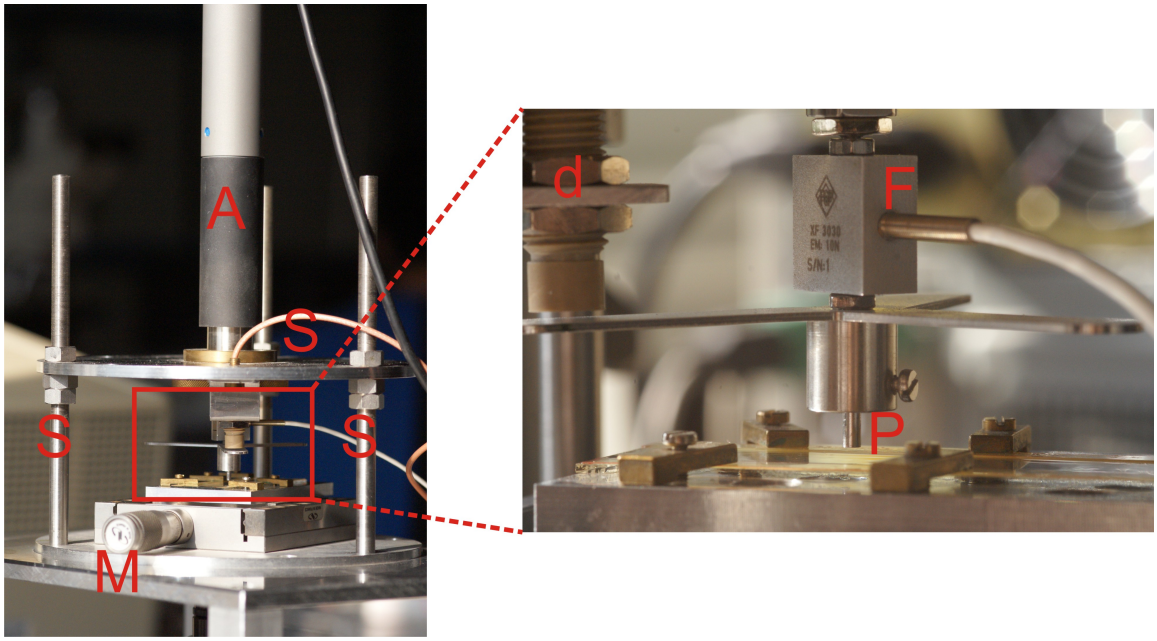

Figure 3.8: *Left: Photograph of the custom-designed tack tester in operation. Right: Zoom into the region around the probed spot of the sample.*

In the left panel of figure 3.8, the complete tack tester is shown in operation. It was equipped with a *DC-Mike Physik Instrumente M-235.2DD* actuator (A) which was used for the movements of the punch. The necessary alignment of the punch, so that its bottom is oriented parallel to the sample surface, was realized using three screws (S). Owing to a micrometer screw (M), different spots on the sample were accessible without the necessity to remount the sample. Additionally, in order to monitor the cavitation process, the contact area was filmed with a CCD camera from below through a hole in the sample stage (not shown in the image). This optical control was used for the alignment of the punch with respect to the PSA surface, too.

The right panel of figure 3.8 is a magnification of the area around the probed spot on the sample. The sample was fixed with clamps in order to avoid movements of the sample during the measurements. The probe (P), which was fabricated out of stainless steel, is directly connected to a *FGP XF-3030* force sensor (F). In order to record the distance of the punch with respect to the sample surface, the distance from a fixed point in space (d) to a three-arm metal device, which is also directly connected to the punch, is measured. A *Kaman KD-2440* distance sensor (d) is employed for this purpose.

The computer-controlled motor movements were enabled with a *TestPoint* program, which was also capable to record the resulting force-distance curves. The complete setup was designed and constructed by Dr. V. Körstgens.

Two prominent parameters were extracted from the measured data: the force maximum (see figure 2.6) and the tack energy

$$W = \int_0^\infty F(\tilde{d})\,\mathrm{d}\tilde{d}, \tag{3.6}$$

which is equal to the work of debonding. At least 8 repetitions of the tack test were performed per sample so that sufficient statistical significance of these parameters was achieved. The corresponding values which are given in this work are the respective mean values and the errors represent the standard deviation.

The position on the sample was changed after each measurement to ensure that each time a fresh spot with an untouched PSA surface was provided. Between two subsequent measurements the punch was carefully cleaned with a soft tissue soaked with toluene so that possible PSA residues or dust particles were removed.

For all investigated samples, the punch approached and contacted the sample at a velocity of 0.1 mm/s. The movement stopped instantaneously after the desired contact force had been reached. After a waiting time of precisely 10 s, during which no further movements were performed, the punch was retracted with a speed of again 0.1 mm/s and the force and the distance were registered simultaneously.

Two types of punches were used: a highly polished one with a radius of $a = 1$ mm, which was used in the tack measurements of either PSA films with a tailored composition profile or of thin, spin-coated PSA films. A surface characterization of this high performance probe is given in section 3.2.8. The surface of the second punch ($a = 0.5$ mm) exhibited a significantly larger surface roughness. It was used for the samples which were processed under ambient conditions.

3.2.8 Atomic force microscopy (AFM)

The surface of the highly polished punch was characterized with atomic force microscopy. For this purpose, an *ULTRAObjective* (*Surface Imaging Systems GmbH*) embedded in an ellipsometry setup (*Nanofilm EP3*) was employed. The measurement was carried out in ambient air.

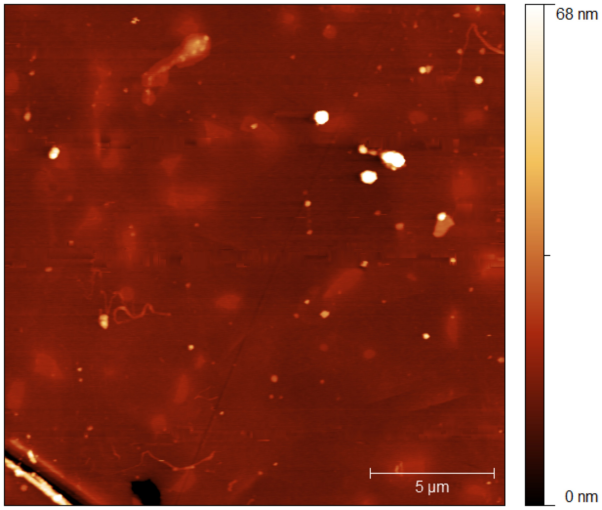

Figure 3.9: *AFM topography image of a punch which was employed for the experiments with thin films and tailored PSA surfaces. The corresponding height information is color-coded (see scale bar).*

The AFM was operated in non-contact mode. The frequency range of the silicon tip was from 146 to 236 kHz. The tip curvature was small compared to the measured structure size. The monitored area was 20 μm $\times$ 20 μm. The recorded image comprised 512 lines, each of which was scanned in 1 s. From the recorded raw data, a polynomial background was subtracted using the *Gwyddion* software.

The described AFM image is shown in figure 3.9. It reveals that the probe surface is smooth over large areas. In addition to that, there are several small, round shaped areas which are significantly elevated (see bright spots). Also a scratch which originated from the polishing process is visible in the lower left corner. Using the shown image, the roughness of the punch is calculated to be $\tau^a = 2.0$ nm. But when the three highest objects are excluded, $\tau^a = 1.7$ nm is obtained.

3.2.9 Optical Microscopy

A further control experiment to ensure the PSA film quality is optical microscopy. A *Zeiss Axiotech 25H* optical microscope with a five-times magnification was used. The micrographs were recorded with a *Hitachi KP-D50* CCD camera. A detailed investigation of the film morphology with optical microscopy was not possible because all PSA films used in this work were transparent.

3.3 PSA film preparation

Using the described characterization techniques, different near-surface morphologies and different mechanical properties were observed even among samples which consisted of the same statistical copolymer. The reason can be found in the different preparation protocols which were applied in this work.

In principle, for the preparation of thick PSA films ($h \approx 50$ μm), the (almost) solvent-free doctor-blading technique and solution casting were used. The latter is performed either under ambient conditions or under controlled atmosphere. Finally, the selected method to produce ultra-thin PSA films ($h < 1.5$ μm) was spin-coating.

The sample preparation was in general performed under a temperature of approximately 20 °C which was kept constant by air-conditioning. Except for the spin-coating, before which a more sophisticated cleaning method was applied, all substrates had been flushed with compressed, oil-free nitrogen before the coating step in order to remove possible dust particles. For the thick films, no further substrate treatment steps have been performed. The reason is that, owing to their short-ranged nature [99, 100], the interactions between the substrate and the near-surface region of the PSAs, which is in the focus of the investigation, can be neglected.

3.3.1 Doctor-blading

The doctor-blading was performed semi-automatically using a *Sheen Automatic Film Applicator 1137*. The polymeric material was distributed manually on a small area on the substrate directly in front of a cylindrical blade. In the subsequent blading step, the polymer is distributed so that, finally, a homogeneous film is obtained. A schematic view of the technique is shown in figure 3.10.

The substrates (*Menzel*, 90 mm × 70 mm × 1 mm) were placed on a plane which is carefully aligned perpendicularly to the gravity field. The blade is equipped with 50 μm deep notches. Although the application speed is adjustable in a range between 50 and 500 mm/s, the best results were achieved with a speed of 200 mm/s.

To rule out edge effects due to the acceleration and deceleration of the blade, three substrates were placed in a row and coated simultaneously. The corresponding XRR measurement was performed only with the sample in the middle. An appropriate polymer viscosity for the blading step was achieved by adding a small amount of isobutanol leading to a solvent concentration of $5 \cdot 10^{-4}$ mL/mg. To achieve sufficiently plane surfaces for XRR measurements, the samples were subsequently stored for one day in a vacuum oven at a temperature of 120 °C.

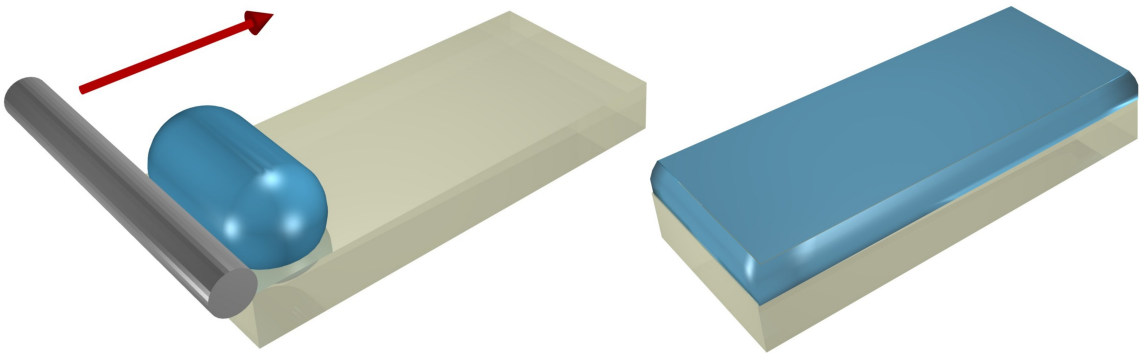

Figure 3.10: *Principle of doctor-blading. Left: The polymer which is to be coated is placed in front of a cylindrical blade. The blade is moved parallel to the substrate (indicated by the arrow). Right: Directly after the blading, a homogeneous PSA film is obtained.*

3.3.2 Solution casting under ambient conditions

In contrast to the solvent-free doctor-blading technique, for the solution casting the PSA was fully dissolved in an organic solvent. For the case of ambient conditions, toluene and isobutanol were selected as solvents. The solution was distributed on glass substrates (*Menzel*, 76 mm × 26 mm × 1 mm) on a carefully aligned surface.

The corresponding point of time is defined as $t = 0$, based on which all given sample ages were calculated. Without touching the samples again, they were covered by an unsealed cubic box (side length 300 mm) to protect the samples from dust, disturbing air flow or UV degradation directly after the casting step. The box was not removed until $t = 24$ h. By this time, weight measurements proved that the solvent had completely evaporated and, thus, fully dried films were obtained. The principle of solution casting is schematically illustrated in figure 3.11.

For all solution cast samples, the initial solution coverage per unit substrate area was set to $s_c = 0.506$ L/m^2. Therefore, the final film thickness h could be controlled via the concentration of the polymer in the solvent c which fulfills the equation

$$c = \frac{h\varrho(\text{polymer})}{s_c}. \tag{3.7}$$

As an example, to obtain a 50 μm thick P(EHA-stat-20MMA) film, the underlying solution concentration had to be $c = 94.5$ g/L. This was confirmed by weight measurements using equation 3.4. Throughout this work, the nominal thickness of all solution cast films was kept fixed at $h = 50$ μm.

The near-surface composition profile of a one day old (which is also referred to as **freshly prepared**) P(EHA-stat-20MMA) film, that was cast under ambient conditions, has al-

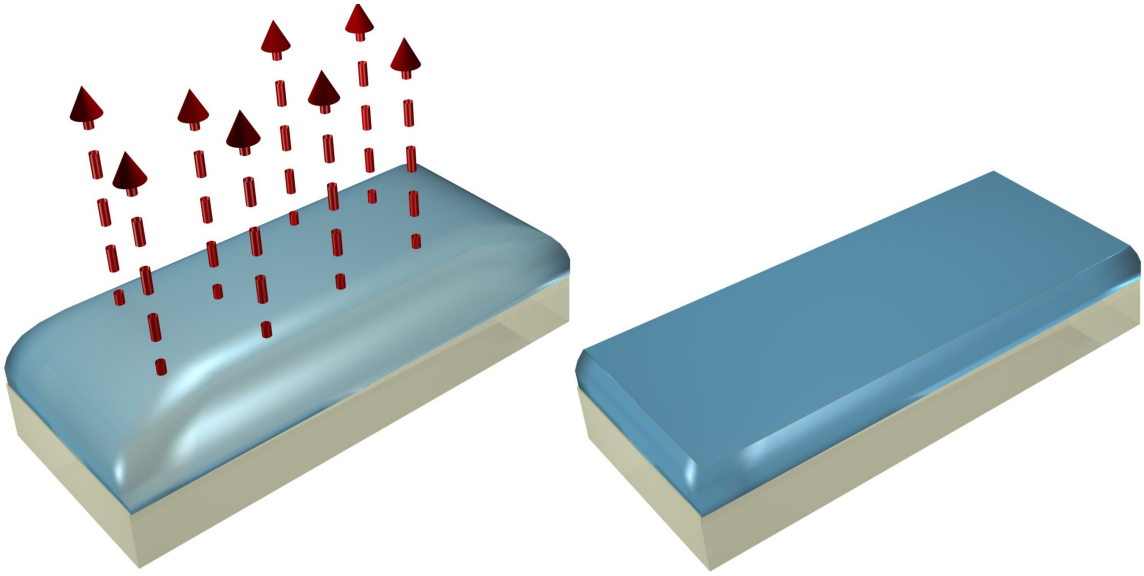

Figure 3.11: *Principle of solution casting. Left: The polymer solution is distributed on a substrate. The solvent evaporates (indicated by the dashed arrows) until the film is fully dried. Right: After a waiting time of one day, a homogeneous PSA film is obtained.*

ready been shown in section 3.2.1. In order to get an estimate of the reproducibility of the experiments, the measurement was repeated with a sample that was prepared using the same preparation protocol but on a different day. The corresponding data is additionally shown in figure 3.12.

From a comparison of the refractive index profiles, it can be concluded that the main features were preserved. There is a pronounced enrichment of PMMA at the sample surface which is followed by an enrichment of PEHA directly underneath. For $z > 100$ nm, both samples consist of 80 % EHA and 20 % MMA, which is the overall monomer composition ratio.

For the preparation under ambient conditions the amplitudes of respective features can be different. Both, the concentrations of PMMA at the surface and of PEHA underneath of the sample corresponding to the solid lines are stronger than those for the sample represented with dashed lines. Also the volumes which are predominantly occupied by one monomer species are not equal for both measurements.

The reason for these slight discrepancies can be found in the not completely controlled external conditions. For example, slight instabilities arising from the climatisation can have an effect regarding the long drying time of the solutions. The main contribution in this context, however, is due to the relative humidity (see section 6.1.1) that can be different in case the corresponding samples are prepared on different days (which is the case for the shown examples). In addition, there might be humidity fluctuations already

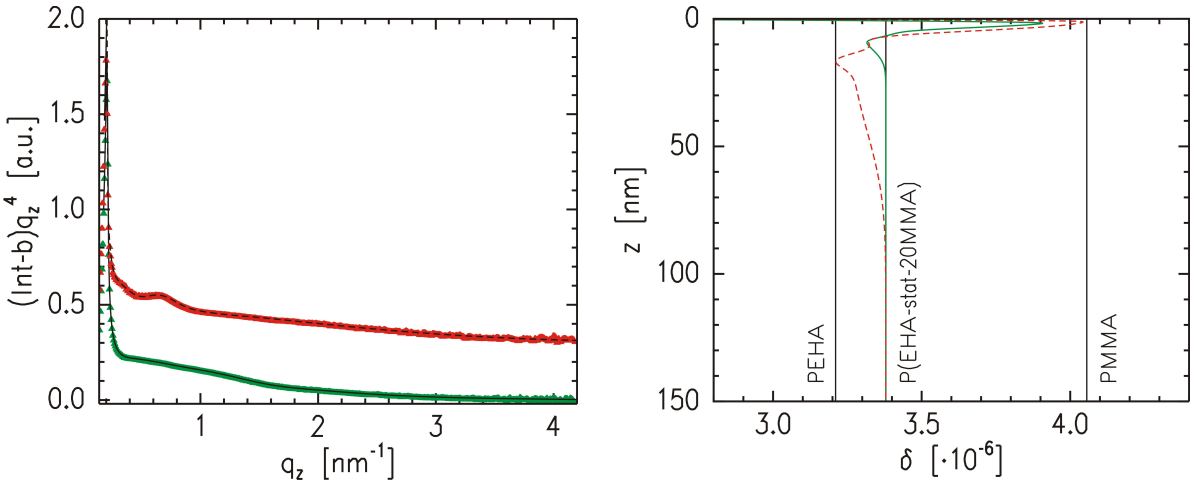

Figure 3.12: *Left: Comparison of XRR data (symbols) and respective fits (solid and dashed lines) of P(EHA-stat-20MMA) films freshly prepared under ambient conditions. The data are shifted along the intensity axis for clarity. Right: Refractive index profiles corresponding to the fits to the data. The solid profile corresponds to the fit illustrated with a solid line in the left panel, and the dashed profile corresponds to the dashed fit. The data presented with dashed lines have already been presented in figure 3.1 and 3.2, respectively.*

during the drying of the cast solution.
Nevertheless, it is important to note that even under ambient conditions the composition profiles can qualitatively be reproduced. Furthermore, it is important to study the performance of the PSAs when they have been prepared under ambient conditions because this case is closest to possible applications of these materials.
However, to get a deeper insight in the driving forces of the resulting composition profiles and to elaborate routes towards a deliberate tailoring, it is necessary to improve the reproducibility. This is achieved by controlling the atmosphere in which the solvent evaporation during the solution casting takes place (see chapter 6). In this work, both, the ambient and the controlled conditions are studied.

3.3.3 Solution casting in controlled atmosphere

A controlled atmosphere during the sample preparation process was achieved by performing the solution casting inside a desiccator (*Schott Duran*, with a flange diameter of 118.5 mm). To avoid unnecessary exposure to ambient air, the desiccator was already pre-aligned before placing the substrate and the lid was closed immediately after the coating step. By filling the desiccator with silica gel (purchased by *Carl Roth GmbH*) a controlled relative humidity (RH) of < 2 % (also referred to as **dry conditions**) was established.
A corresponding control experiment was performed with two freshly prepared P(EHA-

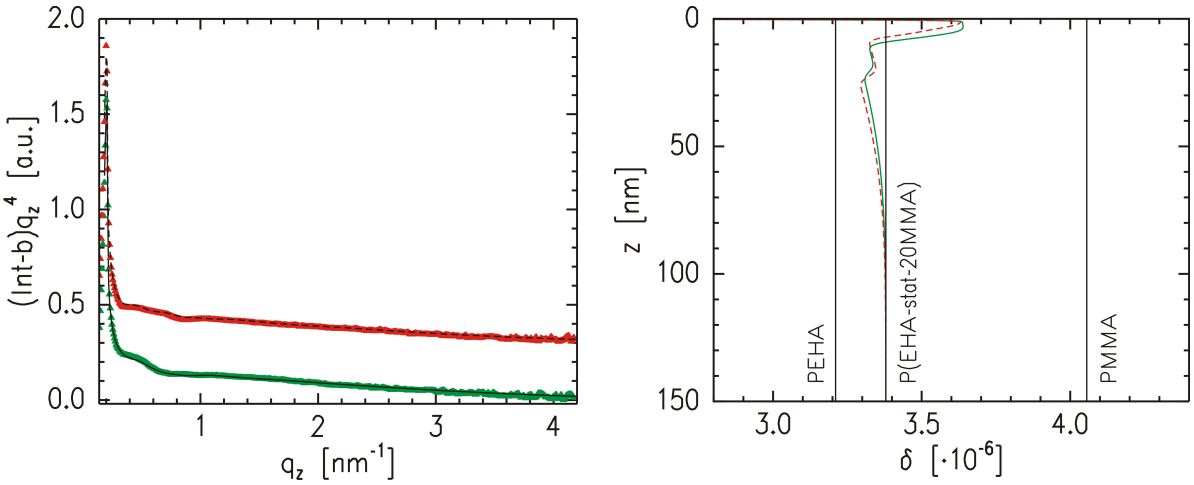

Figure 3.13: *Left: XRR data (symbols) and respective fits (solid and dashed lines) of identically prepared P(EHA-stat-20MMA) films which were solution cast in a desiccator filled with silica gel. The data are shifted along the intensity axis for clarity. Right: Refractive index profiles corresponding to the fits to the data. The solid profile corresponds to the fit illustrated with a solid line in the left panel, and the dashed profile corresponds to the dashed fit.*

stat-20MMA) films, which were solution cast in a desiccator under dry conditions. The improved reproducibility of the composition profiles due to this modified sample preparation is evident from figure 3.13. The XRR data of the identically prepared samples (left panel) already look very similar. The refractive index profiles (right panel) obtained from a fit to the data reveal that the surface PMMA concentrations of the two samples almost coincide. The corresponding maximum concentrations are 49.7 % (dashed profile) and 50.8 % (solid profile), respectively. Also the sub-surface refractive index profile is very well reproduced.

The only difference is that the sample represented by the solid lines has a slightly thicker PMMA enriched zone at the sample surface. This follows from the broader peak of the refractive index profile depicted as solid line for small z values. The described slight difference is also reflected in the XRR data: whereas the first modulation for low q_z values (around $q_z \approx 0.5$ nm^{-1}) is extended up to approximately 0.7 nm^{-1} for the lower curve, it is slightly broader for the upper curve.

The described minor differences in the near-surface composition profiles can have two reasons. First, as already described in section 3.3.2, there might be unavoidable little fluctuations in the laboratory temperature. And second, the time necessary for the manual solution casting is not always exactly the same implying that for different samples the closure of the desiccator lid might be performed at slightly different times. This can result in different amounts of solvent that has already evaporated before closing the desic-

cator. As a consequence, for different samples there are minor variations in the fraction of desiccator volume occupied by the evaporated solvent. These little differences in solvent vapor concentration of the atmosphere surrounding the drying sample are finally mainly responsible for the observed deviations.
It is important to note that the composition profiles of samples obtained from this altered preparation significantly deviate from such which correspond to a preparation under ambient conditions. This is a first hint that a tailoring of the composition profiles seems possible. For this purpose, the desiccator was not only filled with silica gel to provide low humidity but also higher RH atmospheres were generated.
This was enabled by the widely used method to fill the desiccator with saturated salt solutions [101, 102]. If pure water had been used, the RH directly above the surface would have been 100 % by definition. In the salt solution, the presence of ions resulting from the dissolved salt, hinders the water molecules to go into the vapor phase. As a consequence, the RH above the solution is reduced depending on the amount of salt in the solution [103]. A common route to achieve a well-defined amount of ions is to choose the mass of added salt in a way that it exceeds the respective solubility limit. Like this, a saturated salt solution is obtained. The advantage of this method is, that the resulting RH is exclusively determined by the type of the selected salt.

salt	**relative humidity (RH)** [%]	**solubility limit** $\left[\frac{\text{g}}{\text{L}}\right]$
potassium acetate	23.11 ± 0.25	2560
potassium carbonate	43.16 ± 0.33	1120
magnesium nitrate	54.38 ± 0.23	420
sodium chloride	75.47 ± 0.14	359
potassium chloride	85.11 ± 0.66	316

Table 3.5: *List of salts which were used to install different RHs (second column). In addition to that, the respective solubility limits are given.*

In this work the procedure was as follows. First, the desiccator was cleaned with deionized water and that solvent which was also used for the involved solution casting. Then, the desiccator was filled with 60 mL deionized water. In a subsequent step, the salt corresponding to the desired RH was added. The mass of the added salt exceeded the respective solubility limit. That is why the unavailability of the errors to the solubility limits did not play a role. Despite a stirring of the solution, a waiting time of several hours was necessary to ensure saturation. For all salt solutions which were prepared, a certain amount of salt remained undissolved. The different salts together with the corresponding solubility limits and the resulting RHs [104] are listed in table 3.5. All values refer to a

temperature of 20 °C.
Finally, to create a further type of atmosphere the desiccator was filled with 10 mL of non-polar solvent. For this case, the desiccator volume is dominated by solvent vapor. Cyclohexane and n-hexane were selected for this purpose.
In total, the solution casting under controlled atmosphere was performed based on several different solvents for the polymer solutions: n-hexane, cyclohexane, toluene and dichloromethane. Under the chosen conditions, the use of isopropanol and acetone resulted in dewetted films and the drying time of isobutanol exceeded reasonable limits. In addition to that, the attempt to dissolve P(EHA-stat-20MMA) in ethanol or methanol failed.

3.3.4 Spin-coating

For the case of ultra-thin PSA films, spin-coating was chosen as preparation technique. A *Süss Microtec Lithography Delta 6 RC TT* spin-coater was used for this purpose. The substrates were fixed with a vacuum chuck on a plate having the ability to rotate at different velocities. Similar to solution casting, a polymer solution was coated onto the substrate. Immediately after reaching full coverage of the substrate (the solution volume is chosen in a way that s_c is obtained for all samples), the top cover of the spin-coater was closed and the rotation initiated.
The spin-coater was operated at a rotational frequency of $\omega = 2000$ min^{-1} (according to the information of the manufacturer: 1971 min^{-1}). A slow acceleration towards ω was chosen. The rotation at constant frequency was maintained for 30 s. After this time, an ultra-thin and fully dried, homogeneous PSA film was obtained.
The beginning of the rotation and the finally obtained film are schematically illustrated in figure 3.14. The initial coating step, which is equal to that for solution casting, has already been shown in the left panel of figure 3.11.
Similar to solution casting, the final film thickness can be determined by the initial solution concentration. This can be seen from the empirical relationship found by Schubert [105].

$$h = cA_p\omega^{-0.5}M_w^{0.25} \tag{3.8}$$

It reveals a proportionality between the film thickness h and the solution concentration c. A_p is an additional parameter which depends on the external conditions.
In contrast to the solution casting of thick PSA films, for the thin-film case it is important that the polymer-substrate interactions are well defined. This arises from the fact, that in the x-ray based experiments the beam fully penetrates the sample (see equation 2.75). As a consequence, the substrate might influence the complete recorded film morphology. Such a well-defined nature of the substrate surfaces can be achieved with an acid cleaning protocol following reference [106]. First, the substrates remained 15 min in a bath consist-

ing of 70 mL hydrogen peroxide, 165 mL sulfuric acid and 45 mL deionized water which was heated up to 80 °C. To remove possible residues of the bath, the substrates were carefully rinsed with deionized water and dried with compressed nitrogen. The spin-coating was performed subsequently without any unnecessary time delay.

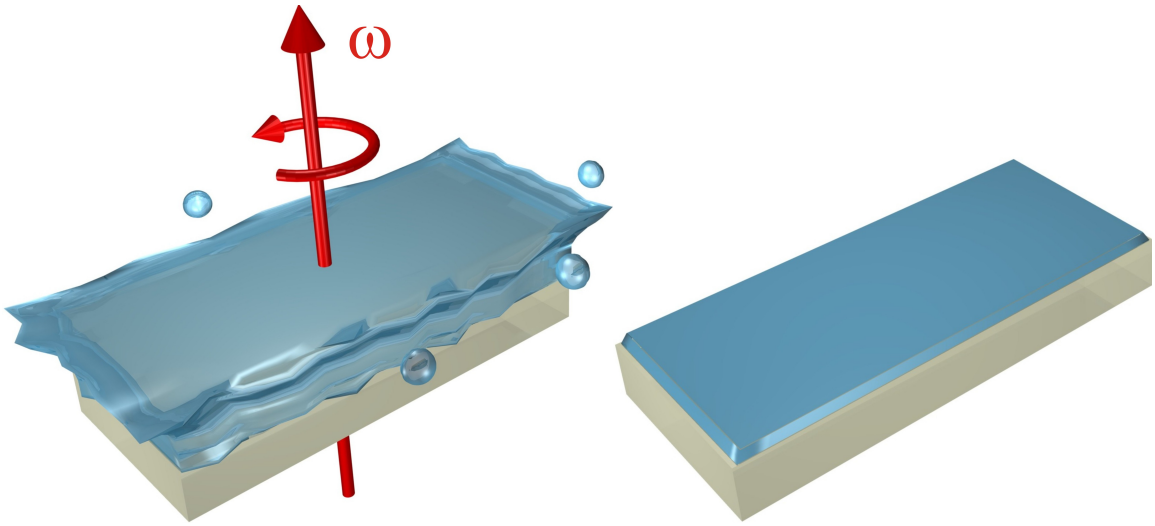

Figure 3.14: *Principle of spin-coating. Left: Beginning of the rotation of the sample (indicated by the arrows). Most of the solution is hurled off the substrate. Right: After* 30 *s, a thin, homogeneous PSA film is obtained.*

The substrate material was either glass (*Menzel*, 76 mm × 26 mm × 1 mm) or highly polished pieces of silicon wafer (20 mm × 20 mm, purchased by *Si-Mat*) for the WLI experiments. In order to rule out aging of the samples and thus, not comparable conditions, all samples were stored for approximately 10 days in a closed cabinet under constant temperature before the individual measurements.

Chapter 4

Near-surface solvent concentration profiles during solution casting

Most PSA films investigated in this work are prepared via solution casting based techniques (see section 3.3.2). Solution casting, however, is very versatile and not only applicable to PSA films. Many other polymer systems are processed using solution casting. Examples are everyday life and high-tech materials such as nylons [107, 108], paints [109, 110], corrosion protections [111], hydrogel films [112], organic solar cells [113], films for medical [114, 115] and biological [116] applications, fuel cell membranes [117, 118], actuators [119, 120] and organic electronic devices [121, 122]. Among the multiple benefits of solution casting are the flexibility in choosing the shape and the size of the cast area and the possibility to produce films over a wide thickness range (see equation 3.7).

But there are more properties of solution cast films which can be directly manipulated. As already indicated in sections 3.3.2 and 3.3.3, the choice of the external conditions during the solvent evaporation process can result in different near-surface composition profiles. Moreover, it has been shown that for example the underlying solution evaporation rate can be used to tune the film morphology [123, 124] or the film roughness [125, 126]. Furthermore, the installed solvency condition can influence the polymer chain conformations [127]. Controlling these parameters is not only interesting from a scientific point of view, but also the performance of the final product depends on the conditions during the solution casting. This has been shown for the examples of PSAs [128] and polymer blend solar cells [129, 130].

The reason for the observed dependencies is the solvent distribution inside the drying film that is caused by the applied external conditions during the solution casting. In the context of this work, where the focus is on near-surface phenomena, the solvent distribution close to the surface and its changes as a function of time are of special interest. This work presents the first successful attempt to monitor the time-dependent

near-surface solvent concentration profile throughout the complete drying process. In-situ neutron reflectivity (NR) (see sections 2.3.3 and 3.2.2) is the ideal tool for this purpose. Some of the results are rather surprising because classical diffusion theory would predict a solvent loss that is proportional to t^{α}, with $0.5 \leq \alpha \leq 1$, depending on the relaxation times of the involved polymers [131, 132]. For the extreme cases, the underlying mechanism is called **case I** or **Fickian diffusion** for $\alpha = 0.5$ and **case II** for $\alpha = 1$. This work reveals different stages of the drying process, during some of which the solvent loss of the near-surface region even exceeds case II behavior.

In this context, a molecular dynamics study by Tsige and coworkers showed that by choosing a proper molecular weight and initial solvent concentration, it is possible to achieve a non-uniform evaporation velocity [133]. Similar to the results of this work, two distinct stages were found: an initially slow evaporation regime which is followed by a phase of accelerated solvent evaporation.

This chapter is organized as follows: first, the static measurements are presented and discussed. Then, the results of the kinetic experiment are shown and interpreted. Finally, the observations are compared to the macroscopic weight loss during drying as obtained with gravimetric measurements.

Results of this chapter have been published in reference [134].

4.1 Residual solvent content in dried films

The solution casting is performed using protonated P(nBA-stat-MA) which is dissolved in deuterated toluene. As a consequence, a high contrast in (the real part of the) scattering length density (SLD) between the polymer and the solvent is achieved. The SLD values of the involved materials are $\delta_N(\text{toluene}) = 5.22 \cdot 10^{-4}$ nm^{-2} and $\delta_N(\text{P(nBA-stat-BA)}) = 0.806 \cdot 10^{-4}$ nm^{-2}. The contrast is dominated by the deuterated toluene, so that the components of the statistical copolymer are not distinguished on purpose and the resulting average SLD is used for the data analysis. P(nBA-stat-MA) with the three different molecular weights $M_w = 54$, 192 and 600 kg/mol is investigated in this study.

To have a starting point for the data analysis of the kinetic measurement, first the static reflectivity curves of the dry copolymer films are analyzed. Figure 4.1 shows from top to bottom the NR curves of the samples with molecular weights $M_w = 54$, 192 and 600 kg/mol. Throughout this chapter, a double-logarithmic plot is chosen because the curves exhibit no modulations which would become visible in the Fresnel-normalized representation (see figure 3.1). Furthermore, the q_z values around the critical edge, which is mainly discussed in this chapter, are more pronounced as compared to a single-logarithmic plot. The NR data of all three polymers are very similar. The curves show no prominent feature

in the whole accessible q_z range which is already indicative of homogeneous material. Consequently, the data can be modeled with two free parameters: the SLD of the bulk material and the surface roughness. Similar to the x-ray experiments with thick PSA films, the substrate is not visible in the measured data. From the fits, a surface roughness of 0.3 nm is deduced for all molecular weights. Moreover, a constant SLD of $0.837 \cdot 10^{-4}$ nm^{-2} leads to the best fit for all the three curves.

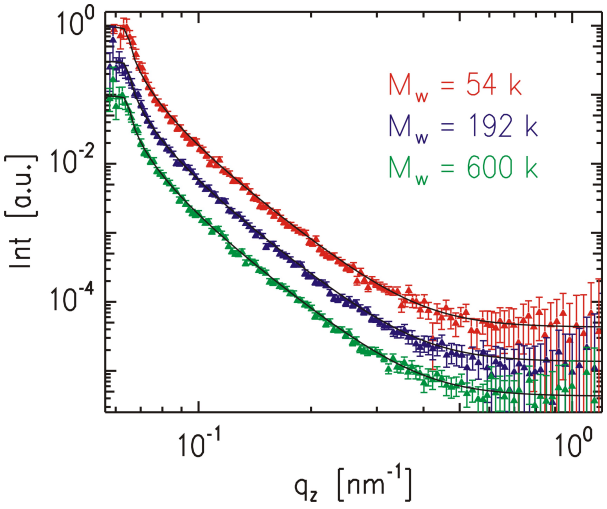

Figure 4.1: *Measured static NR data (symbols) with corresponding model fits (solid lines) of dried P(nBA-stat-MA) films with different molecular weights. The data are shifted along the intensity axis for clarity.*

The detected SLD value is higher than that of P(nBA-stat-MA) which means that the samples still contain a fraction of the higher-SLD material toluene. It can be further concluded that, within the precision of the performed experiment, no differences in remaining solvent contents resulting from the different molecular weights of the copolymers are detected. From the obtained bulk SLD value a solvent content of (0.7 ± 0.3) % is calculated, irrespective of the molecular weight.

For the calculations of the solvent concentrations, including those which appear during the kinetic experiment, equation 3.1 is used. To make the equation applicable, δ(PEHA) and δ(PMMA) are replaced by δ_N(P(nBA-stat-BA)) and δ_N(toluene), respectively. As a consequence, throughout this work the calculated solvent concentrations are to be understood as volume ratios.

For the error calculation, an interval around the mean SLD value was determined in a way that all corresponding reflectivity curves remain within the experimental error bars of the NR data for all three molecular weights. In more detail, if and only if the assumed SLD value is chosen between $0.824 \cdot 10^{-4}$ nm^{-2} and $0.851 \cdot 10^{-4}$ nm^{-2}, the calculated curves represent fits within the accuracy given by the error bars. These two limiting values correspond to solvent contents of 0.4 % and 1.0 %, respectively. In summary, the claimed residual solvent concentration of (0.7 ± 0.3) % follows.

It is important to note that the residual solvent is homogeneously distributed over the

whole penetration depth of the neutrons. This implies that there is no detectable solvent enrichment layer in the near-surface region of the dried sample. A possible solvent enrichment at the interface between the polymer and the substrate is not resolvable with the employed experimental setup.

4.2 In-situ observation of solvent evaporation

Applying equation 3.7, the thickness of the dried film is set to 50 μm by using a solution concentration of 109 g/L and casting a solution volume of 3.2 mL. The substrates are bare silicon wafers which are cut to almost rectangular shape (70 mm $\times$ 90 mm). The initial thickness of the liquid on the substrate is on the order of 500 μm.

In order to provide reproducible and well-controlled conditions, the solution casting is performed in the center of a custom-designed rectangular chamber (300 mm $\times$ 300 mm $\times$ 200 mm) with a removable lid manufactured from an aluminum/magnesium alloy to prevent radioactive activation. In addition, the chamber is equipped with aluminum windows (diameter: 100 mm) that are transparent for neutrons. The background is minimized by placing the samples on aluminum feet with a height of 20 mm. The feet are shielded using a sandwiched material of boron carbide and cadmium. Interactions between the walls of the chamber and the drying solutions can be excluded due to the chosen dimensions of both.

After casting the solution onto the substrate, the lid of the chamber is closed without delay and the safety procedure of the beamline is initiated. In summary, the start of the NR experiment is approximately one minute after the end of the solution deposition. The start of the NR experiment defines $t = 0$ (see section 3.2.2).

As already pointed out in section 3.2.2, the bare silicon substrate is used for the sample alignment. Resulting from the large initial thickness of the liquid coating, the footprint of the beam for small times t is not centered on the sample. Therefore, a fraction of the neutrons misses the sample as long as the drying film is not thin enough that the full cross-sectional area of the beam hits the film.

Sketches of the most important beam positions are shown in figure 4.2: directly after the alignment, the center of the neutron beam coincides with the center of the substrate (top panel). Then, the solution is distributed on the substrate at a time $t < 0$. Due to the shrinkage of the drying film with time, the area on which the neutrons impinge on the film surface moves towards the sample center. The movement of the neutron beam on the sample and the corresponding reduction in film thickness are illustrated by the arrows in the panel in the middle.

The first time, at which the full footprint is situated on the sample, is denoted with t_1.

For $t \geq t_1$, meaningful NR data are recorded. It would be very difficult to analyze the data obtained for $t < t_1$ because the curves would need to be corrected for the missing neutrons. Gravitational effects, which lead to a wavelength dependent distribution of the neutrons on the beam cross-section, make the problem even more complex.

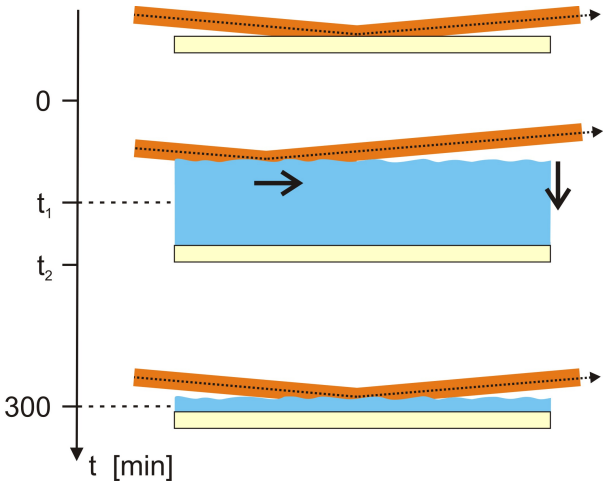

Figure 4.2: *Timeline of the kinetic experiment. The time axis is explained in the main text. The panel on top illustrates the situation of the sample alignment. The panel in the middle sketches the moment when for the first time the full footprint is on the drying solution. The bottom panel represents the dried sample.*

The beam translation velocity on the sample surface is estimated by assuming that the film shrinks from 500 μm to 50 μm in the interval $0 < t < 70$ min. The assumption is justified by the gravimetric measurements presented in section 4.3. Under the additional appraisal that, during the first 70 min, the beam travels a distance that is equal to half of the substrate length (45 mm), a mean horizontal footprint translation velocity of 0.6 mm/min is calculated.

The next sections show that for all molecular weights, the NR data for times $t \geq t_1$ are in the beginning dominated by the large toluene volume ratio. Close to t_1, the presence of dissolved P(nBA-stat-BA) is even not evident from the reflectivity curves which completely coincide with such of pure deuterated toluene. The time at which the last toluene curve is measured is defined as t_2. For $t > t_2$, solvent concentration profiles deviating from pure toluene can be monitored. At least one toluene curve is monitored for each molecular weight or, in other words, $t_2 \geq t_1$ for all measurements. Therefore, no information is lost due to the missing data originating from the footprint effect for $t < t_1$. Finally, for large times t, the beam illuminates nearly the same spot as for the aligned substrate (see bottom panel of figure 4.2).

The exact values of t_1 and t_2 depend on the individual experimental conditions. They are affected by errors in the initial solution volumes or varying substrate areas arising from the manual breaking. Another contribution lies in the different waiting times between the casting and the start of the NR measurement, which defines $t = 0$. Furthermore, the appearance of a small rim on the sample edges which is slightly elevated compared to the rest of the surface could have an effect. It is, however, important to note that

	$M_w = 54\ \frac{\text{kg}}{\text{mol}}$	$M_w = 192\ \frac{\text{kg}}{\text{mol}}$	$M_w = 600\ \frac{\text{kg}}{\text{mol}}$
$\boldsymbol{t_1}$ [min]	9.5	13.5	23.0
$\boldsymbol{t_2}$ [min]	22.0	16.0	23.0

Table 4.1: *Different values for t_1 and t_2 which are obtained in the individual measurements.*

the measurement is not influenced for $t \geq t_1$. The values of t_1 and t_2 for the individual measurements are listed in table 4.1.

4.2.1 Solvent concentration profiles as a function of time

As already pointed out in section 3.2.2, some of the 30 s measurements composing the NR data are merged according to the achieved counting rates and the solvent evaporation speed. In more detail, the data are reduced to 33 curves for $M_w = 54$ kg/mol, 30 curves for $M_w = 192$ kg/mol and 36 curves for $M_w = 600$ kg/mol, respectively.
As an example, for $M_w = 54$ kg/mol (see left panel of figure 4.3) each of the first 19 curves consist of five short measurements, which is equal to a total accumulation time of 2.5 min. These data are followed by three curves with an integration time of 5 min, then four with 10 min, five with 25 min and, finally, two with 32 min.
Furthermore, a monotonic decrease of the background with time during the kinetic experiment is obtained. It covers a range between approximately $4 \cdot 10^{-5}$ and $4 \cdot 10^{-4}$. The reason can be found in the decreasing amount of deuterated toluene close to the probed interface as drying proceeds.
From top to bottom, the left panel of figure 4.3 shows the evolution of the NR data for $t \geq t_1$. The time interval between t_1 and t_2 is represented by the first 6 curves. For all stages of the drying sample, the surface roughness coincides with that of the dried sample. The corresponding value of 0.3 nm is equal to that of a water surface measured with XRR [135]. As a conclusion, the roughness of the final polymer melt film is determined by the solvent used for the solution casting.
For $t > t_2$ (starting from curve number seven), a prominent shift of the critical edge from approximately $q_z = 0.16$ nm^{-1} to $q_z = 0.0065$ nm^{-1} (see last curve) is obtained. This is reflected in a shift of the SLD of the material as shown in the right panel of figure 4.3. Starting from the value of pure deuterated toluene, it moves towards the value of protonated P(nBA-stat-MA). For times $t > t_2$ which are close to t_2, the shift of the critical edge is relatively slow, resembling a low evaporation speed of toluene. The movement of the edge and, thus, the reduction of the SLD accelerate before they slow down and finally converge to zero. This behavior will be discussed in more detail in section 4.2.3.
An explanatory approach might include the high vapor density above the topmost layer

of the freshly cast solution. This results in an initially slow solvent evaporation. With increasing amount of solvent vapor that has vanished (the chamber is not sealed), more liquid toluene can be released from the solution and the evaporation accelerates. At later stages, only little amount of toluene is left in the sample. The remaining solvent, part of which is also located deeper in the film, slowly diffuses to the surface and evaporates. Therefore, a deceleration of the solvent evaporation speed towards zero is observed for large t values.

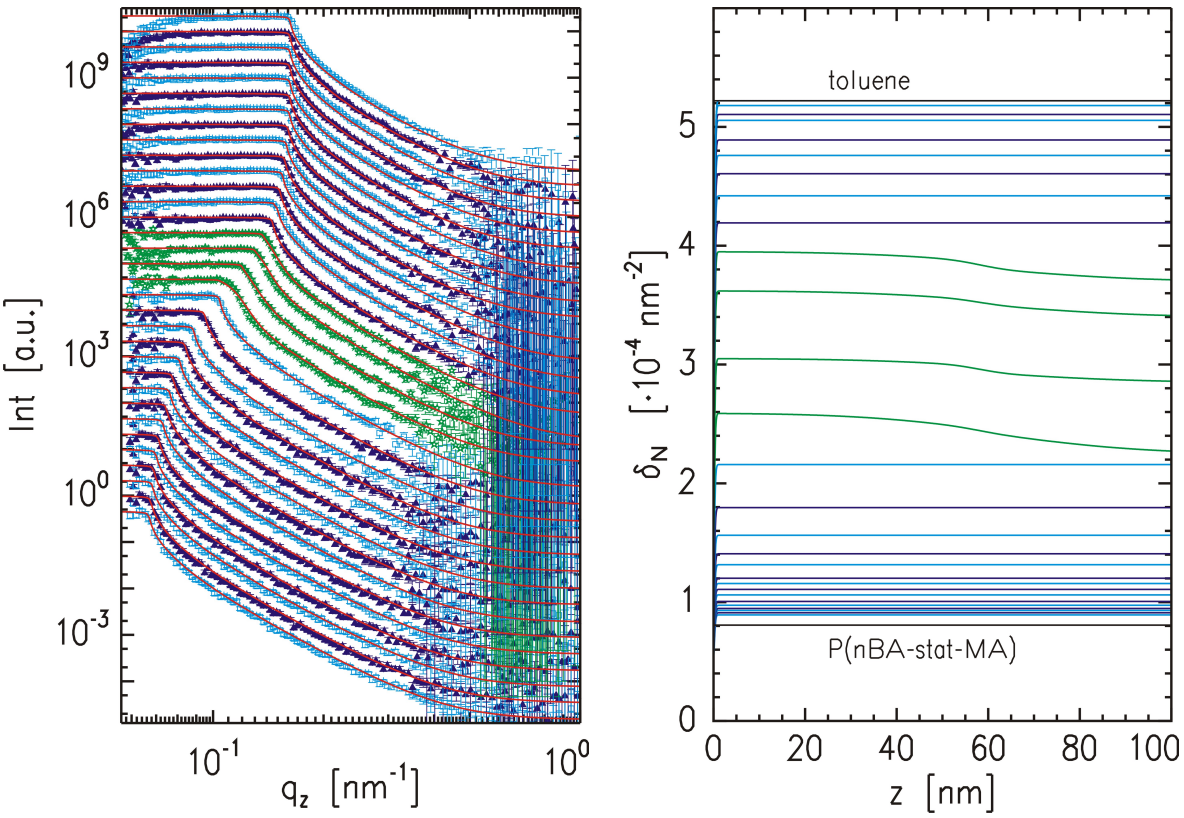

Figure 4.3: *Left: Evolution of the reflectivity curves (symbols: squares, triangles, stars) with time and the corresponding fits (solid lines) for M_w = 54 kg/mol. The data for which green stars are chosen as symbols represent the phase of the evaporation process which is characterized by non-uniform solvent concentration profiles. The time increases from top to bottom. The curves are shifted along the intensity axis for clarity. Right: SLD profiles extracted from the fits to the data. From top to bottom the time increases. The labeled vertical lines are positioned at the values of the SLDs of the involved materials, toluene and P(nBA-stat-MA). For presentation reasons, the axes are interchanged as compared to the refractive index profiles introduced in section 3.2.1.*

All NR curves except those four for which stars are chosen as symbols (number 15 to 18 in green color) are fitted using only the bulk SLD as free parameter. This is similar to what is described for the static measurements in section 4.1. Consequently, during these stages of the drying process the solvent is distributed homogeneously over an area that

has a thickness which is at least in the range of the scattering depth of the neutrons.

The remaining four curves cannot be fitted with such a simple model. This is evident from the round shaped critical edges which are present in all four curves. The position of these edges shifts from approximately $q_z = 0.14$ nm^{-1} to $q_z = 0.11$ nm^{-1} during the 10 min covered by this data. The reason for the round shapes is an increased solvent content in the upper 60 nm of the samples. The intensity of the enrichment decays monotonically to a constant bulk value for $z > 60$ nm. The corresponding SLD profiles in the right panel of figure 4.3 are the highlighted ones which are not represented by a straight line. The near-surface solvent enrichment is concluded from the higher SLD for small z values as compared to the constant bulk value. A detailed discussion why the data simulation with only bulk material, which was successful for the other NR curves, failed is given in section 4.2.2.

The increased solvent concentration near the surface, as compared to what is detected in the bulk, originates from the fast evaporation of toluene in combination with a trapping of the solvent by P(nBA-stat-MA). Therefore, it only occurs during the stage which is characterized by an accelerated shift of the critical edge. For the sample with $M_w = 54$ kg/mol, the enrichment layer is found for 44.5 min $< t <$ 54.5 min.

The presence of such non-homogeneous solvent concentration profile is in good agreement with a computational study carried out by Peter and coworkers [136]. Using molecular dynamics simulations, they investigated the drying process of a polymer solution, too. As a result, they also observe an increased solvent content at the free surface and at the supporting wall. It has to be noted that the latter is not accessible with the present setup and, therefore, a possible solvent enrichment at the substrate cannot be confirmed.

In accordance to the results of this work, Peter et al. introduced three drying regimes [137]: for small t, the film thickness varies only slightly. This is followed by a second, intermediate regime which exhibits a strong shrinkage of the film. Finally, the authors observe a slow convergence towards the final thickness value. In summary, comparing the work of Peter et al. to this study, the near-surface solvent content and the overall film thickness seem to follow similar time dependencies.

In contrast to the value of the molecular weights of the PSAs, that are investigated in this work, Peter's simulated polymers comprise only 64 monomers. Moreover, this work exceeds the consideration of only one polymer chain towards the investigation of three different molecular weights. The same kinetic experiment, that was so far presented for P(nBA-stat-MA) with $M_w = 54$ kg/mol, is also performed with the molecular weights 192 kg/mol and 600 kg/mol. The NR data and the corresponding SLD profiles are depicted in figures 4.4 and 4.5, respectively.

As a result, also the samples with the two higher molecular weights exhibit slow evapo-

ration for the freshly coated films which is followed by a phase of accelerated solvent loss and a final decay of the evaporation speed to zero. As a further similarity, both higher-molecular weight samples have a solvent gradient perpendicular to the surface during a certain time interval. In figures 4.4 and 4.5, the corresponding measurements are highlighted and stars as symbols for the measured data are chosen. As can be seen from the right panels of figures 4.4 and 4.5, again, the detected enrichment layers are approximately 60 nm thick and converge to a constant (lower) bulk value for all molecular weights.

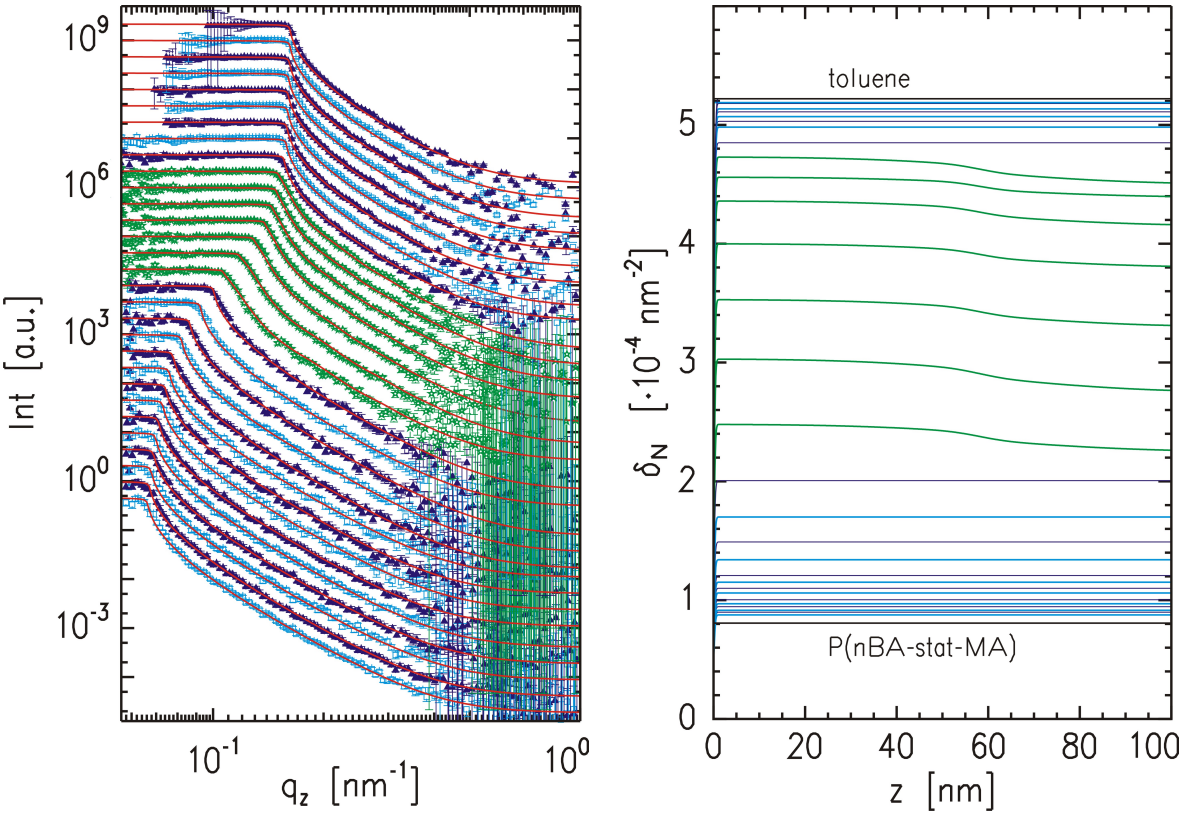

Figure 4.4: *In-situ NR data of a drying P(nBA-stat-MA) film with M_w = 192 kg/mol displayed in analogy to figure 4.3.*

However, there are also differences. One of them concerns the length of the time interval in which the inhomogeneous solvent distribution is present. For M_w = 192 kg/mol, it is 17.5 min and for M_w = 600 kg/mol, it is 20 min which is twice as long as in the case of the sample with the lowest molecular weight. Furthermore, with increasing molecular weight also the amplitudes of the solvent content difference between the surface and the bulk increase.

This can for example be seen from the maximum values which are calculated from the curve of the kinetic dataset exhibiting the highest difference. The amplitudes are calculated as the ratio between the surface SLD and the bulk SLD. The resulting values are 7.7

% for $M_w = 54$ kg/mol (counted from the top, see curve number 4 of the highlighted data in figure 4.5), 10.1 % for $M_w = 192$ kg/mol (curve 6) and 15.8 % for $M_w = 600$ kg/mol (curve 4), respectively.

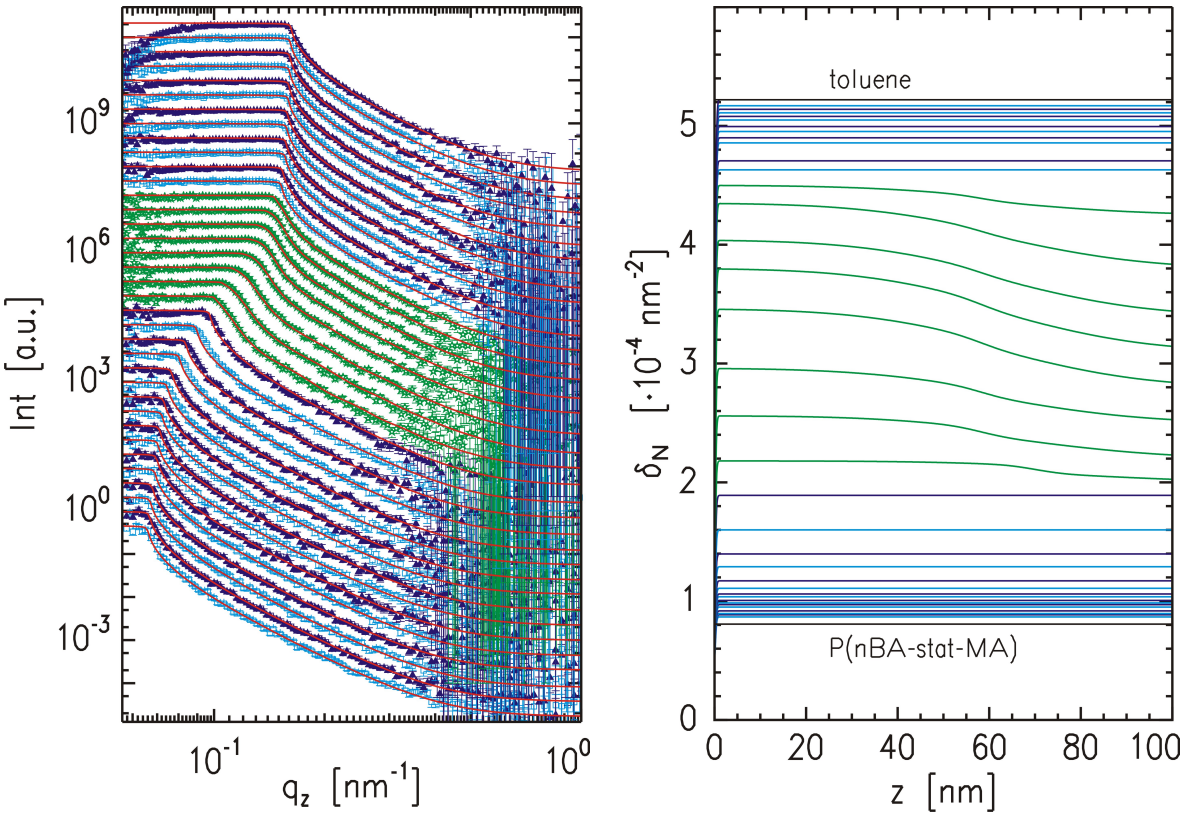

Figure 4.5: *In-situ NR data of a drying P(nBA-stat-MA) film with $M_w = 600$ kg/mol displayed in analogy to figure 4.3.*

It is important to note that the observed molecular weight dependence implies that not only the solvent vapor above the drying sample drives the observed evaporation kinetics and the phenomenon of inhomogeneous solvent distribution. The reason is that, due to the constant volume of initial solvent and the identical experimental conditions for all measurements, these effects should not be influenced by the molecular weight. As a consequence, an additional process which is related to the polymer chain length and which supports the trapping of solvent plays a role. Further details and a quantification of the molecular weight dependence of the evaporation process will be given in section 4.2.3.

4.2.2 Stages of inhomogeneous solvent distribution

In the previous section, it has been pointed out that the stage of inhomogeneous solvent distribution can be concluded from the shape of the critical edges of the NR data dur-

ing the corresponding time interval. The data can only be modeled with an increased SLD close to the sample surface. That the corresponding NR curves cannot be fitted successfully when only bulk material is assumed is demonstrated exemplarily for $M_w = 600$ kg/mol. Both panels of figure 4.6 show the region around the critical edge of the respective eight curves in a magnified way. In both panels, the solid lines are the fits to the data. On the left side, the already explained enrichment layers are assumed and in the right panel, the solid lines represent the best fit to the data using the simpler model based on a constant solvent concentration. The deviation of the fit from the data points is obvious for all eight curves in the right graph.

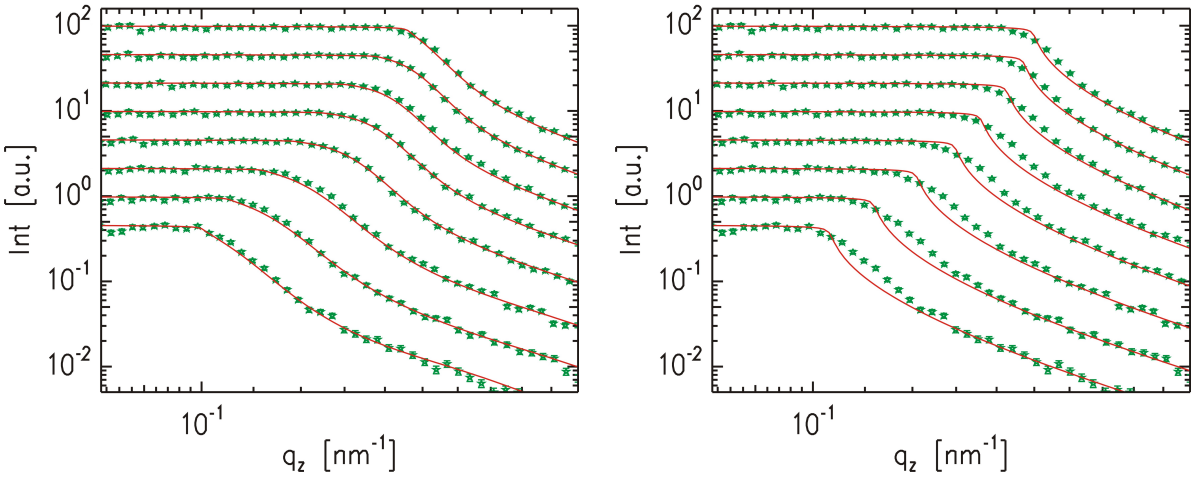

Figure 4.6: *Close-up of the region around the critical edge of the NR data (symbols) of a drying, solution cast P(nBA-stat-MA) film at the stages with a round-shaped critical edge. Left: The data are fitted (solid line) with a solvent enrichment layer as described. Right: Fit with homogeneous bulk material as the only free parameter.*

Finally, it has to be ruled out that the shape of the NR data itself is an artifact of the fast movement of the critical edge during the corresponding time interval originating from a possibly too long accumulation time of 2.5 min. The clarification of this issue is of utmost importance because it is the shape of the reflectivity curves from which the presence of an inhomogeneous solvent distribution is concluded. For this purpose, each of the 30 s measurements in the corresponding time interval, five of which comprise the analyzed curves in this stage, are carefully examined. Although for larger q_z values the statistics of the data is quite poor, it is still sufficient in the plateau region of the curves. This can for example be seen from figure 4.7 which depicts the underlying 30 s measurements of the last curve of figure 4.6. Even for such a short counting time, the commensurate shape of the edge is preserved in all of the five NR curves.

It can also be excluded that already the shape of the critical edge of the underlying 30 s

measurements is an artifact. The reason is that, despite a slight change of the data within the 2.5 min that are encompassed in figure 4.7, the position of the last point of the plateau is the same for all of the five curves (it is marked with s dashed line in figure 4.7). Therefore, the round shaped edge of the individual curves cannot be a consequence of a too fast moving sharp edge. If that was the case, then also the end of the plateau would have to change from one 30 s measurement to the next. But, obviously, it stays constant.

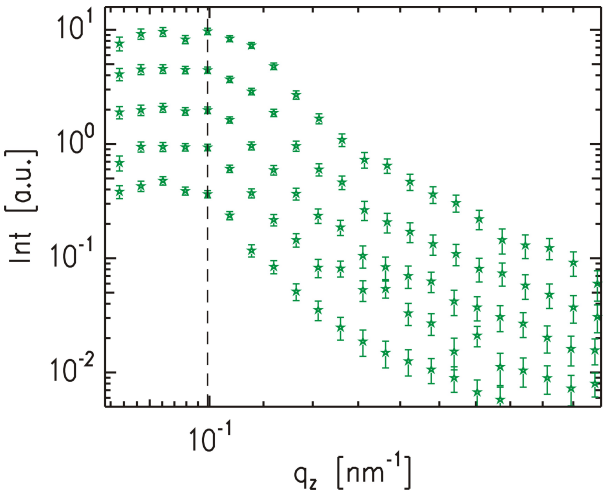

Figure 4.7: *Example of five* 30 *s measurements which compose the last curve of figure 4.6. The dashed line marks the end of the plateau region.*

In summary, the kinetic data fully justify the appearance of solvent enrichment close to the surface in a certain time interval. The respective molecular weight dependence is discussed in the next section.

4.2.3 Molecular weight dependence of the near-surface solvent loss kinetics

In analogy to the calculations presented for the dried films in section 4.1, the near-surface volume ratio of the solvent C_{toluene} (also referred to as solvent content or solvent concentration) is calculated from each of the SLD profiles shown in section 4.2.1. For the non-constant solvent distributions, C_{toluene} is determined by calculating the average SLD of the region between the sample surface and a depth of $z = 100$ nm.

A direct comparison of C_{toluene} as a function of time for the different molecular weights is only possible by introducing a common time axis for the three kinetic measurements. The reason is that t_1 and t_2 depend on the individual experimental conditions. In order to do so, the point of origin is defined as the time corresponding to the last NR curve which coincides with such of pure, deuterated toluene. Therefore, C_{toluene} is given as a function of $t_n = t - t_2$. The resulting functions $C_{\text{toluene}}(t_n)$ are plotted in the left panel of figure 4.8. Data points obtained for stages with an inhomogeneous solvent concentration

profile close to the surface are marked as filled symbols, whereas open symbols represent a constant solvent distribution throughout the near-surface area.

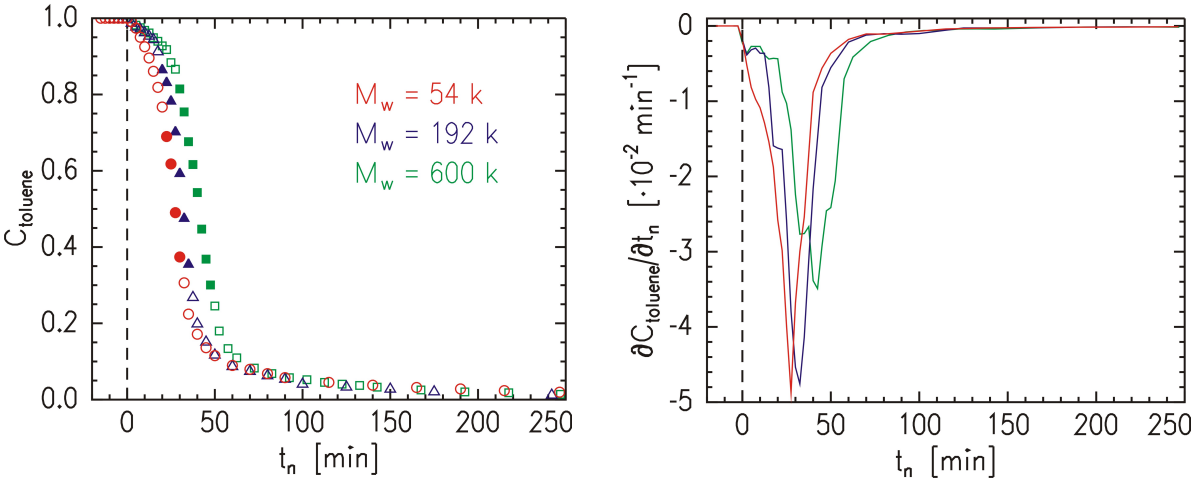

Figure 4.8: *Left: Toluene content as a function of normalized time t_n for solution cast P(nBA-stat-MA) with M_w = 54 kg/mol (circles), M_w = 192 kg/mol (triangles) and M_w = 600 kg/mol (squares). Open symbols represent constant solvent concentration, whereas filled symbols are used for stages of inhomogeneous solvent distribution. Right: Time derivative of $C_{toluene}$. The molecular weight increases from left to right.*

As a result, for small $t_n > 0$, the amount of evaporating toluene decreases with increasing molecular weight. Also the onset of the accelerated evaporation is delayed for the higher molecular weights. An explanatory approach is based on the free-volume theory which is crucial for transport phenomena of macromolecular materials [138, 139]. The higher the available free volume in a certain region of the film is, the more solvent can be captured. It is important to note that the available free volume density is not constant throughout the sample. Especially in the near-surface region the free volume density differs from the bulk value because it is closely related to the density of polymer chain ends. Mayes claims that close to the surface the density of polymer chain ends is proportional to the square root of the degree of polymerization [140]. Therefore, the near-surface chain-end density increases as a function of the molecular weight.

Consequently, an enhanced difference in chain-free volume between bulk and surface with increasing molecular weight is to be expected. The resulting increased ability to trap solvent near the surface is responsible for the retarded onset of fast evaporation. This also explains the molecular weight dependence of the amplitude of the difference of toluene concentration between the surface and the bulk during the stages of inhomogeneous solvent concentration (see section 4.2.1). It follows from the increased amount of trapped toluene near the surface with increasing molecular weight, while the overall amount of

remaining solvent in the bulk is almost independent of the polymer chain length. However, due to the lack of theoretical studies concerning the near-surface region, a model calculation is not performed. Additionally, it might be possible that altered rheological properties close to the surface play a role.
Obviously, such a gradient in solvent concentration can only occur in samples that are sufficiently dry to already exhibit polymer melt properties. At the same time, in section 4.2.1 it was observed that the near-surface solvent enrichment does not appear towards the end of the drying process. In combination, the enrichment effect can only take place in a limited time window.
Furthermore, no molecular weight dependence is detected after the accelerated solvent evaporation ($t_n > 70$ min). For such large times t_n all three functions $C_{\text{toluene}}(t_n)$ coincide within the given experimental accuracy.
In order to quantify the solvent evaporation kinetics, the near-surface solvent evaporation rate, which is the time derivative of the solvent content $\partial C_{\text{toluene}}/\partial t_n$, is plotted for the different molecular weights in the right panel of figure 4.8. For $M_w = 192$ kg/mol and $M_w = 600$ kg/mol, a period of constant solvent loss for $0 < t_n \lesssim 20$ min is found. In contrast to that, a similar constant regime is not observed for the sample with $M_w = 54$ kg/mol. The corresponding evaporation rate increases monotonically for $0 < t_n < 28$ min. This might be attributed to the comparably short polymer chains and the resulting reduced ability to capture toluene.

	$M_w = 54\ \frac{\text{kg}}{\text{mol}}$	$M_w = 192\ \frac{\text{kg}}{\text{mol}}$	$M_w = 600\ \frac{\text{kg}}{\text{mol}}$
$\boldsymbol{t_n^{max}}$ [min]	27.5	32.5	42.5
$\left(\frac{\partial C_{\text{toluene}}}{\partial t_n}\right)\left(\boldsymbol{t_n^{max}}\right)$ $\left[\cdot 10^{-2}\text{min}^{-1}\right]$	−4.98	−4.76	−3.49

Table 4.2: *Time and amplitude of the fastest solvent evaporation in the kinetic experiment listed for the three investigated molecular weights.*

Furthermore, also the point t_n^{max} of fastest solvent evaporation is molecular weight dependent. It is reached later for higher molecular weights and the respective evaporation speed is lower. The exact values are listed in table 4.2. Please note that the unit 10^{-2}min^{-1} can be interpreted as the solvent volume loss per minute in percent. The molecular weight dependence of the fastest evaporation can again be explained by the increased availability of free volume with increasing chain length. For higher M_w values it takes longer to fill the space and the trapped solvent is finally released more slowly.
It is common to plot $1 - C_{\text{toluene}}(t_n)$ which is the time-dependent near-surface solvent volume loss as a function of time (see figure 4.9). For $t_n > 70$ min, the reduction of the remaining solvent is a linear process as it is demonstrated by the fitted straight line in

the left graph of figure 4.9. This is in accordance with the almost constant first derivative of the solvent content for the same time interval which was shown in the right panel of figure 4.8. The proportionality of the solvent loss to the time in the late stages of the drying process is indicative for a process that is driven by case II diffusion.

For the beginning of the evaporation process a double-logarithmic plot is most suitable to extract the underlying kinetics (see right panel of figure 4.9). As a result, besides the already described molecular weight dependent onset of accelerated solvent evaporation, the solvent loss kinetics of the sample with $M_w = 54$ kg/mol clearly deviates from the higher molecular weight PSAs. The solvent evaporation for small t_n of the two polymers with the higher molecular weight can both be described by two regions exhibiting power law behavior. In contrast to that, the evaporation characteristics of the low molecular weight sample does not change in an obvious way for small t_n.

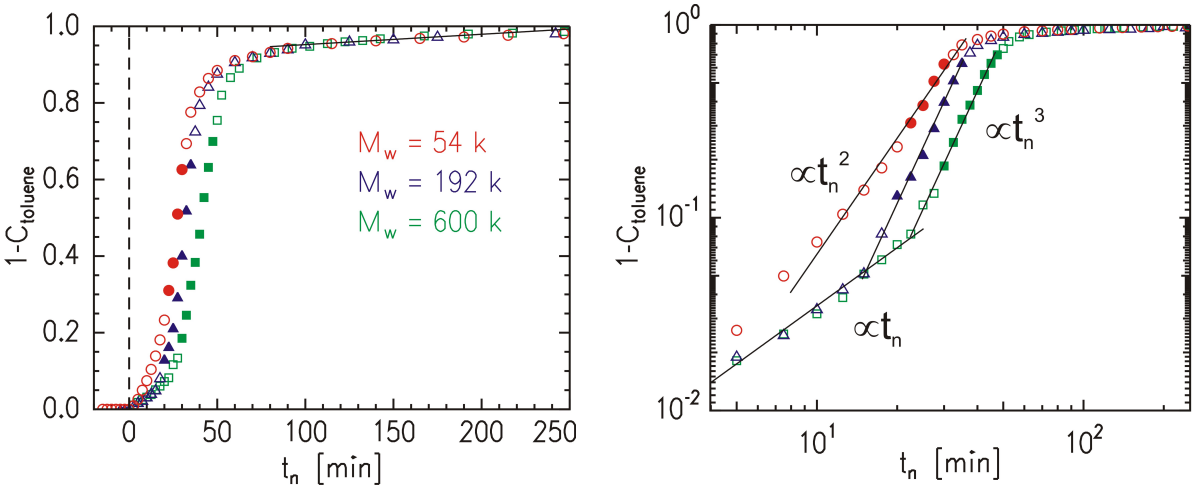

Figure 4.9: *Left: Near-surface solvent loss as a function of time t_n for solution cast P(nBA-stat-MA) with $M_w = 54$ kg/mol (circles), $M_w = 192$ kg/mol (triangles) and $M_w = 600$ kg/mol (squares). The solid line is a fit to the data for large t_n. Right: Respective double-logarithmic representation of the solvent loss. Power laws are extracted as indicated by the fitted solid lines and the corresponding labels.*

In more detail, the samples with $M_w = 192$ kg/mol and 600 kg/mol exhibit case II diffusion in the interval $0 < t_n \lesssim 20$ min (which can also be deduced from the derivative of the solvent content). Despite the retarded onset for $M_w = 600$ kg/mol, the subsequent accelerated solvent evaporation of both molecular weights is exactly proportional to t_n^3. Power law behavior with such a high exponent exceeds all reported solvent evaporation velocities obtained in drying experiments. Because the gravimetric measurements (see section 4.3), which monitor the macroscopic solvent loss of the complete film, reveal classical case II behavior, the phenomenon of such fast solvent loss per unit volume can only be restricted to the near-surface region which is investigated with NR. Possibly, this

accelerated phase can be explained by the toluene which was stored in the enhanced near-surface free volume during earlier stages of the drying process and which is subsequently released. This additional contribution to an ongoing case II evaporation could be the reason for the higher exponent.

As it has already been pointed out, the impact of solvent trapping is weaker for the sample with $M_w = 54$ kg/mol as compared to the higher molecular weights. The corresponding solvent volume loss for $t_n < 28$ min is proportional to t_n^2 as indicated by the respective label in the right panel of figure 4.9. The first two data points deviate from this power law. Due to the short time interval which is covered by the two data points and the comparably small extent of solvent content change, the introduction of a separate power law regime for these points does not appear to be justified.

It is likely that not only the described differences in free volume or rheological properties between the near-surface region and the bulk drive the observed molecular weight kinetics of the near-surface solvent loss. Also the overall different rheological properties originating from the different molecular weights [38] might contribute. Similar to classical theories, softer low molecular weight materials exhibit faster relaxation times and lower exponents in the power laws that describe diffusion processes. However, as explained in the introduction to this chapter, such exponents classically do not exceed the value 1. As a consequence, conventional theories cannot explain the near-surface solvent evaporation, even not for the lowest molecular weight which exhibits a strong deviation from case II diffusion, too.

4.3 Solvent loss monitored with gravimetry

It is a priori not clear whether the observed molecular weight dependence of the near-surface solvent evaporation kinetics has a measurable influence on the macroscopic mass loss of the drying sample. In order to clarify this issue, gravimetric measurements under comparable conditions are performed. For all three molecular weights, the mass m of the film is measured as a function of time t until no more changes are detected.

To have a better comparison to the information gathered from the NR experiments and to eliminate experimental errors like slightly different initially coated solution volumes, the relative mass loss as a function of time is shown. It is calculated via $1 - m(t)/m_0$, where m_0 is the mass of the initially casted solution. To make the values of $m(t)$ and m_0 accessible, the precision balance is tared after placing the substrate.

The left panel of figure 4.10 shows the relative mass loss as a function of time for the three different molecular weights M_w. Irrespective of M_w, there is first a linear weight loss regime for small t indicating case II diffusion on a macroscopic scale. This first regime

is followed by a monotonic convergence of the relative mass loss to 1. As a consequence, there is no indication of accelerated solvent evaporation which would by accessible by means of gravimetric methods. The macroscopically dominating processes do not exceed case II diffusion. This proves that the power law behavior with exponents of 2 or 3 of the solvent evaporation is solely an interfacial phenomenon.

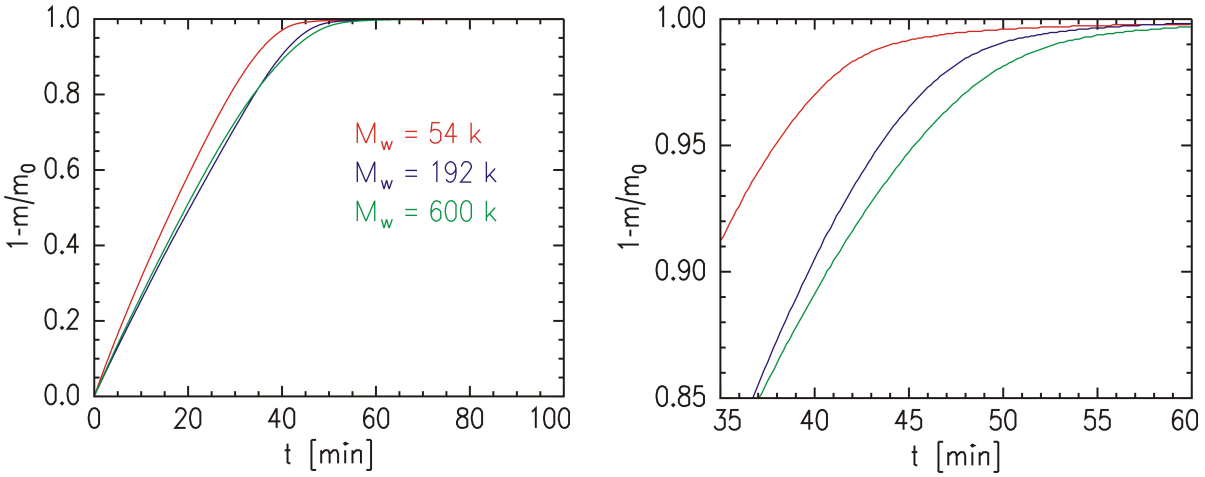

Figure 4.10: *Left: Relative mass loss during the solvent evaporation process of solution cast P(nBA-stat-MA) for three different molecular weights. From left to right, the molecular weights are* $M_w = 54$ *kg/mol (red),* $M_w = 192$ *kg/mol (blue) and* $M_w = 600$ *kg/mol (green). Right: Zoom into the region of interest* $35\ min \leq t \leq 60\ min$.

For $t > 80$ min, the gravimetric measurements cannot resolve any further mass changes. The reason is that, in comparison to the NR experiment, the sensitivity towards very small amounts of remaining solvent is reduced by some orders of magnitude. Furthermore, the time axes of the kinetic NR and the gravimetric data are not exactly interchangeable since the measurements have been performed in different laboratories. The ambient conditions of the NR experiments are not exactly replicated in the gravimetric measurements. Anyhow, the experimental conditions are similar enough so that the main effects stay comparable and can be reproduced.

The gravimetric experiments confirm the different behavior of the sample with a molecular weight of 54 kg/mol which has already been observed with in-situ NR. This low molecular weight PSA exhibits a higher macroscopic evaporation rate in the beginning of the drying process. In contrast, the evaporation is slower for the samples with $M_w = 192$ kg/mol and $M_w = 600$ kg/mol. Within the experimental accuracy, the relative mass loss of these two polymers even coincides for times $0 < t < 36$ min.

A zoom into the region between $t = 36$ min and 60 min (see right panel of figure 4.10), however, reveals that, within this time interval, differences arise between the two polymers

with the highest molecular weights. In accordance to the results obtained with in-situ NR, the solvent evaporation of the sample with $M_w = 192$ kg/mol is faster than that of $M_w = 600$ kg/mol. It has to be noted that the origin of this effect cannot be fully clarified. It could either be related to the solvent trapping, which was described in the previous sections, or to the altered rheological properties. Possibly, both phenomena contribute to the observed deviations.

4.4 Conclusion

In this work, the complete near-surface evaporation process of a solution cast polymer melt film has been monitored for the first time. Owing to the method in-situ neutron reflectivity the solvent concentration profile is additionally extracted at any time t of the drying process. Statistical copolymer based PSAs with different molecular weights are chosen as a sample system and the corresponding impact on the speed of the evaporation and the shape of the solvent distribution are investigated.

The time dependence of the near-surface solvent content can be divided into approximately three regimes. For all molecular weights, directly after the casting of the solution only slow solvent evaporation is detected. The intermediate regime is characterized by an accelerated solvent evaporation which exceeds the predictions of conventional diffusion based theories. Solvent loss rates proportional to t^3 are obtained for the two highest molecular weights and the sample with the lowest molecular weight exhibits t^2 behavior. Finally, for large times, the solvent loss converges to zero and there is no molecular weight dependence. Moreover, the surface roughness is independent of both, the time which has passed after the casting and the polymer chain length.

Concerning the shape of the near-surface solvent distribution, two cases have been identified. Most of the time it is constant throughout the probed area of the drying film. Within the stages of accelerated solvent evaporation, however, there is a certain time interval during which more solvent per unit volume is present close to the surface than in the bulk. The width of the region of enhanced solvent concentration is on the order of 60 nm. The lifetime of this solvent enrichment as well as its amplitude increase as a function of the molecular weight. The effect is related to the molecular-weight dependent chain end density close to the surface and, thus, the accessible free volume. This free volume enables the PSA to trap a higher solvent concentration in a near-surface region than in the bulk.

The solvent is not extracted completely during the probed time interval. The amount of remaining solvent, which is in the sub-volume percent regime, is independent of the molecular weight. Furthermore, it is homogeneously distributed within the probed near-

surface region.
The influence of the molecular weight, and most likely also the related interfacial contributions, are also gravimetrically measurable via the macroscopic mass loss during drying. The sample with the lowest molecular weight dries fastest. The solvent loss rates of the PSAs with the higher molecular weights are identical except during a time interval which is characterized by a deceleration of the evaporation speed towards zero.
In summary, the near-surface area during drying of a polymer solution exhibits so far unknown behavior. In particular, the extracted power laws, which significantly exceed case II diffusion, are not predicted by conventional theories. An extension towards interfacial effects concerning altered free-volume and/or rheological properties would be beneficial. Furthermore, more experiments with different solvents and other classes of polymers would bring even more insight.

Chapter 5

Characterization of PSA films prepared under ambient conditions

Throughout this work, the solvent evaporation behavior during the drying of solution cast PSA films, that was presented in the previous chapter, plays a central role for the near-surface composition of the resulting samples. This is mainly because in the investigated statistical copolymer based PSAs, the solvent can selectively transport material to the sample surface and, thus, contribute to deviations from the chemical composition of the bulk. This chapter is mainly dedicated to the investigation of these so-called enrichment layers and their influence on the adhesive properties. Thereby, we focus on the preparation under ambient conditions which is closest to standard applications of PSA films.

Although a computational study predicted such enrichment layers for statistical copolymer films under the presence of a selective interface (see section 2.2.4), an experimental proof was still missing. This work represents the first successful direct measurement of such enrichment layers in statistical copolymers close to polymer-air interface. Moreover, owing to the method x-ray reflectivity, even the complete near-surface composition profile can be monitored for two-component systems.

In contrast to statistical copolymers, the enrichment of one component has already been reported for some classes of polymer systems, among which are for example polymer blends. As an example, the composition profile of a polymer blend film consisting of deuterated polystyrene (dPS) and poly(para-methylstyrene) (PpMS) was probed with neutron reflectivity [141]. Directly after the preparation, a surface enrichment of dPS was detected. In agreement with this study, the authors observed an internal reorganization process which was initialized by increasing the temperature, so that finally PpMS formed the top layer. Many other polymer blend films exhibit a similar surface enrichment of one component, too. Examples are PS/polybromostyrene [142], PS/dPS [143] or PS/poly(vinyl methyl ether) [144].

A further mechanism of enrichment layer formation is present in block copolymers which form lamellae or other structures (see section 2.2.3). Such phase separation induced enrichment has been investigated with various techniques, among which are grazing incidence small-angle x-ray scattering [145], atomic force microscopy [146], neutron reflectivity [69] and transmission electron microscopy [147].
In this work, not only the simple presence of compositional fluctuations close to the surface is monitored, but also the the driving forces, which are responsible for the layering, are investigated. Such knowledge is very beneficial because a deliberate manipulation of such driving forces would enable a tailoring of the distribution of the components in the near-surface area. The final goal is to use the near-surface composition profile for a fine-tuning of the adhesive performance.
In literature, there are already hints that this goal is achievable. Aymonier and coworkers, for example, varied the λ^* parameter (see section 2.2.4) in order to obtain copolymers of PEHA and PMMA that range from a statistical monomer distribution to more and more phase separating copolymers [148]. The resulting adhesive performance differs even among copolymers which contain the same overall monomer ratio. In another study, it was shown that the composition profiles of EHA/MMA latex particles are crucial for the resulting film performance [149]. With decreasing molecular weight of the particles, the influence of the different composition profiles increased.
Motivated by the high potential to tune the adhesive properties without the need to change the underlying material, the focus of this chapter is on parameters which influence the near-surface composition profiles of the statistical copolymer based PSA films under ambient conditions. A direct tailoring via controlled atmospheres is discussed in the next chapter.
In detail, the influence of the preparation protocol, the chemical properties of the comonomers and the molecular weight is investigated. Furthermore, the near-surface composition of three-component statistical copolymers is studied before finally, the internal reorganization of the films with time is described.
Results of this chapter have been published in references [38] and [150].

5.1 Composition profiles and tackiness of freshly prepared samples

The desired tailoring of the spatial distribution of the involved components close to the interface to the air is only possible when the response of the PSAs to different stimuli is understood. That is why in this section different controll parameters are systematically varied and the impact on the resulting near-surface composition profiles is described.

Some of these influencing factors even affect the adhesive performance of the PSA film.

5.1.1 Influence of the preparation protocol

In order to demonstrate how different preparation protocols can result in significantly different near-surface composition profiles, films are processed via two contrary pathways: the almost solvent-free method doctor-blading technique (see section 3.3.1) is compared to the solution casting method (see section 3.3.2). For the latter, the two solvents isobutanol and toluene are used. Both techniques are well suited to produce films with a thickness on the order of 50 μm. P(EHA-stat-20MMA) is chosen for the investigation of the effect of the different preparation protocols.
Starting with the doctor-blading, only little near-surface composition variations are present as can be seen from figure 5.1. The refractive index for very small distances from the surface z is almost equal to that of P(EHA-stat-20MMA). An explanation might be the absence of any selectivity provided either by the surrounding atmosphere or by evaporating solvent. Nevertheless, a weak PMMA enriched layer is detected in the sub-surface region. It has a maximum concentration of 59.9 % in a depth of 5.6 nm. Underneath, a broad zone exhibiting a slight PEHA enrichment follows before a final homogeneous bulk material is reached for $z > 100$ nm.

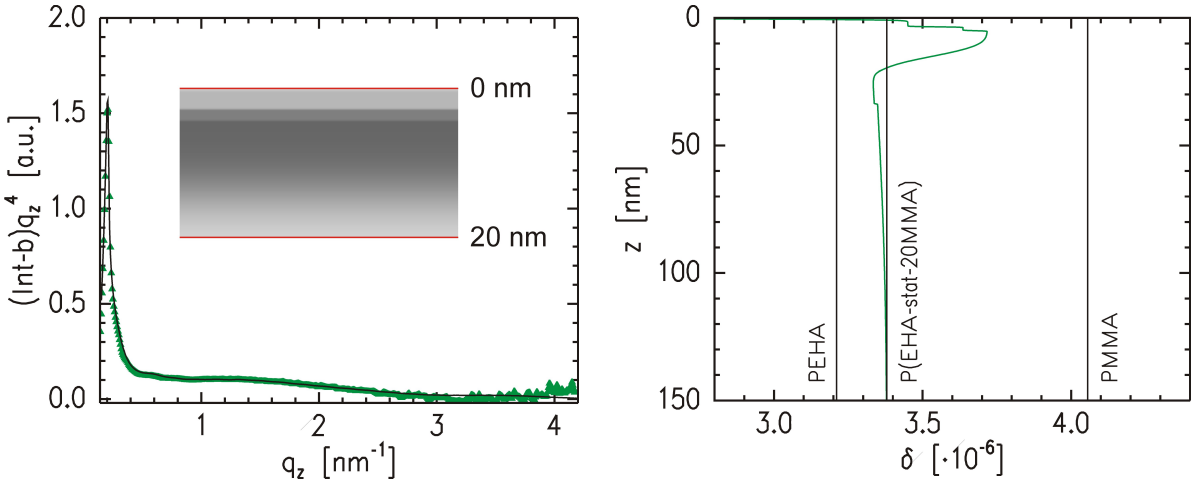

Figure 5.1: *Left: XRR data (symbols) and respective fit (solid line) of a doctor-bladed P(EHA-stat-20MMA) film. The inset shows the grayscale-coded (for definition see figure 3.3) composition profile. Right: Refractive index profile corresponding to the fit to the data. The vertical lines are positioned at the refractive indices of PEHA, PMMA and P(EHA-stat-20MMA).*

When in contrast to doctor-blading solvent based preparation methods are employed, it is possible that the presence of the solvent influences the composition profiles. During

the solution casting the unidirectional evaporation of solvent (for details, please refer to chapter 4) enables a transport of dissolved material towards the surface.

It is important to note that possible non-extractable, residual solvent is not expected to influence the interpretation of the composition profiles. First, it has been shown in section 4.1 that five hours after the solution casting the total amount of remaining solvent is distributed homogeneously over the near-surface region and the total content is already in the sub-percent regime. Second, Perlich and coworkers showed that in thin polystyrene films a small amount of residual solvent enriches at the interface to the substrate. However, there is no residual solvent close to the air-interface [151]. In this work, the interfacial region near the solid support is not investigated anyway.

The evaporation-induced material transport arising during the film drying is a selective process. The component which is preferred by the employed solvent remains longer in a dissolved state and is therefore preferentially transported to the surface. Suitable parameters to quantify the tendency of one component to be dissolved in a given solvent are the Hildebrand solubility parameter (see section 2.1.1) or the polarity, which can for example be measured as the dielectric constant or the ratio between the polar component and the total surface tension (see section 2.1.4).

The selective transport does not lead to a migration of solely one type of monomer towards the air interface. The different components cannot be decoupled from each other because they are copolymerized in a statistical copolymer. This implies that the selective transport of one component is inevitably connected with the transport of the other component. Anyway, two phenomena enable a pronounced enrichment of one component: first, due to the very large amount of polymer chains in the system, there are molecules which comprise almost exclusively one component. The transport of such homopolymer-type chains is not connected with an enrichment of both components. Second, even for polymer chains with a mixed composition, surface enrichment layers are possible because the chains can orient in a way that the preferred monomers are mostly situated at the surface. In this second scenario, a sub-surface enrichment layer of the less soluble component should consequently be generated.

Indeed, these compositional oscillations are observed for all PSA films investigated in this work. The thickness of the surface enrichment layers is in a regime which is smaller than the radius of gyration of the polymers. For example, on the basis of a freely jointed chain, $R_g = 11.2$ nm is estimated for P(EHA-stat-20MMA) and most of the enrichment layers are thinner. As a consequence, conformational changes of the polymer chains close to the surface are necessary supporting the existence of the second type of transport mechanism. Moreover, the integrated amount of the individual components in the near-surface region does not reflect the overall composition ratio which proves that also the

first type of transport contributes. In other words, mass conservation does not apply. This is, however, no contradiction because there might be as well enrichment layers at the interface to the substrate. The other interface is not accessible with the employed technique XRR. Thus, substrate-near enrichment layers can neither be confirmed nor excluded.

Figure 5.2 shows XRR data of two P(EHA-stat-20MMA) films, one of which was prepared via solution casting from a isobutanol and the other one from a toluene solution. The samples are measured 24 h after the deposition of the solution. The sample age being calculated from the time of the coating step plays a central role because the polymer chains reorganize as a function of time and, thus, change the composition profile. This so-called aging of the samples is detailed in section 5.3. Therefore, when composition profiles of different samples are compared it is important that they are of equal age. In the context of solution casting under ambient conditions, only freshly prepared samples are compared. This means that the solution casting has been performed 24 h before the beginning of the XRR measurement (see also in section 3.3.2). Freshly prepared samples are chosen to investigate the initial state of the near-surface chemical composition.

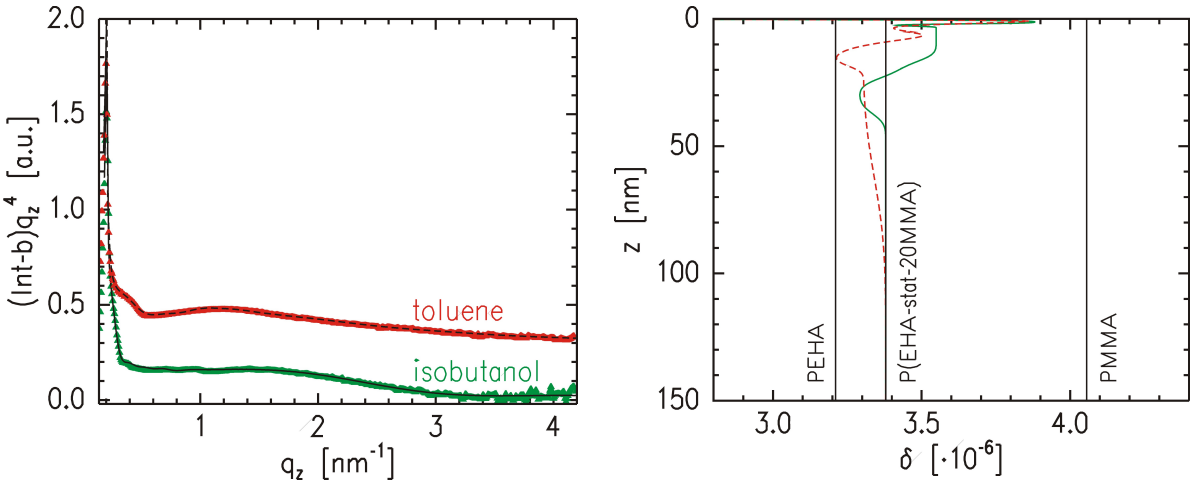

Figure 5.2: *Left: Comparison of the XRR data (symbols) and the corresponding fits (lines) of isobutanol based (bottom) and toluene based (top) solution cast films of P(EHA-stat-20MMA). The data are shifted along the intensity axis for clarity. Right: Respective refractive index profile for the samples cast from isobutanol (solid line) and toluene (dashed line).*

The choice of isobutanol and toluene as solvents for the solution casting under ambient conditions is based on their relatively high boiling points of 108 °C and 111 °C, respectively. The resulting comparably slow drying process enables the production of PSA films with a surface roughness in the sub-nanometer regime [126]. The low roughness, which is on the order of 0.5 nm for all investigated samples that were prepared under ambient

conditions, is very convenient for the data interpretation. If the surface roughness was very high a distinction of the involved components only via their refractive index would be impossible. For such cases of high surface roughness values, a reliable identification of individual components would have required the use of additional techniques like atomic force microscopy or photoelectron spectroscopy.

The near-surface composition profiles of the two solution cast PSA films differ significantly from that prepared via doctor-blading. The only similarity is the PEHA enrichment which converges to homogeneous bulk material for large z values. The main differences become evident close to the top surface. Both solution cast samples exhibit considerable PMMA enrichment at the surface. The corresponding concentrations are 79.2 % for isobutanol and 77.0 % for toluene, respectively. Furthermore, both sub-surface compositions oscillate as a function of z. The shape of the compositional oscillations, however, depends on the type of solvent. Comparing these two solution cast samples, the PEHA enriched region is more extended for the case of toluene as solvent. But as explained in section 3.3.2, under ambient conditions the sub-surface composition profiles of identically prepared samples may not coincide completely and therefore, a more detailed comparison is not possible.

Nevertheless, an enrichment of PMMA directly at the surface and a broad PEHA enrichment underneath is observed in all measurements for both solvents, toluene and isobutanol. Both are consistent with the already described mechanism of selective transport. The solubility parameters of the involved materials are $\mathfrak{D}(\text{PEHA}) = 18.37\ \text{MPa}^{0.5}$, $\mathfrak{D}(\text{PMMA}) = 18.27\ \text{MPa}^{0.5}$, $\mathfrak{D}(\text{isobutanol}) = 22.7\ \text{MPa}^{0.5}$ and $\mathfrak{D}(\text{toluene}) = 18.2\ \text{MPa}^{0.5}$ [8, 152]. The solubility parameter of PMMA is closer to that of toluene explaining the PMMA surface enrichment and, thus, the sub-surface PEHA enrichment for the toluene based sample.

This explanation based on solubility parameters does not work for the relatively polar isobutanol having a dielectric constant of 17.95 [153]. One reason is that the applicability of the Hildebrand solubility scale is limited when higher polarities are involved [7]. Another reason is that the absolute difference of $\mathfrak{D}$(isobutanol) to both, $\mathfrak{D}$(PEHA) and $\mathfrak{D}$(PMMA) is comparably large. Relative to each other, the difference in solubility according to the Hildebrand parameters is almost negligible: $\mathfrak{D}(\text{isobutanol}) - \mathfrak{D}(\text{PEHA}) = 0.98 \cdot (\mathfrak{D}(\text{isobutanol}) - \mathfrak{D}(\text{PMMA}))$.

As a consequence, the solubility parameter is not suitable to predict the surface enrichment behavior of the sample system with isobutanol and does therefore not contradict the described mechanism. Instead, it is very likely that the predominantly polar interactions between the polar solvent and the more polar component PMMA (see next chapter) favor the dissolution of PMMA. In summary, both solvents tend to transport PMMA to the sample surface during the drying step explaining the similar composition profiles.

5.1.2 Influence of the comonomer

The next examined parameter is the chemistry of the copolymerized materials. For this purpose, freshly prepared films of P(EHA-stat-MMA), P(EHA-stat-S) and P(EHA-stat-MAA) are investigated leaving the solvent toluene unchanged. So, all samples of this series contain 90 % of the sticky component EHA and the type of glassy minority component is varied.

The resulting XRR data together with the extracted profiles are plotted in figure 5.3. Significant compositional fluctuations are restricted to a thinner near-surface area as compared to P(EHA-stat-20MMA), which was the sample containing a higher ratio of glassy component (20 % instead of 10 %). Within the comonomer series, homogeneous bulk is already reached for $z \approx 40$ nm for all investigated samples. That is why the z axis of the left graph of figure 5.3 is only shown up to $z = 50$ nm. Furthermore, the labels of the bulk refractive indices of the statistical copolymers are sacrificed for clarity reasons.

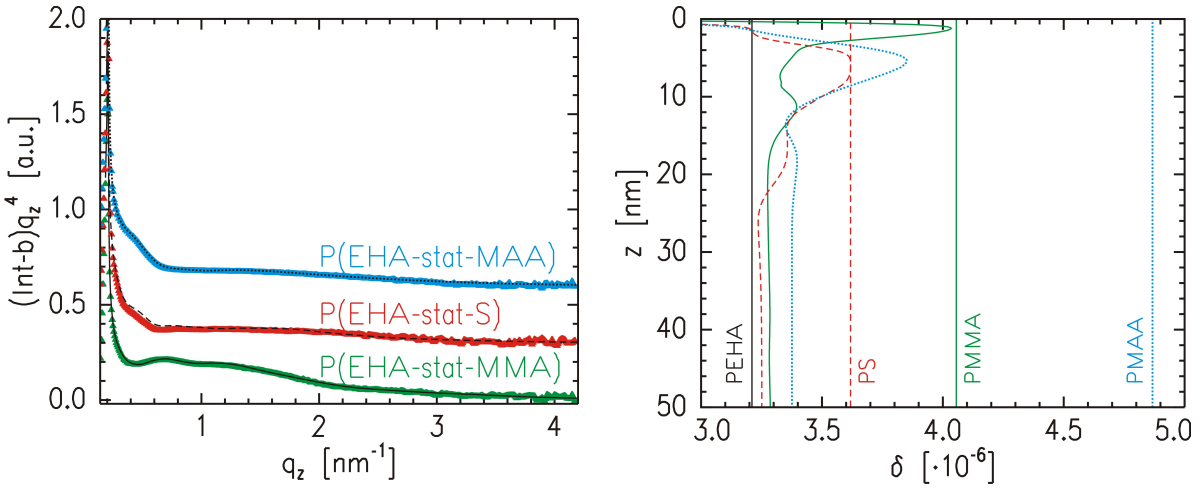

Figure 5.3: *Left: XRR data (symbols) and the corresponding fits (lines) of freshly prepared statistical copolymer films consisting of* 90 *% EHA and* 10 *% of a glassy comonomer as shown by the labels. The data are shifted along the intensity axis for clarity. Right: Respective refractive index profiles to the shown fits. The solid profile represents P(EHA-stat-MMA), the dashed profile P(EHA-stat-S) and the dotted profile P(EHA-stat-MAA), respectively. The vertical lines are positioned at the refractive indices of PEHA and the homopolymers related to the involved glassy components (see labels).*

The near-surface composition of P(EHA-stat-MMA) is very similar to that of P(EHA-stat-20MMA). The PMMA enrichment layer at the surface for the sample with 10 % MMA is even more pronounced than that of the sample with 20 % MMA shown in figure 5.2. Moreover, both samples exhibit connatural subsurface compositional oscillations. Therefore, it can be concluded that the difference in the overall polymer composition does not tremendously affect the near-surface composition profile. The lower amout of

MMA monomers in P(EHA-stat-MMA) as compared to P(EHA-stat-20MMA) cannot outweigh the mechanism of selective transport which is described in section 5.1.1.

For all investigated samples, the near-surface composition mainly depends on the chemistry of the involved components and on the type of solvent and less on the ratio of the copolymerized monomers. Further details cannot be derived because the molecular weights of the two MMA containing samples are not the same. A detailed discussion concerning the influence of the molecular weight is provided in section 5.1.4.

When S or MAA are chosen as comonomers instead of MMA, the resulting near-surface composition profiles of P(EHA-stat-S) and P(EHA-stat-MAA) exhibit the opposite shape as compared to P(EHA-stat-MMA). For both polymers, P(EHA-stat-S) and P(EHA-stat-MAA), the tacky component PEHA is enriched at the topmost layer. This can be deduced from the shoulders of the respective refractive index profiles at the value of PEHA (see right panel of figure 5.3). In contrast to P(EHA-stat-MMA), there is an enrichment of the minority component underneath the top layer. For the investigated samples the corresponding maximal concentrations are 100 % PS and 61.3 % PMAA, and they are reached in depths of 5.9 nm and 5.4 nm, respectively. For larger z values, the composition converges in an oscillating way towards the bulk composition which is characterized by the overall monomer ratio.

At least the composition profile of P(EHA-stat-S) is consistent with the already described selective transport because the solvent toluene clearly favors PEHA due to the high solubility parameter of PS: $\mathfrak{D}(\mathrm{PS}) = 22.47\ \mathrm{MPa}^{0.5}$ [8]. $\mathfrak{D}$(PMAA) is not available in literature and, thus, P(EHA-stat-MAA) cannot be used for a confirmation of the proposed mechanism. However, due to the strong similarity of $\mathfrak{D}$(toluene) and $\mathfrak{D}$(PEHA) it is very likely that also in this system, the majority component PEHA is the better soluble material.

It is important to note that such solubility driven morphologies are already known for other classes of polymeric samples such as polymer blend films [154, 155] or block copolymer films [156]. Closer to this work, solubility driven compositional variations of random multiblock copolymers are reported by Zhuang and Gardella [157]. However, with the chosen methods angle-dependent electron spectroscopy for chemical analysis and attenuated total reflection Fourier transform infrared spectroscopy, only four sampling depths were investigated and their sample system differs from the statistical copolymer based PSAs of this work. But nevertheless, the findings of Zhuang and Gardella strongly support the presented observations.

The shown solubility driven morphologies still appear when more extreme temperature conditions are chosen. For comparison purposes, P(EHA-stat-MAA) has been cast at a temperature of 6 °C. In figure 5.4, the obtained XRR data are shown together with those which were obtained for P(EHA-stat-MAA) prepared at room temperature. The dotted

fit and the dotted profile have already been presented in figure 5.3 and the respective solid lines represent the preparation under low temperature conditions.
As a result, the composition profiles are very similar. The surface is still dominated by PEHA and the amplitudes of the sub-surface PMAA enrichment do not differ significantly. Only the compositional oscillations are more pronounced for the case of low temperature conditions. This is reflected in the data by a more pronounced modulation in the range $0.35\ \mathrm{nm}^{-1} < q_z < 0.7\ \mathrm{nm}^{-1}$. Such improved layering might arise from the slower solvent evaporation at low temperature.

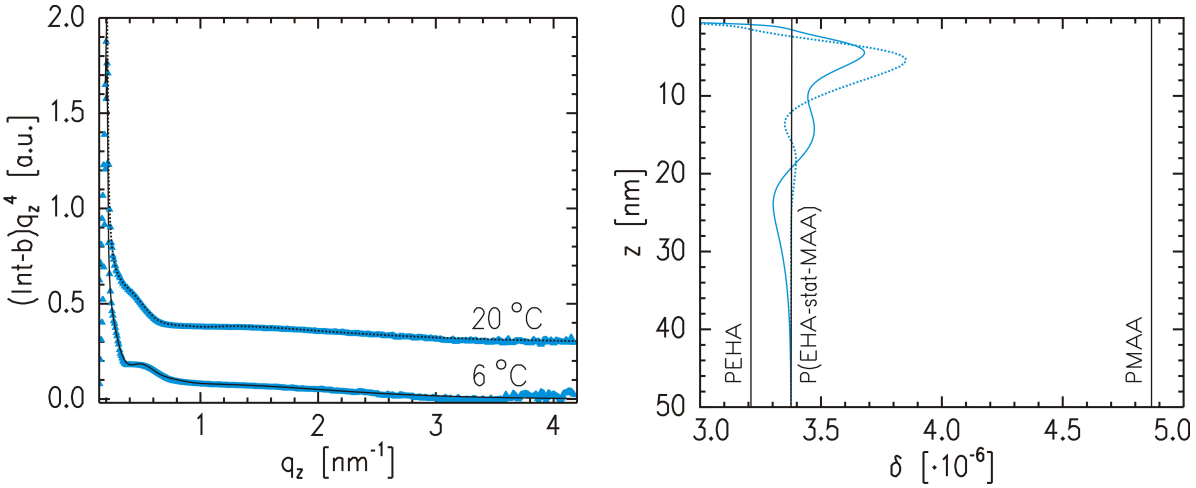

Figure 5.4: *Left: XRR data (symbols) and the corresponding fits (lines) of P(EHA-stat-MAA) films freshly prepared under different temperatures as shown by the labels. The data are shifted along the intensity axis for clarity. Right: Respective refractive index profiles to the shown fits. The solid profile represents a temperature of* 6 °*C and the dotted profile* 20 °*C, respectively. The vertical lines are positioned at the refractive indices of PEHA and PMAA (see labels).*

In order to investigate whether the observed differences in the near-surface composition profiles, which are induced by the chemical nature of the involved comonomers, influence the adhesive properties of the PSAs, tack measurements have been carried out with the three samples prepared under room temperature conditions. A relatively high contact force of 3 N was chosen leading to a nominal contact pressure of 3.8 MPa. As a consequence, the surface sensitivity of the tack experiment is lower compared to that chosen for the samples prepared under controlled atmosphere (see section 6.1.3). Another reason for the lower surface sensitivity is the higher roughness of the punch used for the solution cast PSA films under ambient conditions.
All measured tack data are depicted in figure 5.5. At least 11 sampling points were taken for each of the three films to reduce the statistical error. The curves of all three statistical copolymers contain the main features which are proposed in Creton's four stage model (see

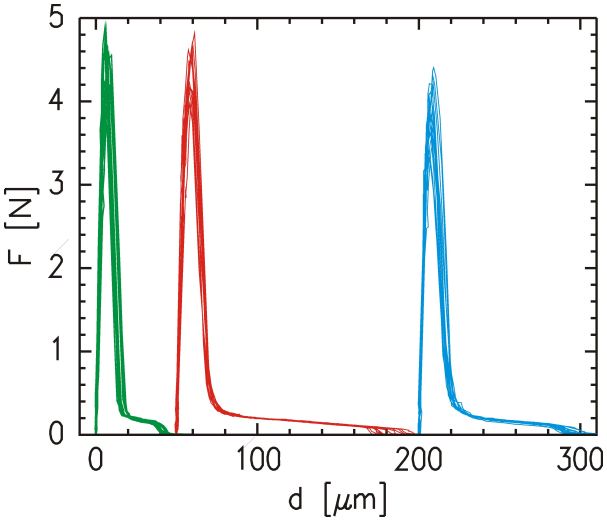

Figure 5.5: *Tack data (punch radius: 0.5 mm) of the three 50 μm thick samples composing the comonomer series (from left to right: P(EHA-stat-MMA), P(EHA-stat-S) and P(EHA-stat-MAA)). Each sampling point is represented by one single line. The curves corresponding to different statistical copolymers are shifted along the d-axis for clarity.*

figure 2.6): the sharp force maximum is reached for $d \approx 6$ μm. It drops down to a value of $F \approx 0.23$ N, which is reached at an elongation of approximately 16 μm. From this point on, the plateau characteristic of stage IV begins. The length of the plateau is different for the individual statistical copolymers. It mainly reflects the obtained differences in tack energy W.

For the formation of fibrils, which are elongated up to 130 μm, a lot of material is necessary compared to the thin near-surface composition oscillations covering a range of 40 nm. Therefore, it is to be expected that the observed differences in tack energy are mainly attributed to the comonomer dependent mechanical properties of the bulk material. However, despite the different maximal length of the fibrils, the force maximum of P(EHA-stat-MMA) equals that of P(EHA-stat-S) within the achieved experimental accuracy. Moreover, for P(EHA-stat-MAA) F_{max} is significantly lower than for the other two copolymers. The corresponding values of the force maximum and the tack energy are listed in table 5.1.

	P(EHA-stat-MMA)	P(EHA-stat-S)	P(EHA-stat-MAA)
$\boldsymbol{W}$ [μJ]	45.4 ± 4.9	73.2 ± 4.5	58.6 ± 5.4
$\boldsymbol{F_{max}}$ [N]	4.49 ± 0.27	4.39 ± 0.29	3.93 ± 0.30

Table 5.1: *Extracted values of the force maximum F_{max} and the tack energy W obtained in probe tack experiments with the samples in the comonomer series.*

It is interesting to note that the maximal force obtained in a tack test is closely correlated with the overall content of the minority component close to the surface. In more detail, by integrating the composition profiles over $0 < z < 4$ nm, the respective volume ratios of the minority component within the upper 4 nm of the PSA films are calculated. As a result,

the minority component content in this near-surface region is 58.2 % for P(EHA-stat-MMA), 57.1 % for P(EHA-stat-S) and 37.3 % for P(EHA-stat-S). The strong similarity of P(EHA-stat-MMA) and P(EHA-stat-S) is also reflected in the tack data. In contrast, P(EHA-stat-MAA) exhibits both, the lowest force maximum and the lowest near-surface content of the glassy component.
An explanation might be found in the four-stage model. The force maximum is determined by the performance of the film during the stages I and II, where the material first expands homogeneously and then the cavities are formed. As already pointed out in section 2.1.6, the cavities appear predominantly near the accessible interface [40]. Therefore, it is very likely that, due to the improved stiffness of interface-material, the necessary force to create cavities is higher. To finally prove that the near-surface composition has an impact on the adhesive performance, it is, however, inevitable to carry out experiments with identical bulk material. Such measurements are presented in the next chapter.

5.1.3 Comparison of different composition ratios

The previous section was dedicated to the estimation of the change in tackiness induced by the chemistry of the involved components. It is now interesting to quantify the influence of the overall monomer composition leaving the type of monomer unchanged. For this purpose, the adhesive performances of P(EHA-stat-20MMA), P(EHA-stat-MMA) and pure PEHA are compared in probe tack tests. The measured data is plotted in figure 5.6, where the curves for P(EHA-stat-MMA) are those already presented in figure 5.5. The three films are freshly prepared from toluene based solutions under ambient conditions. The experimental conditions are identical to those described in section 5.1.2.

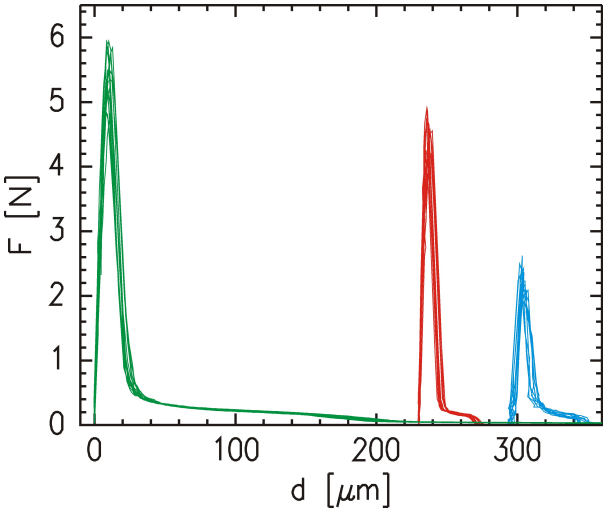

Figure 5.6: *From left to right: tack data (punch radius: 0.5 mm) of 50 μm thick films consisting of P(EHA-stat-20MMA), P(EHA-stat-MMA) and PEHA. Each sampling point is represented by one single line. The curves corresponding to different material are shifted along the d-axis for clarity.*

A clear trend is evident from the measured tack data. Within the investigated range of overall MMA composition ratios, the tackiness increases with increasing MMA content.

This can be understood from the improved balance of adhesion and cohesion in the PSA film with a higher content of the glassy component. Table 5.2 lists the corresponding force maxima and tack energies. The result is in accordance with findings by Aymonier and coworkers [158], who also varied the MMA content in statistical copolymers being composed of EHA and MMA. According to their work, the tack energy is optimized for a critical MMA content of 25 %.
Comparing the two samples P(EHA-stat-20MMA) and P(EHA-stat-MMA) with pure PEHA, it is obvious that the rheological properties of the MMA containing polymers lead to the improved performance. But it cannot be clarified to what extent the near-surface compositions contribute to the observed behavior because PEHA is a single-component material and compositional fluctuations are absent. Therefore, a full interpretation of the data remains difficult.

	P(EHA-stat-20MMA)	P(EHA-stat-MMA)	PEHA
$\boldsymbol{W}$ [μJ]	120.5 ± 9.3	45.4 ± 4.9	26.4 ± 3.4
$\boldsymbol{F_{max}}$ [N]	5.41 ± 0.41	4.49 ± 0.27	2.30 ± 0.19

Table 5.2: *Extracted values of the force maximum F_{max} and the tack energy W obtained probe tack tack experiments with samples of different MMA content.*

More insight can be gained from a comparison of the sample with 20 % MMA to that with 10 % MMA. As it has been pointed out in section 5.1.2, there is only minor influence of the overall monomer ratio on the main features of the near-surface composition profile. For example, the integrated MMA concentration within the upper 4 nm of P(EHA-stat-20MMA) is 42.5 %, which is even lower than that of P(EHA-stat-MMA) for the investigated samples. Following the argumention in the previous section, the lower value for P(EHA-stat-20MMA) should even lead to a slightly lower adhesive performance regarding exclusively the influence of the interfacial area. However, the tack energy of P(EHA-stat-20MMA) is higher than that of P(EHA-stat-MMA) by almost a factor of three. As a consequence, the differences in tackiness of the MMA containing samples is entirely a bulk phenomenon.

5.1.4 Influence of the molecular weight

Another controll parameter which is important for both, the bulk and the interfacial properties of the solution cast PSAs is the molecular weight of the underlying statistical copolymer. In this work, a detailed discussion of the bulk properties is omitted in order to focus on the interfacial aspects. The copolymer which was available with different molecular weights is P(nBA-stat-MA). In more detail, samples with the three molecular

weights M_w = 54 kg/mol, 192 kg/mol and 600 kg/mol being cast from a toluene based solution under ambient conditions are investigated.

The x-ray refractive index of PnBA is significantly higher than that of PEHA (see table 3.1) and that of PMA similar to PMMA. As a consequence, the contrast in the system is reduced and the exact determination of the depth dependent composition ratios is more difficult. Nevertheless, it is still possible to identify areas which are considerably enriched with one component.

Figure 5.7 shows the obtained XRR data together with the corresponding refractive index profiles. Similar to the samples with EHA as the majority component, all samples exhibit a pronounced enrichment of PnBA for $z > 20$ nm. For larger distances from the sample surface it converges towards the average composition ratio of approximately 80 % nBA and 20 % MA. Homogeneous bulk composition is reached for $z > 150$ nm.

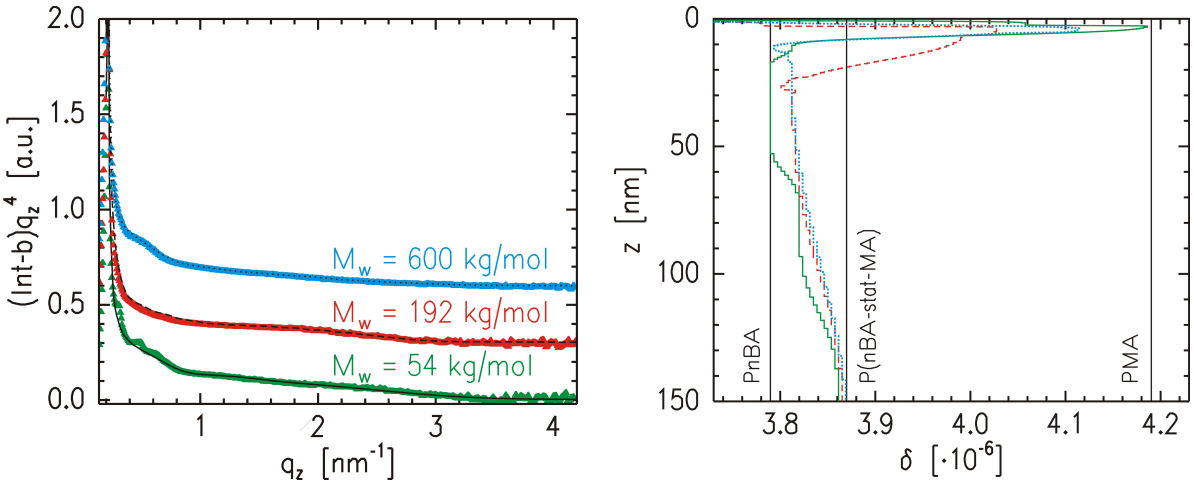

Figure 5.7: *Left: XRR data (symbols) and the corresponding fits (lines) of freshly prepared P(nBA-stat-MA) films with different molecular weights as shown by the labels. The data are shifted along the intensity axis for clarity. Right: Respective refractive index profiles to the shown fits. The solid profile represents M_w = 54 kg/mol, the dashed profile M_w = 192 kg/mol and the dotted profile M_w = 600 kg/mol, respectively. The vertical lines are positioned at the refractive indices of P(nBA-stat-MA) and the related homopolymers PnBA and PMA (see labels).*

However, there also qualitative differences, especially for very small z values. These differences are not easily visible in the right panel of figure 5.7. They become evident in a close-up of the region close to the sample surface which is shown in figure 5.8.

The surface of the two samples with the higher molecular weights is dominated by nBA. This enrichment can be seen from the respective shoulders in the refractive index profile at the value of PnBA for low z values. The reason can be found in the relatively high value of the solubility parameter $\mathfrak{D}$(PMA) = 20.7 MPa$^{0.5}$ [159]. Therefore, it is very likely that

the corresponding (unavailable) parameter of PnBA is closer to that of toluene explaining the observed PnBA enrichment. Furthermore, a prominent enrichment of PMA follows directly underneath.

Why the sub-surface PMA enrichment for the sample with $M_w = 192$ kg/mol is weaker than that for $M_w = 600$ kg/mol, while at the same time having a more pronounced PnBA shoulder, is not fully understood. An explanatory approach might be based on the different effective sample ages. Although both samples were measured precisely one day after casting the respective solutions, the speed of the internal molecular reorganization (see section 5.3) is different for the two polymers because the longer the polymer chains are, the lower their mobility is.

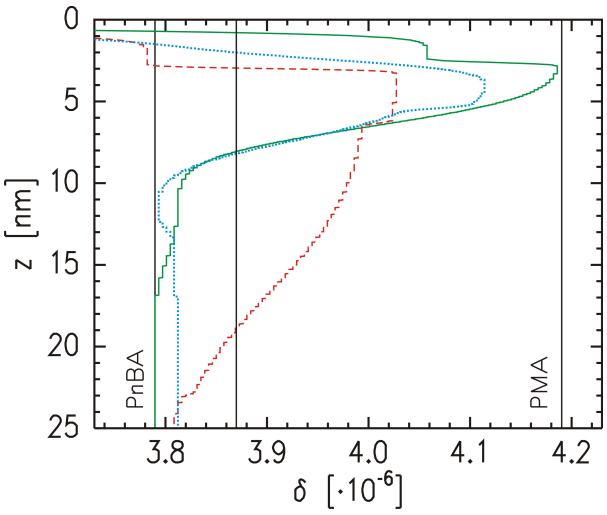

Figure 5.8: *Zoom into the region close to the sample surface of the refractive index profiles of the P(nBA-stat-MA) samples of the molecular weight series. The line types match with figure 5.7.*

In contrast to the samples with $M_w = 192$ kg/mol and $M_w = 600$ kg/mol, PnBA is not enriched at the surface of the sample with the lowest molecular weight. Directly at the interface and also up to a depth of 7 nm, the material composition is dominated by PMA. The reason for this behavior might also be related to the comparably short polymer chain length and the resulting fast reorganization kinetics. Another explanatory approach could be the strongly deviating solvent evaporation kinetics during the drying process which was described in chapter 4. Due to the weaker solvent enrichment layers during the stages of accelerated near-surface solvent evaporation and the on average faster solvent loss, the capability of the system to transport the favored PnBA to the sample surface is significantly reduced. Possibly, both proposed phenomena contribute to the observed PMA surface enrichment.

5.2 Statistical copolymers with three components

Additional complexity is introduced into the systems by copolymerizing a third type of monomer so that statistical copolymers with three components are obtained. The investigated three-component materials are P(nBA-stat-MA-stat-AA), P(nBA-stat-MA-stat-MMA) and P(nBA-stat-MA-stat-HEA) with composition ratios as listed in table 3.2. XRR experiments are performed with freshly prepared films which have been solution cast under ambient conditions.

With XRR it is not possible to quantify the exact composition as a function of distance from the surface for the three-component systems because equation 3.1 is only applicable when two components are involved. However, at least enrichment layers of components having either the lowest or the highest refractive index compared to the other two components in the system can be identified.

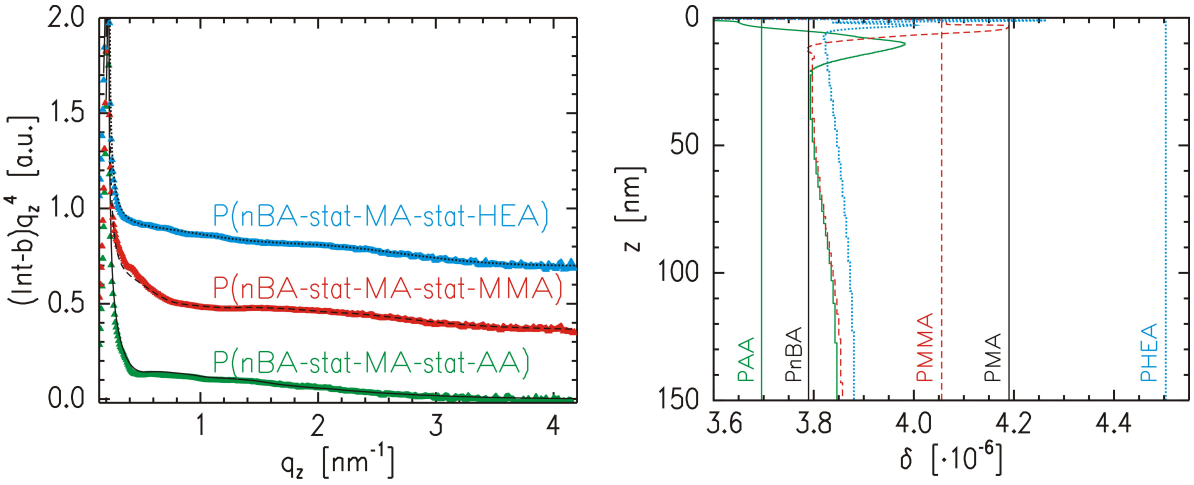

Figure 5.9: *Left: XRR data (symbols) and the corresponding fits (lines) of freshly prepared three-component statistical copolymer films as shown by the labels. The data are shifted along the intensity axis for clarity. Right: Respective refractive index profiles to the shown fits. The solid profile represents P(nBA-stat-MA-stat-AA), the dashed profile P(nBA-stat-MA-stat-MMA) and the dotted profile P(nBA-stat-MA-stat-HEA), respectively. The vertical lines are positioned at the refractive indices of the homopolymers related to the involved monomers (see labels).*

The resulting XRR data together with the extracted refractive index profiles are plotted in figure 5.9. Similar to P(nBA-stat-MA), there is a pronounced nBA enriched region for $z > 20$ nm for at least P(nBA-stat-MA-stat-MMA) and P(nBA-stat-MA-stat-HEA). This nBA enrichment can be concluded from the combination of two observations: first, the refractive index in the corresponding region has a value close to PnBA and, second, PnBA is the lowest involved refractive index for these two statistical copolymers.

The shape of the refractive index profile of P(nBA-stat-MA-stat-AA) almost coincides

with that of P(nBA-stat-MA-stat-MMA) for $z > 20$ nm. It is therefore likely that in this region nBA is enriched for P(nBA-stat-MA-stat-AA), too. For all three statistical copolymers, homogeneous bulk material is reached for depths of approximately 150 nm. So, especially for large z values the composition profiles of the three-component PSAs are very similar to those of the two-component systems P(nBA-stat-MA).

The main impact originating from the copolymerization of a third type of monomer concerns the region close to the surface. A corresponding close-up of the refractive index profiles is depicted in figure 5.10.

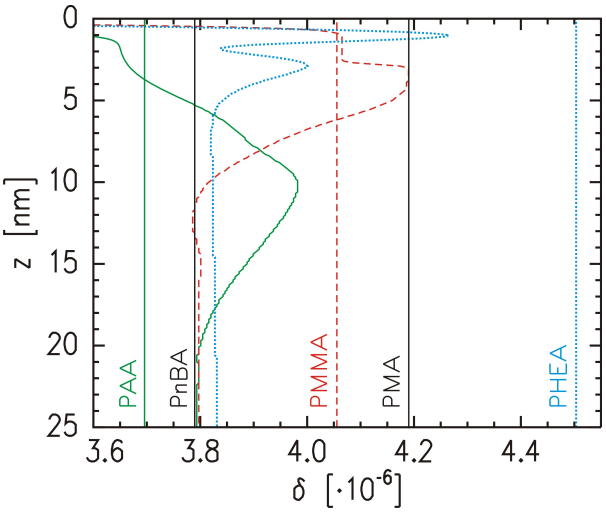

Figure 5.10: *Zoom into the region close to the sample surface of the refractive index profiles of the statistical copolymer films comprising three different types of monomers. The line types match with figure 5.9.*

In the P(nBA-stat-MA-stat-AA) film, there is a clear surface enrichment of the material with the lowest refractive PAA, which can be seen from the shoulder at the value of PAA for small z values. Underneath, the refractive index is higher reaching a maximum at $z = 10.3$ nm. The corresponding peak value is in between δ(PnBA) and δ(PMA) implying the presence of PMA. In general, as long as $\delta(z) > \delta$(PnBA), there is a always certain amount of PMA in P(nBA-stat-MA-stat-AA) because otherwise $\delta(z)$ would be a linear combination of δ(PAA) and δ(PnBA) and, thus, would be smaller than δ(PnBA). Therefore, PMA contributes to the sample composition at least for $z > 5.4$ nm. However, as explained above, a detailed composition profile cannot be extracted.

Although a proof is not possible, it is very likely that the top layer of the P(nBA-stat-MA-stat-MMA) film is dominated by PMMA. One reason is that PMMA is strongly favored by toluene, as it has been shown in section 5.1.1, and is therefore preferentially transported to the surface during the drying process. Another indication is that the refractive index for low z values almost coincides with that of PMMA. Furthermore, between this surface layer and the already discussed sub-surface PnBA enriched region a pronounced enrichment of PMA is found. It is situated at 2.6 nm $< z <$ 6.2 nm and reaches its maximum at a depth of $z = 3.5$ nm.

Finally, PHEA is situated at the sample surface of the P(nBA-stat-MA-stat-HEA) film. This follows from the peak-like shape of the refractive index profile for low z values exceeding the refractive index of PMA. Judging only from the profile, it could be that the surface is dominated by PMA and only a little amount of PHEA is involved. However, it has to be taken into account that, neither for the other two three-component systems nor for P(nBA-stat-MA) with the higher and, thus, comparable molecular weights, PMA is enriched at the surface. It is, therefore, likely that the PHEA concentration at the surface is rather high. In other words, the high near-surface refractive index is more a consequence of the strong presence of PHEA rather than of PMA.
Furthermore, besides the already discussed broad PnBA enrichment, an interpretation of the sub-surface refractive index profile is difficult for P(nBA-stat-MA-stat-HEA). The reason is that $\delta(z)$ remains between δ(PnBA) and δ(PMA) for $z > 1.3$ nm. Therefore, the role of the highest-refractive index material PHEA remains unclear for the sub-surface region.

5.3 Composition profiles as a function of time

So far, only the composition profiles of freshly prepared samples have been examined. Furthermore, for the solution cast PSA films the near-surface distribution of the components is strongly influenced by the corresponding solubilities of the related homopolymers with respect to the solvent (see sections 5.1.1 and 5.1.2). As a consequence, it is not to be expected that equilibrium structures are obtained. On the contrary, once the solvent has evaporated an internal molecular reorganization sets in.

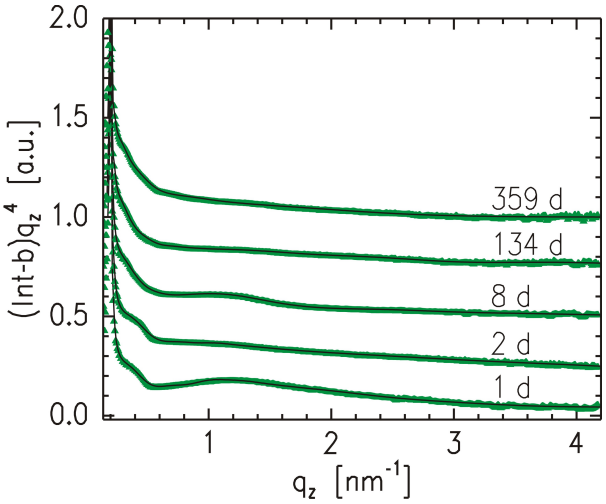

Figure 5.11: *XRR data (symbols) and the corresponding fits (lines) of a time series of P(EHA-stat-20MMA) films cast from a toluene based solution. The sample ages are indicated by the labels. The data are shifted along the intensity axis for clarity.*

Such internal reorganization processes, which are also referred to as aging, are monitored in detail for a P(EHA-stat-20MMA) film being cast from a toluene based solution. This

is a rather mobile system originating from the low glass transition temperature of the majority component PEHA of −50 °C [8]. The near-surface composition profiles are monitored with XRR as a function of time. The sample ages 1 (freshly prepared), 2, 8, 134 and 359 days are selected for this purpose. The term sample age is defined in section 3.3.2.

As it has been further pointed out in section 3.3.2, for the preparation under ambient conditions there are slight differences in the near-surface composition profiles among identically prepared samples. To rule out misinterpretation of the XRR data, the aging experiment is performed with one polymer film. It starts with the freshly prepared sample that was presented in figure 5.2 (top curve). Between subsequent measurements, the samples were stored in a closed cabinet situated in the preparation laboratory in order to avoid UV degradation as well as the contamination from dust particles. The measured XRR data together with the corresponding fits are shown in figure 5.11.

The position and the shape of the features in the reflectivity curves, which have been initially obtained for the freshly prepared sample, change as a function of time. Such a variation in the XRR data already indicates a time-dependence of the near-surface composition profile and, thus, a spatial reorganization of the molecules in the PSA. For a better illustration, the corresponding composition profiles are shown in figure 5.12 in grayscale-coded representation.

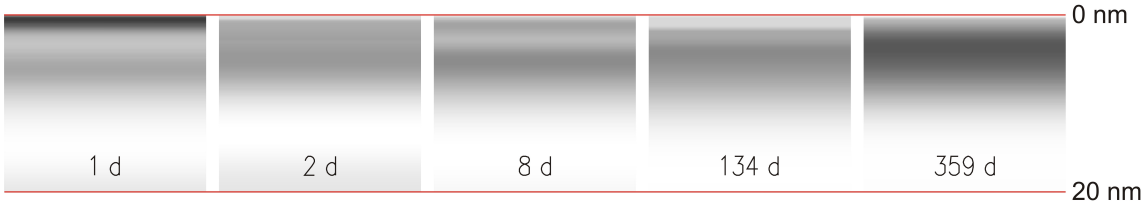

Figure 5.12: *Grayscale-coded near-surface composition profiles of an aging series of P(EHA-stat-20-MMA). The data correspond to the fits shown in figure 5.11. The grayscale code is defined in figure 3.3.*

As it has been explained in section 5.1.1, the solubility driven composition profile of the freshly prepared sample exhibits a pronounced PMMA enrichment at the sample surface. The sub-surface composition oscillations lead to a second, weakly PMMA enriched layer situated in a depth of 6.5 nm. After two days, these initially separated regions merge so that a broader, but less pronounced PMMA enriched zone is obtained.

In the following, PEHA starts to move to the sample surface. After 8 d, this can be seen from the (bright) PEHA material in a depth of 3.8 nm, which has penetrated the broadly distributed near-surface PMMA. The PEHA finally reaches the surface as can be seen from the pronounced PEHA surface enrichment layer after 134 d. The sub-surface region

is still PMMA dominated. The maximum PMMA concentration for $t = 134$ d is 45.8 % and it is detected at $z = 5.8$ nm.

Comparing only the XRR data of the two mostly aged samples ($t = 134$ and 359 d), no prominent changes are observed. This is also reflected in the two corresponding composition profiles which exhibit strong similarities. Most prominent is the preservation of the PEHA surface enrichment layer. Slight differences, however, are found in the sub-surface composition. The volume occupied mostly by PMMA contracts in the last step of the time series and its position shifts a little towards the surface. This shift can be seen from the increase of the maximum PMMA concentration to 65.5 % which is finally found in a lower depth of 4.4 nm. This sub-surface PMMA densification might be attributed to the self-attraction of the MMA monomers. The reason is the more favorable interaction between chemically identical monomers as compared to that between different ones (see section 2.2.2).

In summary, the near-surface composition of the aged sample is completely inverted as compared to the freshly prepared state. The absence of solvent-induced driving forces allows the now purely two-component polymer system to minimize its surface tension. The literature values of the surface tensions of the related homopolymers are γ(PEHA) = 30 mN/m and γ(PMMA) = 38.5 mN/m [160, 161] so that, indeed, the component with the lower surface tension enriches at the sample surface after a sufficiently long aging time. Because this process requires a collective motion of all polymer chains in the near-surface region, it is very difficult to predict the time scale of the aging. For example, conventional diffusion theories focus on the displacement of a single molecule only [162] and are, hence, not capable of a successful modeling.

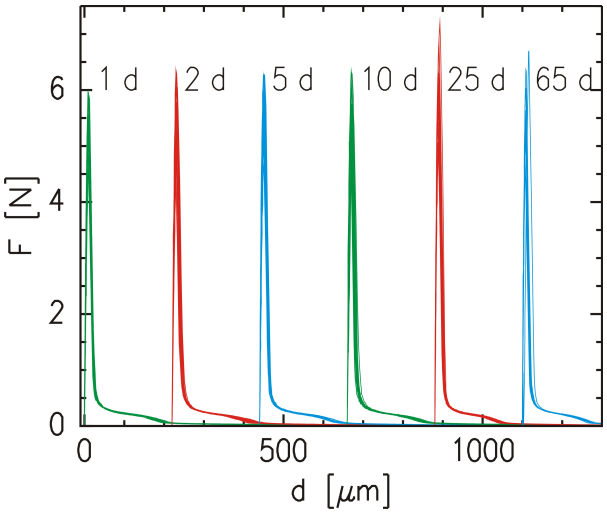

Figure 5.13: *Tack data (punch radius: 0.5 mm) of an aging series of 50 μm thick P(EHA-stat-20MMA) films. Each sampling point is represented by one single line. The curves corresponding to different sample age are shifted along the d-axis for clarity. The respective sample ages are indicated by the labels.*

In order to check whether the observed reorganization process has a measurable impact on the adhesive performance of the PSA films, tack measurements have been carried out

under the same conditions as for the comonomer series (see section 5.1.2). The probe tack tests are performed for six P(EHA-stat-20MMA) films covering a range from being freshly prepared up to a sample age of 65 days. Figure 5.13 shows the resulting force-distance curves. The data of the freshly prepared sample (1 d) have already been presented in figure 5.6 (left curves).

The force-distance curves corresponding to the different sample ages look very similar and indicate only minor changes of the tackiness within the selected time window. This is confirmed by plotting the resulting force maxima as well as the tack energies as a function of time (see figure 5.14). As a result, no detectable time-dependence of the two parameters is obtained.

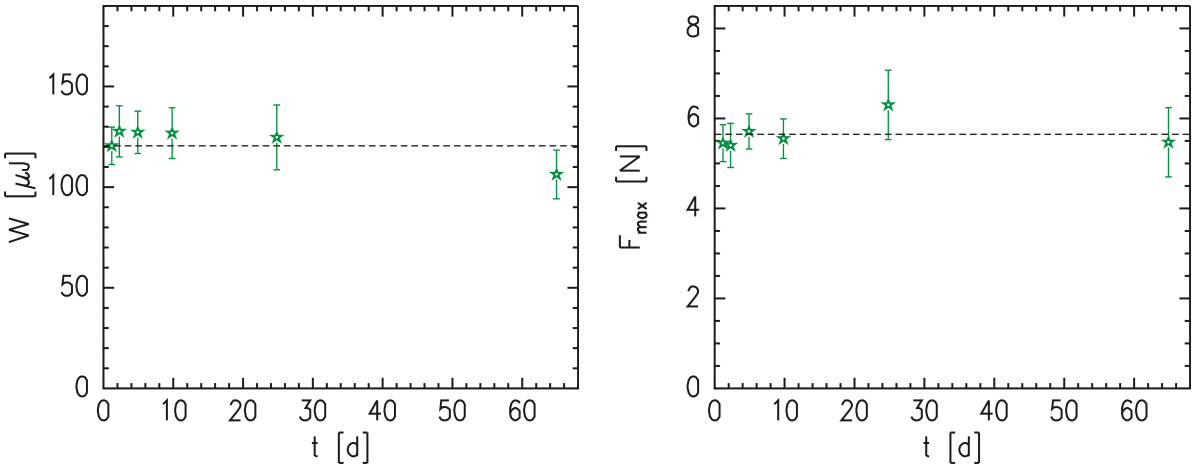

Figure 5.14: *Left: Tack energy as a function of time for an aging series of solution cast P(EHA-stat-20MMA) prepared and stored under ambient conditions. The dashed line marks the mean value of the six data points. Right: Corresponding force maximum as a function of time.*

The reason for the constant adhesive performance might be attributed to the low surface sensitivity of the probe tack tests due to the chosen experimental parameters. Furthermore, the calculation of the near-surface PMMA content of the upper 4 nm, as it was introduced in section 5.1.2, reveals that only a quite narrow concentration range between 42.5 % and 27.9 % is covered regarding the time interval which is represented by the tack experiments. Therefore, under these conditions interfacial effects play only a minor role for the adhesive performance. It could also be that, due to the bulk driven overall higher values of W and F_{max} as compared to the comonomer series, small contributions of the near-surface region are more difficult to resolve.

In summary, averaging over all six measured data points leads to a mean tack energy of (120.5 ± 8.2) μJ and a mean force maximum of (5.65 ± 0.34) N. In order to be able to detect the influence of the near-surface composition on the macroscopic tackiness without

changing the underlying statistical copolymer, it would be important to optimize the experimental conditions and to generate higher deviations in the composition profiles. Such experiments will be shown in the next chapter.

Depending on the chosen statistical copolymer, the described near-surface compositional changes do not necessarily always have to involve a complete inversion of the composition profile. Such a situation would arise when the component, which is favored by the employed solvent and, hence, adsorbs at the surface of the freshly prepared sample, is also the component with the lowest surface tension. In this case, no major molecular reorganization as a function of time is to be expected.

P(EHA-stat-S) is a good candidate for such a weak aging behavior because, on the one hand, in section 5.1.2 it was shown that PEHA enriches at the surface already for the freshly prepared sample. On the other hand, the surface tension of PS is 38 mN/m [163] which is higher than γ(PEHA). In figure 5.15, the fitted XRR data and the resulting composition profile of the already discussed freshly prepared P(EHA-stat-S) film are compared to a film having a sample age of 25 d.

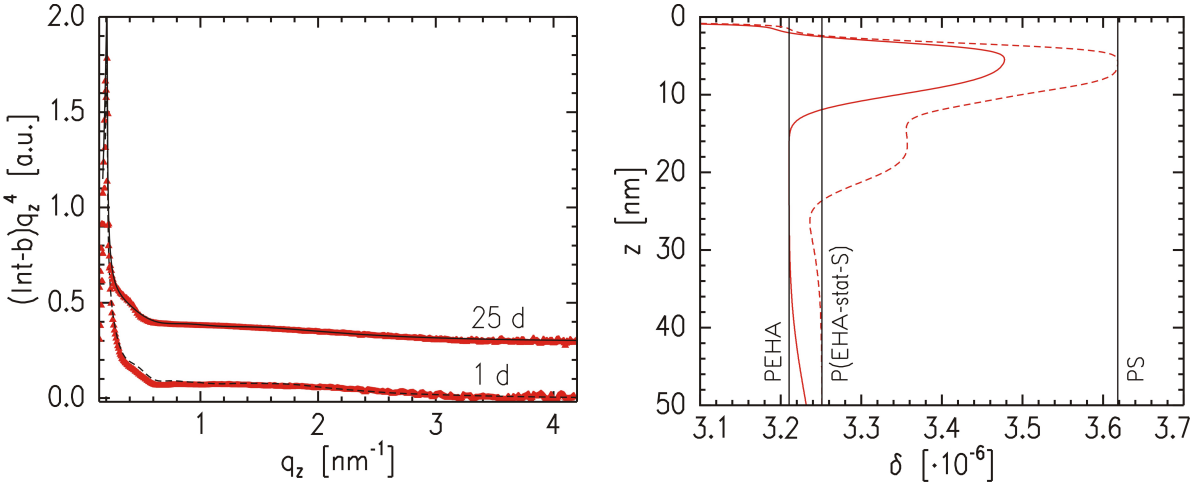

Figure 5.15: *Left: XRR data (symbols) and the corresponding fits (lines) of P(EHA-stat-S) films of two different sample ages as shown by the labels. The data are shifted along the intensity axis for clarity. Right: Respective refractive index profiles to the shown fits. The dashed profile represents a sample age of* 1 *d and the solid profile of* 25 *d, respectively. The vertical lines are positioned at the refractive indices of PEHA, PS and P(EHA-stat-S).*

Indeed, the near-surface composition profile of the aged sample behaves as predicted. This is already indicated by the strong similarity of the XRR data implying similar refractive index profiles. Especially the shoulder at the value of the refractive index of PEHA for low z values is preserved. So, there is a PEHA enrichment layer at the sample surface for both, the freshly prepared and the aged sample. In addition, minor changes occur in the

sub-surface region. The initial region of pure PS is for the aged sample characterized by a lower PS concentration having a maximum value of 65.6 %. A further difference is found for the region around $z \approx 26$ nm: the dominance of PEHA is extended so that for the aged sample there is a layer of almost pure PEHA for 15 nm $< z <$ 35 nm. This behavior follows the already described self-attraction of equal monomers in the sub-surface region.

5.4 Conclusion

The composition profiles perpendicular to the sample surface of statistical copolymer based PSA films are successfully monitored with XRR. At least in the upper 40 nm, the composition is not uniform but exhibits damped oscillatory behavior before a final convergence towards homogeneous bulk composition. This composition of the bulk is characterized by the overall monomer ratio of the copolymer.

Doctor-blading as an almost solvent-free preparation technique leads to a different near-surface composition profile as compared to solution casting. The surface composition of the freshly solution cast samples is mainly driven by a selective transport of material during the drying process. The component with the better solubility with respect to the employed solvent is preferentially transported to the interface to the air. The phase of the compositional oscillation is determined by the type of component at the surface. Moreover, changing the overall composition does not influence the type of monomer forming the top layer.

Despite missing information in XRR experiments with three-component systems, parts of the depth dependent composition can be deduced from the refractive index profiles. It is for example possible to unambiguously identify enrichment layers of the component with either the highest or the lowest refractive index in the system. The copolymerization of a third component is well suited for an additional tuning of the composition profiles.

Furthermore, the molecular weight of the involved statistical copolymer plays an important role. First, the solvent evaporation process and, thus, the involved material transport processes are significantly influenced. Second, the shorter the polymer chains are, the higher the mobility in the system is.

The mobility of the chains is responsible for an internal reorganization process once the solvent has evaporated. As a consequence, the near-surface composition profiles are time-dependent. After a sufficiently long aging time, the component with the lower surface tension enriches at the air-interface, irrespective of the initial composition profile. So, in case the surface is enriched with the component with the lower surface tension for the freshly prepared sample, only minor morphological changes arise.

In the opposite case of initial surface enrichment with the higher surface energy compo-

nent, however, major changes of the near-surface composition profile as a function of time are detected. The higher surface energy material forms a sub-surface layer and the lower surface energy material enriches at the film surface. In total, for this case the near-surface composition of the aged sample is almost inverted as compared to the freshly prepared state.

With the chosen experimental parameters, the mechanical properties obtained in probe tack tests do not change with time. They mostly depend on the overall monomer ratio and, thus, are driven by the bulk composition. However, slight changes are detected when only the comonomer is exchanged. It is very likely that the altered near-surface composition is responsible for this behavior.

In summary, for the first time the complete near-surface composition profiles of statistical copolymer based PSA films are monitored. Different control parameters have been identified to influence the composition close to the surface. Even more influence can be achieved when the sample preparation is performed under controlled atmosphere. Details are elaborated in the following chapter.

Chapter 6

Tailoring the interfacial properties of P(EHA-stat-20MMA)

The mechanical properties of the PSA films, which have been described so far in this work, entirely result from the material properties in combination with the chosen preparation method solution casting. For special applications, however, it is desirable to tune the tackiness of a given adhesive without the necessity to exchange the underlying material. For this purpose, different approaches can be found in literature.

One possibility is to apply a certain external stimulus. The nature of such stimuli can be very different. It has been reported that adhesive films respond to temperature [164, 165], exposure to light [166], presence of water [167] or water vapor [168, 169] and the application of an electric field [170]. But the adhesive can also be designed in a way that its performance depends on the type of mechanical stimulus. By using aligned carbon nanotubes, for example, it can be achieved that the normal adhesion force is much weaker than the shear adhesion force [171, 172]. Furthermore, adhesives can also be kinetically switchable as it has been shown by Feng and coworkers in the context of transfer printing [173]. The authors demonstrated that the relative velocity of the film with respect to the stamp determines whether the film is picked up or deposited on a substrate.

In this work, the focus is on strategies that include morphological changes of the adhesive. The altered molecular arrangement is then supposed to induce different in tackinesses. For certain types of adhesives, similar ideas have already been realized, mostly by varying the temperature. For example, the strong influence of the side-chain orientation on the tackiness of liquid crystalline polymers and their easy orientational tunability within a narrow temperature range has turned out to be very effective in modifying the adhesive performance [174, 175]. Another possibility is the use of semicrystalline polymers. Annealing the material above the melting temperature of the crystals results in a significant change in shear resistance and peel strength [176].

For statistical copolymer melt based PSAs, such approaches are new. The stimulus which is investigated in this work, is the interaction of the PSA film with the surrounding atmosphere. The atmosphere either consists of solvent vapor or of air with well-defined relative humidity (RH). With this procedure, the material is neither destroyed nor changed upon any chemical reaction.

Selective solvents, for example, have been successfully employed for the case of switchable polymer brushes. It is reported that the adhesion can be altered by switching the properties of the adherent, which was a polystyrene/poly(2-vinylpyridine) brush [177]. The adhesive itself was not changed. Inverse to that, there are also brushes that can be switched from a sticky to a nonsticky state [178, 179].

For the RH as a controll parameter, there are promising studies concerning non-tacky polymers. By selecting the appropriate RH, for example, it is possible to tune the morphology in phase separating systems [180]. With this concept, the order-disorder transition was affected in block copolymer electrolytes [181] and the demixing of polymer blends on prepatterned substrates was controlled [182].

This chapter begins with the investigation of the influence of the RH on the near-surface composition of solution cast P(EHA-stat-20MMA). The resulting surface tensions and tackinesses are discussed based on the knowledge of the spatial distribution of the components. The second part is dedicated to the impact of different solvents on the resulting composition profiles. In this context, the solvent for the underlying solution is varied as well as the films are either exposed to solvent vapor or humid air. Like this, it is possible to attract either the sticky or the glassy component to the surface.

Results of this chapter have been published in references [183] and [184].

6.1 Exposure to controlled humid environment

In order to be able to influence the near-surface composition profiles of solution cast PSAs on purpose, it is inevitable to provide a controlled environment during the drying process. That is why the samples, which are described within this chapter, are entirely prepared in a desiccator as described in section 3.3.3. In contrast to the preparation under ambient conditions, the closed sample chamber (desiccator) prevents an exchange of gas with the surrounding air of the laboratory.

The composition profiles are very sensitive to the solvent evaporation rate, which is strongly connected with the accessible volume for the evaporating solvent. Therefore, the type of solvent, the temperature as well as the size and shape of the desiccator are decisive parameters which are kept constant. For a better comparison of the results, P(EHA-stat-20MMA) is exclusively selected as PSA model system. For the investigation

of the impact of the relative humidity (RH), toluene is chosen as solvent.

There are several reasons for the choice of P(EHA-stat-20MMA). First, EHA/MMA containing statistical copolymers are prominent PSA model systems and the composition of 80 % EHA and 20 % MMA is close to the mechanically optimized ratio (see section 5.1.3). Second, the polarities of the related homopolymers PEHA and PMMA are 0.026 and 0.357, respectively [185, 186]. Both values represent the ratio of the polar component of the surface tension to the total surface tension. As a consequence, the contrast in polarity between the relatively polar PMMA and the practically unpolar PEHA is well suited to be used for attraction mechanisms involving the polarity. The third reason is the excellent contrast of the two components in their refractive indices (see table 3.1), which enables a reliable determination of the near-surface composition profiles with x-ray reflectivity (XRR).

In order to isolate the effect of the relative humidity (RH), the sample preparation has been performed in two steps. In step 1, the casting is performed under dry (RH < 2 %) conditions realized by filling the desiccator with silica gel. After a drying time of 24 h at such low RH, a well-defined and reproducible near-surface distribution of components is obtained. The corresponding composition profile after step 1 has already been presented in figure 3.13.

In the second step, the dried sample is taken from the first desiccator and placed into a second desiccator containing air with a well-defined RH provided by saturated salt solutions. This second desiccator is already prealigned in order to keep the exposure to ambient air and, thus, less controlled conditions as short as possible. In general, the lids of the desiccators are closed immediately after casting the solution (step 1) or placing the sample (step 2). The sample is stored for another 24 h in the second desiccator resulting again in a well-defined and reproducible near-surface structure.

In total, the influence of six different RHs is investigated. Five of them are realized by the described procedure using the salts listed in table 3.5. The sixth RH is represented by dry conditions. The corresponding sample does not leave the desiccator after step 1 but is stored for the entire 48 h in the first desiccator. The subsequent XRR, contact angle and probe tack measurements are performed directly after step 2, i. e. 48 h after the coating step.

In summary, the presented preparation procedure ensures that the observed near-surface composition profiles exclusively depend on the installed RH. The isolation of the influence of the RH would not be realizable if the solution was deposited directly under humid conditions. In that case, two effects would be present at the same time: a certain interface selectivity due to the polar water molecules in the surrounding atmosphere would occur and, following from the constant desiccator volume, the solvent evaporation rate would be

reduced due to the presence of the water molecules. Both phenomena would influence the distribution of monomers near the PSA surface and their individual contributions could not be separated.

6.1.1 Humidity dependent composition profiles

The fitted XRR data of the six samples composing the RH series are depicted in the left panel of figure 6.1. With increasing RH, an increased intensity of the modulations at low q_z values with respect to the background level is obtained. This is indicative for an increased amplitude of the variations of the refractive index in the near-surface region. As a consequence, larger compositional heterogeneities are to be expected for the higher RHs.

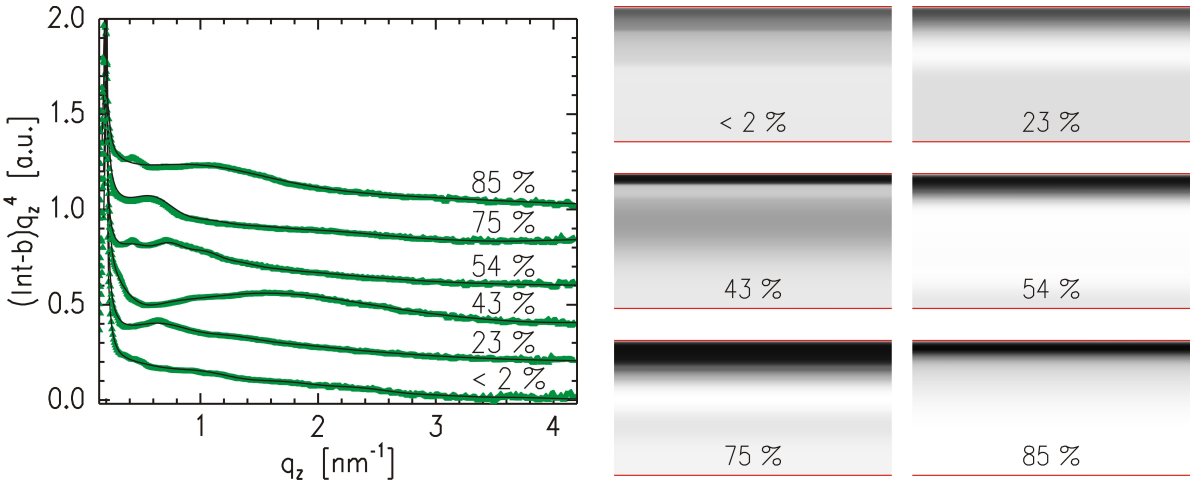

Figure 6.1: *Left: XRR data (symbols) and the corresponding fits (lines) of a humidity series of P(EHA-stat-20MMA) films. The individual RHs are indicated by the corresponding label of each curve. The data are shifted along the intensity axis for clarity. Right: Respective grayscale-coded composition profiles to the shown fits. Each profile represents the near-surface region covering the range* $0 < z < 20$ *nm. The grayscale code is defined in figure 3.3.*

The corresponding grayscale-coded composition profiles (see right panel of figure 6.1) confirm this observation. Close to the surface, a prominent PMMA enrichment is detected for all samples. The corresponding concentration increases as a function of RH as can be deduced from the darker color close to the surface for the higher RHs. Except for a RH of 85 %, also the thickness of the PMMA-rich top layer increases with increasing RH. Closely related to the PMMA enrichment layers are the PEHA enriched zones in the sub-surface region that are also more intense for large humidities.
Interestingly, comparing the PMMA surface enrichment of the sample prepared under dry conditions (48 h) with that obtained after step 1 (24 h), slight differences arise. Whereas

after step 1 the maximum PMMA concentration is not higher than 50.8 % (see section 3.3.3), it is 63.7 % after step 2. The reason for this increase can be found in a fraction of toluene which has not yet been evaporated after 24 h.

Although a very small amount of residual solvent is not detectable (see section 5.1.1), it might still be present after 24 h regarding the slower evaporation in the desiccator. Such residual solvent after step 1 explains the increased PMMA content at the surface after 48 h. Solvent that was situated deeper in the film after 24 h is still capable of transporting an additional small amount of PMMA to the surface explaining the change from step 1 to step 2.

It is not likely that this additional PMMA enrichment is a result of the tendency of the polymer material to reorganize towards an equilibrium structure. The reason is that without the presence of an additional stimulus and especially in a dry, unpolar environment, PEHA should enrich at the surface due to the minimization of the surface energy as it has been shown in section 5.3. An investigation of the internal reorganization process after step 1 upon storage under ambient conditions is provided in the next chapter.

In contrast to the increase in PMMA concentration from step 1 to step 2, the increase in PMMA concentration as a function of RH for the 48 h old samples cannot by explained via the residual solvent. This is because the residual solvent would even evaporate more slowly upon the presence of water vapor. All samples are of equal age and, thus, a slower residual solvent evaporation implies a lower total amount of evaporated solvent. As a further consequence, with increasing RH less PMMA can be transported to the surface and, hence, the PMMA concentration should even be lower for higher RHs, which is not the case. This argumentation is consistent with a study of Gu and Alexandridis reporting that the drying rate decreases with increasing RH [187].

The explanation for the surface PMMA concentration increase as a function of RH must be based on the increased presence of the polar water vapor molecules surrounding the sample. Under such conditions, it is more favorable for the surface of the P(EHA-stat-20MMA) films to be enriched with the more polar PMMA. The more water vapor molecules there are in the desiccator and, hence, in the vicinity of the sample, the more PMMA can be attracted to the surface. Under constant temperature (which is the case), the amount of water vapor increases monotonically with the RH explaining the observed RH dependence of the surface PMMA enrichment.

In order to relate the observed near-surface composition profiles to the measured surface tensions and tackinesses, it is necessary to quantify the enrichment of one component. In section 5.1.2, the usefulness of the averaged minority component content within a certain near-surface region has been demonstrated. Within the approach to tailor the mechanical properties via the near-surface composition profiles it is important to analyze the average

PMMA content over near-surface regions of different thickness. For this purpose, the mean PMMA concentration κ_{PMMA} in the region between the sample surface ($z = 0$) and a certain depth $z > 0$ is calculated via

$$\kappa_{\mathrm{PMMA}}(z) = \frac{1}{z} \int_0^z c_{\mathrm{PMMA}}(\tilde{z})\, \mathrm{d}\tilde{z}. \tag{6.1}$$

$c_{\mathrm{PMMA}}(z)$ is calculated from the corresponding refractive index profile for each z using equation 3.1.

Figure 6.2 exemplarily shows the integrated near-surface PMMA content for selected depths $z = 2$, 4, 15, 50 and 100 nm. The plot confirms what has already been indicated by the grayscale-coded composition profiles. Considering only a narrow region with $z = 2$ nm, a monotonic increase of the corresponding PMMA concentration from 55 % for dry conditions up to 85 % for a RH of 75 % is obtained. For RHs higher than 75 %, no further near-surface PMMA adsorption is detected. The clear trend, which is observed for $z = 2$ nm, is less pronounced for larger z values. When finally $z \geq 50$ nm is selected, the average PMMA content is even constant as a function of RH.

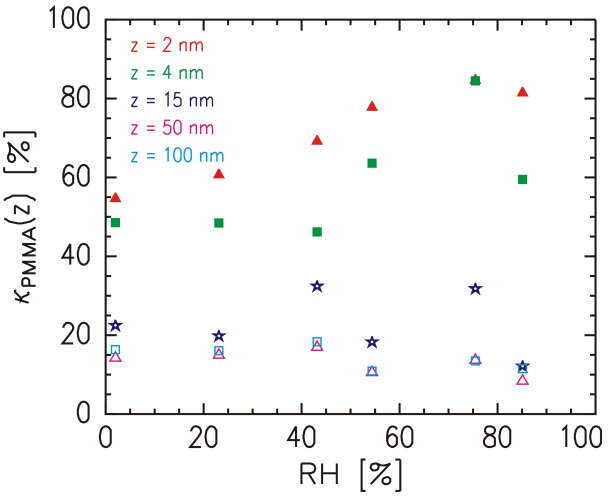

Figure 6.2: *Mean PMMA content in the near-surface region ranging from the sample surface to different depths z. From top to bottom the thickness of the integration region increases as shown by the labels.*

The symbol size in figure 6.2 is chosen so that it equals the error of $\kappa_{\mathrm{PMMA}}(z)$, which is approximately 3 %. The error is estimated by varying the refractive index profile corresponding to the best fit of the respective XRR curve. A fit is considered to be acceptable as long as it does not exceed the symbols chosen for plotting the XRR data.

6.1.2 Humidity dependent surface tension

In order to investigate whether the installed RH dependent composition profiles are capable to alter the mechanical properties of the P(EHA-stat-20MMA) films, the corresponding surface tensions are measured. For this purpose, contact angle measurements,

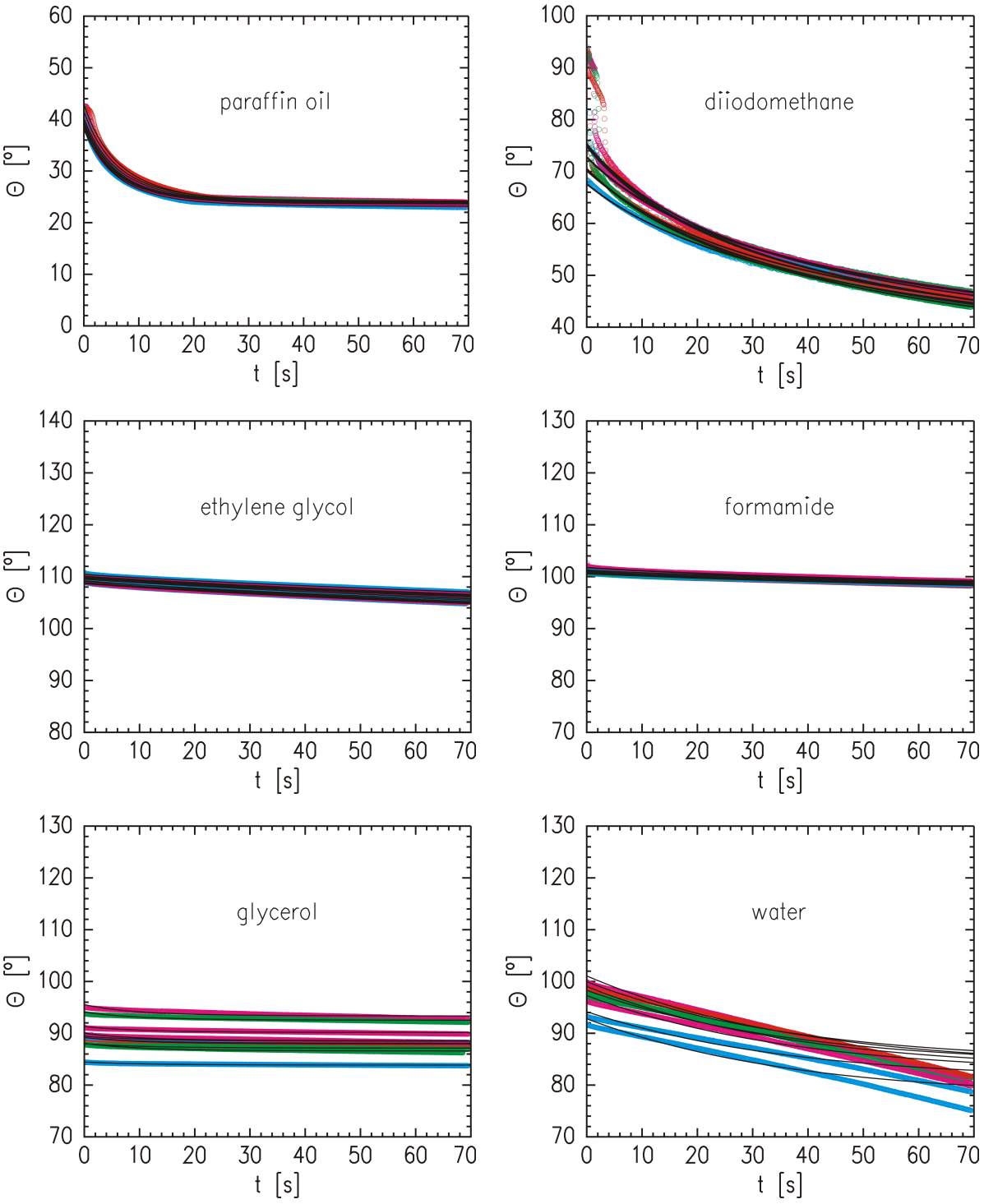

Figure 6.3: *Time dependent contact angles of droplets of the test liquids paraffin oil, diiodomethane, ethylene glycol, formamide, glycerol and water on a P(EHA-stat-20MMA) film prepared under dry conditions. Measured data are represented by colored symbols and the solid lines are the corresponding fits.*

as it has been described in section 3.2.6, are carried out for all six samples composing the humidity series.

The corresponding data are exemplarily shown for the film being completely prepared under dry conditions in figure 6.3. For a more straightforward presentation, the plots of the contact angle data corresponding to the other five samples are shifted to the appendix A.3. The data are fitted using equation 3.5. The extracted equilibrium contact angles Θ_f for all six samples are listed in table 6.1. From top to bottom, the polarity of the test liquids increases.

As a result, the fitted equilibrium angles cover a range from 22° to approximately 90°. With increasing polarity of the test liquid, also the corresponding contact angle increases within the achieved experimental accuracy. As a consequence, an improved wetting of P(EHA-stat-20MMA) is obtained the lower the polarity of the liquid is. This is a first indication that the overall PSA polarity, that is probed by the liquid droplets, is rather low. Furthermore, the experimental errors are significantly lower for the less polar liquids. However, from a comparison of the contact angles corresponding to one fixed test liquid with respect to the samples prepared under different RH conditions, no clear trend is visible. The respective values are very similar.

test liquid	RH < 2 %	RH = 23 %	RH = 43 %
paraffin oil	$(23.7 \pm 0.4)°$	$(23.4 \pm 0.5)°$	$(22.3 \pm 0.3)°$
diiodomethane	$(41.4 \pm 1.0)°$	$(42.5 \pm 0.6)°$	$(48.0 \pm 0.8)°$
ethylene glycol	$(55.8 \pm 1.3)°$	$(59.7 \pm 0.9)°$	$(59.3 \pm 2.1)°$
formamide	$(74.9 \pm 0.6)°$	$(72.1 \pm 1.8)°$	$(72.3 \pm 2.3)°$
glycerol	$(88.4 \pm 2.6)°$	$(85.5 \pm 5.5)°$	$(82.0 \pm 5.7)°$
water	$(82.5 \pm 2.3)°$	$(88.4 \pm 7.4)°$	$(92.0 \pm 6.0)°$
	RH = 54 %	RH = 75 %	RH = 85 %
paraffin oil	$(22.7 \pm 0.2)°$	$(24.1 \pm 0.4)°$	$(22.3 \pm 0.2)°$
diiodomethane	$(47.8 \pm 1.0)°$	$(41.6 \pm 0.8)°$	$(42.7 \pm 0.7)°$
ethylene glycol	$(56.3 \pm 1.3)°$	$(55.5 \pm 2.2)°$	$(57.0 \pm 0.5)°$
formamide	$(73.4 \pm 1.7)°$	$(74.7 \pm 1.0)°$	$(77.5 \pm 4.5)°$
glycerol	$(81.3 \pm 7.4)°$	$(82.2 \pm 5.0)°$	$(86.3 \pm 3.6)°$
water	$(97.6 \pm 1.2)°$	$(84.1 \pm 3.4)°$	$(85.1 \pm 3.5)°$

Table 6.1: *Fitted equilibrium contact angles of the six test liquids corresponding to the samples composing the humidity series of P(EHA-stat-20MMA).*

For the case of ethylene glycol and formamide, the equilibration times are comparably long. Therefore, the selected time window in figure 6.3 is not sufficiently large to be able

to obtain the approach towards Θ_f. Furthermore, due to the chosen range of the axes, it appears as if the shape of the data would not coincide with the exponential decay towards an equilibrium value as modeled with equation 3.5. On a first glance, the curves rather seem to obey linear functions.
In order to rule out such different behavior it is necessary to conduct test measurements covering a larger time interval. At least the ethylene glycol droplets are sufficiently stable that accordingly longer measurements are possible. In this context, six test measurements are performed using ethylene glycol droplets on a P(EHA-stat-20MMA) film prepared under dry conditions. The contact angle as a function of time is monitored for approximately 100 min.

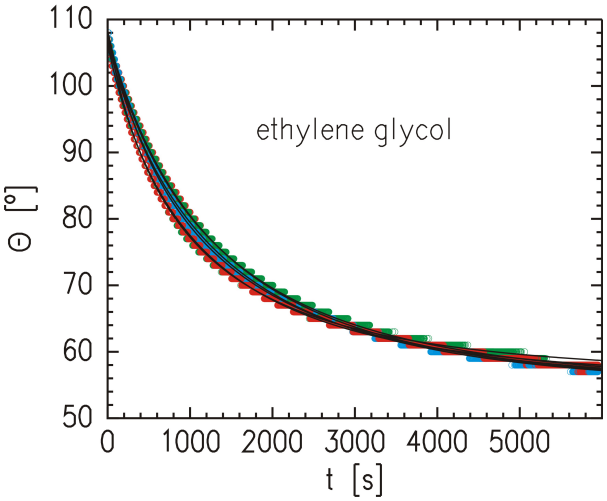

Figure 6.4: *Long-time measurement of the contact angle of ethylene glycol droplets on a P(EHA-stat-20MMA) film prepared under ambient conditions. Colored symbols represent measured data points and the fits are plotted as solid lines.*

The data of the long-time ethylene glycol measurement are shown in figure 6.4. The measured curves appear rather step-like originating from the extremely slow change of the contact angle. Within the time represented by such a step, a constant contact angle is detected. Nevertheless, with such a long measurement time the expected exponential decay becomes evident justifying the application of the fit function 3.5 also to the formamide and ethylene glycol droplets. Fitting the measured data leads to an equilibrium angle of $\Theta_f = (55.1 \pm 0.7)°$, which matches the value obtained from the 70 s measurements. The good agreement is also a proof that it is sufficient to perform such short measurements in order to obtain the equilibrium angle.
With the method of Owens and Wendt (see section 2.1.4), both, the dispersive and polar contribution of the surface tension of all six samples composing the humidity series can be extracted. The corresponding six Owens-Wendt plots are depicted in figure 6.5 using the nomenclature of equation 2.27. The solid line is a linear fit to the Θ_f-dependent data points which enter the plot according to equation 2.27.
For the calculation of the error bars in direction of the ordinate within the Owens-Wendt

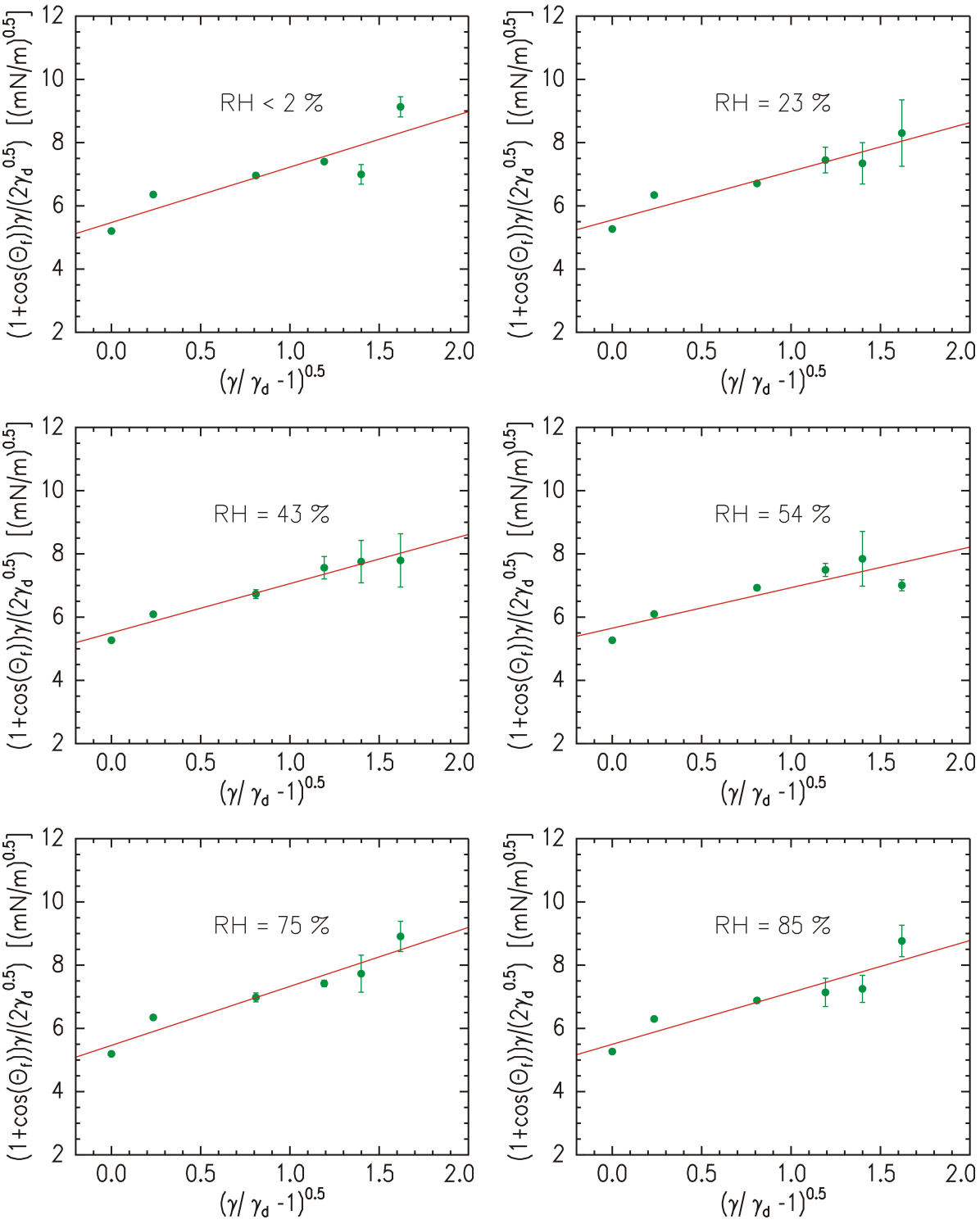

Figure 6.5: *Owens-Wendt plots corresponding to the six P(EHA-stat-20MMA) films composing the humidity series. The RH increases in reading direction.*

plots, the standard equation of the propagation of uncertainty is used. The ordinate is determined via

$$y_{OW} = \frac{(1+\cos(\Theta_f))\,\gamma}{2\sqrt{\gamma_d}}. \tag{6.2}$$

Therefore, the corresponding error follows as

$$\Delta y_{OW} = |\Delta\Theta_f| \left|\frac{\partial y_{OW}}{\partial \Theta_f}\right| = |\Delta\Theta_f|\,|\sin(\Theta_f)|\,\frac{\gamma}{2\sqrt{\gamma_d}}, \tag{6.3}$$

where Θ_f is the mean value and $|\Delta\Theta_f|$ the experimental error of the equilibrium contact angle.

In summary, the resulting Owens-Wendt plots are very similar. This is also reflected in the extracted values of the polar and dispersive contribution of the surface tension. The corresponding values are plotted in figure 6.6 as a function of the RH. As a result, within the achieved experimental accuracy both surface tension contributions and, hence, the total surface tension are independent of the RH. The respective mean values averaged over all six measurements of the humidity series are γ_p(P(EHA-stat-20MMA)) = (2.6 ± 0.6) mN/m, γ_d(P(EHA-stat-20MMA)) = (30.5 ± 0.8) mN/m and γ(P(EHA-stat-20MMA)) = (33.1 ± 0.3) mN/m. So, the surface tension of P(EHA-stat-20MMA) is in between those of the involved components PEHA and PMMA. However, it cannot be calculated by weighting the surface tensions of the constituents according to their composition ratio.

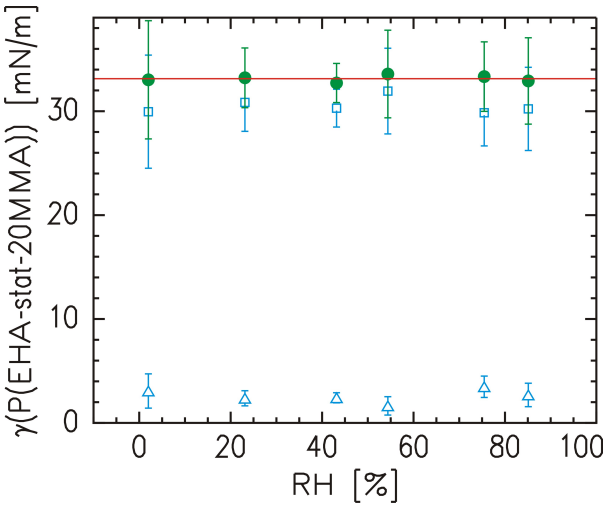

Figure 6.6: *Polar (open triangles) and dispersive (open squares) components of the total surface tension (filled circles) of P(EHA-stat-20MMA) films as a function of the RH. The horizontal line is positioned at the mean value of the total surface tension.*

Nevertheless, the obtained constancy of the surface tension can be related to the near-surface composition profiles presented in section 6.1.1. Although PMMA is significantly enriched at the sample surface, the thickness of the corresponding layer is thinner than the radius of gyration of the copolymer (see section 5.1.1). In contrast, the surface tension is determined by the interactions of the droplets with the complete near-surface region

up to a certain depth. As it has been shown in figure 6.2, the correlation of the average PMMA content with the RH is already very weak for an integration region of $z = 15$ nm and it is completely lost for $z \geq 50$ nm.
As a consequence, the sensitivity of the contact angle measurements with respect to the very weak integrated compositional variations (especially for $z \geq 15$ nm) is too small that an impact on the surface tension could be resolved. If there actually was a RH dependent variation in surface tension, it would anyhow not exceed the obtained error bars and would, thus, be very small.
Similar observations supporting these findings have already been reported in literature. For example, Staeger and coworkers produced poly(styrene-b-butadiene-b-styrene) triblock copolymer films with different copolymer formulations and investigated the influence of UV light exposure on the nanomechanical properties [188]. The authors obtained a strong variation of the surface stiffness and the adhesive properties. The surface tension determined via contact angle measurements, however, remained constant. In accordance with the study of Staeger, changing the acrylic acid content of P(EHA-co-acrylic acid) elastomers did not result in a change of the surface tension of the material, too [189]. It is very likely that the variations of the respective controll parameters in both studies had also an impact on the near-surface composition, which was just not in the scope of the respective publications.

6.1.3 Humidity dependent tackiness

From an application point of view, it is even more interesting to measure the tackiness of the PSAs of the humidity series rather than the surface tension. However, the observation of the constant surface tension as a function of the RH is important for the interpretation of the data measured in the probe tack tests. The reason is that, due to the Young-Dupré equation 2.22, the constant surface tension implies a constant thermodynamic work of adhesion as a function of RH for a given punch material.
Probe tack tests have been performed for all six P(EHA-stat-20MMA) samples composing the humidity series. A highly polished punch fabricated out of stainless steel is used for this investigation. A detailed characterization of the punch surface is given in section 3.2.8. In order to optimize the surface sensitivity of the tack experiments, a contact force of only 1 N is selected. Together with the comparably large punch diameter of 2 mm, the nominal contact pressure is reduced to 0.32 MPa. Please note that the contact pressure for the samples prepared under ambient conditions was 12 times higher emphasizing the improved sensitivity.
Figure 6.7 shows all tack data for the six samples of the humidity series. The RH increases in reading direction. Each single curve represents one sampling point corresponding to

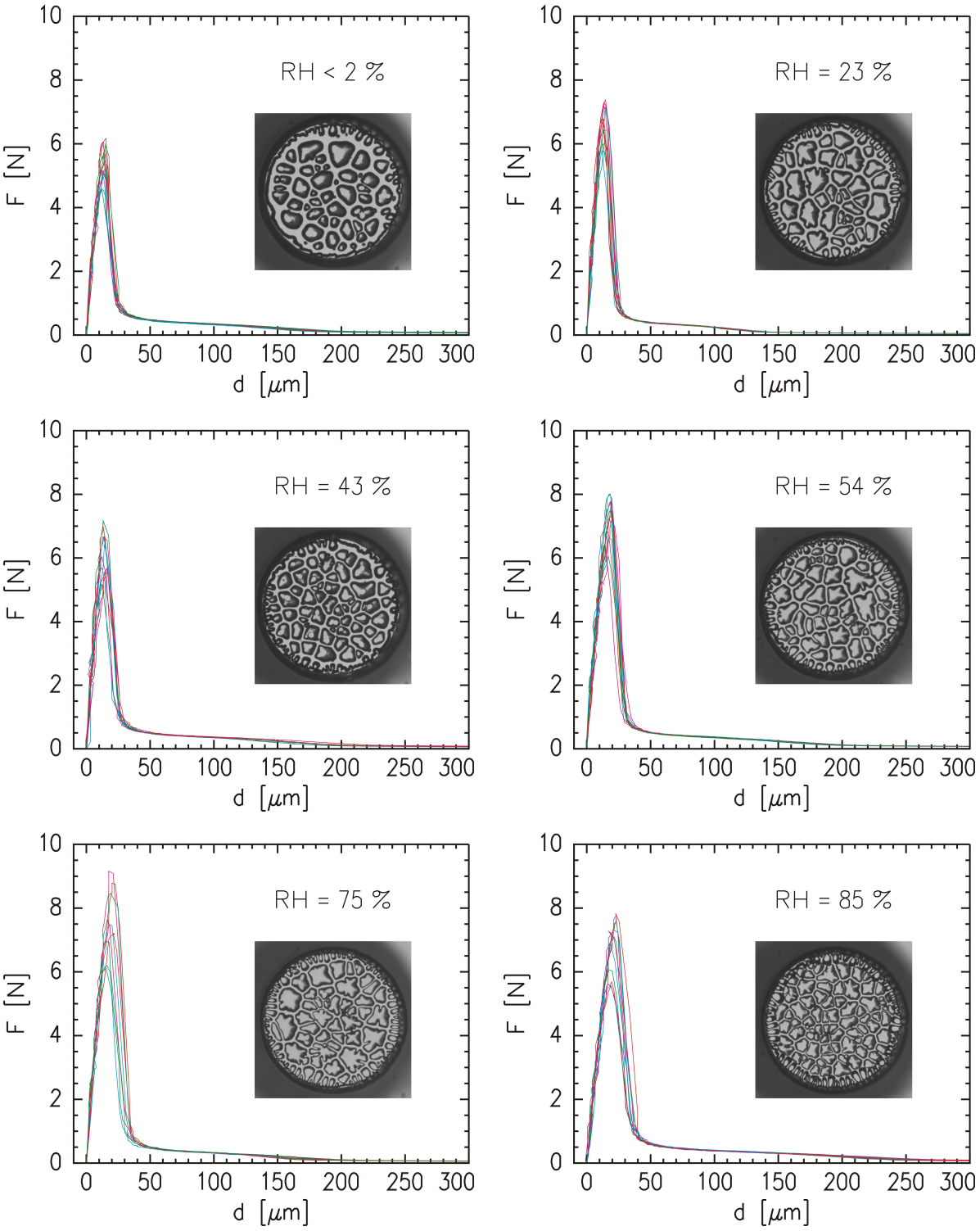

Figure 6.7: *Force-distance curves obtained for the P(EHA-stat-20MMA) films composing the humidity series. The insets are representative images of the punch area at the time when all cavities have evolved.*

one RH. All curves exhibit the typical shape of a non-crosslinked PSA as introduced in section 2.1.6 and as already described in the previous chapter for the samples prepared under ambient conditions. As a consequence, the shape of the force-distance curve is not altered qualitatively upon the change in experimental parameters.
Representative microscope images of the punch area, which are the insets in the individual plots in figure 6.7, exhibit a clear RH dependence. The images are snapshots of the cavitation process at a point during stage III of the four-stage model of a probe tack experiment (see section 2.1.6). All images are taken at the moment when the maximum number of cavities has been reached. As a result, the total number of cavities increases with increasing RH.
The tack energy and the force maximum are extracted out of the measured data for all six samples. These parameters are plotted as a function of the RH in figure 6.8. As a result, both, the force maximum and the tack energy increase with increasing RH. For the tack energy the biggest step occurs between a RH of 23 % and 54 %. In total, the tack energy covers a range between (143.1 ± 11.0) μJ and (222.7 ± 21.4) μJ. This means, that despite the unchanged bulk material, the tack energy can be increased by a factor of approximately 1.6 upon the exposure to humid air. Due to the corresponding larger error bars, such details cannot be derived for the force maximum. But anyhow, the force maxima measured for the samples prepared at RHs larger than 54 % are significantly higher than those for the lower RHs.

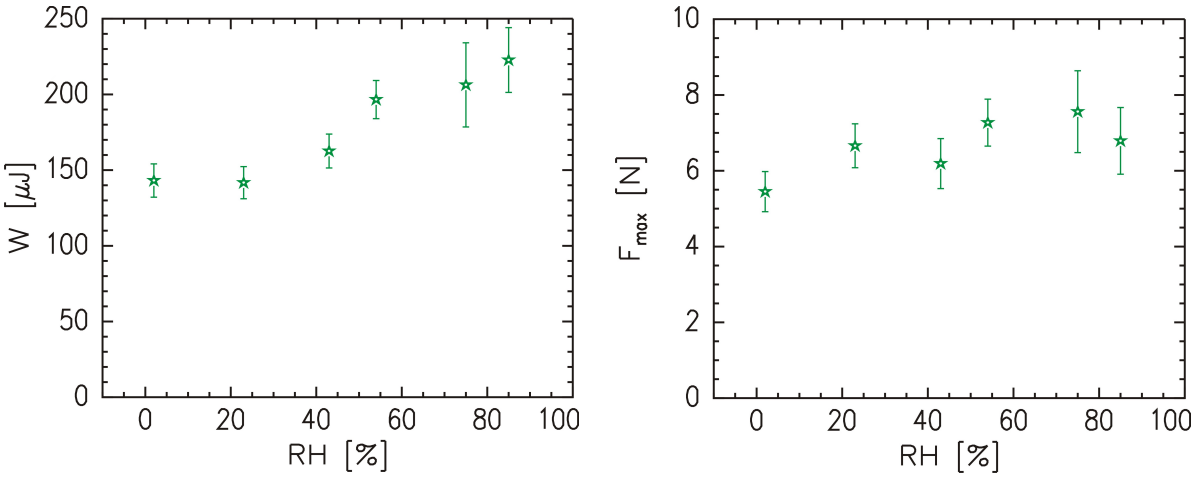

Figure 6.8: *Tack energy (left) and force maximum (right) as a function of RH obtained for the P(EHA-stat-20MMA) films composing the humidity series.*

The obtained humidity dependence of the tackiness is solely a consequence of the altered near-surface mechanical properties related to the installed composition profiles because of two circumstances. First, the selected preparation protocol ensures equal bulk material of

all six samples. And second, as already mentioned, the thermodynamic work of adhesion is constant as a function of the RH.

In this context, for an EHA based random copolymer Lakrout and coworkers found an almost linear relation between the shear storage modulus and the maximum stress emphasizing the close connection between the mechanical properties and the resulting adhesive performance [40]. A direct comparison to the findings of Lakrout, however, remains difficult because in the presented study the bulk rheological properties are not affected by the installed differences in near-surface composition.

The explanation to the observed behavior must rather be related to the observed cavitation process. This is because the cavities predominantly appear in a region close to the punch (see section 2.1.6) and, thus, in that region which is mostly affected by the change in the RH. Therefore, the medium in which the cavities are created and then elongated changes within the humidity series.

The influence on the cavitation process becomes evident from the increasing number of cavities with increasing RH. For the higher RHs, a higher fraction of the less mobile and stiffer component PMMA is located close to the PSA-punch interface. The reduced mobility in the near-surface material restricts the growth of the cavities. As a consequence, the merging of two appearing cavities is less likely for the cases of higher PMMA concentration implying a higher total number of cavities with a smaller area. Indeed, figure 6.7 proves the described dependence of the number of cavities on the RH and, thus, the near-surface PMMA concentration. These findings are consistent with the work by Lakrout and coworkers who carried out probe tack experiments and compared the maximum average area of a cavity in pure PEHA films to the corresponding area in P(EHA-stat-AA) [40].

However, a complete theoretical description is not possible because existing theories do not distinguish between bulk and near-surface material. Nevertheless, the approach to attribute the existence of cavities to interfacial defects arising from the different roughness length scales of the punch compared to the PSA surface (see section 2.1.6) is very promising.

In the underlying work of Gay and Leibler [37], it is claimed that the true contact area of the punch with the PSA becomes smaller with increasing rigidity of the surface because the contact area is more restricted to the summits of the rough surfaces. The XRR measurements show that the PSA surface roughness does not change as a function of RH. Moreover, with increasing RH an increased content of the more rigid component PMMA is found at the surface. From the results by Gay and Leibler, it can therefore be concluded that, due to the constant nominal contact force of 1 N, the effective contact pressure increases as a function of RH. As a further consequence, the tack energy and the

force maximum increase, too.
The trend that a higher tack energy is to be expected for a higher RH and, thus, a higher near-surface PMMA concentration also follows from the theoretical description of the expansion of the cavities in section 2.1.6. According to equation 2.34, the energy necessary to elongate an existing void increases with both, the surface tension and the Young's modulus of the medium in which the cavity is embedded. Both values are higher for PMMA than for PEHA. So, in summary, also the theoretical consideration of cavity growth predicts an improved tackiness for the P(EHA-stat-20MMA) films prepared under higher RHs.

6.2 Variation of the solvent

The preparation protocol, which is elaborated in section 6.1, is very useful to isolate and understand the influence of the RH. Both, toluene as a solvent and the polar environment favor the surface segregation of the more polar PMMA. In the following, routes involving the choice of solvent and the type of atmosphere surrounding the sample are presented to attract either PEHA or PMMA to the surface. From an application point of view, these methods are easier to apply because a change of the sample environment is not involved. The samples are not cast under dry conditions first.

6.2.1 Attraction of PEHA

The attempt to attract the unpolar PEHA towards the sample surface is rather contrary to what is presented in section 6.1. For the solution casting, toluene is replaced by the very unpolar solvents n-hexane or cyclohexane. In addition, the saturated salt solutions producing the well-defined RHs are replaced by 10 mL of the respective solvent leading to a solvent vapor atmosphere. Like this, also the interactions of the sample with the surrounding medium are predominantly dispersive.
A useful side-effect is that, despite the relatively high volatility of the solvents (the boiling points are 69 °C for n-hexane and 81 °C for cyclohexane), the presence of solvent vapor in the desiccator slows down the evaporation process. As a consequence, also for these samples (for XRR) convenient surface roughness values on the order of 0.5 nm are obtained (see section 5.1.1).
The decelerated solvent evaporation is responsible that after only one day, the samples are not fully dried. That is why for the investigation of the influence of the different solvents, the drying time in the solvent-filled desiccators is extended to three days. Depending on the employed solvent, there is still a certain amount of residual solvent as it is proposed in section 6.1.1. The remaining solvent evaporates between the opening of the desiccator

lid and the start of the XRR measurements. Therefore, the interpretation of the XRR data is not affected. Nevertheless, it is important to quantify the amount of remaining solvent in order to understand the obtained near-surface composition profiles.
For this purpose, gravimetric measurements are carried out for each sample of the solvent series. The relative mass loss Δm_r is monitored as a function of time. It is important to note that it is impossible to measure the mass of a sample simultaneously with removing the lid of the desiccator. To solve this problem, all curves are normalized to the mass of the sample exactly 2 min after opening the desiccator $m(2\text{ min})$. From this point on, the mass m of the sample is recorded as a function of time t. The relative mass loss then follows as

$$\Delta m_r(t) = \frac{m(2\text{ min}) - m(t)}{m(2\text{ min}) - m_S}, \tag{6.4}$$

where m_S is the mass of the pristine substrate. The latter was measured before the solution casting. The data obtained for the n-hexane and cyclohexane based preparation protocol are plotted in figure 6.9. Due to the high precision of the employed balance (see section 3.2.5), the error bars are smaller than the selected symbol size.

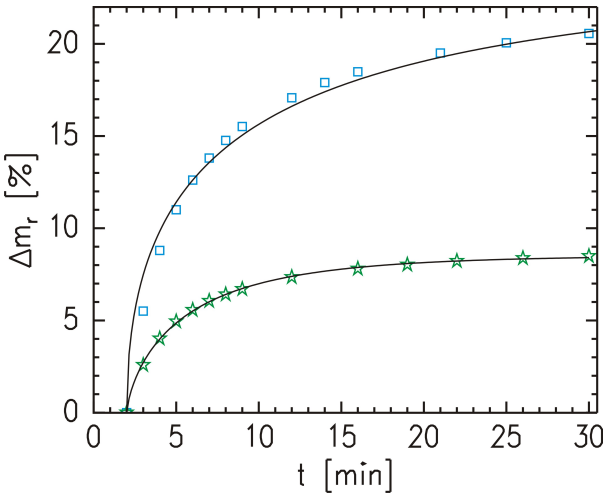

Figure 6.9: *Relative mass loss as a function of time of solution cast P(EHA-stat-20MMA) films under solvent vapor conditions. The underlying solvents are n-hexane (stars) and cyclohexane (squares). The solid lines are the respective fits to the data.*

The shape of the mass loss curves indicates an approach to a limiting value for large times. The limiting value S_r is extracted by fitting an exponentially approaching function to the measured data. For $t \geq 2$ min, the fit function is defined as

$$\Delta m_r(t) = S_r \left(1 - \exp\left[\frac{-(t - 2\text{ min})}{T_r}\right]^{c_r}\right). \tag{6.5}$$

T_r is the time constant of the decay and c_r an additional damping parameter necessary to match the shape of the data. For large times t, the fit function converges to S_r, which can be understood as both, the limiting value of the relative mass loss or the mass fraction of the remaining solvent 2 min after opening the desiccator.

solvent	S_r [%]	c_r	T_r [min]
n-hexane	8.5 ± 0.1	0.7 ± 0.1	3.8 ± 0.1
cyclohexane	24.0 ± 0.2	0.5 ± 0.1	7.2 ± 0.2

Table 6.2: *Fit parameters of the mass loss curves of P(EHA-stat-20MMA) films solution cast under solvent vapor atmosphere.*

The corresponding fitted functions are the solid lines in figure 6.9 and the underlying fit parameters are listed in table 6.2. The errors to the fitted parameters are provided by the fitting routine. As a result, the remaining solvent for the cyclohexane based preparation is significantly higher than for n-hexane. A clear trend for the other two parameters T_r and c_r cannot be extracted.

The low value of c_r for cyclohexane is remarkable. It implies a large damping of the curve. The reason might be that during the gravimetric measurement the sample is in an unsealed, but enclosed volume provided by the precision balance. The volume provided by the balance is approximately 6.2 L. Therefore, the solvent cannot vanish immediately and may cause a decelerated evaporation for high remaining solvent contents. Opening the windows of the balance is, however, not an option because disturbing air flow would prevent the necessary high precision of the obtained values. Anyhow, S_r as the most important parameter is reliably extracted.

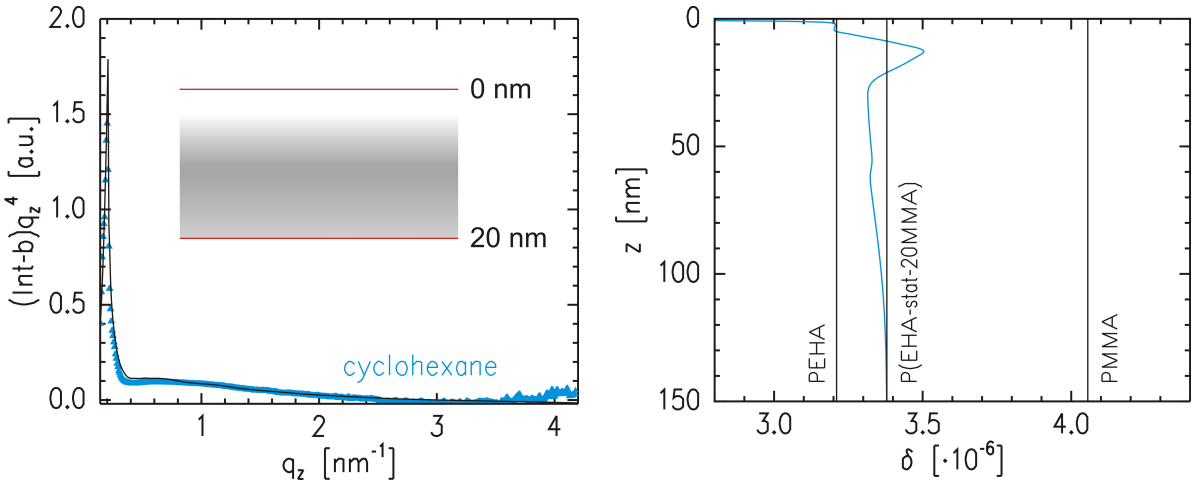

Figure 6.10: *Left: XRR data (symbols) and respective fit (solid line) of a P(EHA-stat-20MMA) film prepared with the cyclohexane based protocol. The inset shows the grayscale-coded (for definition see figure 3.3) composition profile. Right: Refractive index profile corresponding to the fit to the data. The vertical lines are positioned at the refractive indices of PEHA, PMMA and P(EHA-stat-20MMA).*

Starting with the cyclohexane based sample, the corresponding analyzed XRR data are de-

picted in figure 6.10. As expected, a pronounced PEHA enrichment layer with a thickness of 4.5 nm is situated on top of the sample. Similar to all other PSA films, an oscillating composition is obtained in the sub-surface region. This results in a weak PMMA enrichment layer reaching its highest concentration at a depth of 13.8 nm. The homogeneous bulk material is again approached from a broad PEHA dominated region.
Surprisingly, the situation changes when cyclohexane is replaced by the even less polar n-hexane. The corresponding XRR data are shown in figure 6.11. Although the complete near-surface region ($z < 150$ nm) is still dominated by the almost unpolar PEHA, directly at the surface the PEHA concentration is significantly lower than for the cyclohexane based protocol. The corresponding minimal PEHA content for the n-hexane based preparation is 49.1 % and it is obtained at $z = 1.5$ nm.
This behavior can be understood from the lower boiling point of n-hexane. Due to the high tendency of n-hexane to go into the vapor phase, the capability of the solvent to transport PEHA towards the surface is reduced. So, not only the polarity of the surrounding atmosphere and the involved solubility parameters are important for the obtained composition profiles, but also the solvent evaporation rate is decisive. Thus, the interplay of all influencing factors makes the near-surface adsorption processes very complex.

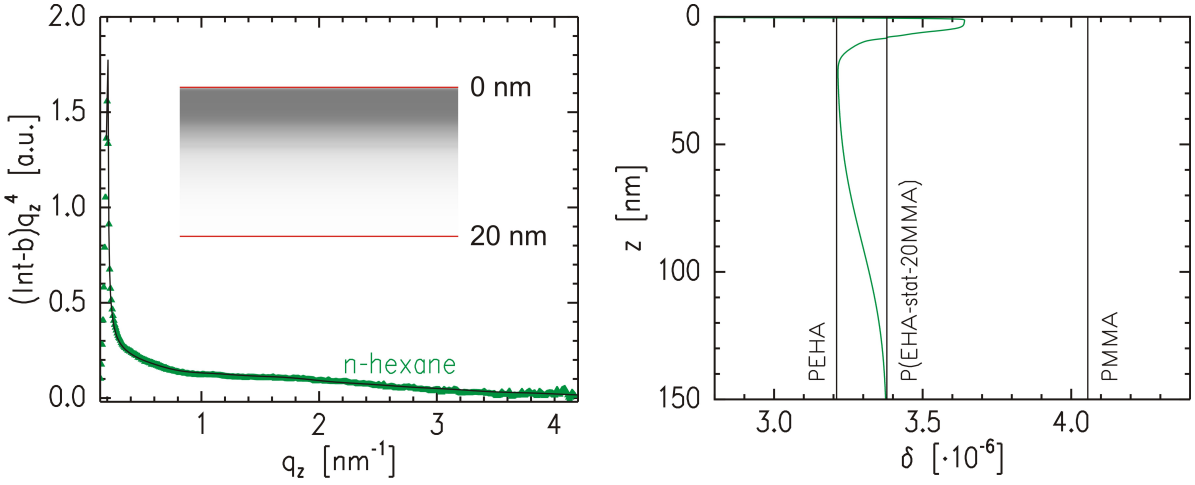

Figure 6.11: *Left: XRR data (symbols) and respective fit (solid line) of a P(EHA-stat-20MMA) film prepared with the n-hexane based protocol. The inset shows the grayscale-coded (for definition see figure 3.3) composition profile. Right: Refractive index profile corresponding to the fit to the data. The vertical lines are positioned at the refractive indices of PEHA, PMMA and P(EHA-stat-20MMA).*

Nevertheless, when the average PEHA content of the complete near-surface region is considered, the corresponding values are as expected. For example, $\kappa_{\mathrm{PEHA}}(100\ \mathrm{nm}) = 92.3$ % for the n-hexane and 82.5 % for the cyclohexane based protocol (for definition see equation 6.1). These integrated PEHA concentrations are in accordance with the lower

polarity of n-hexane as compared to cyclohexane.
In summary, the presented preparation protocol based on non-polar solvents is capable of attracting the sticky component PEHA to the sample surface. However, a precise prediction of the near-surface composition profiles remains difficult. Further fine-tuning of the composition profiles would require the exact controll over the solvent evaporation rate. This might be achievable by using solvent mixtures or adjusting the temperature.

6.2.2 Attraction of PMMA

In order to attract the more polar PMMA to the film surface, the surrounding atmosphere is exchanged towards a more polar environment. The filling of the desiccator (non-polar solvent) is replaced by a saturated sodium chloride solution providing a RH of 75 %. Different solvents are used to dissolve P(EHA-stat-20MMA). The humid atmosphere in the desiccator is not varied. With increasing porlarity, the addressed solvents are n-hexane, cyclohexane, toluene and dichloromethane.
For the unpolar liquids, it is interesting to investigate the competition between the PEHA favoring solvent evaporation and the PMMA favoring (see section 6.1.1) polar atmosphere. The more polar solvents together with the water vapor are supposed to strongly attract PMMA. However, as it has been shown in section 6.2.1, the amount of remaining solvent after the one-step preparation has to be taken into account. For this purpose, gravimetric measurements are carried out for all four samples. The corresponding data are shown in figure 6.12.

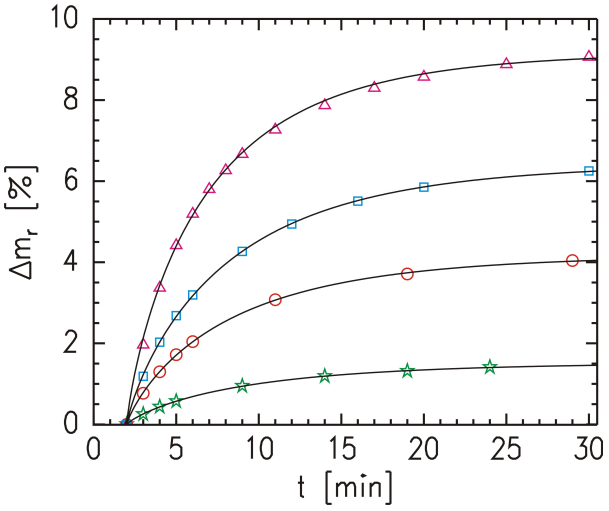

Figure 6.12: *Relative mass loss as a function of time of solution cast P(EHA-stat-20MMA) films under humid air. The underlying solvents are n-hexane (stars), dichloromethane (circles), cyclohexane (squares) and toluene (triangles). The error bars are smaller than the symbol size. The solid lines are the respective fits to the data.*

As it is described in section 6.2.1, the data are fitted using equation 6.5 in order to obtain the remaining solvent content after opening the desiccator S_r. The extracted parameters corresponding to the four different liquids are listed in table 6.3. The errors to the fitted

parameters are provided by the fitting routine.
Comparing the evaporation behavior of n-hexane and cyclohexane to that obtained for the solvent vapor based protocol, significantly less solvent remains for the case of a humid drying environment. The corresponding values of S_r differ at least by a factor of 3. It can be concluded that the humid environment is less effective in reducing the evaporation rate than the solvent vapor. Moreover, the constant and relatively high value of c_r indicate that the damping of the solvent evaporation arising from the experimental setup plays only a minor role for such low remaining solvent contents.

solvent	ϑ_b [°C]	ε	S_r [%]	c_r	T_r [min]
n-hexane	69	1.9	1.5 ± 0.1	0.8 ± 0.1	7.3 ± 0.2
dichloromethane	40	8.9	4.2 ± 0.1	0.8 ± 0.1	6.4 ± 0.1
cyclohexane	81	2.0	6.4 ± 0.1	0.8 ± 0.1	6.3 ± 0.1
toluene	111	2.4	9.2 ± 0.2	0.8 ± 0.1	5.0 ± 0.1

Table 6.3: *Fit parameters of the mass loss curves of P(EHA-stat-20MMA) films solution cast in humid environment. In addition, the respective dielectric constants ε as a measure for the polarity and the boiling points ϑ_b are provided for each test liquid.*

The values of S_r and T_r are neither monotonic functions of the polarity (see dielectric constant) nor of the boiling point. As a consequence, the presence of the polymer influences both, the amount and the evaporation rate of the remaining solvent. A suitable measure for the polymer-solvent interactions are the respective solubility parameters $\mathfrak{D}$ (see section 2.1.1). In figure 6.13, S_r and T_r are plotted as a function of the difference in solubility parameter between the majority component PEHA and the respective solvent. The involved solvent solubility parameters are taken from reference [152].

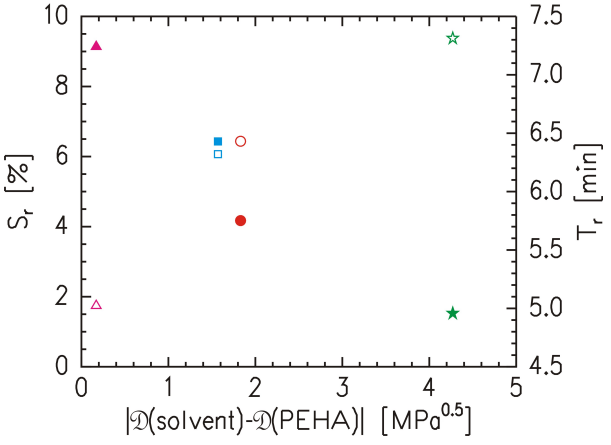

Figure 6.13: *Residual solvent S_r (filled symbols) and time constant T_r (open symbols) as a function of solubility parameter difference. The symbol types match with figure 6.12. The error bars are on the order of the symbol size.*

As a result, S_r decreases and T_r increases almost linearly as a function of difference in solubility parameters $|\mathfrak{D}(\text{solvent}) - \mathfrak{D}(\text{PEHA})|$. So, the better the solubility of the

majority component PEHA with respect to the employed solvent is, the more solvent remains in the sample within the three days in the desiccator. Besides, after removing the lid also a faster evaporation of the residual solvent occurs.
These observations related to the solvent are also reflected in the near-surface distribution of components. The corresponding XRR data together with the grayscale-coded near-surface composition profiles are shown in figure 6.14. For the case of the non-polar solvents n-hexane and cyclohexane, which exhibit small S_r values, the residual solvent effect is less evident. The profiles are dominated by the already mentioned competition between the PEHA and the PMMA favoring phenomena.

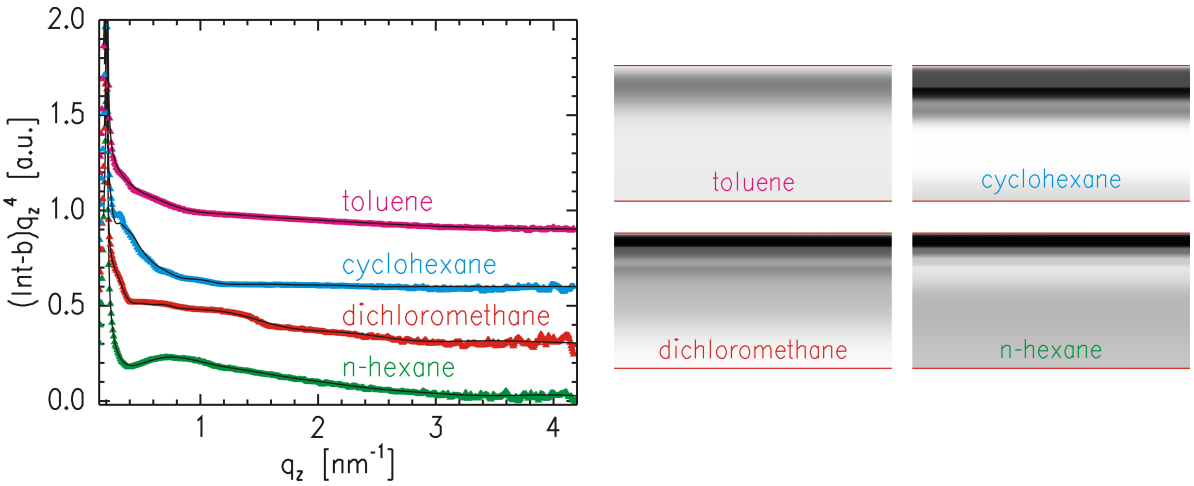

Figure 6.14: *Left: XRR data (symbols) and the corresponding fits (lines) of the solvent series of P(EHA-stat-20MMA) films prepared under humid conditions in a one-step protocol. The individual solvents are indicated by the corresponding label of each curve. The data are shifted along the intensity axis for clarity. Right: Respective grayscale-coded composition profiles to the shown fits. Each profile represents the near-surface region covering the range* $0 < z < 20$ *nm. The grayscale code is defined in figure 3.3.*

For both of these unpolar solvents, the solubility effects are outweighed by the polar interactions with the environment so that a PMMA enrichment is obtained at the surface. A 3.0 nm thick PMMA enriched layer with a concentration of 70.8 % is found at the air-interface for cyclohexane. Underneath, there is a narrow region with even more MMA monomers per unit volume. The respective maximum concentration is 96.2 %. In the case of P(EHA-stat-20MMA) cast from an n-hexane based solution, the maximal concentration (99.3 %) is obtained directly at the sample surface. Before the convergence towards homogeneous bulk material, there is a second, weaker PMMA enriched zone at a depth of $z = 11.5$ nm.
A similar trend has already been observed for the preparation under solvent vapor: for n-hexane there was already a considerable amount of PMMA at the sample surface and

for cyclohexane it was not (see section 6.2.1). The main difference is, that for the humid environment in total much more PMMA is obtained in the near-surface region as compared to the solvent vapor case. It can be concluded, that despite the still visible impact of the non-polar solvents, dominant polar interactions are present. Furthermore, also following from the similarity to the solvent vapor based protocol, the drying speed is still an influencing factor.

A different situation arises for the more polar toluene. Starting from the PSA surface, the PMMA content increases monotonically up to a depth of $z = 3.8$ nm, where the maximum concentration of 70.8 % is found. This is followed by a PEHA enriched zone converging towards homogeneous bulk material. Especially the compositon for small z values is very different from what is known for the preparation under ambient (see section 5.1.1) and dry (see section 6.1.1) conditions, where PMMA formed a pronounced top layer. From a first glance, it is to be expected that the humidity in the atmosphere should even attract more PMMA towards the surface.

The reason for this behavior can be found in the comparably large amount of solvent which is still present when the desiccator is opened after a storage time of three days (see table 6.3). The PMMA transport due to the very slowly evaporating solvent has not yet been completed. Removing the lid of the desiccator enables a comparably quick volatilization of the toluene and the spatial distribution of the polymer chains almost freezes in. It is to be expected that, regarding the uniquely PMMA favoring conditions, a longer storage time in the desiccator should lead to the expected amplification of the PMMA enrichment. This is investigated in a time series and is presented in section 7.2.

Finally, the circumstances for a PMMA enrichment in the dichloromethane based PSA film are ideal: dichloromethane is the most polar of all test liquids and the amount of remaining solvent is so low, that most of the PMMA transport should be finished. And indeed, the surface consists of 100 % PMMA and also a second, weaker PMMA enriched zone is detected in a depth of 5.8 nm. An interesting question is whether, upon storage under ambient air, such intense enrichment layers can withstand the PEHA favoring reorganization process presented in section 5.3. Corresponding time series, starting with the presented state after the dichloromethane and the n-hexane based preparation under humid conditions, are discussed in section 7.1.2.

In summary, the polarity of the chosen solvent is important but it is only dominant for a non-polar environment in combination with a low remaining solvent content. When different external parameters are chosen, then the polarity effects are still visible but they are outweighed by the volatility and solubility of the solvent as well as the type of surrounding atmosphere.

6.3 Conclusion

Regarding the results presented in this chapter, it can be concluded that it is possible to tailor the near-surface composition of a P(EHA-stat-20MMA) film. Although the processes which are involved in the solution casting based PSA film processing methods are very complex, key parameters have been identified which determine the near-surface distribution of the components PEHA and PMMA.

One of them is the relative humidity (RH) or, in other words, the polarity of the surrounding medium. A suitable sample preparation protocol has been developed to isolate the effect of the RH. As a result, the concentration of the more polar component PMMA increases with increasing RH and, thus, with increasing number of water molecules in the atmosphere. Mostly affected by this enrichment are the upper 2 nm of the PSA film.

The effect gets less pronounced when the average PMMA content of thicker near-surface regions is considered. No correlations are obtained when the corresponding integration is performed over more than 50 nm measured from the film surface. Mechanical properties determined with contact angle measurements and probe tack tests can be explained with the observed composition profiles.

The with the method of Owens and Wendt extracted surface tension is constant as a function of RH. This is because the involved interactions between the test liquid droplets and the PSA exceed the range for which a pronounced PMMA enrichment is detected. In contrast, the tack experiments reveal a clear dependence of the adhesive performance on the RH. The tack energy and the force maximum increase (within the error bars) monotonically as a function of RH. An explanation is based on the altered near-surface mechanical properties originating from the RH dependent near-surface composition.

Further tuning of the composition profiles can be achieved by using both, different solvents for the polymer solutions and different types of media surrounding the drying films. The combination of a non-polar solvent with the corresponding solvent vapor atmosphere leads on average to a strong surface enrichment of the less polar PEHA. The exact shape of the composition profiles, however, depends also on the evaporation speed of the solvent.

Non-polar solvent combined with humid atmosphere leads to a preferential adsorption of the more polar PMMA. Although the influence of the solvent is still reflected in the near-surface composition, it is outweighed by the polar interactions. Finally, polar solvents combined with a polar environment lead in principle to a strong PMMA enrichment. However, this is not true for scenarios in which the MMA transport process has not yet been completed originating from a very slow solvent evaporation.

In summary, for an exact tailoring of the complete near-surface composition profiles, there are several key parameters among which are the involved solubilities of the polymer with respect to the solvent, the drying rate, the surrounding atmosphere and the sample age

(see next chapter). These parameters are not independent from each other and there are many ways how to influence them. Future experiments might involve temperature gradients, solvent mixtures, variations of the geometry of the sample environment or different types of gases for the surrounding medium.

Chapter 7

Aging of P(EHA-stat-20MMA)

In section 5.3, it has been shown that the near-surface composition profiles of the studied statistical copolymer films are time-dependent. The minimization of the surface energy as the driving force is responsible for an internal molecular reorganization which in this work is referred to as aging. Depending on the initial state of the molecular arrangement and the type of the involved components, it has been shown that the change of the composition profile can be more or less significant.

In literature, a detailed analysis of the location of the individual components as a function of time and distance from the sample surface is still missing. Nevertheless, there are some publications addressing the aging of adhesives. For example, a clear change in surface morphology of industrial acrylic latices was observed with atomic force microscopy [190]. Furthermore, the impact on the mechanical properties does not seem to follow a clear trend. The monitored behavior depends on the investigation technique as well as on the selected sample system. In this context, a nanoindentation study of blends of amorphous hydrogenated polyisoprene and n-butyl ester of abietic acid reveals that the work of adhesion decreases as a function of time [191]. In contrast, Czech demonstrated that PSA films based on EHA and AA exhibit an increase in peel force as a function of time [192].

Similar to these observations, the previous chapter showed that, by choosing an appropriate preparation protocol, the mechanical properties of samples of the same material and of equal age can exhibit different mechanical properties. That is why for the investigation of aging it is inevitable to start from a well-defined state of the samples. Such well reproducible structures are achieved with the preparation under controlled atmosphere, which has been elaborated in the previous chapter.

In this chapter, four different aging series of P(EHA-stat-20MMA) films are presented. Each of them is based on a different initial near-surface composition profile and depends on the history of the preparation. First, the aging under ambient conditions is described.

The results are then compared to a sample that is prepared and stored under humid environment. For the aging under ambient conditions, samples with different initial degree of PMMA enrichment are chosen.
Results of this chapter have been published in reference [184].

7.1 Aging under ambient conditions

The investigation of the molecular reorganization under ambient conditions is the most relevant situation for PSAs in standard applications. As already mentioned, a corresponding sample series was presented in section 5.3 for the case of a PSA film being already solution cast under ambient conditions. One difference resulting from the choice of controlled atmosphere (and the related limited accessible volume for the evaporating solvent) during the film drying is the presence of remaining solvent in the freshly prepared sample (see sections 6.1.1 and 6.2).
It is to be expected that, in contrast to the drying under ambient conditions, this remaining solvent influences the near-surface composition profiles especially for low sample ages. Due to this reason the focus in this chapter is on shorter time scales as compared to the 359 d selected in section 5.3. Once the extractable remaining solvent has evaporated, the PSAs will (for long times) behave as described for the preparation under ambient conditions. For shorter times, the influence of initial near-surface PMMA concentration of the P(EHA-stat-20MMA) films on the aging behavior is investigated.

7.1.1 Low initial near-surface PMMA enrichment

For the examination of aging in the case of freshly prepared samples with only weak PMMA surface enrichment, a 24 h old P(EHA-stat-20MMA) film prepared under dry conditions is chosen. The sample is cast from a toluene based solution. In section 6.1, when describing the processing protocol for the investigation of the relative humidity, the corresponding distribution of components has been referred to as “composition profile after step 1”. So, by choosing this sample as starting point of an aging series, also the question about what will happen if the sample was not subsequently placed in a second desiccator is answered.
The analyzed XRR data together with the corresponding grayscale-coded near-surface composition profiles are depicted in figure 7.1. The XRR data for $t = 1$ d have already been shown in figure 3.13 (where the fit and the refractive index profile are represented as dashed lines). Also the state of the freshly prepared sample has been discussed in detail in section 3.3.3. The main result concerning the aging series is a weak enrichment of the surface with PMMA. For the samples of all aging series, a broad sub-surface PEHA

enrichment is found in depths around roughly 50 nm. This extended PEHA enriched zone decays in intensity and converges to homogeneous bulk material for large z values.
For 1 d $\leq t \leq$ 8 d, the thickness of the PMMA (black color) surface enrichment layer as well as the corresponding PMMA concentration increase until a maximum is reached after 8 d (see right panel of figure 7.1). For the next investigated sample (t = 11 d), a fraction of the MMA monomers has migrated from the surface into the film volume leading to a lower surface PMMA concentration. At the same time, PEHA starts to move towards the air-interface as can be seen from the bright area in a depth of 4.3 nm.

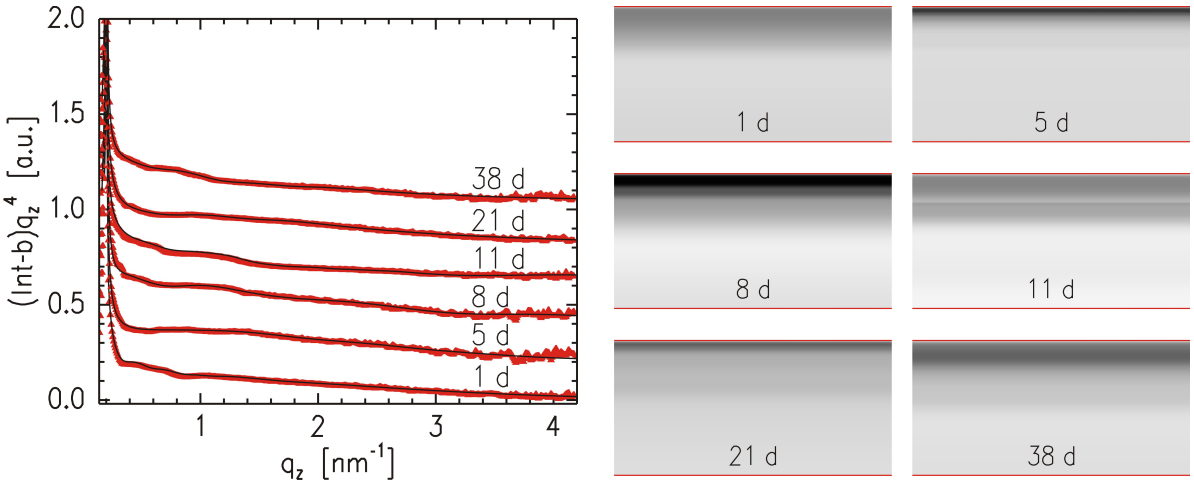

Figure 7.1: *Left: XRR data (symbols) and the corresponding fits (lines) of an aging series of P(EHA-stat-20MMA) films starting with low near-surface PMMA enrichment. The individual sample ages are indicated by the corresponding label of each curve. The data are shifted along the intensity axis for clarity. Right: Respective grayscale-coded composition profiles to the shown fits. Each profile represents the near-surface region covering the range* $0 < z < 20$ *nm. The grayscale code is defined in figure 3.3.*

After 21 d, the PMMA surface enrichment is already relatively weak and the MMA monomers are broadly distributed over a larger zone as can be seen from the gray color of the corresponding composition profile. In the final step, at t = 38 d, this broadly distributed PMMA densifies towards a more pronounced layer. As explained in 5.3, this densification can be attributed to the preferential attraction of alike monomers. In total, the overall amount of PEHA in the near-surface region after 38 d is considerably higher than for the 11 d old sample. Furthermore, the weak PMMA enrichment layer in the last measurement of the aging series has shifted slightly towards higher z values indicating that PEHA starts to enrich on top of the sample.
More details can be extracted from the integrated PMMA concentrations over regions of different thickness measured from the film surface. In analogy to figure 6.2, $\kappa_{\mathrm{PMMA}}(z)$ (for definition see equation 6.1) is calculated for z = 2, 4, 15, 50 and 100 nm as a function

of time. The resulting values are plotted in figure 7.2.

The described behavior of increasing surface PMMA enrichment until $t = 8$ d can be seen from the monotonic increase of $\kappa_{\mathrm{PMMA}}(z)$ within 1 d $\leq t \leq$ 8 d for $z \leq 15$ nm. The increase is less pronounced for broader integration regions and it is not evident for $z \geq 50$ nm. For such large z values, the PMMA concentration is constant as a function of time. A similar large-z behavior has already been detected for the case of the relative humidity (see section 6.1.1).

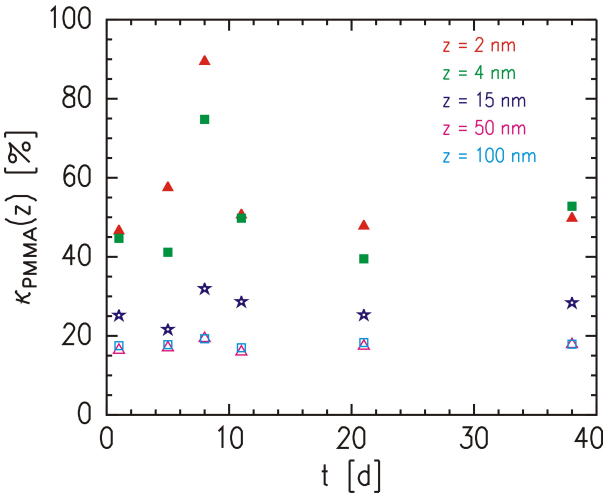

Figure 7.2: *Mean PMMA content in the near-surface region of an aging series of P(EHA-stat-20MMA) which exhibits low initial PMMA enrichment. From top to bottom the thickness of the integration region increases as shown by the labels. The error bars coincide with the symbol size (see section 6.1.1).*

For $t = 11$ d, the described loss of the PMMA enrichment is reflected in a significant reduction of κ_{PMMA} for the three lowest z values ($z \leq 15$ nm). Within the investigated time interval, a slight increase in the mean near-surface PMMA content is detected for $t \geq 11$ d. The described onset of PEHA adsorption at the topmost layer is not yet visible in the integrated κ_{PMMA} values.

The observed time dependence of the PMMA distribution within the near-surface region can be explained via the presence of remaining solvent in the freshly prepared PSA film, which has been proposed in section 6.1.1. The slow evaporation of small amounts of remaining solvent is still ongoing and is gravimetrically not measurable. As a consequence, the PMMA (which is the better soluble material with respect to toluene) transport towards the surface is kept alive over a remarkably long time of eight days.

Once this PMMA migration stops due to the lack of remaining solvent, a PEHA enrichment arising from the minimization of the surface energy (see section 5.3) sets in. Although first hints of a PEHA top layer are visible for $t = 38$ d, the total time of this aging experiment is far too short to observe a pronounced PEHA layer. For comparison, in section 5.3 (solution casting under ambient conditions) the necessary time to observe a PEHA top layer was 134 d. Moreover, in contrast to the molecular reorganization presented in this section, the PMMA transport to the surface has already been completed

for the sample freshly prepared under ambient conditions (see section 5.3). Therefore, for the preparation under dry conditions it is to be expected that the time needed to obtain a PEHA surface layer is even longer than 134 d.
In addition to the XRR experiments, GISAXS (see sections 2.3.4 and 3.2.3) measurements have been carried out in order to investigate whether lateral structures are present in the PSA films. Such in-plane compositional variations are indeed found and their size is monitored as a function of time. The measured two-dimensional (2D) scattering pattern corresponding to the freshly prepared P(EHA-stat-20MMA) film is exemplarily shown in figure 7.3. The respective counting time per 2D scattering pattern was 40 min. The beamstop (B) shields the detector from the high intensity of the specularly reflected beam.

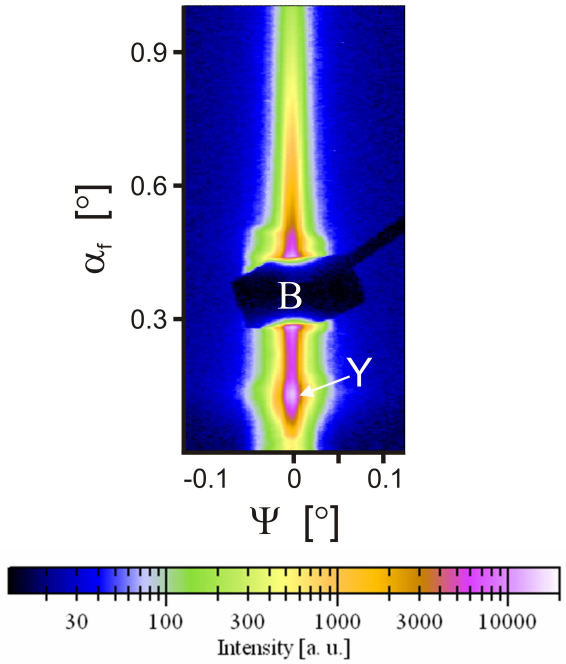

Figure 7.3: *2D scattering image obtained in a GISAXS experiment with a P(EHA-stat-20MMA) film freshly prepared under dry conditions. The labels B and Y mark the beamstop and the Yoneda peak, respectively. The scale bar depicts the intensity distribution defining the color code in the 2D image.*

As a result, the exit angle α_f, at which the Yoneda peak Y (for explanation see section 2.3.4) is positioned, coincides with the critical angle of the majority component PEHA. In contrast, no increased intensity is detected at the critical angle of the substrate. Therefore, as it was seen in the XRR data, the PSA films are sufficiently thick, so that no signal from the substrate is obtained.
This observation has two important consequences for the data analysis. First, the obtained out-of-plane signal arises from lateral structuring situated in a region near the surface and not at the interface to the substrate. And second, similar to the XRR data interpretation, because the substrate is not seen in the data, the bulk material of the thick P(EHA-stat-20MMA) films enters the corresponding model as if it was the substrate. From the XRR investigation, it is known that the composition of the bulk material does not fluctuate in z-direction. This justifies the choice of δ(P(EHA-stat-20MMA)) as refractive index for

the substrate within the GISAXS data analysis of thick PSA films.
The data analysis is performed using the *IsGISAXS* software [86]. Among the available possibilities for data modeling, the "Distorted Wave Born Approximation for inclusions encapsulated in a layer on a substrate" is closest to the obtained distribution of components and, thus, chosen for all samples composing the aging series. To account for the different involved object sizes, the local monodisperse approximation is selected (see section 2.3.4).

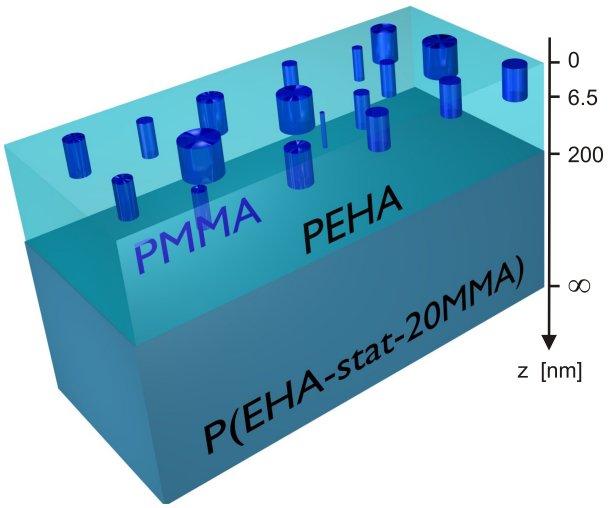

Figure 7.4: *Schematic illustration of the model applied for the IsGISAXS data analysis of the 50 µm thick P(EHA-stat-20MMA) films composing an aging series under ambient conditions. PMMA cylinders embedded in a PEHA matrix are situated on top of the bulk material.*

In more detail, there are cylindrical objects at the sample surface that are all extended in z direction to a depth of 6.5 nm matching approximately the extension of the top surface PMMA enrichment layer for all samples. The cylinders are embedded in a PEHA matrix of 200 nm thickness. In the model, this EHA/MMA composite material is placed on top of a semi-infinite, homogeneous P(EHA-stat-20MMA) substrate material. A sketch of the described model for the data analysis is provided in figure 7.4. It is important to note that with the available software, it is not possible to model even more realistic scenarios including, for example, objects which are situated in different depths.
As it has been explained in section 2.3.4, two types of cylindrical objects are introduced. In the case of the presented aging series, a probability of 0.5 is assigned to each particle type. The probability density of the radii R, heights H and center-to-center distance D is broadly distributed following equation 2.95. The height distribution does not play a role because the top end of the cylinders practically coincides with the sample surface. To account for a rather smooth transition between the bulk material and the PEHA overlayer as it is observed in the XRR investigation, the interfacial root mean square roughness is set to 1.5 nm.
The model parameters are fitted to the corresponding out-of-plane cuts (taken at the exit angle α_f corresponding to the critical angle of the majority component PEHA) which are

extracted from of each of the 2D scattering patterns. The out-of-plane cuts are chosen because these cuts contain information about the lateral structuring (see section 3.2.3). The cuts together with the respective model fits are shown in figure 7.5.

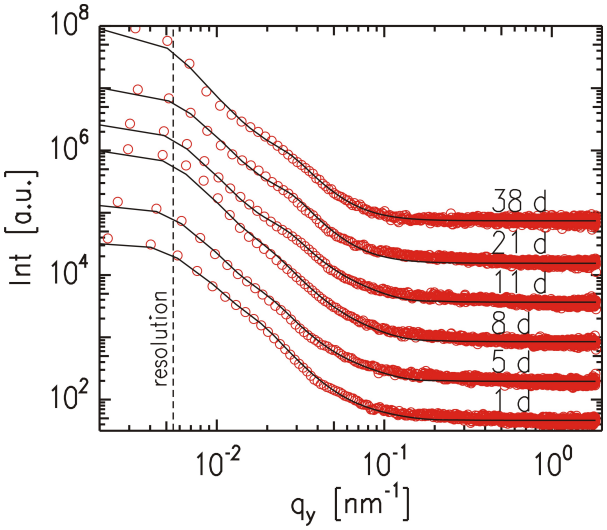

Figure 7.5: *Measured out-of-plane cuts (symbols) and respective fits (solid lines) of the P(EHA-stat-20MMA) aging series. The data are shifted along the y-axis for clarity. The dashed line marks the resolution limit of the experimental setup.*

Figure 7.6 shows the time evolution of the central values of the distribution functions of the two cylinder radii (left panel) as well as of D (right panel). As a result, the radii of both particle types increase monotonically while at the same time the inter-particle distance decreases during aging. In more detail, for both particle types the increase in radius is very small for short times t. Almost constant values of 23 nm and 49 nm are obtained for cylinder 1 and cylinder 2, respectively. However, both particles exhibit a strong increase in size for $t > 11$ d. In contrast, the time-dependence of D is very similar to an exponential decay approaching a limiting value of approximately 145 nm.

The errors to the central values of the radii and the center-to-center distances are estimated by varying the respective parameter in the model corresponding to the best fit of the individual out-of-plane cuts. A fit is considered to be acceptable as long as it does not exceed the symbols chosen for plotting the cuts. As a result, the calculated cuts (solid lines in figure 7.5) are more sensitive to the assumed values of R_c as compared to the values of D_c. Whereas the determined error is approximately ± 1 nm for the radii (and is therefore on the order of the size of the symbols in the left graph of figure 7.6), it is estimated to be ± 4 nm for the center-to-center distances.

Interestingly, the accelerated gain in particle size occurs at a time ($t > 11$ d) when the pronounced PMMA surface layering has already vanished (see figure 7.2). This is in accordance with the described sub-surface densification of the PMMA material. Furthermore, the evolution of the lateral structures is independent of the rather complex reorganization of the composition profile in vertical direction as revealed by the XRR data analysis.

The explanation to the missing correlation between lateral and vertical structure sizes is

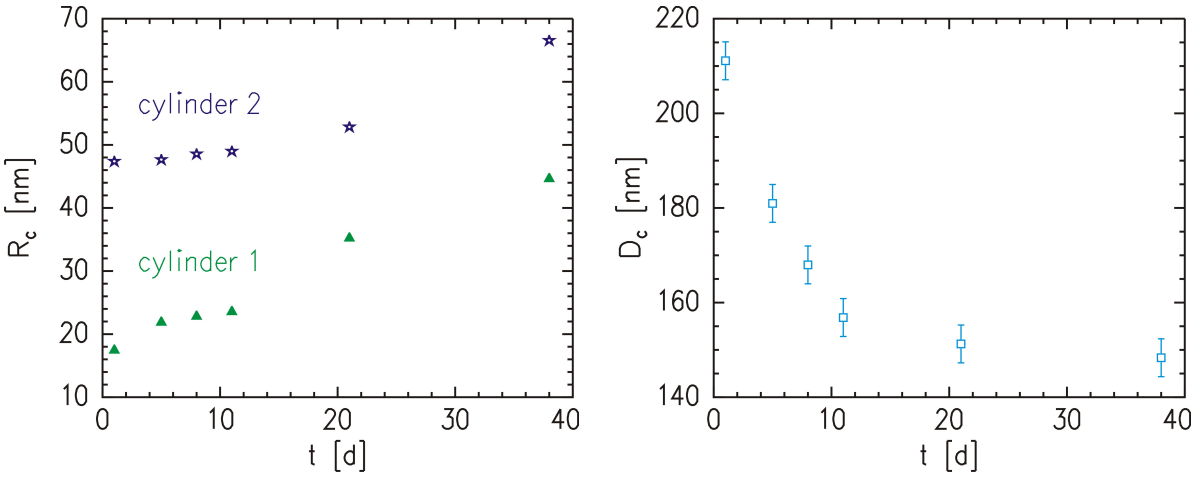

Figure 7.6: *Left: Central value of the distribution of the two cylinder radii as a function of time for the P(EHA-stat-20MMA) films composing the aging series. The error bars are on the order of the symbol size. Right: Corresponding central value of the cylinder center-to-center distance as a function of time.*

that the driving forces of the molecular reorganization, such as the unidirectional evaporation of remaining solvent and the tendency to minimize the surface energy, only act in z-direction. Besides the self-attraction of identical monomers, no prominent forces act in the plane parallel to the film surface. For small times ($t \leq 11$ d), the enormous solvent-driven changes in the composition profiles prevent the lateral growth of the near-surface PMMA particles. The lateral growth becomes more pronounced once the remaining solvent has vanished sufficiently.

The GISAXS data cover a comparably short time window during which the aging is monitored. Therfore, it cannot be deduced whether the particle growth continues and lateral structures vanish due to the onset of merging of the cylinders or whether the radii approach a limiting value. However, considering the simulation study of Houdayer (see section 2.2.4), it is very likely that the second scenario is valid and, thus, irrespective of the sample age, there will always be lateral structuring in the investigated PSA films.

7.1.2 High initial near-surface PMMA enrichment

The near-surface composition profiles obtained for weak initial PMMA enrichment layers are now compared to samples which exhibit a high surface PMMA concentration in the freshly prepared state. One example for such a high initial surface PMMA concentration is the sample which is solution cast under humid atmosphere using n-hexane as the underlying solvent. The XRR data of the freshly prepared sample (see figure 6.14) have been discussed in section 6.2.2.

Due to the altered preparation protocol (humid atmosphere replaces dry conditions), the sample age of the freshly prepared sample is 3 d, and not 1 d as it was in section 7.1.1. Figure 7.7 shows the aging process of the n-hexane based sample over 66 d monitored with XRR.

In summary, a comparably strong PMMA surface enrichment layer is preserved throughout the investigated time window. The PMMA concentration of the top layer decreases slightly as can be seen from the fading of the black color close to $z = 0$. In the sub-surface region, directly underneath the topmost layer, PEHA (bright area) starts to form a layer. For $t = 24$ d, the maximum PEHA concentration is found at $z = 4.5$ nm. The corresponding PEHA enriched layer thickness becomes smaller for 6 d $\leq t \leq$ 24 d and remains constant for $t \geq 47$ d.

Almost simultaneously ($t \geq 24$ d), PMMA densifies at a depth of approximately 9.2 nm. This sub-surface PMMA densification is again a strong hint for the attraction of identical monomers. Finally, as for all investigated PEHA containing samples, a broad PEHA enriched zone encompassing more than 50 nm precedes the convergence towards homogeneous bulk material (not shown in the composition profiles).

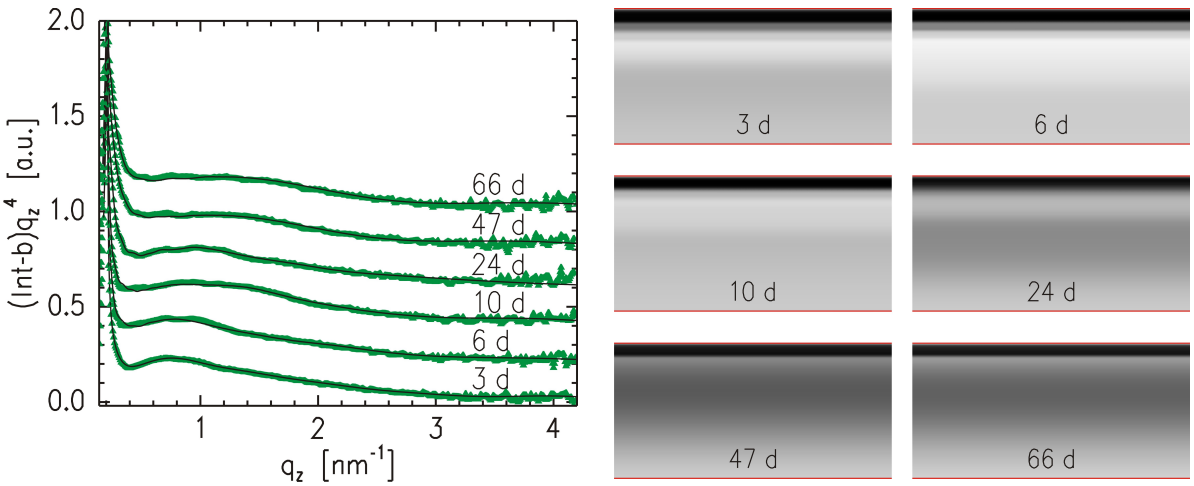

Figure 7.7: *Left: XRR data (symbols) and the corresponding fits (lines) of an aging series of P(EHA-stat-20MMA) films starting with high near-surface PMMA enrichment. The freshly prepared sample is cast from an n-hexane solution. The individual sample ages are indicated by the corresponding label of each curve. The data are shifted along the intensity axis for clarity. Right: Respective grayscale-coded composition profiles to the shown fits. Each profile represents the near-surface region covering the range* $0 < z < 20$ *nm. The grayscale code is defined in figure 3.3.*

The aging behavior of the n-hexane based sample is compared to a P(EHA-stat-20MMA) film which has been cast from a dichloromethane based solution. For this dichloromethane based sample, a similar PMMA surface enrichment in the freshly prepared state is obtained

as compared to the n-hexane based sample. However, the freshly prepared samples differ significantly in remaining solvent content (see section 6.2.2).
Both, the conditions for the solution casting (humid) and for the subsequent storage (ambient air) are equal for the two P(EHA-stat-20MMA) films. The corresponding aging series for the dichloromethane based preparation has been performed over almost the same duration as for the n-hexane based sample. The near-surface composition profile of the freshly prepared dichloromethane based film has already been shown in figure 6.14. The XRR data together with the extracted near-surface composition profiles of the aging series for the dichloromethane based sample are shown in figure 7.8.

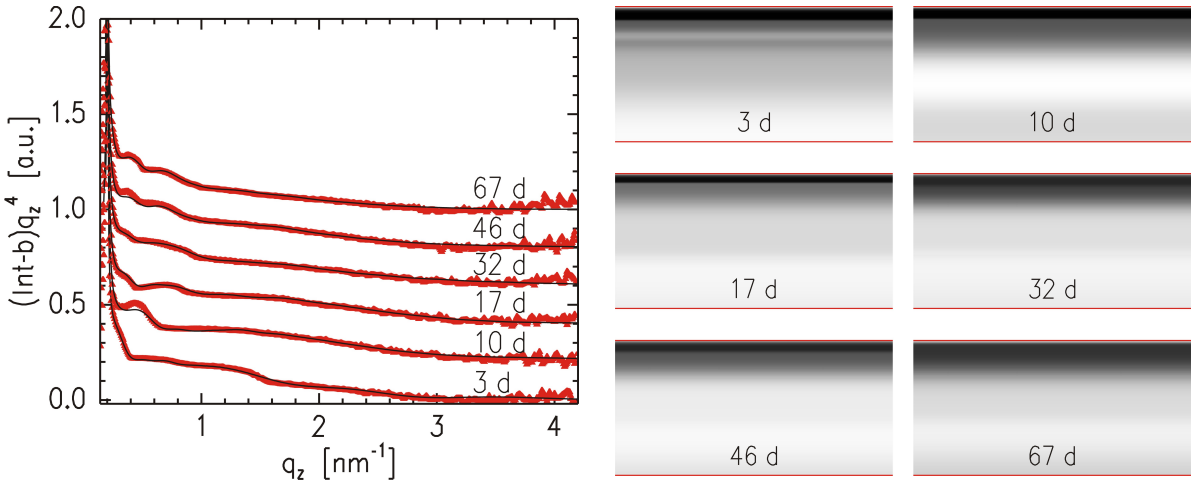

Figure 7.8: *Left: XRR data (symbols) and the corresponding fits (lines) of an aging series of P(EHA-stat-20MMA) films starting with high near-surface PMMA enrichment. The freshly prepared sample is cast from a dichloromethane solution. The individual sample ages are indicated by the corresponding label of each curve. The data are shifted along the intensity axis for clarity. Right: Respective grayscale-coded composition profiles to the shown fits. Each profile represents the near-surface region covering the range* $0 < z < 20$ *nm. The grayscale code is defined in figure 3.3.*

Regarding the topmost layer, both aging series are very similar. Also for the case of dichloromethane, the initially very pronounced PMMA top layer becomes weaker and washed out with time. However, differences arise in the sub-surface region. Whereas for large times t a comparably strong second PMMA enriched zone evolves for the case of n-hexane, such sub-surface PMMA densification does not play a prominent role for dichloromethane. For $t \geq 32$ d, such PMMA enrichment is only slightly indicated by a region of marginally increased PMMA content in a depth of 9.4 nm, which is very similar to the corresponding depth in the case of n-hexane. In total, the sub-surface amount of PEHA is higher for the sample prepared from dichloromethane.
The observed differences can be quantified by calculating the average PMMA content of

near-surface regions of different thicknesses for both samples. For this purpose, again, $\kappa_{\mathrm{PMMA}}(z)$ (for definition see equation 6.1) is calculated for $z = 2$, 4, 15, 50 and 100 nm as a function of time. The resulting values for both solvents, n-hexane and dichloromethane, are plotted in figure 7.9.

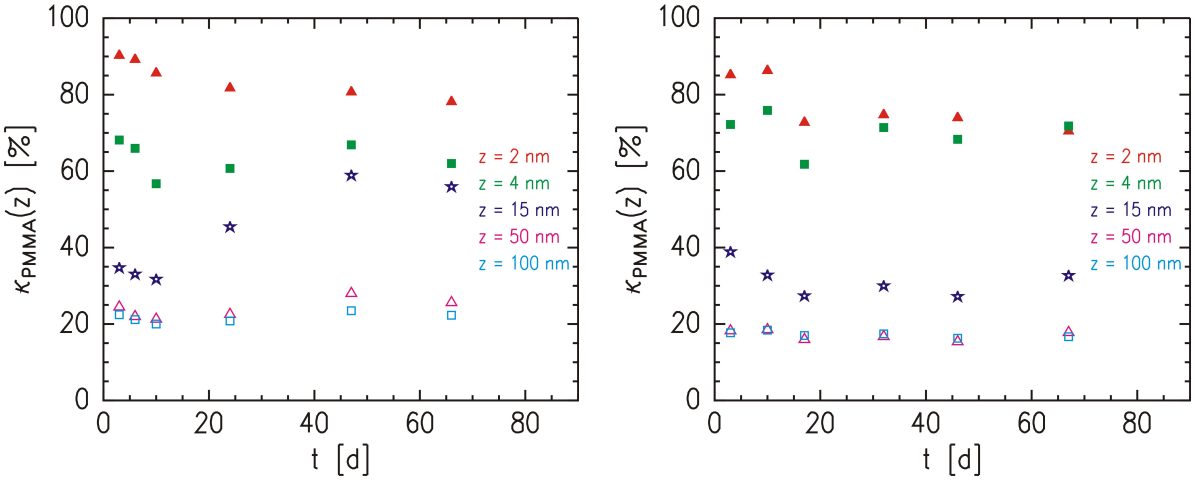

Figure 7.9: *Mean PMMA content in the near-surface region of two aging series of P(EHA-stat-20MMA) which exhibit high initial PMMA enrichment. From top to bottom the thickness of the integration region increases as shown by the labels. The error bars coincide with the symbol size (see section 6.1.1). The left panel represents the case of an n-hexane based preparation protocol and the right panel represents dichloromethane, respectively.*

In contrast to the sample prepared under dry conditions (see section 7.1.1), there is no increase in surface PMMA concentration for small times t, as can be seen from the almost constant value of $\kappa_{\mathrm{PMMA}}(2\ \mathrm{nm})$ for both samples prepared in humid environment. Obviously, saturation has been reached and the ongoing evaporation of residual solvent cannot add further MMA monomers per unit volume.

Subsequently (for $t \geq 10$ d), a decrease of $\kappa_{\mathrm{PMMA}}(2\ \mathrm{nm})$ is observed for both samples represented in figure 7.9. The onset of this decrease is on a very similar time scale as compared to the sample preparation under dry conditions (see figure 7.2). Such reduction in surface PMMA concentration can be explained by the tendency of PEHA being the lower surface energy material to enrich at the sample surface. Furthermore, both samples (like for all other aging series in this work) do not reveal significant compositional variations for depths $z \geq 50$ nm.

Moreover, the described differences in sub-surface PMMA densification between the two samples prepared under humid conditions are well visible in the graphs of figure 7.9. They become most evident when $z = 15$ nm is considered. Both sample exhibit a monotonic decrease of $\kappa_{\mathrm{PMMA}}(15\ \mathrm{nm})$ as a function of time for the first three data points. This

decrease originates from the migration of PEHA towards the surface in both samples.
The situation changes for $t \geq 20$ d, but in each of the two films in a qualitatively different way. Whereas $\kappa_{\mathrm{PMMA}}(15\ \mathrm{nm})$ increases significantly for the n-hexane based PSA film, it increases only slightly for the dichloromethane based sample during the same time interval. In other words, for $t > 17$ d, a prominent sub-surface PMMA enrichment measurable with the integrated PMMA contents takes place for n-hexane. On the contrary, this is not the case for dichloromethane.
For an explanation of the differences concerning the formation of a sub-surface PMMA layer, the amount of remaining solvent in the freshly prepared samples has to be considered. It is significantly higher when dichloromethane is used as underlying solvent (see figure 6.13) than for the case of n-hexane. In addition, according to the GISAXS investigation presented in section 7.1.1, a significant lateral growth of PMMA domains only sets in once the evaporation of remaining solvent has been sufficiently completed. As a consequence, the onset of sub-surface PMMA densification can occur earlier when n-hexane is chosen as a solvent. It is very likely that a pronounced formation of a sub-surface PMMA enrichment in the case of dichloromethane will take place at a time beyond the time window of the experiment.

7.2 Aging under humid atmosphere

Further complexity is added when not only the sample preparation is performed under humid environment but also the subsequent storage. In this case, additional interface selectivity originating from the polar water molecules and a decelerated solvent evaporation throughout the complete storage period are present.
Such a scenario is realized by casting the sample in a desiccator filled with saturated sodium chloride solution (see section 6.2.2). So, the conditions for the coating step are equal to those applied in section 7.1.2. However, in contrast to the aging under ambient conditions, the lid of the desiccator is not removed until approximately one hour before the corresponding near-surface composition profiles are monitored with XRR. In the time between removing the films from the desiccator and starting the XRR experiment, gravimetric measurements have been carried out in order to determine the amount of extractable remaining solvent for each sample.
The aging series under humid conditions is performed with P(EHA-stat-20MMA) films cast from a toluene based solution. The sample ages 3, 5, 11, 16 and 29 d are addressed for this investigation.
For the respective freshly prepared film ($t = 3$ d), it has been shown in section 6.2.2 that the remaining solvent content is comparably large ($S_r = (9.2 \pm 0.2)$ %, see table 6.3).

In addition to the freshly prepared sample, the corresponding relative mass loss curves $\Delta m_r(t)$ (see equation 6.4) are monitored for all samples composing this aging series. The obtained data including the respective fits using equation 6.5 are depicted in figure 7.10.

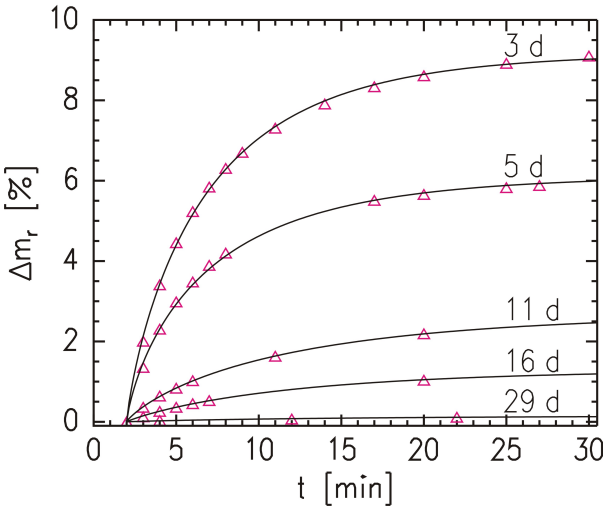

Figure 7.10: *Relative mass loss as a function of time of solution cast P(EHA-stat-20MMA) films composing the aging series under humid air. The sample age increases from top to bottom as indicated by the labels. The errors bars are smaller than the symbol size. The solid lines are the respective fits to the data.*

Table 7.1 lists the fitted remaining solvent contents S_r, the damping exponents c_r and the time constants T_r for all samples of the aging series. The errors to the fitted parameters are provided by the fitting routine. As a result, both parameters, S_r and T_r decrease as a function of sample age. This means that with increasing sample age of the P(EHA-stat-20MMA) films prepared and stored under humid conditions less remaining solvent is present in the samples and the remaining solvent evaporates slower. Moreover, damping due to solvent vapor saturation effects within the setup of the precision balance (for more details, see section 6.2.1) are negligible as can be seen from the values of c_r, all of which are close to 1.

sample age	$\boldsymbol{S_r}$ [%]	$\boldsymbol{c_r}$	$\boldsymbol{T_r}$ [min]
3 d	9.2 ± 0.2	0.8 ± 0.1	5.0 ± 0.1
5 d	6.1 ± 0.1	0.8 ± 0.1	5.2 ± 0.1
11 d	2.7 ± 0.1	0.8 ± 0.1	9.8 ± 0.2
16 d	1.3 ± 0.1	0.9 ± 0.1	10.4 ± 0.5
29 d	0.2 ± 0.1	0.9 ± 0.1	15.0 ± 0.8

Table 7.1: *Fit parameters of the mass loss curves of the P(EHA-stat-20MMA) films composing the aging series under humid conditions.*

The analyzed XRR data together with the corresponding near-surface composition profiles for all P(EHA-stat-20MMA) films of the aging series performed throughout under humid

conditions are depicted in figure 7.11. The data of the freshly prepared film has already been shown in figure 6.14.

The main result of the discussion provided in section 6.2.2 was that PMMA is not yet enriched at the sample surface for the freshly prepared film. The explanation was based on the high remaining solvent content and the resulting uncompleted PMMA transport process. It was further presumed that a PMMA surface enrichment layer should appear for higher sample ages.

The composition profiles in the right panel of figure 7.11 confirm this presumption. Indeed, already after 5 d, a weak enrichment of PMMA is found at the surface. This surface PMMA layer becomes more and more pronounced up to a sample age of 16 d. Also an upward migration of PEHA is visible for 5 d $\leq t \leq$ 16 d. However, the PEHA does not reach the top layer for 5 d $\leq t \leq$ 16 d. At a sample age of 16 d, for example, the maximum PEHA concentration is obtained in a depth of 10.2 nm. Finally, for $t = 29$ d, PEHA starts to enrich at the sample surface (see gray color), and the pronounced PMMA layer has migrated deeper into the film. Most MMA monomers per unit volume are detected in a depth of 3.9 nm.

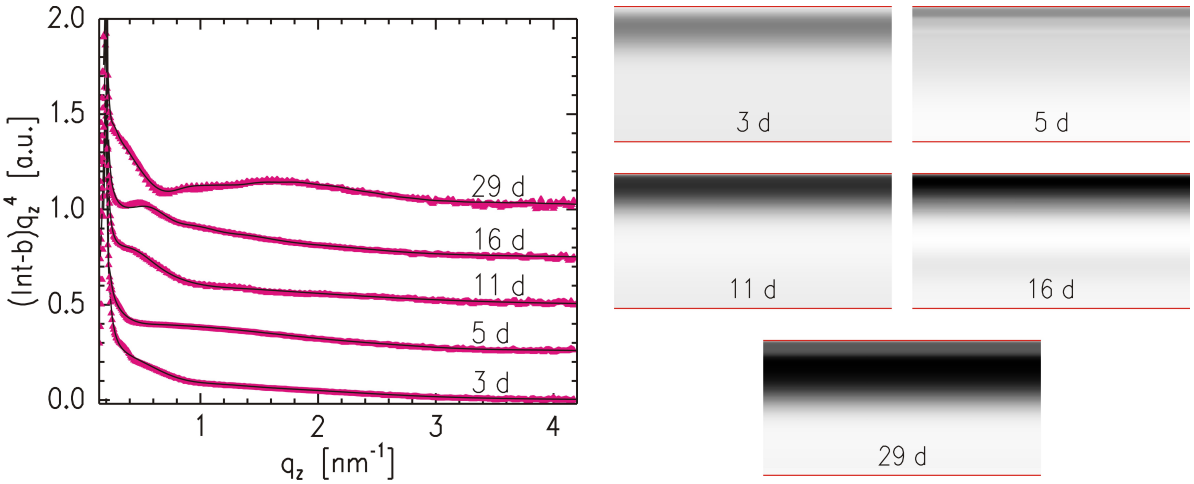

Figure 7.11: *Left: XRR data (symbols) and the corresponding fits (lines) of an aging series of P(EHA-stat-20MMA) films performed under humid conditions. The individual sample ages are indicated by the corresponding label of each curve. The data are shifted along the intensity axis for clarity. Right: Respective grayscale-coded composition profiles to the shown fits. Each profile represents the near-surface region covering the range* $0 < z < 20$ *nm. The grayscale code is defined in figure 3.3.*

More details are determined from $\kappa_{\mathrm{PMMA}}(z)$ which is exemplarily calculated for $z = 2$, 4, 15, 50 and 100 nm as a function of time (see figure 7.12). In this context, $\kappa_{\mathrm{PMMA}}(2\ \mathrm{nm})$ increases monotonically as a function of time for 3 d $\leq t \leq$ 16 d, reflecting the PMMA transport towards the surface owing to the evaporation of small amounts of remaining

solvent in combination with the more attractive atmosphere with respect to the more polar PMMA.

The final decrease of $\kappa_{\mathrm{PMMA}}(2\ \mathrm{nm})$ for $t = 29$ d is attributed to the onset of PEHA (as the lower surface energy material) adsorption at the sample surface. As an important consequence, for large times t, the tendency of the lowest surface energy material to adsorb at the air-interface outweighs the polar interactions with the other component. The affected region has a thickness of at least 2 nm.

The effect of large-time PEHA surface enrichment is still visible for an integration region of 4 nm. It is, however, less pronounced as can be seen from the comparably small decrease of $\kappa_{\mathrm{PMMA}}(4\ \mathrm{nm})$ in the last step. In the intermediate regime ($5\ \mathrm{d} \leq t \leq 16$ d), $\kappa_{\mathrm{PMMA}}(4\ \mathrm{nm})$ exhibits a strictly positive slope due to the ongoing PMMA surface enrichment. In contrast, $\kappa_{\mathrm{PMMA}}(4\ \mathrm{nm})$ decreases from the freshly prepared state to a sample age of 5 d which originates from the shift of the initial sub-surface PMMA enriched region to the film surface.

This shift even affects the values of $\kappa_{\mathrm{PMMA}}(15\ \mathrm{nm})$ for small times t. For older samples, however, $\kappa_{\mathrm{PMMA}}(15\ \mathrm{nm})$ increases monotonically. In a first phase ($5\ \mathrm{d} \leq t \leq 16$ d), a comparably small slope is observed before in the last step, the mean PMMA concentration of the upper 15 nm increases more drastically.

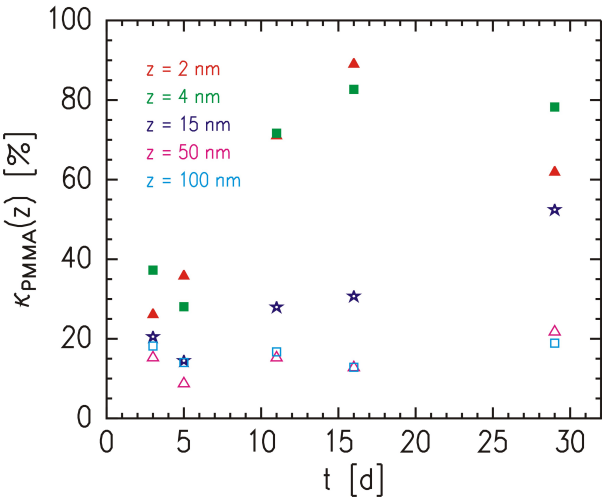

Figure 7.12: *Mean PMMA content in the near-surface region of an aging series of P(EHA-stat-20MMA) films which is completely performed under humid conditions. From top to bottom the thickness of the integration region increases as shown by the labels. The error bars coincide with the symbol size (see section 6.1.1).*

The origin of this behavior cannot be fully clarified. On the one hand, it has been shown in section 6.2.1 that the range of influence of the polar interactions covers a rather broad near-surface region. It is therefore possible that the surface tension driven PEHA enrichment affects only an approximately 2 nm thick region and that on a larger scale of, for example, 15 nm the polar interactions dominate and attract PMMA. On the other hand, section 7.1.1 revealed that a sub-surface PMMA densification related to an accelerated growth of the lateral structures sets in once sufficient remaining solvent is extracted. This second

scenario is also realistic because the 29 d old sample only contains 0.2 % of remaining solvent (see table 7.1). Possibly, both phenomena contribute to the observed behavior of $\kappa_{\mathrm{PMMA}}(15\ \mathrm{nm})$. Finally, again, no strong correlations are observed for integration regions larger than 50 nm.

7.3 Conclusion

Irrespective of the chosen solution casting based sample preparation protocol or the applied storage conditions, the near-surface composition profiles of P(EHA-stat-20MMA) films change with time. In all investigated cases, the lower surface energy material PEHA enriches at the sample surface for large times.

A narrow near-surface zone having a thickness of approximately 2 nm is strongly affected by this surface energy driven PEHA adsorption. Furthermore, the average near-surface PMMA concentration exhibits a significant time-dependence when it is calculated over less than 50 nm.

All freshly prepared PSA films representing the starting point of each time series contain a certain amount of remaining solvent. For short times, the evaporation of this residual solvent induces a migration of the better soluble PMMA towards the surface. For samples which do not exhibit a pronounced PMMA top layer in the freshly prepared state, an increase in the surface PMMA concentration follows. In contrast, saturation is observed in films which exhibit a high initial surface PMMA content. In these cases, the PMMA concentration integrated over 2 nm does not increase any further.

Once the upward PMMA transport is stopped due to the lack of remaining solvent, the onset of PEHA surface adsorption is observed. Even the attraction of the more polar PMMA arising from the choice of a humid environment during aging cannot prevent an enrichment of PEHA at the film interface to the surrounding air.

Moreover, grazing incidence small angle x-ray scattering revealed that the statistical copolymer based material is also structured parallel to the film surface. A successful modeling of the out-of-plane cuts is achieved by introducing cylindrical PMMA particles underneath the film surface. The cylinders are embedded in a PEHA matrix. As a result, the cylinder radii increase as a function of time while the corresponding mean center-to-center distance decreases.

The cylinder growth in lateral directions is more prominent when a sufficient amount of residual solvent has evaporated. Almost at the same time, a densification of the sub-surface PMMA material is observed with x-ray reflectivity. Such pronounced sub-surface PMMA layers are not detected for samples which exhibit large remaining solvent contents in the initially prepared state.

Chapter 8

Characterization of ultra-thin PSA films

Up to this point, the focus of the presented study was on macroscopically thick PSA films. In contrast, within the following chapter the structural and mechanical investigation of ultra-thin PSA films is presented. Opposite to approaches, which influence the adhesion by coatings on a molecular scale, like for example self-assembled monolayers [193, 194], this work focuses on spin-coated statistical copolymer based PSA films.

Spin-coating is a well-established technique (see section 3.3.4) having the potential to create polymer films over a thickness range covering several orders of magnitude. Possible fields of applications of thin, spin-coated PSA films are such where the downsizing of devices plays an important role. Examples can be found in microelectronic circuits [195], micro-devices for the analysis of biological nanoparticles [196], micro-patterned surfaces [197], or polymer photonic devices [198].

The knowledge about mechanical and structural properties of 50 μm thick PSA films, which is elaborated in the previous chapters, cannot be transferred to the case of ultra-thin films. The reason is not only that the thickness of the investigated near-surface areas of the solution cast films are smaller than the overall thicknesses of the spin-coated films. It is also known that if the film thickness undergoes a certain limit, properties like the morphology [199, 200] or the thermal expansion coefficient [201] will start to deviate from the bulk behavior.

Closely related to the tackiness of thin films are the corresponding viscoelastic properties which often differ from the thick-film case. With lateral force microscopy, for example, Akabori and coworkers discovered an additional surface relaxation process for films which are thinner than a certain threshold value [202]. Despite the technical challenges arising when small film thicknesses are involved, there are also studies which directly access the viscoelastic parameters of ultra-thin films using a surface forces apparatus [203, 204] or

an atomic force microscope (AFM) [205]. However, the viscoelastic behavior can also be investigated indirectly, for example via buckling-based metrology [206], thermal wrinkling [207] and dewetting experiments [208].

A direct monitoring of the adhesive properties of ultra-thin films can be achieved by performing so-called nano-tack or atomic force microscopic adhesion measurements [29, 30]. Even the adhesion and deformation of single nanoscopic latex particles have been probed with these methods [209]. The involved forces, however, are in the nN regime and are only measurable at very short length scales. Therefore, the AFM based techniques are not suitable to record the macroscopic tackiness of ultra-thin films.

Although so far only established for much higher film thicknesses, the macroscopic tackiness can be monitored with probe tack tests (see section 3.2.7). The thinner the film under investigation is, the higher the confinement in the system for a given punch radius is (for details, see section 2.1.6). The aim of this work is to monitor the tackiness as a function of the confinement in the system. Different confinement values are realized by producing ultra-thin PSA films of different thicknesses. In this context, successful tack experiments are performed at confinement values that exceed the reported literature values by at least one order of magnitude [43].

This chapter is organized as follows: first the involved film thicknesses are determined with x-ray reflectivity and white light interferometry. A full morphological characterization is provided by grazing incidence small angle x-ray scattering experiments. And finally, the adhesive properties of the PSA films are examined in probe tack tests.

Results of this chapter have been published in reference [210].

8.1 Film thickness determination

For the investigation of the tackiness as a function of the film thickness h, P(nBA-stat-MA) with a molecular weight of $M_w = 600$ kg/mol is chosen as PSA model system. The spin-coating (for details, see section 3.3.4) is performed with toluene based solutions of different concentrations in order to achieve different film thicknesses (see equation 3.8). For this purpose, eight different solutions with concentrations ranging from $c = 2.0$ g/L to 220 g/L are prepared.

X-ray reflectivity (XRR) (see section 3.2.1) and white light interferometry (WLI) (see section 3.2.4) are employed to measure the resulting film thicknesses. In order to obtain precise values of the film thicknesses, the XRR data are fitted with the *Parratt32* software. The corresponding XRR data together with the fits are shown in the left panel of figure 8.1. In contrast to the XRR data of the thick PSA films presented in the previous chapters, a single-logarithmic plot is more advantageous for a pronounced representation of the

appearing Kiessig fringes (see section 2.3.2).

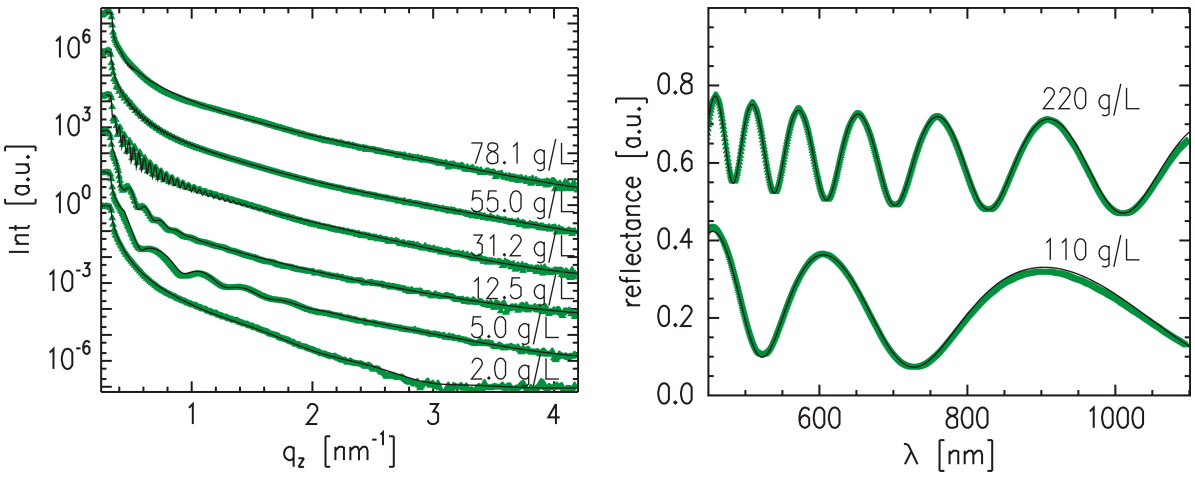

Figure 8.1: *Left: XRR data (symbols) and the corresponding fits (lines) of a thickness series of spin-coated P(nBA-stat-MA) films. The underlying solution concentrations are indicated by the corresponding label of each curve. The data are shifted along the intensity axis for clarity. Right: WLI data displayed in analogy to the left panel.*

The wavelength of the Kiessig fringes decreases with increasing film thickness h. For thickness values which are on the order of some hundred nanometers, the fringes cannot be resolved within the available angular resolution of the XRR instrument. Therefore, WLI measurements are carried out for a reliable thickness determination of the two samples related to the highest solution concentrations. The WLI data are depicted in the right panel of figure 8.1.

$\boldsymbol{c}$ [g/L]	2.0	5.0	12.5	31.2	55.0	78.1	110	220
$\boldsymbol{h}$ [nm]	2.2	17.6	44.4	133	243	363	607	1543
$\boldsymbol{\Delta h}$ [nm]	0.4	0.2	0.5	1	5	5	3	7

Table 8.1: *Extracted thickness values h from the fits to the XRR and WLI data of P(nBA-stat-MA) films. The values of Δh are the corresponding errors. The films are spin-coated from toluene based solutions of different concentration.*

Table 8.1 lists the resulting eight thickness values h obtained from the different solution concentrations c. The corresponding errors Δh are estimated by varying the value of h in the modeling of the XRR and WLI data, respectively. A fit is considered to be acceptable as long as it does not exceed the symbols chosen for plotting the data. The smallest error bars are obtained for XRR data which exhibit pronounced Kiessig fringes.

As expected, h increases monotonically as a function of c. According to equation 3.8, the respective data points should be situated on a line through the origin. A corresponding plot is provided in figure 8.2. As a result, equation 3.8 does not hold for the complete range of selected concentrations. It is only valid for $c \leq 78.1$ g/L. A fit to the data (solid line) with A_p as the only free parameter leads to a value of $A_p = 5.23 \cdot 10^{-6}$ $(\mathrm{Lmol}^{0.25}\mathrm{m})/(\mathrm{kg}^{1.25}s^{0.5})$. Due to the rather exotic unit originating from the empirical formula, the value is not very intuitive. A probably more illustrative value is the slope of the solid fit which is 4.52 $(\mathrm{nm} \cdot \mathrm{L})/\mathrm{g}$.

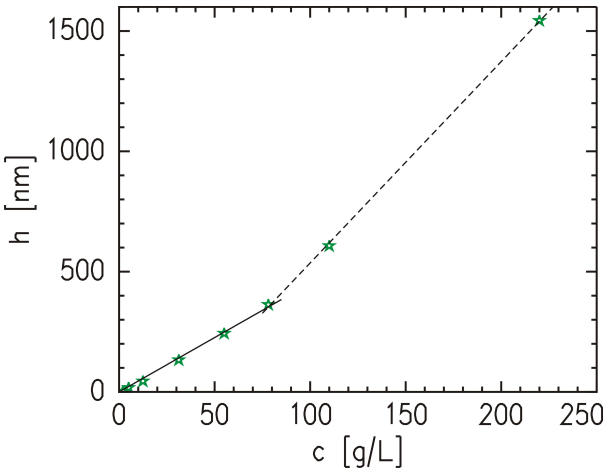

Figure 8.2: *Film thickness as a function of the solution concentration. The error bars are smaller than the symbol size. Two different linear regimes are obtained. Each of the two different lines (solid and dashed) is a linear fit within the corresponding subset of concentrations.*

The second region ($c \geq 78.1$ g/L), which is marked by the dashed line, does not follow a line through the origin and, thus, cannot be described by equation 3.8. A linear fit to the data leads to a y-axis intercept of -300 nm and a slope 8.36 $(\mathrm{nm} \cdot \mathrm{L})/\mathrm{g}$ which is almost twice the value as compared to that obtained for the low concentration regime. From the higher slope, it can be concluded that the sensitivity of the thickness towards the concentration is enhanced for $c \geq 78.1$ g/L.
Interestingly, a study by Ruderer and coworkers exhibited similar deviations [211]: they observed the onset of deviations from the behavior predicted by equation 3.8 of spin-coated polypyrrole films for thicknesses between approximately 70 nm and 150 nm. The reason for this change in the slope when plotting the film thickness as a function of the solution concentration is the onset of entanglements in the polymer solution. Once the polymer chains are entangled it becomes more difficult to spin them off the substrate at constant rotation speed [211].

8.2 Morphological characterization

The morphology of the ultra-thin PSA films is analyzed with grazing incidence small angle x-ray scattering (GISAXS) (see sections 2.3.4 and 3.2.3). The extracted structural sizes

do not exhibit a strong thickness dependence within the region that is relevant for the mechanical characterization. Therefore, only the samples with $h = 44.4$, 133 and 363 nm are exemplarily chosen for this GISAXS study.

Due to the small film thicknesses, the x-ray beam fully penetrates the sample and, thus, in contrast to the thick PSA films presented in section 7.1.1, a prominent signal of the solid support is obtained. This strong reflection from the glass substrate results in high intensities for small out-of-plane angles ψ. Please refer to figure 2.17 to recall the GISAXS geometry.

In order not to damage the detector, a maximal acquisition time of 5 min was selected to record the two-dimensional (2D) diffuse scattering patterns. A point-like beamstop is used for these measurements to protect the detector from the specular reflection (as shown in figure 7.3). Moreover, the investigated statistical copolymer based PSAs are only weakly structured in the (x,y)-plane and, hence, unlike the region around $\psi = 0$, the signal for high ψ values is not very intense and exhibits a poor signal to noise ratio.

The experimental background is approximately 58 counts for the out-of-plane cuts which are taken at the critical angle of the majority component PnBA. For low counting times, the corresponding features for large ψ (or q_y) values are, therefore, hardly visible in the cuts. Nevertheless, the intensity distribution for higher ψ values is very important for the data analysis. But such improved statistics can only be realized with higher counting times. To be able to apply higher counting times, each of the three investigated samples is measured a second time with an additional, rod-like beamstop to block the high intensities for small out-of-plane angles. With the installed protection, the integration time of the second measurement is set to 40 min.

For the data analysis of each of the three samples, first the corresponding out-of-plane cut and the detector cut are fitted and, second, the full 2D scattering pattern is simulated. In order to include the weak, but important signal corresponding to high q_y values in the analysis of the out-of-plane cut for each sample, the data of the two described measurements are merged. The two underlying measurements are depicted in the left panel of figure 8.3 for the example of $h = 363$ nm.

In the image, the data of the measurement performed without rod-like beamstop are already multiplied by 1.43. The factor is obtained by calculating the intensity ratios of the corresponding first four data points that are not affected by the rod-like beamstop (see arrow in the left panel of figure 8.3). To account for the experimental background within the calculation of the shift factor, in both cuts 58 counts are subtracted from each of the involved four points. The shift factor for the cut corresponding to the measurement without rod-like beamstop is finally calculated by averaging over the four individual intensity ratios.

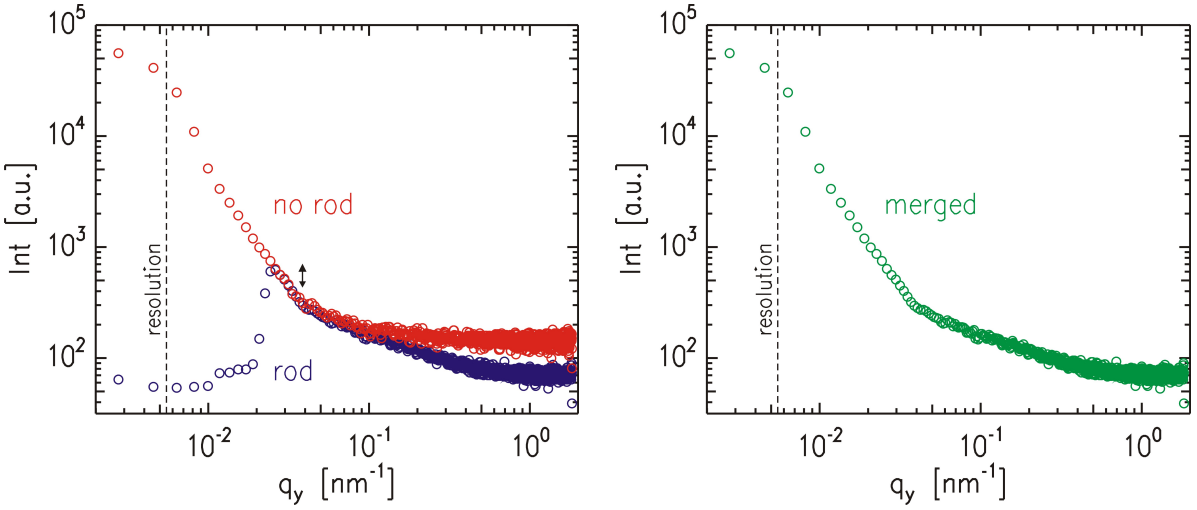

Figure 8.3: *Left: Out-of-plane cuts measured for a P(nBA-stat-MA) film with a thickness of* 363 *nm. The blue symbols are measured using a rod-like beamstop and the red symbols represent data obtained without the rod-like beamstop (see labels). The red symbols are shifted to match the intensity of the blue symbols within the region covered by the small arrow. Right: Resulting merged out-of plane cut of the two single measurements shown in the left panel. The dashed line in both graphs marks the resolution limit of the experimental setup.*

The right graph of figure 8.3 is the finally merged out-of-plane cut. For low q_y values, the data are the shifted points of the short measurement and, for large q_y values, the data coincide with those of the measurement performed with the rod-like beamstop. The small deviations within the four overlapping data points are negligible.

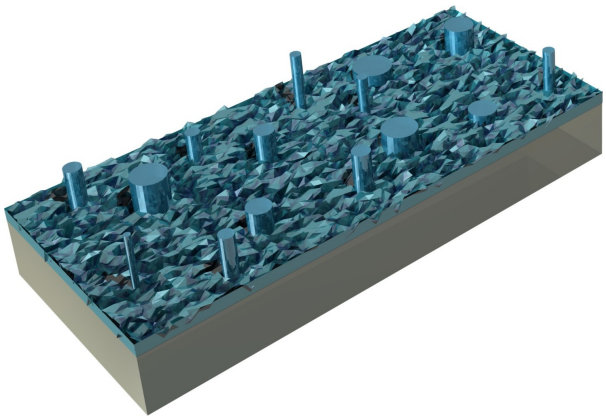

Figure 8.4: *Schematic illustration of the model applied for the IsGISAXS data analysis of ultra-thin P(nBA-stat-MA) films. PMA cylinders are situated on a rough, but homogeneous P(nBA-stat-MA) film supported by a glass substrate.*

For the described procedure of the data analysis, which is performed with the *IsGISAXS* software [86], a suitable model of the samples has to be assumed. In contrast to the modeling of the thick PSA films (see section 7.1.1), the assumption of cylindrical objects embedded in a polymer matrix does not lead to successful fits of the measured data.

Instead, cylindrical objects consisting of pure PMA have to be situated on top of a P(nBA-stat-BA) film exhibiting no compositional fluctuations. The type of object material follows from fitting the refractive index of the cylinders to the data. As a result, the refractive index of PMA is obtained. Furthermore, a fit to the data leads to a surface roughness of 5.6 nm for all investigated samples. The described scenario is included in the *IsGISAXS* algorithm as "islands supported on a layer on a substrate". A schematic view of the applied model is provided in figure 8.4.
Data fitting was performed simultaneously with the corresponding out-of-plane and detector cuts. For the out-of-plane cuts, the respective merged data are used (see figure 8.3). The detector cuts are extracted from the corresponding short measurements without the rod-like beamstop. The cuts together with the respective fits are shown in figure 8.5.

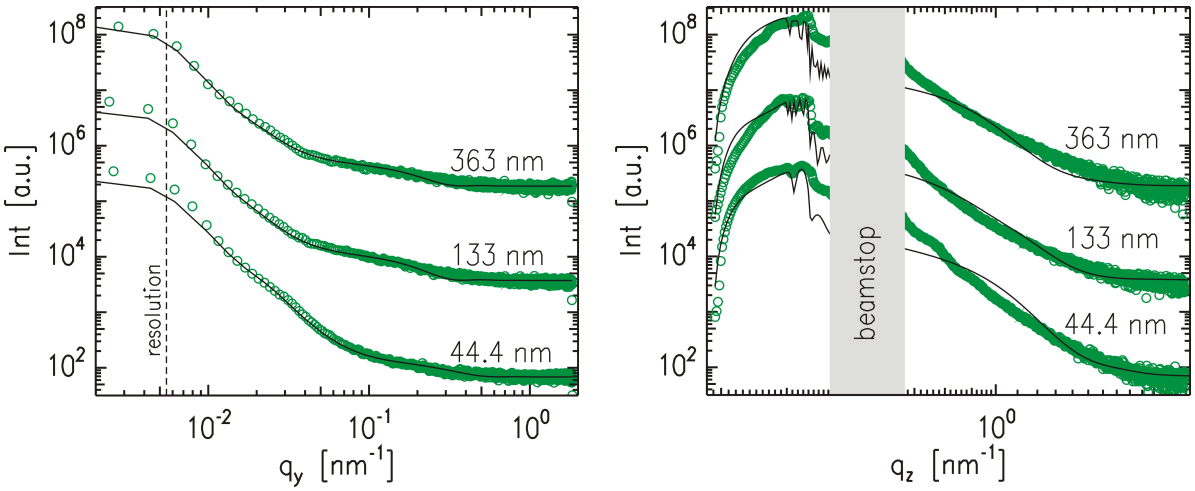

Figure 8.5: *Left: Measured out-of-plane cuts (symbols) and respective fits (solid lines) of P(nBA-stat-MA) films of different thickness as indicated by the labels. The dashed line marks the resolution limit of the experimental setup. The data are shifted along the intensity axis for clarity. Right: Corresponding detector cuts displayed in analogy to the left panel. The gray area marks the area which is shielded by a point-like beamstop.*

In order to achieve such fits, it is necessary to include two types of cylinders in the model (similar to what is described for thick films in section 7.1). The individual radii R_1 and R_2, as well as the cylinder height H and the center-to-center distance D follow distribution functions according to equation 2.95. For the calculation of the shown cuts and the simulation of the 2D images, the number of sampling points composing each of the two radius distribution functions is set to 100. Furthermore, 50 points modeling the height distribution are assigned to each of the 200 radii.
Each of the two cylinder types is needed to model the different features of the out-of-plane cuts presented in the left panel of 8.5. The majority of the cylinders have a comparably

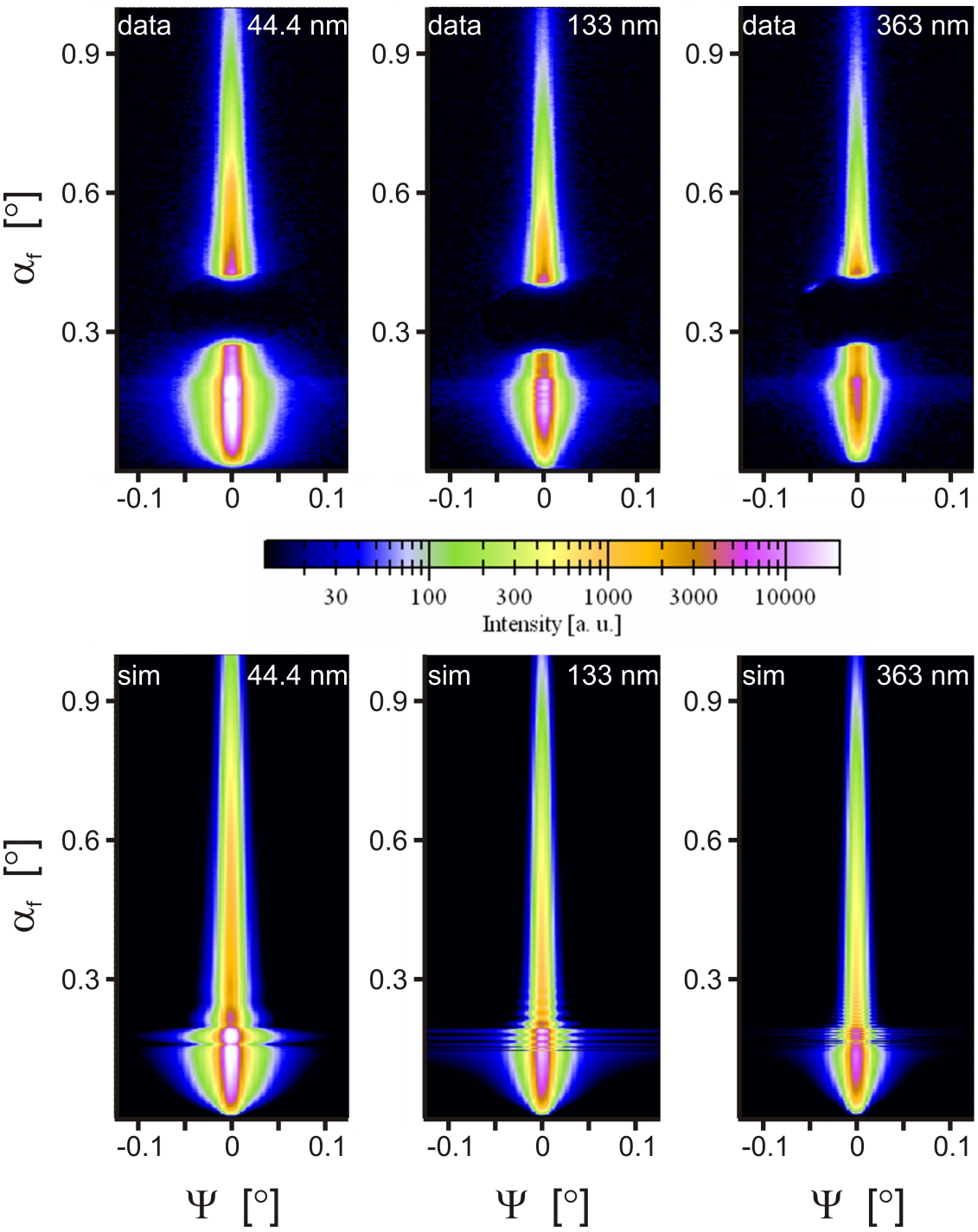

Figure 8.6: *Top: Measured 2D GISAXS scattering patterns of spin-coated P(nBA-stat-MA) films with thicknesses of* 44.4, 133 *and* 363 *nm (see labels). Bottom: Corresponding 2D IsGISAXS simulations to the data shown in the first line. All six patterns cover the same* α_f *and* ψ*-range and refer to the same logarithmic intensity scale bar as indicated.*

small and narrowly distributed radius. These cylinders are referred to as type 1. Owing to their presence, the broad shoulder in the out-of-plane cuts around $q_y = 10^{-1}$ nm^{-1} can be fitted. Due to their small size and the resulting comparably weak scattering, the probability of a cylinder to be of type 1 has to be quite large. Fitting revealed that the corresponding probability is approximately 99.5 %. In contrast, the radii of the cylinders of type 2 are relatively large and exhibit a broad size distribution. Only approximately 0.5 % of the objects are of type 2. Anyhow, strong diffuse scattering arises from the bigger cylinders. This second type of cylinders is responsible for the overall intensity decay of the three out-of-plane cuts.

Furthermore, the fitted mean height averaged over all cylinders of type 1 and type 2 covers a range between 24 nm and 28 nm for the three investigated samples. As a consequence, the cylinder heights do not appear to depend strongly on the chosen film thickness.

With this model, not only the out-of-plane and the detector cuts are successfully fitted, but also the main features of the complete 2D scattering patterns are simulated. The measured data together with the performed simulations are presented in figure 8.6. The shown data are the described short measurements using exclusively the point-like beamstop which shields the specular reflection. The specular reflection is also not included in the simulation because *IsGISAXS* only simulates the diffusely scattered intensity.

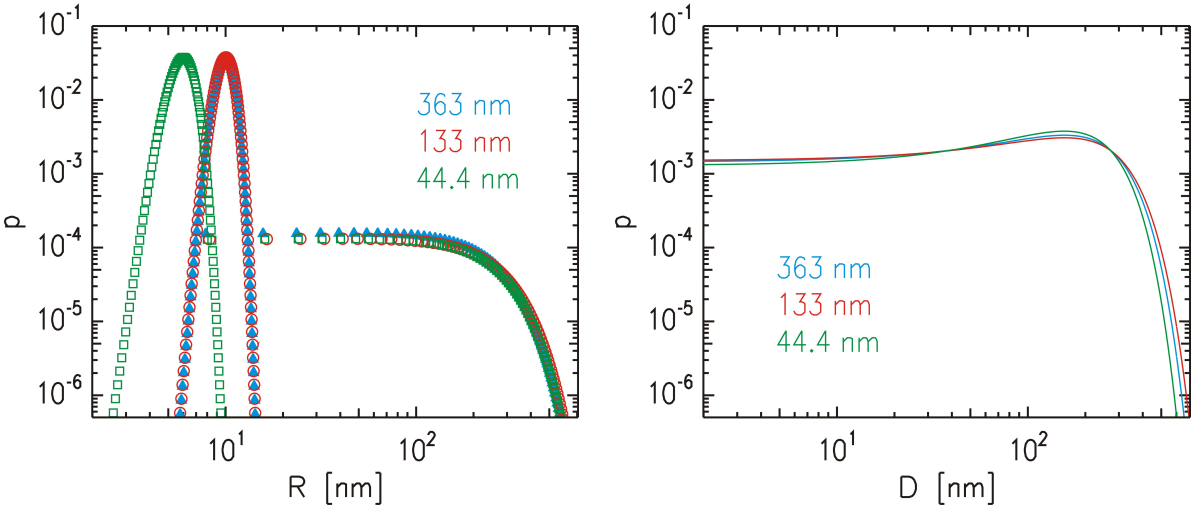

Figure 8.7: *Left: Probability distribution functions of the cylinder radii for spin-coated P(nBA-stat-MA) films with a thickness of* 44.4 *nm (squares),* 133 *nm (circles) and* 363 *nm (triangles). Each symbol represents one radius sampling point for the simulation of the diffuse scattering patterns depicted in figure 8.6. Right: Probability distribution functions of the corresponding center-to-center distances. The color-code is adapted from the left panel.*

Details of the underlying model can be seen from the involved probability distribution functions. They are plotted for each of the three samples in figure 8.7. All radius dis-

tribution functions (left panel) exhibit a strong peak at either approximately 10 nm (for $h = 133$ and 363 nm) or 6 nm ($h = 44.4$ nm). The peak originates from the type 1 cylinders. The broadly distributed radii, attributed to which are probabilities not exceeding 10^{-4}, correspond to the objects of type 2.

As already mentioned, the object sizes do not strongly correlate with the film thickness. The probability distribution functions of both, the radius and the center-to-center distance almost coincide for the two thicker films (133 and 363 nm). For $h = 44.4$ nm, also $p(D)$ does not deviate significantly from the other two samples. The only remarkable difference concerns the radii of the type 1 cylinders of the thinnest film. The corresponding central value of the radius distribution is reduced by a factor of 0.6 for a film thickness of 44.4 nm. However, the total surface coverage, which is calculated as the integrated cross-sectional area of all cylinders per unit film surface area, is almost the same for all investigated samples. The values of the surface coverages are between 2.9 % and 3.3 %.

An explanatory approach to the presence of the PMA cylinders on top of a homogeneous P(nBA-stat-MA) film might be based on the extremely fast solvent loss related to the preparation method spin-coating. In section 5.1.4 it is shown that for thick, solution cast P(nBA-stat-MA) films, PnBA enriches at the surface for high molecular weights and PMA forms the top layer for low molecular weights. The observation has been related to the faster drying process of the low molecular weight sample as revealed in sections 4.2.3 and 4.3. In the case of spin-coating, the solvent loss is much faster as compared to solution casting. Possibly, the resulting tendency of PMA to adsorb at the surface is even so strong that PMA-rich parts of the statistical copolymer chains exceed the boundary of the film-air interface. In addition, the fast solvent loss during spin-coating also explains the high surface roughness values.

8.3 Investigation of the tackiness

The investigation of the morphologies of ultra-thin PSA films is interesting from a fundamental polymer science point of view. But for applications, the knowledge about their mechanical performance as adhesive films is even more important. Probe tack tests (see sections 2.1.6 and 3.2.7) are performed with all eight P(nBA-stat-MA) films with thicknesses ranging from 2.2 nm to 1543 nm. For the presented tack experiments, the high performance punch characterized in section 3.2.8 is used. The study of the tackiness of ultra-thin PSAs is supposed to answer two questions. First, does the contact force in a tack experiment influence the results in the case of such thin films? And second, how does the tackiness of the PSAs change as a function of the film thickness?

8.3.1 Variation of the contact force

P(nBA-stat-MA) films with a thickness of 363 nm are chosen for investigating the influence of the contact force. In detail, the PSA films are contacted with the punch until contact forces of either 1, 2, 3 of 4 N are reached. All other experimental parameters are kept constant (see section 3.2.7 for details).
Compared to the tack experiments with the approximately 140 times thicker solution cast films shown in the previous chapters, some differences arise. First, probe tack tests with ultra-thin films are much more challenging and, therefore, special care has to be taken for the alignment procedure. Second, a different shape of the punch area during the contact of the punch with the PSA is obtained. A representative sequence of optical images for the bonding and the debonding process is provided in figure 8.8.

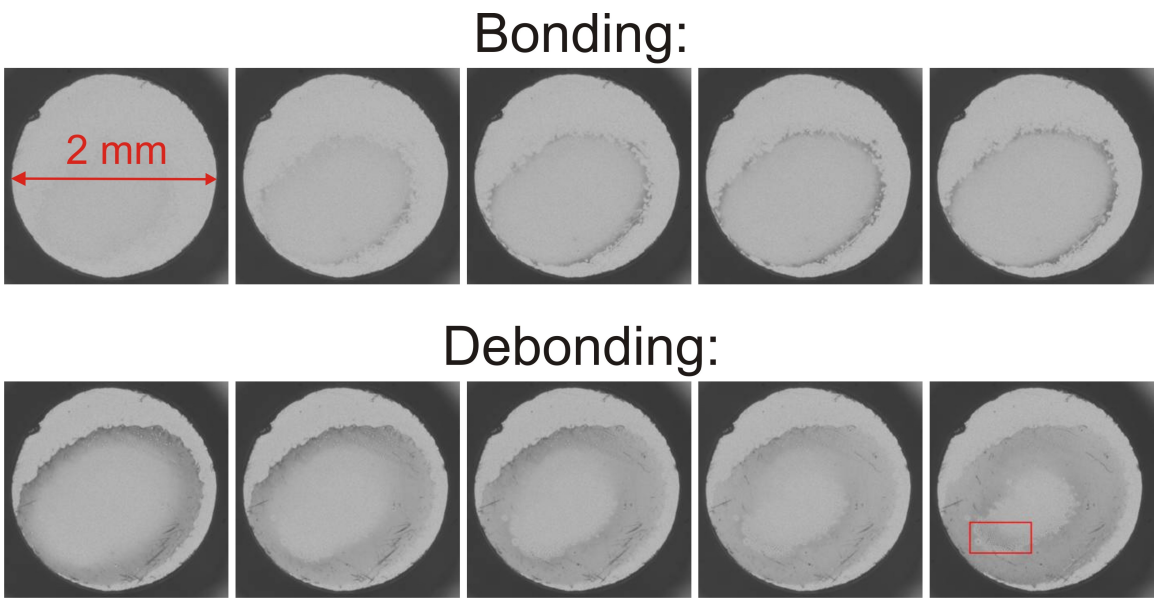

Figure 8.8: *Top: Series of representative optical images of the punch area during the bonding process. Bottom: Series of representative optical images of the punch area during the debonding process. The red box in the last image is the region which is magnified in figure 8.9. The time increases from left to right in both lines.*

During the bonding process (first line of figure 8.8), the PSA material is not homogeneously distributed under the punch. With time an increasing amount of polymer is collected in the center of the punch area. Saturation is not reached at the end of the bonding process (see last image of the first line). After the usual contact time of 10 s, the amount of polymer underneath the punch appears to have still increased (see first image of the second line). The images of the second line cover the complete debonding process during which the punch moves approximately 20 μm.

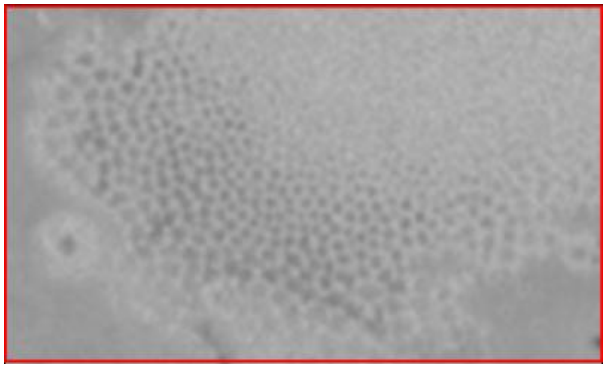

Figure 8.9: *Close-up of the region of the punch area which is marked with a red box in figure 8.8. Small cavities appear shortly before completion of the debonding process.*

With increasing punch distance d during debonding, the area that is preferentially wetted by the PSA decreases as can be seen from the shrinking bright area near the punch center. In very late stages before losing the contact (see last image of second line), there is a very short period on the time scale of the frame rate of the video observation (approximately 17 ms) during which small cavities are observed. These cavities are visible as small dark dots situated at the edge of the bright material (red box in the last image of the second line). They disappear immediately after the final debonding. In order to enhance the visibility of the cavities, a magnification of the region covered by the red box is shown in figure 8.9.

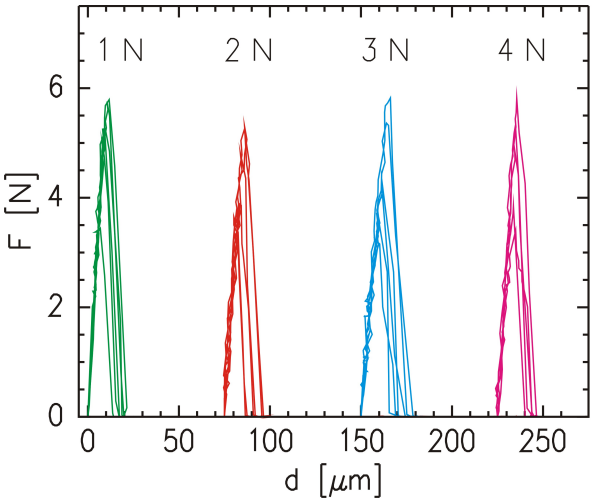

Figure 8.10: *Force-distance curves (punch radius: 1 mm) of 363 nm thick P(nBA-stat-MA) films obtained via probe tack tests. Four different contact forces are applied for the experiment (see labels). Each measurement is represented by one single line. The curves corresponding to different contact forces are shifted along the d-axis for clarity.*

The described observations indicate that the "bulk cavitation" failure mode predicted by Creton for high confinement values is present (see section 2.1.6). Together with the loss of contact between the punch and the PSA film, an audible crack occurs. Moreover, there is no indication for any fibrillation processes. This may be plausible from the low available PSA volume preventing the formation of elongated structures. The absence of fibrils is further confirmed by the shape of the force-distance curves obtained in the probe tack experiments because the data exhibit no plateau region. The corresponding data are

depicted in figure 8.10.
In more detail, all recorded force-distance curves exhibit a peak-like shape. The force maximum is reached for $d \approx 9$ μm and the debonding is completed for $d \approx 18$ μm. The curves corresponding to different contact forces are very similar to each other. For a quantitative description of the contact force dependence on the adhesive performance, the corresponding force maxima and tack energies are extracted. Figure 8.11 depicts these parameters as a function of the contact force.

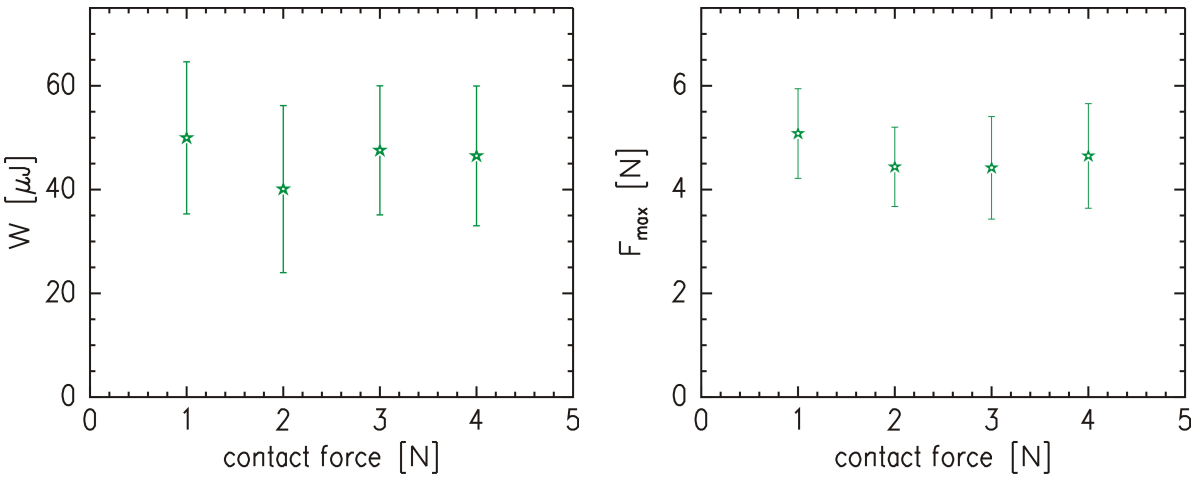

Figure 8.11: *Tack energy (left) and force maximum (right) as a function of the contact force obtained for* 363 *nm thick P(nBA-stat-MA) films.*

As a result, within the error bars, both, the tack energy and the force maximum are constant as a function of the contact force. Averaging over all four contact forces leads to mean values of $W = (46.0 \pm 4.2)$ μJ and $F_{max} = (4.6 \pm 0.3)$ N. It is important to note that a remarkably high force maximum is obtained for these ultra-thin PSA films. The value is even comparable to what is obtained for the 50 μm thick films presented in section 6.1.3. For a contact force of 1 N, those thick films have been measured under the same experimental conditions.

8.3.2 Variation of the film thickness

The next aspect, which is investigated for the ultra-thin P(nBA-stat-MA) films, is the influence of the film thickness on the adhesive performance. For this purpose, probe tack experiments are performed with all eight P(nBA-stat-BA) films introduced in section 8.1. A contact force of 4 N is selected for all investigated samples. Within the accuracy of the experimental setup, no measurable tackiness is detected for the two thinnest samples ($h = 2.2$ and 17.6 nm).

The force-distance curves of the six remaining samples are shown in figure 8.12. Although the data are more noisy for the thinner films, the shape described in section 8.3.1 is preserved irrespective of the film thickness. Differences arise in the peak height and the peak width. In more detail, the punch position d corresponding to the force maximum as well as the smallest d corresponding to the finally debonded state both increase with increasing PSA film thickness.

For a better comparison, representative curves for each thickness are chosen and plotted in one graph (left panel of figure 8.12). As a result, the force maximum increases with increasing film thickness for $h \leq 363$ nm. For $h \geq 607$ nm, however, the force maxima of the different sampling points are very similar. Due to the large range of forces covered by the successfully measured six samples, the tack data of the two thinnest films with detectable tackiness ($h = 44.4$ and 133 nm) are barely visible in the left panel of figure 8.12. They are separately shown as a close-up in the right panel.

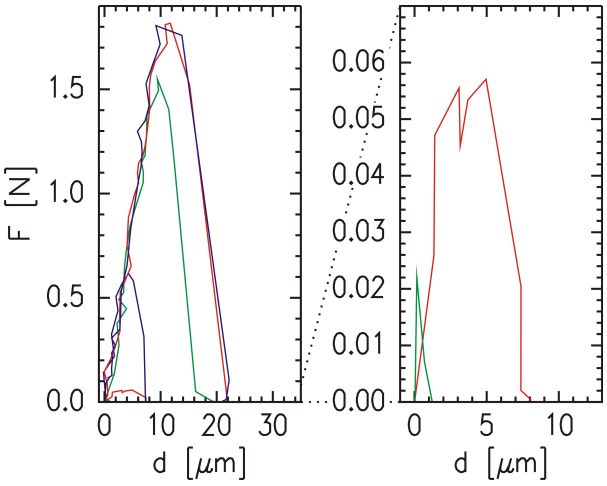

Figure 8.12: *Left: Representative tack data (punch radius: 1 mm) of the six tacky samples composing the thickness series of P(nBA-stat-MA) films. The thickness increases with increasing force maximum. Right: Close-up of the tack data corresponding to the two thinnest films with measurable tackiness (44.4 and 133 nm).*

Further details of the thickness dependence of the tackiness can be derived by extracting the tack energy W and the force maximum F_{max} from the measured force-distance curves. Both parameters are plotted as a function of h in figure 8.13. Due to the already mentioned broad range of appearing force maxima and tack energies, a logarithmic scale is chosen for the representation.

As a result, not only the force maximum increases monotonically as a function of the film thickness for $h \leq 363$ nm, but so does the tack energy as well. Both parameters remain constant within the achieved experimental error for $h \geq 607$ nm. Consequently, the adhesive performance is very sensitive to the PSA film thickness below a threshold value of approximately 363 nm. Above this threshold, no major changes are detected for the investigated range of film thicknesses indicating a bulk-like behavior.

Furthermore, the described monotonic increase of W and F_{max} for low h follows an exponential law. This can be seen from the fitted linear functions in the graphs of figure 8.13,

for both of which a logarithmic scale is selected. The exponential laws can be written as

$$W(h) = w_1 \exp[w_2 h] \qquad \text{and} \qquad F_{max}(h) = f_1 \exp[f_2 h], \tag{8.1}$$

respectively. The coefficients w_1, w_2, f_1 and f_2 follow directly from the linear fitting. The corresponding values are $w_1 = (3.7 \pm 0.4) \cdot 10^{-2}$ μJ, $w_2 = (1.9 \pm 0.1) \cdot 10^{-2}$ nm^{-1}, $f_1 = (4.1 \pm 1.7) \cdot 10^{-2}$ N and $f_2 = (1.3 \pm 0.2) \cdot 10^{-2}$ nm^{-1}.

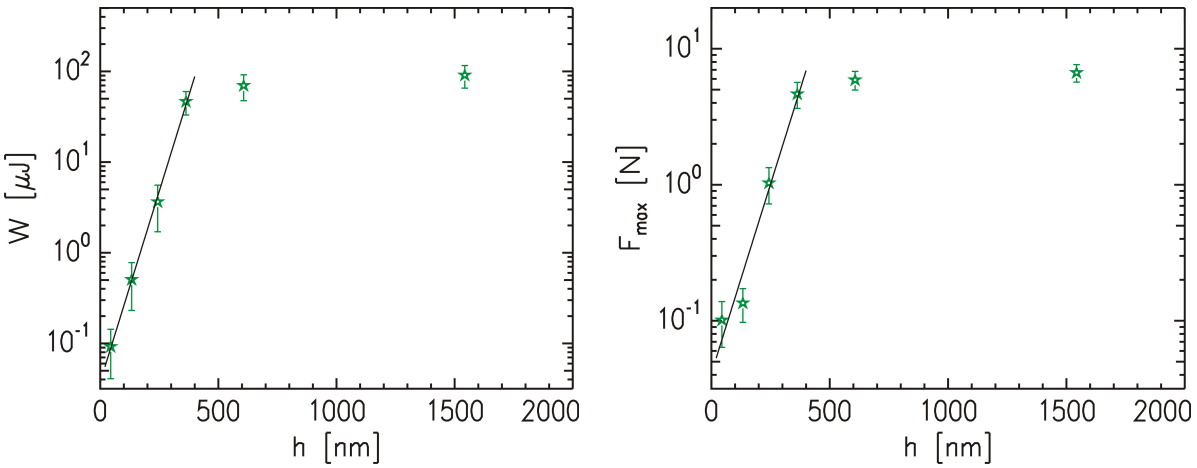

Figure 8.13: *Tack energy (left) and force maximum (right) as a function of the thickness obtained for spin-coated P(nBA-stat-MA) films in logarithmic representation. The solid lines in both panels are linear fits to the respective data for $h \leq 363$ nm.*

It is important to note that the validity of equations 8.1 is limited to a certain thickness regime because of two reasons. First, a constant regime of W and F_{max} is experimentally detected for $h > 363$ nm. This constancy is clearly different from an exponential law behavior. And second, an extrapolation towards thickness regions close to zero is also not possible since for $h = 0$, a non-vanishing tack energy would be predicted. As a consequence, additional correction terms would be necessary or there is a lower limit for the validity of equations 8.1.

8.4 Conclusion

Ultra-thin films of a PSA model system are processed via spin-coating. The film thickness is varied by selecting appropriate concentrations of the underlying solutions. The resulting thickness values, which are determined with x-ray reflectivity (XRR) and white light interferometry (WLI), only follow the behavior predicted in literature for low concentrations. For the high concentration regime, the involved high solution viscosities cause deviations.

A full morphological characterization of selected films is provided by grazing incidence small angle x-ray scattering (GISAXS) experiments. The distribution of the components in the films does not strongly correlate with the thickness. Moreover, the data analysis reveals a comparably large surface roughness. In addition to the root-mean-square roughness, the surface is decorated with objects that purely consist of the glassy minority component of the PSA. The data are successfully modeled by assigning a cylindrical shape to these objects. From a fit to the data, the radius, height and center-to-center distance probability distribution functions are extracted. As a result, the cylinders cover approximately 3 % of the surface for all investigated samples.
In contrast to the morphology, the adhesive performance as studied in probe tack tests is very sensitive to the film thickness. Below a film thickness of approximately 500 nm, both, the tack energy and the force maximum follow an exponential law behavior. For thicker films, these parameters remain constant within the investigated range of film thicknesses. For all samples, the corresponding force-distance curves exhibit a peak-like shape being closely related to the absence of any fibrillation processes. Finally, for a film thickness of 363 nm, no dependence on the applied contact force is detected.

Chapter 9

Summary and outlook

The chemical composition as a function of distance from the sample surface is investigated for different model systems of acrylic pressure sensitive adhesive (PSA) films. X-ray reflectivity as the main characterization method is the ideal tool for this purpose. The strength of the technique is that, for two-component PSAs, the near-surface composition profiles can be deduced from the measured refractive index profiles. When more components are involved, at least the location of enrichment layers of the component with either the highest or the lowest refractive index is possible.

Using the preparation techniques solution casting and doctor-blading, films with a thickness of 50 μm are successfully prepared. In all investigated samples the near-surface distribution of the involved components deviates from the bulk. The obtained deviations encompass a region covering a range of approximately 100 nm measured from the interface to the air.

With solution casting under ambient conditions, the type of copolymerized material has a strong influence on the obtained near-surface composition profile. The driving force is a selective upward transport of the material exhibiting the higher solubility with respect to the involved solvent. As a consequence, by choosing the appropriate type of copolymerized material, either the sticky or the glassy component can form the top surface layer. An exception to this behavior is observed for a low molecular weight statistical copolymer based PSA.

The molecular weight dependence of the near-surface composition profile is related to the corresponding solvent evaporation kinetics during the drying process. Although all samples in the examined molecular weight range show the same amount of homogeneously distributed remaining solvent in the dried state, the preceding evaporation rates are molecular weight dependent and change as a function of time. By monitoring exclusively the solvent distribution within a near-surface region with neutron reflectivity, it is seen that the solvent loss rates follow power laws exceeding significantly classical diffusion driven

behavior. Moreover, in all investigated samples a gradient in solvent concentration during a limited time window is found.

The impact of the solvent evaporation characteristics cannot only be seen from a comparison of the near-surface composition profiles of solution cast films to a doctor-bladed film representing an almost solvent free technique. Also the altered conditions for the solvent evaporation upon performing the solution casting in an enclosed, controlled environment have a strong influence. For example humid environments are less efficient in slowing down the evaporation rate than solvent vapor atmospheres.

An appropriate sample preparation protocol is developed to isolate the effect of the relative humidity (RH) on the near-surface composition profiles and the related mechanical properties. For this purpose, an acrylic PSA with two components of different polarity is chosen. The more polar component is the glassy and the less polar component the sticky material. As a result, with increasing RH the surface concentration of the more polar component of the statistical copolymer increases. In addition, probe tack tests reveal an increase in tackiness as a function of the RH related to the enhanced presence of the harder material. In contrast, there is no detectable influence of the RH on the surface tension as determined via contact angle measurements. The results are explained via the installed near-surface composition.

The polar interactions between the humid atmosphere and the PSA film are so strong, that even upon switching to an unpolar solvent for the solution casting, still the more polar component forms the topmost layer. Exceptions can occur for high remaining solvent contents and, thus, uncompleted selective transport processes. Almost the inverse composition profile with a surface enrichment layer of the unpolar component is obtained by performing the solution casting with a non-polar solvent in an enclosed atmosphere of the corresponding solvent vapor.

For all investigated PSA films, the freshly prepared sample is not in an equilibrium state. During aging, the component with the lowest surface tension enriches at the sample surface even when the storage conditions favor the other component. For a sample preparation under ambient conditions, the underlying molecular reorganization driven by the minimization of the free-surface energy density can take almost one year. For short times on the order of weeks, the distribution of components depends on the initial state of the sample and, thus, on the selected preparation conditions. Furthermore, also lateral compositional fluctuations on a length scale of some tens of nanometers are found in the near-surface region. Interestingly, also these lateral domain sizes are time dependent.

Such domains are also detected when analyzing the morphology of spin-coated, ultra-thin acrylic PSA films. However, their position and size distribution is significantly different from what is observed in the case of thick, solution cast films. Also the mechanical

behavior as investigated with probe tack tests deviates. In the ultra-thin regime, the tackiness shows an exponential thickness dependence for very thin films. Above a certain threshold value, the tackiness is almost constant within the investigated range of film thicknesses. In addition, the role of the contact force is only minor for ultra-thin PSA films.

In upcoming projects it might be meaningful to extend the investigation of ultra-thin PSAs in a similar way as compared to the thick PSA films. Possibly, a fine tuning of the mechanical properties is also realizable by tailoring the morphology via the external conditions during the spin-coating. Also different types of substrate treatment appear to be promising routes in the case of ultra-thin PSA films.
Concerning thick PSA films, the focus of this work was on the free interface to the air. A meaningful extension to the presented work would be the characterization of the PSA films under the influence of an adherent. One natural adherent is already provided by the solid support of the PSA films. It is therefore worth investigating if there are also enrichment layers of one component in the vicinity of the substrate and if also the near-substrate region undergoes aging. In addition, it would be interesting whether the corresponding local structure affects the bonding with the solid support.
A further tuning of the bonding by employing substrates with different surface roughness values or even regularly structured substrates is conceivable. The resulting adhesion between the PSA film and the substrate could be tested in so-called peel tests. For the investigation of possible near-substrate compositional fluctuations of the PSA, neutron scattering based characterization techniques would be suitable.

Appendix

A.1 Program code for the justification of the layer model

In the following, the code of a *Microsoft Excel* based *Visual Basic* program is presented, with which a many-layer model in the syntax of the *Parratt32* is created. The purpose of this program is to cross-check if the simple layer model leads to the correct refractive index profile. For more details, please refer to section 3.2.1. The program is executable when the refractive index profile extracted from a fit to the data by *Parratt32* is inserted into the first two columns of an empty *Microsoft Excel* sheet.

```
Sub Modelfile()

    Dim n As Integer
    Dim nmax As Integer

    Range("D1").Select
    ActiveCell.FormulaR1C1 = "=COUNTA(C[-3])"

    nmax = Cells(1, 4).Value

    Columns("C:C").Select
    Selection.NumberFormat = "@"
    Range("A1").Select
    Cells(1, 3).Value = 1
    Cells(2, 3).Value = "7 9"
    Cells(4, 3).Value = "d / Å"
    Cells(5, 3).Value = "Im(rho) / Å^-2"
    Cells(6, 3).Value = "sigma / Å"
    Cells(7, 3).Value = "R(mag)"
```

```
    Cells(8, 3).Value = "I(mag)"
    Cells(9, 3).Value = "R(mag)"
    Cells(10, 3).Value = "air"
    Cells(11, 3).Value = "N/A"
    Cells(12, 3).Value = "0E+0"
    Cells(13, 3).Value = "0E+00"
    Cells(14, 3).Value = "N/A"
    Cells(15, 3).Value = "0"
    Cells(16, 3).Value = "0"

    For n = 1 To nmax
        Cells(10 + 7 * n, 3).Value = n
        Cells(11 + 7 * n, 3).Value = "1.00"
        Cells(12 + 7 * n, 3).Value = Cells(n, 2).Value
        Cells(13 + 7 * n, 3).Value = "1.496E-08"
        Cells(14 + 7 * n, 3).Value = "0"
        Cells(15 + 7 * n, 3).Value = "0"
        Cells(16 + 7 * n, 3).Value = "0"
    Next n

    Cells(17 + 7 * nmax, 3).Value = "bulk"
    Cells(18 + 7 * nmax, 3).Value = "N/A"
    Cells(19 + 7 * nmax, 3).Value = "8.953E-6"
    Cells(20 + 7 * nmax, 3).Value = "1.496E-08"
    Cells(21 + 7 * nmax, 3).Value = "0"
    Cells(22 + 7 * nmax, 3).Value = "0"
    Cells(23 + 7 * nmax, 3).Value = "0"
    Cells(24 + 7 * nmax, 3).Value = "1"
    Cells(25 + 7 * nmax, 3).Value = " 3.80000000000000E-0007"
    Cells(26 + 7 * nmax, 3).Value = "1"
    Cells(27 + 7 * nmax, 3).Value = "0"
    Cells(28 + 7 * nmax, 3).Value = "0"

End Sub
```

A.2 Program code for the grayscale coding

Another *Visual Basic* program is developed for the illustration of the grayscale coded composition profiles of P(EHA-stat-20MMA). For this purpose, the corresponding refractive index profile has to be inserted as the first two columns of an empty *Microsoft Excel* sheet. In a first step, with the following code each refractive index is converted into the respective grayscale value (see section 3.2.1) and the grayscale image of the complete profile is plotted.

```
Sub Makro1()

    Dim peha As Double
    peha = 0.0000085054289
    Dim pmma As Double
    pmma = 0.0000107447079
    Dim quotient As Double
    quotient = pmma - peha
    Dim dicke As Double
    dicke = 0.1

    Dim n As Integer
    n = 1
    Do Until IsEmpty(Cells(n, 1)) = True
    Cells(n, 3).Value = Round(255 * (Cells(n, 2).Value - peha)
                              / quotient, 0)
    If Cells(n, 3).Value < 0 Then
        Cells(n, 3).Value = 0
    End If
    If Cells(n, 3).Value > 255 Then
        Cells(n, 3).Value = 255
    End If
    Cells(n, 4).Value = 255 - Cells(n, 3).Value
    n = n + 1
    Loop

    n = 1
```

```
Do Until IsEmpty(Cells(n, 1)) = True
    ActiveSheet.Shapes.AddShape(msoShapeRectangle, 300, 99 + (n + 1)
                                            * dicke, 300, dicke). _
    Select
    Selection.ShapeRange.Fill.Visible = msoTrue
    Selection.ShapeRange.Fill.Solid
    Selection.ShapeRange.Fill.ForeColor.RGB = RGB(Cells(n, 4).Value,
                               Cells(n, 4).Value, Cells(n, 4).Value)
    Selection.ShapeRange.Fill.Transparency = 0#
    Selection.ShapeRange.Line.Weight = 0.75
    Selection.ShapeRange.Line.DashStyle = msoLineSolid
    Selection.ShapeRange.Line.Style = msoLineSingle
    Selection.ShapeRange.Line.Transparency = 0#
    Selection.ShapeRange.Line.Visible = msoFalse

    n = n + 1
Loop

ActiveSheet.Shapes.AddShape(msoShapeRectangle, 300, 99 + n
                               * dicke, 300, 0.8 * 1.5). _
    Select
    Selection.ShapeRange.Fill.Visible = msoTrue
    Selection.ShapeRange.Fill.Solid
    Selection.ShapeRange.Fill.ForeColor.RGB = RGB(255, 0, 0)
    Selection.ShapeRange.Fill.Transparency = 0#
    Selection.ShapeRange.Line.Weight = 0.75
    Selection.ShapeRange.Line.DashStyle = msoLineSolid
    Selection.ShapeRange.Line.Style = msoLineSingle
    Selection.ShapeRange.Line.Transparency = 0#
    Selection.ShapeRange.Line.Visible = msoFalse

ActiveSheet.Shapes.AddShape(msoShapeRectangle, 300, 99 + 201
                                  * dicke, 300, 0.8 * 2). _
    Select
    Selection.ShapeRange.Fill.Visible = msoTrue
    Selection.ShapeRange.Fill.Solid
    Selection.ShapeRange.Fill.ForeColor.RGB = RGB(255, 0, 0)
```

```
        Selection.ShapeRange.Fill.Transparency = 0#
        Selection.ShapeRange.Line.Weight = 0.75
        Selection.ShapeRange.Line.DashStyle = msoLineSolid
        Selection.ShapeRange.Line.Style = msoLineSingle
        Selection.ShapeRange.Line.Transparency = 0#
        Selection.ShapeRange.Line.Visible = msoFalse

    n = 1
    ActiveSheet.Shapes.AddShape(msoShapeRectangle, 300, 98.2 + n
                                        * dicke, 300, 0.8 * 2). _
        Select
        Selection.ShapeRange.Fill.Visible = msoTrue
        Selection.ShapeRange.Fill.Solid
        Selection.ShapeRange.Fill.ForeColor.RGB = RGB(255, 0, 0)
        Selection.ShapeRange.Fill.Transparency = 0#
        Selection.ShapeRange.Line.Weight = 0.75
        Selection.ShapeRange.Line.DashStyle = msoLineSolid
        Selection.ShapeRange.Line.Style = msoLineSingle
        Selection.ShapeRange.Line.Transparency = 0#
        Selection.ShapeRange.Line.Visible = msoFalse

    Cells(1, 6) = "zoom-in from"
    Cells(2, 6) = "zoom-in to"
    Cells(3, 6) = "linewidth"

End Sub
```

In a second step, the region of interest can be selected and the zoomed-in profile is provided as an output. For the execution of the second program, the line corresponding to the lower and the upper boundary as well as the desired linewidth have to be provided in cells "A7", "B7" and "C7", respectively. Throughout this work, a linewidth of 0.8 is chosen for the composition profiles representing the region $0 < z < 20$ nm. The program code for the second step is listed below.

```
Sub Makro2()
    Dim n As Integer
    Dim dicke As Double
    dicke = Cells(3, 7).Value

    For n = Cells(1, 7).Value To Cells(2, 7).Value

        ActiveSheet.Shapes.AddShape(msoShapeRectangle, 300, 300 + (n + 1)
                                                * dicke, 300, dicke). _
        Select
        Selection.ShapeRange.Fill.Visible = msoTrue
        Selection.ShapeRange.Fill.Solid
        Selection.ShapeRange.Fill.ForeColor.RGB = RGB(Cells(n, 4).Value,
                                Cells(n, 4).Value, Cells(n, 4).Value)
        Selection.ShapeRange.Fill.Transparency = 0#
        Selection.ShapeRange.Line.Weight = 0.75
        Selection.ShapeRange.Line.DashStyle = msoLineSolid
        Selection.ShapeRange.Line.Style = msoLineSingle
        Selection.ShapeRange.Line.Transparency = 0#
        Selection.ShapeRange.Line.Visible = msoFalse

    Next n
End Sub
```

A.3 Contact angle measurements

In this final section of the appendix, the contact angle data with the respective fits of the humidity series of P(EHA-stat-20MMA) (see section 6.1.2) are presented. The data corresponding to the preparation protocol under dry conditions has been shown in figure 6.3. The following five figures show the data corresponding to the higher RHs.

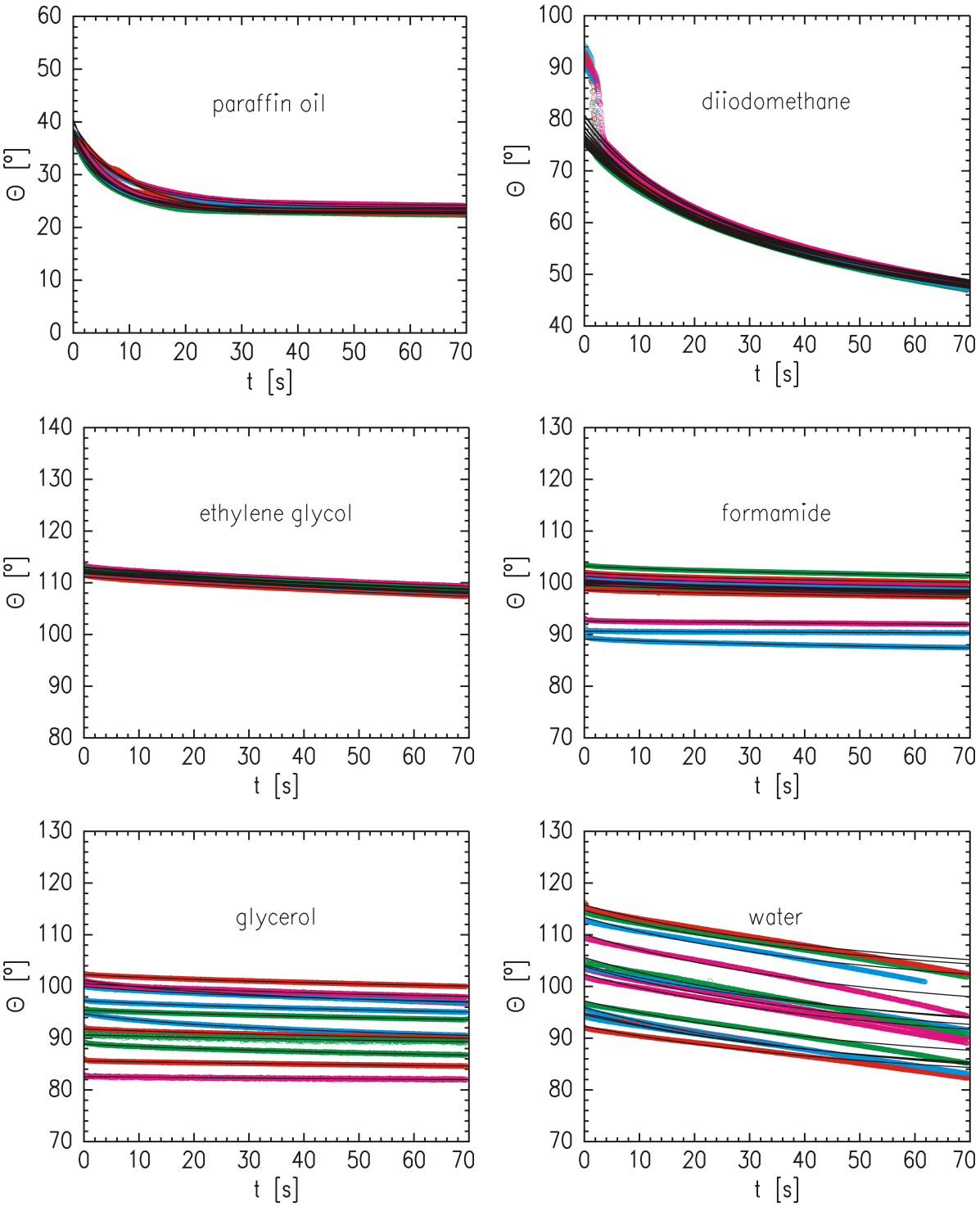

Figure A.1: *Time dependent contact angles of droplets of the test liquids paraffin oil, diiodomethane, ethylene glycol, formamide, glycerol and water on a P(EHA-stat-20MMA) film prepared under an RH of 23 %. Measured data are represented by colored symbols and the solid lines are the corresponding fits.*

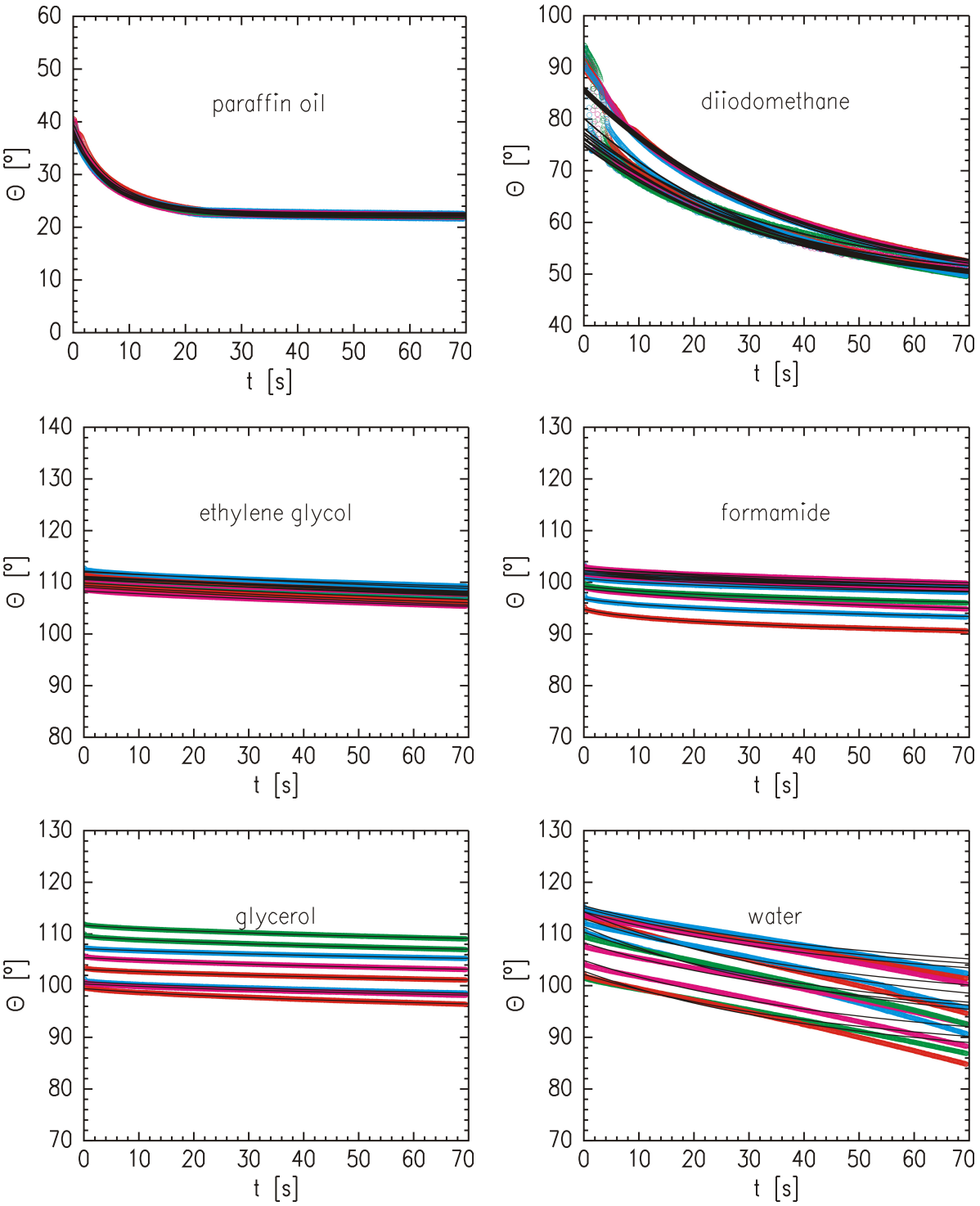

Figure A.2: *Time dependent contact angles of droplets of the test liquids paraffin oil, diiodomethane, ethylene glycol, formamide, glycerol and water on a P(EHA-stat-20MMA) film prepared under an RH of 43 %. Measured data are represented by colored symbols and the solid lines are the corresponding fits.*

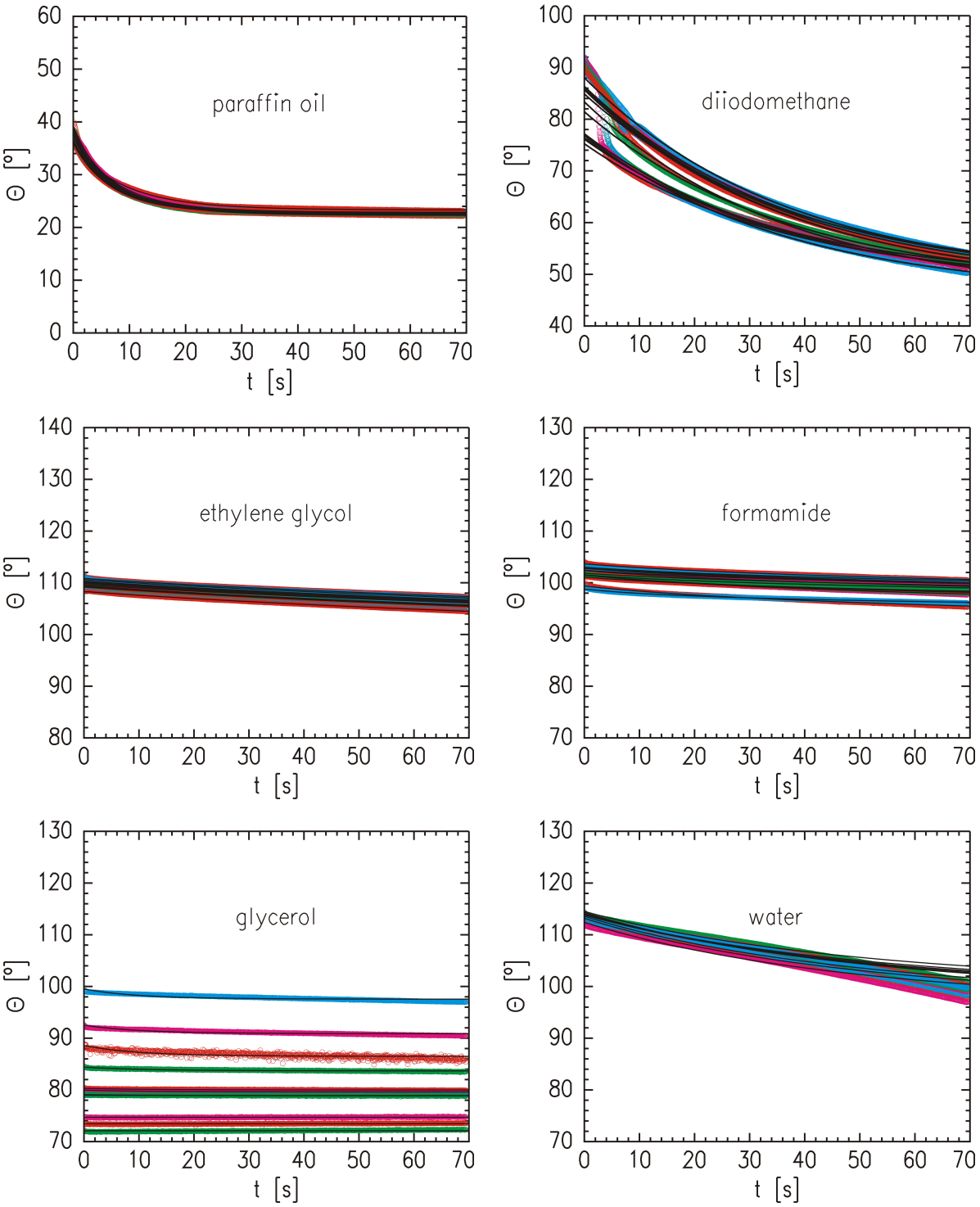

Figure A.3: *Time dependent contact angles of droplets of the test liquids paraffin oil, diiodomethane, ethylene glycol, formamide, glycerol and water on a P(EHA-stat-20MMA) film prepared under an RH of 54 %. Measured data are represented by colored symbols and the solid lines are the corresponding fits.*

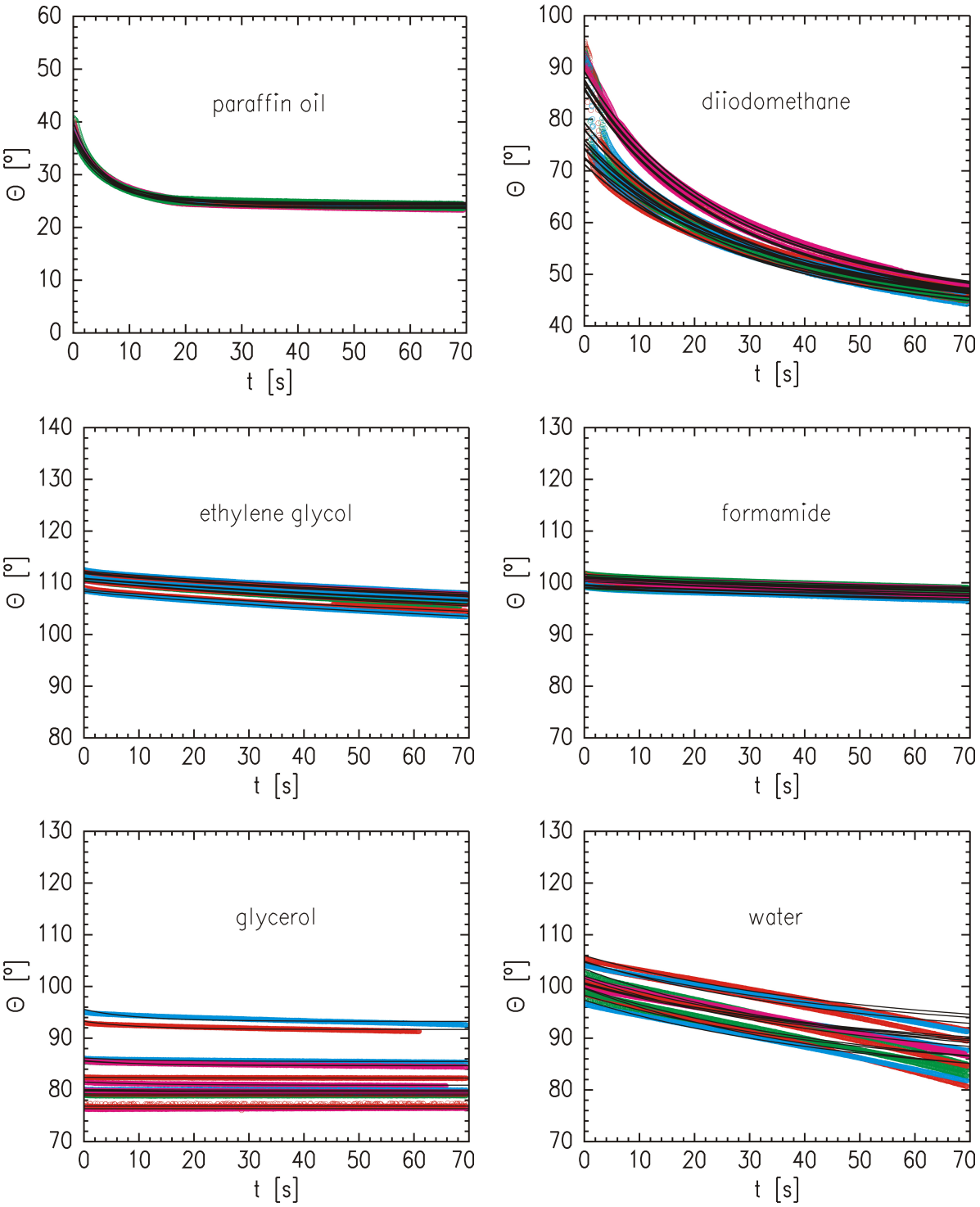

Figure A.4: *Time dependent contact angles of droplets of the test liquids paraffin oil, diiodomethane, ethylene glycol, formamide, glycerol and water on a P(EHA-stat-20MMA) film prepared under an RH of 75 %. Measured data are represented by colored symbols and the solid lines are the corresponding fits.*

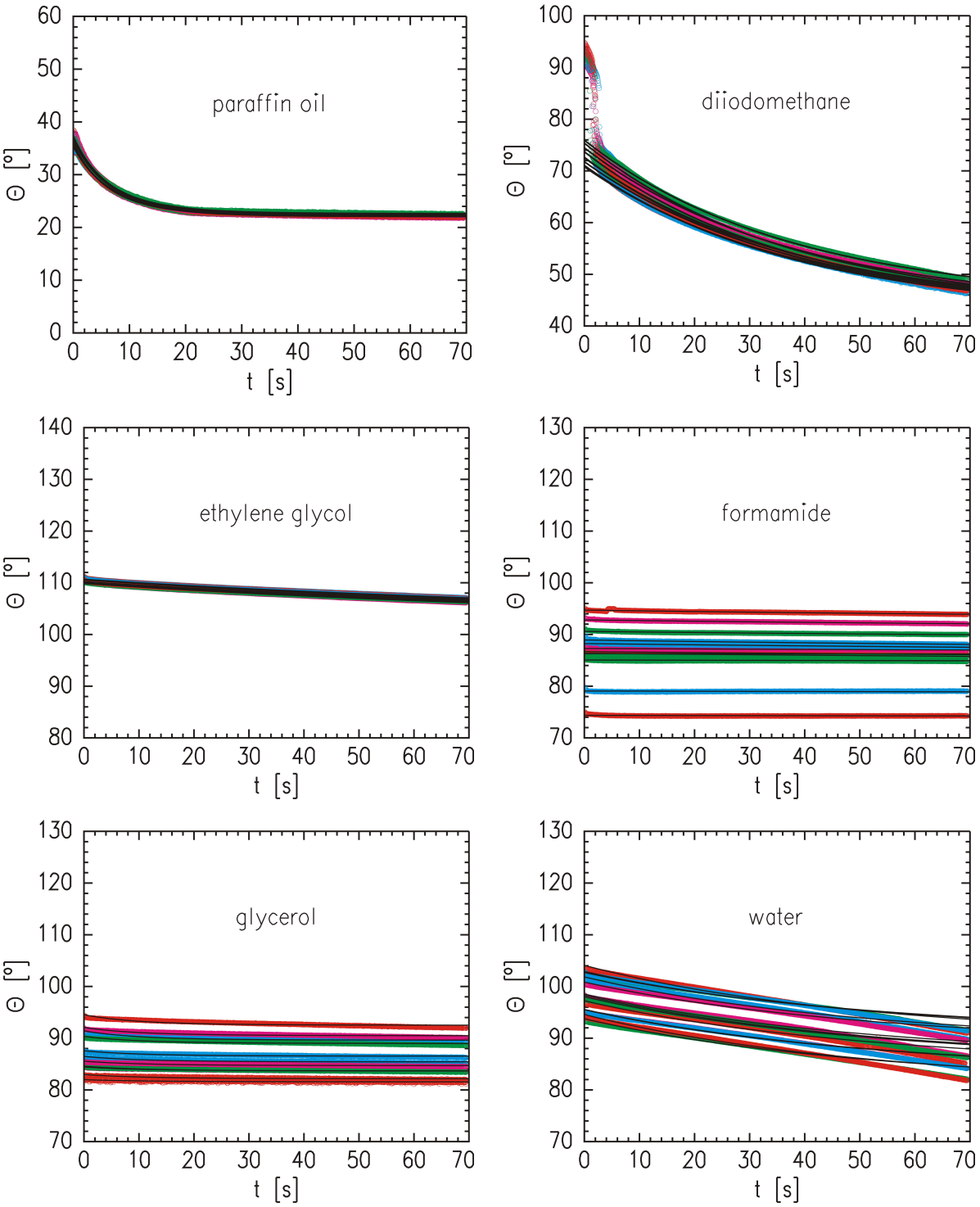

Figure A.5: *Time dependent contact angles of droplets of the test liquids paraffin oil, diiodomethane, ethylene glycol, formamide, glycerol and water on a P(EHA-stat-20MMA) film prepared under an RH of 85 %. Measured data are represented by colored symbols and the solid lines are the corresponding fits.*

Bibliography

[1] Elias, H.-G. *Macromolecules, Volume 4: Applications of Polymers*; Wiley-VCH Verlag, 2009.

[2] Creton, C. *MRS Bulletin* **2003**, *28*, 434–439.

[3] Anderson, C. C. *Ind. Eng. Chem.* **1969**, *61*, 48–52.

[4] Maurer, E.; Loi, S.; Wulff, D.; Willenbacher, N.; Müller-B, *Physica B* **2005**, *357*, 144–147.

[5] Lindner, A.; Maevis, T.; Brummer, R.; Lühmann, B.; Creton, C. *Langmuir* **2004**, *20*, 9156–9169.

[6] Rockford, L.; Mochrie, S. G. J.; Russell, T. P. *Macromolecules* **2001**, *34*, 1487–1492.

[7] Burke, J. *Solubility Parameters: Theory and Application*; AIC Book and Paper Group Annual, 1984; Vol. 3.

[8] Bandrup, J.; Immergut, E. H. *Polymer Handbook*; John Wiley & Sons Inc., 1989.

[9] Hildebrand, J. H.; Scott, R. L. *The Solubility of Nonelectrolytes*; Reinhold Pub. Corp., 1924.

[10] Scatchard, G. *Chem. Rev.* **1931**, *8*, 321–333.

[11] Butt, H.-J.; Graf, K.; Kappl, M. *Physics and Chemistry of Interfaces*; Wiley-VCH Verlag, 2003.

[12] Seemann, R.; Herminghaus, S.; Jacobs, K. *Phys. Rev. Lett.* **2001**, *86*, 5534–5537.

[13] Henderson, D.; Duh, D.-M.; Chu, X.; Wasan, D. *J. Colloid Interf. Sci.* **1997**, *185*, 265–268.

[14] Israelachvili, J. *Intermolecular & Surface Forces*; Academic Press Inc., 1991.

[15] Erbil, H. Y. *Surface Chemistry of Solid and Liquid Interfaces*; Blackwell Publishing Ltd, 2006.

[16] Owens, D. K.; Wendt, R. C. *J. Appl. Polym. Sci.* **1969**, *13*, 1741–1747.

[17] Fowkes, F. M. *Ind. Eng. Chem.* **1964**, *56*, 40–52.

[18] Pocius, A. V.; Dillard, D. A.; Chaundry, M. *Adhesion Science and Engineering: Vol. 1 - The Mechanics of Adhesion*; Elsevier, 2002.

[19] Strobl, G. *The Physics of Polymers*; Springer, 2007.

[20] Zosel, A. *J. Adhesion* **1994**, *44*, 1–16.

[21] Falsafi, A.; Bates, F. S.; Tirrell, M. *Macromolecules* **2001**, *34*, 1323–1327.

[22] Kamagata, K.; Saito, T.; Toyama, M. *J. Adhesion* **1970**, *2*, 279–291.

[23] Miyagi, Z.; Yamamoto, K. *J. Adhesion* **1987**, *21*, 243–250.

[24] Cantor, A. S. *J. Appl. Polym. Sci.* **2000**, *77*, 826–832.

[25] González, I.; Leiza, J. R.; Asua, J. M. *Macromolecules* **2006**, *39*, 5015–5020.

[26] Mizumachi, H. *J. Appl. Polym. Sci.* **1985**, *30*, 2675–2686.

[27] Plaut, R. H.; Williams, N.; Dillard, D. A. *J. Adhesion* **2001**, *76*, 37–53.

[28] Amouroux, N.; Petit, J.; Léger, L. *Langmuir* **2001**, *17*, 6510–6517.

[29] Phillips, J. P.; Deng, X.; Stephen, R. R.; Fortenberry, E. L.; Todd, M. L.; McClusky, D. M.; Stevenson, S.; Misra, R.; Morgan, S.; Long, T. E. *Polymer* **2007**, *48*, 6773–6781.

[30] Wang, X. P.; Xiao, X.; Tsui, O. K. C. *Macromolecules* **2001**, *34*, 4180–4185.

[31] Agirre, A.; Nase, J.; Degrandi, E.; Creton, C.; Asua, J. M. *J. Polym. Sci. Part A: Polym. Chem.* **2010**, *48*, 5030–5039.

[32] Müller-Buschbaum, P.; Ittner, T.; Maurer, E.; Körstgens, V.; Petry, W. *Macromol. Mater. Eng.* **2007**, *292*, 825–834.

[33] Zosel, A. *Int. J. Adhes. Adhes.* **1998**, *18*, 265–271.

[34] Webber, R. E.; Shull, K. R.; Roos, A.; Creton, C. *Phys. Rev. E* **2003**, *68*, 021805.

[35] Gent, A. N.; Lai, S.-M.; Nah, C.; Wang, C. *Rubber Chem. Technol.* **1994**, *67*, 610–619.

[36] Shull, K. R.; Creton, C. *J. Polym. Sci. Part B: Polym. Phys.* **2004**, *42*, 4023–4043.

[37] Gay, C.; Leibler, L. *Phys. Rev. Lett.* **1999**, *82*, 936–939.

[38] Peykova, Y.; Guriyanova, S.; V., L. O.; Diethert, A.; Müller-Buschbaum, P.; Willenbacher, N. *Int. J. Adhes. Adhes.* **2010**, *30*, 245–254.

[39] Creton, C. *Proc. Swiss Bonding* **2002**, 83–91.

[40] Lakrout, H.; Sergot, P.; Creton, C. *J. Adhesion* **1999**, *69*, 307–359.

[41] Chikina, I.; Gay, C. *Phys. Rev. Lett.* **2000**, *85*, 4546–4549.

[42] Yamaguchi, T.; Morita, H.; Doi, M. *Eur. Phys. J. E* **2006**, *20*, 7–17.

[43] Crosby, A. J.; Shull, K. R.; Lakrout, H.; Creton, C. *J. Appl. Phys.* **2000**, *88*, 2956–2966.

[44] Creton, C.; Hooker, J.; Shull, K. R. *Langmuir* **2001**, *17*, 4948–4954.

[45] Gedde, U. W. *Polymer Physics*; Springer, 1995.

[46] McNaught, A. D.; Wilkinson, A. *IUPAC. Compendium of Chemical Terminology*; Blackwell Scientific Publications, 1997.

[47] Flory, P. J. *J. Chem. Phys.* **1942**, *10*, 51–61.

[48] Huggins, M. L. *J. Am. Chem. Soc.* **1942**, *64*, 1712–1719.

[49] Leibler, L. *Macromolecules* **1980**, *13*, 1602–1617.

[50] Fredrickson, G. H.; Milner, S. T. *Phys. Rev. Lett.* **1991**, *67*, 835–838.

[51] Shakhnovich, E. I.; Gutin, A. M. *J. Phys. France* **1989**, *14*, 1843–1850.

[52] Houdayer, J.; Müller, M. *Macromolecules* **2004**, *37*, 4283–4295.

[53] Klos, J. S.; Romeis, D.; Sommer, J.-U. *J. Chem. Phys.* **2010**, *132*, 024907.

[54] Tolan, M. *X-Ray Scattering from Soft-Matter Thin Films,*; Springer, 1999.

[55] Müller-Buschbaum, P. *Polymer Surfaces and Interfaces: Characterization, Modification and Applications*; Springer, 2008.

[56] Renaud, G.; Lazzari, R.; Leroy, F. *Surf. Sci. Rep.* **2009**, *64*, 255–380.

[57] Rodrigues, W.; Sakata, O.; Lee, T.-L.; Walko, D. A.; Marasco, D. L.; Bedzyk, M. J. *J. Appl. Phys.* **2000**, *88*, 2391–2394.

[58] Abelès, F. *J. Phys. Radium* **1950**, *11*, 307–310.

[59] Parratt, L. G. *Phys. Rev.* **1954**, *95*, 359–369.

[60] El Feninat, F.; Elouatik, S.; Ellis, T. H.; Sacher, E.; Stangel, I. *Appl. Surf. Sci.* **2001**, *183*, 205–215.

[61] Beckmann, P.; Spizzichino, A. *The Scattering of Electromagntic Waves From Rough Surfaces*; Pergamon, 1963.

[62] Nevot, L.; Croce, P. *Rev. Phys. Appl.* **1980**, *15*, 761.

[63] Schalke, M.; Lösche, M. *Adv. Colloid Interface Sci.* **2000**, *88*, 243–274.

[64] Braun, C. *Parratt32*; HMI Berlin, 2002.

[65] Kiessig, H. *Ann. Phys.* **1931**, *10*, 769–788.

[66] Grillo, I. *Soft Matter Characterization*; Springer, 2008.

[67] Sears, V. F. *Neutron News* **1992**, *3*, 26–37.

[68] Lekner, J. *Physica B* **1991**, *173*, 99–111.

[69] Anastasiadis, S. H.; Russell, T. P.; Satija, S. K.; Majkrzak, C. F. *Phys. Rev. Lett.* **1989**, *62*, 1852–1855.

[70] Müller-Buschbaum, P.; Roth, S. V.; Burghammer, M.; Diethert, A.; Panagiotou, P.; Riekel, C. *Europhys. Lett.* **2003**, *61*, 639–645.

[71] Roth, S. V.; Burghammer, M.; Riekel, C.; Müller-Buschbaum, P.; Diethert, A.; Panagiotou, P.; Walter, H. *Appl. Phys. Lett.* **2003**, *82*, 1935–1937.

[72] Müller-Buschbaum, P. *A basic introduction to grazing incidence small angle X-ray scattering*; Springer, 2009.

[73] Müller-Buschbaum, P. *Anal. Bioanal. Chem.* **2003**, *376*, 3–10.

[74] Vineyard, G. H. *Phys. Rev. B* **1982**, *26*, 4146–4159.

[75] Holý, V.; Baumbach, T. *Phys. Rev. B* **1994**, *49*, 10668–10676.

[76] Sinha, S. K.; Sirota, E. B.; Garoff, S.; Stanley, H. B. *Phys. Rev. B* **1988**, *38*, 2297–2311.

[77] Salditt, T.; Metzger, T. H.; Peisl, J.; Reinker, B.; Moske, M.; Samwer, K. *Europhys. Lett.* **1995**, *32*, 331–336.

[78] Yoneda, Y. *Phys. Rev.* **1963**, *131*, 2010–2013.

[79] Naudon, A.; Babonneau, D.; Thiaudière, D.; Lequien, S. *Physica B* **2000**, *283*, 69–74.

[80] Bronstein, I. N.; Semendjajew, K. A.; Musiol, G.; Mühlig, H. *Taschenbuch der Mathematik*; Verlag Harri Deutsch, 1999.

[81] Hosemann, R.; Vogel, W.; Weick, D.; Baltá-Calleja, F. J. *Acta Cryst.* **1981**, *A37*, 85–91.

[82] Pedersen, J. S. *J. Appl. Cryst.* **1994**, *27*, 595–608.

[83] Babonneau, D.; Videnovic, I. R.; Garnier, M. G.; Oelhafen, P. *Phys. Rev. B* **2001**, *63*, 195401.

[84] Rauscher, M.; Salditt, T.; Spohn, H. *Phys. Rev. B* **1995**, *52*, 16855–16863.

[85] Babonneau, D. *J. Appl. Cryst.* **2010**, *43*, 929–936.

[86] Lazzari, R. *J. Appl. Cryst.* **2002**, *35*, 406–421.

[87] Sauzedde, F.; Hunkeler, D. *Int. J. Polym. Anal. Charact.* **2001**, *6*, 295–314.

[88] Cubitt, R.; Fragneto, G. *Appl. Phys. A* **2002**, *74*, s329–s331.

[89] Perlich, J.; Rubeck, J.; Botta, S.; Gehrke, R.; Roth, S. V.; Ruderer, M. A.; Prams, S. M.; Rawolle, M.; Zhong, Q.; Körstgens, V.; Müller-Buschbaum, P. *Rev. Sci. Instrum.* **2010**, *81*, 105105.

[90] Roth, S. V.; Döhrmann, R.; Dommach, M.; Kuhlmann, M.; Kröger, I.; Gehrke, R.; Walter, H.; Schroer, C.; Lengeler, B.; Müller-Buschbaum, P. *Rev. Sci. Instrum.* **2006**, *77*, 085106.

[91] Meier, R.; Ruderer, M. A.; Diethert, A.; Kaune, G.; Körstgens, V.; Roth, S. V.; Müller-Buschbaum, P. *J. Phys. Chem. B* **2011**, *115*, 2899–2909.

[92] van den Berg, A. M. J.; Smith, P. J.; Perelaer, J.; Schrof, W.; Koltzenburg, S.; Schubert, U. S. *Soft Matter* **2007**, *3*, 238–243.

[93] Dismukes, E. B. *J. Phys. Chem.* **1959**, *63*, 312–314.

[94] Menke, T. J.; Funke, Z.; Maier, R.-D.; Kressler, J. *Macromolecules* **2000**, *33*, 6120–6125.

[95] Erbil, H. Y.; Meric, R. A. *J. Phys. Chem. B* **1997**, *101*, 6867–6873.

[96] Erbil, H. Y.; Avci, Y. *Langmuir* **2002**, *18*, 5113–5119.

[97] Kano, Y.; Akiyama, S. *Polymer* **1993**, *34*, 376–381.

[98] Lavi, B.; Marmur, A. *Colloids Surf. A: Physicochem. Eng. Asp.* **2004**, *250*, 409–414.

[99] Müller-Buschbaum, P.; Stamm, M. *Macromolecules* **1998**, *31*, 3686–3692.

[100] Perlich, J.; Memesa, M.; Diethert, A.; Metwalli, E.; Wang, W.; Roth, S. V.; Timmann, A.; Gutmann, J. S.; Müller-Buschbaum, P. *ChemPhysChem* **2009**, *10*, 799–805.

[101] Giahi, A.; El Alaoui Faris, M.; Bassereau, P.; Salditt, T. *Eur. Phys. J. E* **2007**, *23*, 431–437.

[102] Leonard, M. J.; Strey, H. H. *Macromolecules* **2003**, *36*, 9549–9558.

[103] Lide, D. R. *CRC Handbook of Chemistry and Physics*; CRC Press, 1993.

[104] Greenspan, L. *Res. Natl. Bur. Stand. A* **1977**, *81*, 89–96.

[105] Schubert, D. W. *Polym. Bull.* **1997**, *38*, 177–184.

[106] Müller-Buschbaum, P. *Eur. Phys. J. E* **2003**, *12*, 443–448.

[107] Ishikawa, T.; Nagai, S. *J. Polym. Sci.: Polym. Phys. Ed.* **1977**, *15*, 1315–1317.

[108] Li, Y.; Yan, D.; Zhu, X. *Eur. Polym. J.* **2001**, *37*, 1849.

[109] Osemeahon, S. A.; Barminas, J. T. *Afr. J. Biotechnol.* **2007**, *6*, 1432–1440.

[110] Swamy, T. M. M.; Ramaraj, B.; Siddaramaiah, *J. Appl. Polymer Sci.* **2009**, *112*, 2235–2240.

[111] Jang, J.; Kim, E. K. *J. Appl. Polym. Sci.* **1999**, *71*, 585–593.

[112] Barbetta, A.; Rizzitelli, G.; Bedini, R.; Pecci, R.; Dentini, M. *Soft Matter* **2010**, *6*, 1785–1792.

[113] Wang, T.; Dunbar, A. D. F.; Staniec, P. A.; Pearson, A. J.; Hopkinson, P. E.; MacDonald, J. E.; Lilliu, S.; Pizzey, C.; Terrill, N. J.; Donald, A. M.; Ryan, A. J.; Jones, R. A. L.; Lidzey, D. G. *Soft Matter* **2010**, *6*, 4128–4134.

[114] Tanaka, K.; Okahata, Y. *J. Am. Chem. Soc.* **1996**, *118*, 10679–10683.

[115] Sun, Y.-M.; Huang, W.-F.; Chang, C.-C. *J. Membr. Sci.* **1999**, *157*, 159–170.

[116] Muñoz-Bonilla, A.; Heuts, J. P. A.; Fernández-García, M. *Soft Matter* **2011**, *7*, 2493–2499.

[117] Lin, H.-L.; Yu, T. L.; Huang, C.-H.; Lin, T.-L. *J. Polym. Sci. Part B: Polym. Phys.* **2005**, *43*, 3044–3057.

[118] Curtin, D. E.; Lousenberg, D. R.; Henry, T. J.; Tangeman, P. C.; Tisack, M. E. *J. Power Sourc.* **2004**, *131*, 41–48.

[119] Shankar, R.; Ghosh, T. K.; Spontak, R. J. *Soft Matter* **2007**, *3*, 1116–1129.

[120] Topham, P. D.; Howse, J. R.; Fernyhough, C. M.; Ryan, A. J. *Soft Matter* **2007**, *3*, 1506–1512.

[121] Katz, H. E.; Lovinger, A. J.; Johnson, J. .; Kloc, C.; Siegrist, T.; Li, W.; Lin, Y.-Y.; Dodabalapur, A. *Nature* **2000**, *404*, 478–481.

[122] Cicoira, F.; Santato, C.; Melucci, M.; Favaretto, L.; Gazzano, M.; Muccini, M.; Barbarella, G. *Adv. Mater.* **2006**, *18*, 169–174.

[123] Kim, G.; Libera, M. *Macromolecules* **1998**, *31*, 2569–2577.

[124] Gong, Y.; Hu, Z.; Chen, Y.; Huang, H.; He, T. *Langmuir* **2005**, *21*, 11870–11877.

[125] Anthamatten, M.; Letts, S. A.; Cook, R. C. *Langmuir* **2004**, *20*, 6288–6296.

[126] Benz, M.; Euler, W. B.; Gregory, O. J. *Langmuir* **2001**, *17*, 239–243.

[127] Cosgrove, T.; Phipps, J. S.; Richardson, R. M.; Hair, M. L.; Guzonas, D. A. *Macromolecules* **1993**, *26*, 4363–4367.

[128] O´Connor, A. E.; Macosko, C. W. *J. Appl. Polym. Sci.* **2002**, *86*, 3355–3367.

[129] Campoy-Quiles, T.; Ferenczi, T.; Agostinelli, T.; Etchegoin, P. G.; Youngkyoo, K.; Anthopoulos, T. D.; Stavrinou, P. N.; Bradley, D. C.; Nelson, J. *Nature Materials* **2008**, *7*, 158–164.

[130] Shikler, R.; Chiesa, M.; Friend, R. H. *Macromolecules* **2006**, *39*, 5393–5399.

[131] Müller-Buschbaum, P.; Bauer, E.; Maurer, E.; Nelson, A.; Cubitt, R. *phys. stat. sol. (RRL)* **2007**, *1*, R68–R70.

[132] Grinsted, R. A.; Clark, L.; Koenig, J. L. *Macromolecules* **1992**, *25*, 1235–1241.

[133] Tsige, M.; Grest, G. S. *Macromolecules* **2004**, *37*, 4333–4335.

[134] Diethert, A.; Metwalli, E.; Meier, R.; Zhong, Q.; Campbell, R. A.; Cubitt, R.; Müller-Buschbaum, P. *Soft Matter* **2011**, DOI: 10.1039/c1sm05311f.

[135] Braslau, A.; Deutsch, M.; Pershan, P. S.; Weiss, A. H.; Als-Nielsen, J.; Bohr, J. *Phys. Rev. Lett.* **1985**, *54*, 114–117.

[136] Peter, S.; Meyer, H.; Baschnagel, J. *J. Chem. Phys.* **2009**, *131*, 014902.

[137] Peter, S.; Meyer, H.; Baschnagel, J. *J. Chem. Phys.* **2009**, *131*, 014903.

[138] Yu, Z.; Yashi, U.; McGervey, J. D.; Jamieson, A. M.; Simha, R. *J. Polym. Sci. Part B: Polym. Phys.* **1994**, *32*, 2637–2644.

[139] Harms, S.; Rätzke, K.; Faupel, F.; Egger, W.; Ravello, L.; Laschewsky, A.; Wang, W.; Müller-Buschbaum, P. *Macromol. Rapid Commun.* **2010**, *31*, 1364–1367.

[140] Mayes, A. M. *Macromolecules* **1994**, *27*, 3114–3115.

[141] Müller-Buschbaum, P.; Gutmann, J. S.; Stamm, M. *Macromolecules* **2000**, *33*, 4886–4895.

[142] Schwarz, S. A.; Wilkens, B. J.; Pudensi, M. A. A.; Rafailovich, M. H.; Sokolov, J.; Zhao, X.; Zhao, W.; Zheng, X.; Russell, T. P.; Jones, R. A. L. *Mol. Phys.* **1992**, *76*, 937–950.

[143] Jones, R. A. L.; Kramer, E. J.; Rafailovich, M. H.; Sokolov, J.; Schwarz, S. A. *Phys. Rev. Lett.* **1989**, *62*, 281–283.

[144] El-Mabrouk, K.; Belaiche, M.; Bousmina, M. *J. Colloid Interf. Sci.* **2007**, *306*, 354–367.

[145] Busch, P.; Posselt, D.; Smiglies, D.-M.; Rauscher, M.; Papadakis, C. M. *Macromolecules* **2007**, *40*, 630–640.

[146] Busch, P.; Posselt, D.; Smiglies, D.-M.; Rheinländer, B.; Kremer, F.; Papadakis, C. M. *Macromolecules* **2003**, *36*, 8717–8727.

[147] Coutandin, J.; Ehlich, D.; Sillescu, H.; Wang, C.-H. *Macromolecules* **1985**, *18*, 589–590.

[148] Aymonier, A.; Leclercq, D.; Tordjeman, P.; Papon, E.; Villenave, J.-J. *J. Appl. Polym. Sci.* **2003**, *89*, 2749–2756.

[149] Laureau, C.; Vicente, M.; Barandiaran, M. J.; Leiza, J. R.; Asua, J. M. *J. Appl. Polym. Sci.* **2001**, *81*, 1258–1265.

[150] Diethert, A.; Peykova, Y.; Willenbacher, N.; Müller-Buschbaum, P. *ACS Appl. Mater. Interfaces* **2010**, *2*, 2060–2068.

[151] Perlich, J.; Körstgens, V.; Metwalli, E.; Schulz, L.; Georgii, R.; Müller-Buschbaum, P. *Macromolecules* **2009**, *42*, 337–344.

[152] Barton, A. F. M. *Handbook of Solubility Parameters*; CRC Press, 1983.

[153] Zhang, H.; Wang, J.; Chen, Y.; Zhang, M. *J. Chem. Eng. Data* **2007**, *52*, 982–985.

[154] Walheim, S.; Böltau, M.; Mlynek, J.; Krausch, G.; Steiner, U. *Macromolecules* **1997**, *30*, 4995–5003.

[155] Ngwa, W.; Wannemacher, R.; Gril, W.; Serghei, A.; Kremer, F.; Kundu, T. *Macromolecules* **2004**, *37*, 1691–1692.

[156] Elbs, H.; Fukunaga, K.; Stadler, R.; Sauer, G.; Magerle, R.; Krausch, G. *Macromolecules* **1999**, *32*, 1204–1211.

[157] Zhuang, H.; Gardella Jr., J. A. *Macromolecules* **1997**, *30*, 3632–3639.

[158] Aymonier, A.; Papon, E.; Villenave, J.-J.; Tordjeman, P.; Pirri, R.; Gérard, P. *Chem. Mater.* **2001**, *13*, 2562–2566.

[159] Gardon, J. L. *Encyclopedia of Polymer Science and Technology*; Wiley-Interscience, 1965.

[160] Kwok, D. Y.; Leung, A.; Lam, C. N. C.; Li, A.; Wu, R.; Neumann, A. W. *J. Colloid Interf. Sci.* **1998**, *206*, 44–51.

[161] da Rocha, S. R. P.; Harrison, K. L.; Johnston, K. P. *Langmuir* **1999**, *15*, 419–428.

[162] Frank, B.; Gast, A. P.; Russell, T. P.; Brown, H. R.; Hawker, C. *Macromolecules* **1996**, *29*, 6531–6534.

[163] Sharma, A.; Reiter, G. *J. Colloid Interf. Sci.* **1996**, *178*, 383–399.

[164] Kessel, S.; Schmidt, S.; Müller, R.; Wischerhoff, E.; Laschewsky, A.; Lutz, J.-F.; Uhlig, K.; Lankenau, A.; Duschl, K.; Fery, A. *Langmuir* **2010**, *26*, 3462–3467.

[165] Cooperstein, M. A.; Canavan, H. E. *Langmuir* **2010**, *26*, 7695–7707.

[166] Boyne, J. M.; Millan, E. J.; Webster, I. *Int. J. Adhes. Adhes.* **2001**, *21*, 49–53.

[167] Chivers, R. A. *Int. J. Adhes. Adhes.* **2001**, *21*, 381–388.

[168] Chang, T.; Sproat, E. A.; Lai, Y.; Shephard, N. E.; Dillard, D. A. *J. Adhesion* **1997**, *60*, 153–162.

[169] Moon, S.; Foster, M. D. *Langmuir* **2002**, *18*, 8108–8115.

[170] Shah, S. S.; Howland, M. C.; Chen, L.; Silangcruz, J.; Verkhoturov, S. V.; Schweikert, E. A.; Parikh, A. N.; Revzin, A. *ACS Appl. Mater. Interfaces* **2009**, *1*, 2592–2601.

[171] Qu, L.; Dai, L.; Stone, M.; Xia, Z.; Wang, Z. L. *Science* **2008**, *322*, 238–242.

[172] Hu, S.; Jiang, H.; Xia, Z.; Gao, X. *ACS Appl. Mater. Interfaces* **2010**, *2*, 2570–2578.

[173] Feng, X.; Meitl, M. A.; Bowen, A. M.; Huang, Y.; Nuzzo, R. G.; Rogers, J. A. *Langmuir* **2007**, *23*, 12555–125560.

[174] Cho, K.; Cho, J. H.; Yoon, S.; Park, C. E.; Lee, J.-C.; Han, S.-H.; Lee, K.-B.; Koo, J. *Macromolecules* **2003**, *36*, 2009–2014.

[175] de Crevoisier, G.; Fabre, P.; Corpart, J.-M.; Leibler, L. *Science* **1999**, *285*, 1246–1249.

[176] Agirre, A.; de las Heras-Alarcón, C.; Wang, T.; Keddie, J. L.; Asua, J. M. *ACS* **2010**, *2*, 443–451.

[177] Retsos, H.; Gorodyska, G.; Kiriy, A.; Stamm, M.; Creton, C. *Langmuir* **2005**, *21*, 7722–7725.

[178] Lemieux, M.; Usov, D.; Minko, S.; Stamm, M.; Shulha, H.; Tsukruk, V. V. *Macromolecules* **2003**, *36*, 7244–7255.

[179] Liu, X.; Ye, Q.; Yu, B.; Liang, Y.; Liu, W.; Zhou, F. *Langmuir* **2010**, *26*, 12377–12382.

[180] Caquineau, H.; Menut, P.; Deratani, A.; Dupuy, C. *Polym. Eng. Sci.* **2003**, *43*, 798–808.

[181] Park, M. J.; Balsara, N. P.; Jackson, A. *Macromolecules* **2009**, *42*, 6808–6815.

[182] Geldhauser, T.; Walheim, S.; Schimmel, T.; Leiderer, P.; Boneberg, J. *Macromolecules* **2010**, *43*, 1124–1128.

[183] Diethert, A.; Ecker, K.; Peykova, Y.; Willenbacher, N.; Müller-Buschbaum, P. *ACS Appl. Mater. Interfaces* **2011**, *3*, 2012–2021.

[184] Diethert, A.; Müller-Buschbaum, P. *J. Adhesion* **2011**, accepted.

[185] Wu, S. *Org. Coat. Plast. Chem.* **1971**, *31*, 27.

[186] Piglowski, J. M.; Bryjak, M. *Eur. Polym. J.* **1998**, *34*, 1669–1673.

[187] Gu, Z.; Alexandridis, P. *Langmuir* **2005**, *21*, 1806–1817.

[188] Staeger, M.; Finot, E.; Brachais, C.-H.; Auguste, S.; Durand, H. *Appl. Surf. Sci.* **2002**, *185*, 231–242.

[189] Falsafi, A.; Tirrell, M.; Pocius, A. V. *Langmuir* **2000**, *16*, 1816–1824.

[190] Dimitrova, T. D.; Johannsmann, D.; Willenbacher, N.; Pfau, A. *Langmuir* **2003**, *19*, 5748–5755.

[191] Paiva, A.; Sheller, N.; Foster, M. D.; Crosby, A. J.; Shull, K. R. *Macromolecules* **2001**, *34*, 2269–2276.

[192] Czech, Z. *Int. J. Adhes. Adhes.* **2006**, *26*, 414–418.

[193] Ferguson, G. S.; Chaundry, M. K.; Sigal, G. B.; Whitesides, G. M. *Science* **1991**, *253*, 776–778.

[194] Newby, B. Z.; Chaundry, M. K.; Brown, H. R. *Science* **1995**, *269*, 1407–1409.

[195] Müller, K.-D.; Bacher, W.; Heckele, M. *Int. Workshop on Micro Electro Mechanical Systems* **1998**, 263–267.

[196] Kentsch, J.; Dürr, M.; Schnelle, T.; Gradl, G.; Müller, T.; Jäger, M.; Normann, A.; Stelzle, M. *IEE Proc.-Nanobiotechnol.* **2003**, *150*, 82–89.

[197] Dreuth, H.; Heiden, C. *Mater. Sci. Eng. C* **1998**, *5*, 227–231.

[198] Uddin, M. A.; Ho, W. F.; Chan, H. P. *J. Mater. Sci.: Mater. Electron.* **2007**, *18*, 655–663.

[199] Meng, D.; Wang, Q. *Soft Matter* **2010**, *6*, 5891–5906.

[200] Chremos, A.; Margaritis, K.; Panagiotopoulos, A. Z. *Soft Matter* **2010**, *6*, 3588–3595.

[201] Wu, W.; van Zanten, J. H.; Orts, W. J. *Macromolecules* **1995**, *28*, 771–774.

[202] Akabori, K.; Tanaka, K.; Kajiyama, T.; Takahara, A. *Macromolecules* **2003**, *36*, 4937–4943.

[203] Yamada, S.; Nakamura, G.; Amiya, T. *Langmuir* **2001**, *17*, 1693–1699.

[204] Luengo, G.; Schmitt, F.-J.; Hill, R.; Israelachvili, J. *Macromolecules* **1997**, *30*, 2482–2494.

[205] Domke, J.; Radmacher, M. *Langmuir* **1998**, *14*, 3320–3325.

[206] Stafford, C. M.; Vogt, B. D.; Harrison, C.; Julthongpiput, D.; Huang, R. *Macromolecules* **2006**, *39*, 5095–5099.

[207] Chan, E. P.; Page, K. A.; Hyuk Im, S.; Patton, D. L.; Huang, R.; Stafford, C. M. *Soft Matter* **2009**, *5*, 4638–4641.

[208] Bodiguel, H.; Fretigny, C. *Macromolecules* **2007**, *40*, 7291–7298.

[209] Portigliatti, M.; Koutsos, V.; Hervet, H.; Léger, L. *Langmuir* **2000**, *16*, 6374–6376.

[210] Diethert, A.; Körstgens, V.; Magerl, D.; Ecker, K.; Perlich, J.; Roth, S. V.; Müller-Buschbaum, P. **2011**, submitted.

[211] Ruderer, M. A.; Hirzinger, M.; Müller-Buschbaum, P. *ChemPhysChem* **2009**, *10*, 2692–2697.

List of publications

Publications related to the dissertation

- A. Diethert, K. Ecker, Y. Peykova, N. Willenbacher, P. Müller-Buschbaum: Tailoring the near-surface composition profiles of pressure sensitive adhesive films and the resulting mechanical properties; *ACS Appl. Mater. Interfaces* **2011**, *3*, 2012-2021.

- A. Diethert, E. Metwalli, R. Meier, Q. Zhong, R. A. Campbell, R. Cubitt, P. Müller-Buschbaum: In-situ neutron reflectometry study of the near-surface solvent concentration profile during solution casting; *Soft Matter* **2011**, DOI: 10.1039/c1sm05311f.

- A. Diethert, P. Müller-Buschbaum: Probing the near-surface composition profile of pressure sensitive adhesive films with x-ray reflectivity, *J. Adhesion* **2011**, accepted for publication.

- A. Diethert, Y. Peykova, N. Willenbacher, P. Müller-Buschbaum: Near-surface composition profiles and the adhesive properties of statistical copolymer films being model systems of pressure sensitive adhesive films; *ACS Appl. Mater. Interfaces* **2010**, *2*, 2060-2068.

- Y. Peykova, S. Guriyanova, O. Lebedeva, A. Diethert, P. Müller-Buschbaum, N. Willenbacher: The effect of surface roughness on adhesive properties of acrylate copolymers; *Int. J. Adhes. Adhes.* **2010**, *30*, 245-254.

- A. Diethert, V. Körstgens, D. Magerl, K. Ecker, J. Perlich, S. V. Roth, P. Müller-Buschbaum: Structure and macroscopic tackiness of ultra-thin pressure sensitive adhesive films, submitted.

- A. Diethert, E. Metwalli, R. Meier, Q. Zhong, R. A. Campbell, R. Cubitt, P. Müller-Buschbaum: Near-surface solvent content profiles during solution casting; *Annual Report of the Institut Laue-Langevin (ILL) (Scientific Highlights)* **2011**, 42-43.

Further publications

- P. Müller-Buschbaum, D. Magerl, R. Hengstler, J.-F. Moulin, V. Körstgens, A. Diethert, J. Perlich, S. V. Roth, M. Burghammer, C. Riekel, M. Gross, F. Varnik, P. Uhlmann, M. Stamm, J. M. Feldkamp, C. G. Schroer: Structure and flow of droplets on solid surfaces; *J. Phys. Condens. Matter* **2011**, *23*, 184111.

- R. Meier, M. A. Ruderer, A. Diethert, G. Kaune, V. Körstgens, S. V. Roth, P. Müller-Buschbaum: Influence of Film Thickness on the Phase Separation Mechanism in Ultrathin Conducting Polymer Blend Films; *J. Phys. Chem. B* **2011**, *115*, 2899-2909.

- M. M. Abul Kashem, G. Kaune, A. Diethert, W. Wang, K. Schlage, S. Couet, R. Röhlsberger, S. V. Roth, P. Müller-Buschbaum: Selective doping of block copolymer nanodomains by sputter deposition of iron; *Macromolecules* **2011**, *44*, 1621-1627.

- E. Metwalli, J. Perlich, W. Wang, A. Diethert, S. V. Roth, C. M. Papadakis, P. Müller-Buschbaum: Morphology of semicrystalline diblock copolymer thin films upon directional solvent vapor flow; *Macromol. Chem. Phys.* **2010**, *21*, 2102-2108.

- G. Kaune, M. Memesa, R. Meier, M. A. Ruderer, A. Diethert, S. V. Roth, M. D'Acunzi, J. S. Gutmann, P. Müller-Buschbaum: Hierarchically structured titania films prepared by polymer/colloidal templating; *ACS Appl. Mater. Interfaces* **2009**, *1*, 2862-2869.

- E. Metwalli, J.-F. Moulin, J. Perlich, W. Wang, A. Diethert, S. V. Roth, P. Müller-Buschbaum: Polymer template-assisted growth of gold nanowires using a novel flow-stream technique; *Langmuir* **2009**, *25*, 11815-11821.

- M. M. Abul Kashem, J. Perlich, A. Diethert, W. Wang, M. Memesa, J. S. Gutmann, E. Majkova, I. Capek, S. V. Roth, W. Petry, P. Müller-Buschbaum: Array of magnetic nanoparticles via particle co-operated self-assembly in block copolymer thin film; *Macromolecules* **2009**, *42*, 6202-6208.

- J. Perlich, M. Memesa, A. Diethert, E. Metwalli, W. Wang, S. V. Roth, A. Timmann, J. S. Gutmann, P. Müller-Buschbaum: Layer-by-layer fabrication of hierarchical structures in sol-gel templated thin titania films; *phys. stat. sol. (RRL)* **2009**, *3*, 118-120.

- J. Perlich, M. Memesa, A. Diethert, E. Metwalli, W. Wang, S. V. Roth, A. Timmann, J. S. Gutmann, P. Müller-Buschbaum: Preservation of the Morphology of a

Self-Encapsulated Thin Titania Film in a Functional Multilayer Stack: An X-Ray Scattering Study; *Chem. Phys. Chem.* **2009**, *10*, 799-805.

- A. Diethert, F. Finster, D. Schiefenender: Fermion Systems in discrete space-time exemplifying the spontaneous generation of a causal structure; *Int. J. Mod. Phys. A* **2008**, *23*, 4579-4620.

- S. V. Roth, P. Müller-Buschbaum, M. Burghammer, H. Walter, P. Panagiotou, A. Diethert, C. Riekel: Microbeam grazing incidence small angle x-ray scattering - a new method to investigate nanostructured heterogeneous thin films and multilayers; *Spectrochimica Acta Part B: Atomic Spectroscopy* **2004**, *59*, 1765-1773.

- S. V. Roth, M. Burghammer, C. Ferrero, A. Diethert, P. Müller-Buschbaum: Fatigue behaviour of industrial polymers - a microbeam SAXS investigation; *J. Appl. Cryst.* **2003**, *36*, 684-688.

- S. V. Roth, M. Burghammer, C. Riekel, P. Müller-Buschbaum, A. Diethert, P. Panagiotou, H. Walter: Self-assembled gradient nanoparticle-polymer multilayers investigated by an advanced characterisation method: Microbeam grazing incidence x-ray scattering; *Appl. Phys. Lett.* **2003**, *82*, 1935-1937.

- P. Müller-Buschbaum, S. V. Roth, M. Burghammer, A. Diethert, P. Panagiotou, C. Riekel: Multiple-scaled polymer surfaces investigated with micro-focus grazing incidence small-angle x-ray scattering; *Europhys. Lett.* **2003**, *61*, 639-645.

Scientific reports

- A. Diethert, Y. Peykova, N. Willenbacher, P. Müller-Buschbaum: Near-surface composition profiles of pressure sensitive adhesive films; *Lehrstuhl für Funktionelle Materialien, Annual report 2010.*

- A. Diethert, E. Metwalli, R. Meier, Q. Zhong, R. A. Campbell, R. Cubitt, P. Müller-Buschbaum: Near-surface solvent content profiles evolving during solution casting; *Lehrstuhl für Funktionelle Materialien, Annual report 2010.*

- P. Müller-Buschbaum, A. Diethert: Einfluss von Grenzflächeneffekten auf die Adhäsion weicher Polymere; *Final report to the Deutsche Forschungsgemeinschaft (DFG), project number MU 1487/6, 2010.*

- A. Diethert, E. Metwalli, R. Meier, Q. Zhong, R. A. Campbell, R. Cubitt, P. Müller-Buschbaum: Solvent driven enrichment of monomers; *Experimental Report for the Institut Laue-Langevin (ILL), 2010.*

- A. Diethert, E. Metwalli, W. Wang, J. Perlich, S. V. Roth, P. Müller-Buschbaum: Surface-near structures in pressure sensitive adhesive films; *HASYLAB, Annual report 2009.*

- A. K. Sommer, A. Diethert, P. Müller-Buschbaum: Detection of the surface energy of PSA films by contact angle measurement; *Lehrstuhl für Funktionelle Materialien, Annual report 2009.*

- A.Diethert, P. Müller-Buschbaum: Near-surface Composition Profiles Of Pressure Sensitive Adhesive Films; *Lehrstuhl für Funktionelle Materialien, Annual report 2009.*

- A. Diethert, E. Metwalli, J. Perlich, W. Wang, R. Gehrke, A. Timmann, S. V. Roth, P. Müller-Buschbaum: Surface enrichment layers in pressure sensitive adhesive films; *HASYLAB, Annual report 2008.*

- A. Diethert, P. Müller-Buschbaum: Surface Enrichment Layers In Pressure Sensitive Adhesive Films; *Lehrstuhl für Funktionelle Materialien, Annual report 2008.*

- A. Diethert, P. Müller-Buschbaum: Surface enrichment in statistical copolymer films; *Lehrstuhl für Funktionelle Materialien, Annual report 2007.*

- A. Diethert, P. Müller-Buschbaum: GISAXS study of surface enrichment layers in statistical copolymer films; *HASYLAB, Annual report 2007.*

Conference talks

- A. Diethert, Y. Peykova, N. Willenbacher, P. Müller-Buschbaum: Near-surface composition profiles of pressure sensitive adhesive films and their influence on the mechanical properties; *World Congress of Adhesion and Related Phenomena*, Arcachon (France), September 2010.

- P. Müller-Buschbaum, A. Diethert, V. Körstgens, D. Magerl, Y. Peykova, O. Lebedeva, N. Willenbacher: Surface enrichment layers in pressure sensitive adhesive films; *43rd IUPAC World Polymer Congress: MACRO2010*, Glasgow (Scotland), July 2010.

- A. Diethert, S. V. Roth, P. Müller-Buschbaum: Surface-near structuring of pressure sensitive adhesive films; *DPG spring meeting*, Regensburg (Germany), March 2010.

- A. Diethert, P. Müller-Buschbaum: Surface-near composition profiles of pressure sensitive adhesive films; *4th FRM-II Workshop on Neutron Scattering*, Burg Rothenfels (Germany), June 2009.

- A. Diethert, S. V. Roth, P. Müller-Buschbaum: Surface enrichment layers in pressure sensitive adhesive films; *DPG spring meeting*, Dresden (Germany), March 2009.

- A. Diethert, S. V. Roth, P. Müller-Buschbaum: Surface enrichment layers in pressure sensitive adhesive films; *Congress and general assembly of the international Union of crystallography IUCr2008*, Osaka (Japan), August 2008.

Conference poster presentations

- A. Diethert, K. Ecker, Y. Peykova, N. Willenbacher, P. Müller-Buschbaum: Tailoring the near-surface composition profiles of pressure sensitive adhesive films and the resulting mechanical properties; *DPG spring meeting*, Dresden (Germany), March 2011.

- A. Diethert, E. Metwalli, J. Perlich, W. Wang, S. V. Roth, P. Müller-Buschbaum: Surface-near structures in pressure sensitive adhesive films; *GISAS Conference*, Hamburg (Germany), September 2009.

- A. Diethert, S. V. Roth, Y. Peykova, N. Willenbacher, P. Müller-Buschbaum: Surface enrichment in statistical copolymer films; *Frontiers in Polymer Science*, Mainz (Germany), June 2009.

- A. Diethert, E. Metwalli, J. Perlich, W. Wang, S. V. Roth, A. Timmann, Y. Peykova, N. Willenbacher, P.Müller-Buschbaum: Surface enrichment in statistical copolymer films; *HASYLAB User Meeting*, Hamburg (Germany), January 2009.

- A. Diethert, E. Metwalli, P. Müller-Buschbaum: Surface enrichment in statistical copolymer films; *DPG spring meeting*, Berlin (Germany), February 2008.

- A. Diethert, E. Metwalli, J. Perlich, W. Wang, R. Gehrke, S. V. Roth, A. Timmann, P. Müller-Buschbaum: GISAXS study of surface enrichment layers in statistical copolymer films; *HASYLAB User Meeting*, Hamburg (Germany), January 2008.

Acknowledgements

I want to thank Prof. Dr. P. Müller-Buschbaum for giving me the opportunity to work under his guidance. His critical view on my scientific work and his outstanding experience in the field of polymer science were the prerequisite for this varied, instructive and exciting time as a PhD student. Despite his busy time schedule, there was always time for extended discussions and I benefited from his opinion not only regarding scientific topics.

I am grateful for the good interdisciplinary co-operation with the Institut für Mechanische Verfahrenstechnik und Mechanik at the Karlsruher Institut für Technologie. Especially Prof. Dr. N. Willenbacher and Y. Peykova contributed to my work by interesting and fruitful discussions and meetings. Furthermore, I thank U. Licht from *BASF SE* for her professional advice and for donating the polymers. Also the financial support by the DFG in the project MU 1487/6 is gratefully acknowledged.

Many results of this thesis were gathered at large scale facilities. All of the beamtimes were both, extremely interesting and demanding. Nevertheless, owing to the excellent teamwork I experienced, the beamtimes have always been enjoyable. For the very good team play on a professional and interpersonal level, I want to thank Dr. E. Metwalli, Dr. J. Perlich, Dr. W. Wang, Dr. G. Kaune, Dr. M. Abul Kashem, Dr. J.-F. Moulin, M. Ruderer, D. Magerl, Dr. V. Körstgens, R. Meier, Q. Zhong, M. Schindler and A. Nathan. In addition, I thank M. Rawolle and M. Niedermeier for measuring my samples although I did not join the corresponding beamtime.

I further acknowledge the support of the respective local contact persons during the beamtimes Dr. S. Roth, Dr. A. Timmann and Dr. J. Perlich (HASYLAB, BW4) as well as Dr. R. Cubitt and Dr. R. Campbell (ILL, FIGARO) who did a great job in the preparation and the realization of the large scale facility experiments. Very important technical support was provided by the workshop staff of the Lehrstuhl für Funktionelle Materialen (R. Jahrstorfer and R. Funer) and the ILL (S. Wood).

Concerning the work in the Munich laboratories, I thank B. Russ and Prof. Dr. P. Böni for providing the possibility to use the x-ray reflectometer at the Lehrstuhl E21 and Dr. V. Körstgens who developed a *TestPoint* program for gravimetric measurements.

Special thanks goes to my working students Y. Kirjner, A. Sommer and K. Ecker. My dissertation benefits from their high motivation and precise work in the field of contact angle measurements and probe tack tests. I wish them all the best for their future career.

Moreover, I am very thankful to the people who read the manuscript and contributed to its improvement resulting in the submitted thesis: Dr. M. Philipp, Dr. E. Herzig, D. Magerl, M. Schindler, R. Meier, Dr. E. Metwalli, M. Ruderer, M. Rawolle, M. Niedermeier, A. Nikitopoulos and Dr. V. Körstgens.

Doing science at the Lehrstuhl für Funktionelle Materialen was a very enjoyable time for me. Besides the accessibility of very well equipped laboratories and the many opportunities for presenting and discussing my ongoing research (especially at the IUCr2008 conference in Japan), I particularly want to emphasize the good atmosphere in the offices. For this I want to thank my office mates of my first year in the big office (which sometimes could have been a little bigger), and M. Ruderer for the great time together in the small office.

It is more than remarkable how many activities we did together as a team. I will always remember our soccer matches, our hiking days, our conferences and workshops, and of course our famous and extensive celebrations at the Nockherberg or the Oktoberfest. Also the team members I did not mention so far contributed a lot to the very kind atmosphere: J. Adelsberger, C. Birkenstock, P. Douglas, S. Ener, S. Fink, A. Golosova, S. Guo, M. He, W. Hefter, T. Hoppe, S. Jaksch, D. Müller, Prof. Dr. C. Papadakis, S. Prams, K. Sarkar, Prof. Dr. W. Schirmacher, A. Sepe, K. Wagenbauer, W. Wang, Dr. J. Wiedersich and Y. Yuan.

I apologize to my friends who might have missed me during the time I was busy writing this thesis.

A very big thank-you goes to my family, my mother Sigrid, my father Thomas, my sister Tamara and my grandparents, on all of whom I can always rely. As the first person in the family with the academic degree Dr. rer. nat., I dedicate this thesis to them.

I thank my beloved Alexandra for all her support and all her patience especially during the last months.